



HAL
open science

Transport Tunnel Polarisé en Spin à l'Etat Solide

Martin Bowen

► **To cite this version:**

Martin Bowen. Transport Tunnel Polarisé en Spin à l'Etat Solide. Matériaux. Université Paris Sud - Paris XI, 2003. Français. NNT : . tel-00003921v2

HAL Id: tel-00003921

<https://theses.hal.science/tel-00003921v2>

Submitted on 13 Apr 2004 (v2), last revised 24 May 2004 (v5)

HAL is a multi-disciplinary open access archive for the deposit and dissemination of scientific research documents, whether they are published or not. The documents may come from teaching and research institutions in France or abroad, or from public or private research centers.

L'archive ouverte pluridisciplinaire **HAL**, est destinée au dépôt et à la diffusion de documents scientifiques de niveau recherche, publiés ou non, émanant des établissements d'enseignement et de recherche français ou étrangers, des laboratoires publics ou privés.

ORSAY
N. ORDRE:

UNIVERSITE DE PARIS-SUD
U.F.R. SCIENTIFIQUE D'ORSAY

T H È S E

présentée
pour obtenir le grade de

DOCTEUR EN SCIENCES
DE L'UNIVERSITE PARIS XI, ORSAY

Discipline : **Physique des Solides**

par

Martin O. Bowen

Sujet:

Experimental Insights into Spin-Polarized Solid State Tunneling	Transport Tunnel Polarisé en Spin à l'Etat Solide
--	--

Directeur de thèse : **Albert FERT**
préparée à l'Unité Mixte de Physique CNRS-Thales (UMR 137)

soutenue le lundi 29 septembre 2003
devant la Commission d'examen

M ^{me} Agnès BARTHELEMY	M. Peter LEVY (Président)
M. Albert FERT	M. Alain SCHUHL (Rapporteur)
M ^{me} Anne-Marie HAGHIRI	M. Yoshishige SUZUKI (Rapporteur)

Thanks!

Firstly/Tout d'abord/Para empezar, my gratitudes go to Yoshishige Suzuki and Alain Schuhl for reading this manuscript in the sweltering heat of the summer of 2003. They, along with other jury members Peter Levy and Anne-Marie Haghiri, have made valuable contributions to its contents, toward a maturation of the ideas it contains. I feel very fortunate to have defended my Thesis under their supervision.

This Thesis represents the culmination of a now old dream of mine, that of returning to Europe after my undergraduate work at UC Berkeley for further education so as to balance my French and American cultures. Je remercie ainsi Gérard Martinez de l'introduction à la communauté de physique française que son offre de stage en 1998 m'a fournie. Je dois en partie le succès de cette Thèse à la sagacité de Michel Héritier - directeur du DEA de Physique des Solides, lors de mon transfert académique américano-français, et à son soutien lors de mes multiples difficultés cette année-là. Though in the end we did not work together on experiments contained in this Thesis, I am nevertheless indebted to Qiu at UC Berkeley, and to his then graduate student but still indefatigable Roland Kawakami, for their passion of research which I have strived to emulate. Thanks also to Dan Shortenhaus for furthering my interest in physics upon arriving in the US.

Je remercie Alain Friederich de m'avoir accueilli au sein de l'Unité Mixte, et en particulier du soutien qu'il m'a accordé lors de l'écriture du manuscrit. A l'incontournable Nelly revient ma plus vive sympathie car sans elle rien ne fonctionnerait - tout le monde le sait bien. Grands mercis à Albert et Agnès pour leur encadrement lors de ce parcours académique et intellectuel, ainsi que pour les nombreuses discussions, parfois très animées, que nous avons eues - s'il y a du nouveau sur les hauteurs de barrière d'électrons et de trous, on prend un pot au Guichet! La portée des thématiques présentées dans ce manuscrit témoigne de l'indépendance que vous m'avez accordée au cours de cette Thèse, mais aussi de l'ampleur des notions que vous m'avez introduites. Et puis c'est rare de déconner avec ses chefs. Sur ce registre, un grand merci aussi à toi, Vincent, pour notre travail en commun sur Fe/MgO et les manip sur le synchrotron; ainsi qu'à toi, Frédéric Pétrouff, pour ton soutien implicite. Mille mercis à toi, Jean-Pierre, pour ton savoir-faire côté croissance, sans lequel mon travail n'aurait jamais abouti à de tels résultats. En fait j'aurais dû mieux profiter de tes démonstrations de danse lors des dîners de fin d'année (très

mémorables, surtout pour les nouveaux stagiaires!).

Indeed, my work at the UMR would never have been as productive were it not for the fantastic scientific and social atmosphere at the lab - yes, these two are closely correlated! My heartfelt thanks go to the rest of the team: Josette, Eric et Annie au corps à corps avec les échantillons, Jean-Luc et Frédéric Pailloux au TEM, Ives au canon neutralisé, Denis à la cableuse, Frederic Nguyen van Dau aux (futurs!) brevets, Olivier aux macros Origin, Javier, Michael, Rose (reine du LSMO), Rénato, Pierre "the explicator" et "spin-jazzy" Henri, Manu pour ton sacré coup de main, "Magic" Magid of oxide fame, Dan "comment survivre sans le sous au Biergarten" et "comment bien profiter d'une session poster nocturne" parmi moult autres appellations, Julian à la sympathie infinie, Julie aux rollers nocturnes, Guillemain aux échasses, Karsten "moi, froid?", Rozenn, Laurent Vila, Armando Encinas, Francois Montaigne, Frederic "can't slow me down" Gustavsson... Un merci tout particulier à Raymonde Luzeau et Jacqueline Lehoux pour votre aide et votre gentillesse.

I would like to acknowledge with profound gratitude the numerous collaborations which produced the results in this Thesis. Primero, un gran saludo a Alfonso Cebollaba y su equipo, y en particular a Carlos Martinez-Boubeta, compañero del shilom de la madrugada. Merci aussi à toi, Ricardo Bertacco, pour tes nombreuses collaborations avec notre groupe. Enfin, je remercie Dominique Imhoff et Christian Colliex pour leur proche collaboration sur le sujet des interfaces d'oxydes. On va la faire, cette publi sur les jonctions LSMO/STO/CoCr! Je tiens aussi à saluer Jacques Miltat, André Thiaville et Carole Vouille (reine de l'inversion de GMR); ainsi que l'ensemble de l'équipe Schuhl à Nancy. Greetings to Michel Viret, Ronnie Jansen, Henk Swatgen, Pat "Let's discuss this over absinthe" LeClair, Jagadeesh Moodera, Wulf Wulfhekel, Phivos Mavropoulos, and Olaf Wunnicke for valuable discussions and merriment.

Lorsqu'on se déracine à force de déménager sans arrêt, seuls nos amis les plus proches semblent prévenir la schizophrénie culturo-sociale. Merci donc aux familles Plihon, Lochard, Maurin, et tout particulièrement les Thoraval qui m'ont accueilli en catastrophe pendant mes premiers mois de thèse. Cette généreuse hospitalité, bien française, me fut par ailleurs renouvelée par la famille Laurent qui ne cesse de cumuler de tels actes. Merci aussi de m'avoir prêté un ordinateur pendant la rédaction! Je salue les "usual suspects" de nos soirées endiablées: Rémi, Pauline, Vincent, Kamel, Solio, Alex, Marion, Quittrie, Fabienne. Faut qu'on retourne ensemble à

Burning Man! My warm greeting to you, George! Which language will we speak today?! Grosses bises à toi, mon cher Thomas! Il n'y avait que toi pour me donner l'occasion d'aller bosser au labo en robe de chambre! ¡Mucho cariño para ti, Miguel, y la familia Brauns, para su amistad durante tanto tiempo! Autre ami de toujours, compagnon d'aventures de la rue Léon de Berthalot et ma muse de la débrouillardise, j'ai nommé Camille!

Freundlichen Grüßen, Sascha Albrecht/Nerger! Un coucou rapide aux Versaillais, et à la micro-communauté sympa que vous avez entretenue! Coucou aussi aux habitués de Simplon (chez Dan), fournaise d'écœuvrement conviviale nocturne, et merci de votre bouffée d'air frais! En fait on aurait dû racheter tout l'immeuble pour concrétiser le projet d'une coopérative sur Paris... En revanche, j'ai eu la chance et l'intense plaisir de vivre avec Julien dans trois de mes six demeures parisiennes. Ton soutien et ton amitié sans limites auront rempli mon cœur de cette chaleur de vivre qui peut parfois nous manquer. Nous avons tant vécu ensemble ces neuf dernières années! Je te dois beaucoup. Salut aussi à toi, Ivo, car tout est plus dynamique à trois!

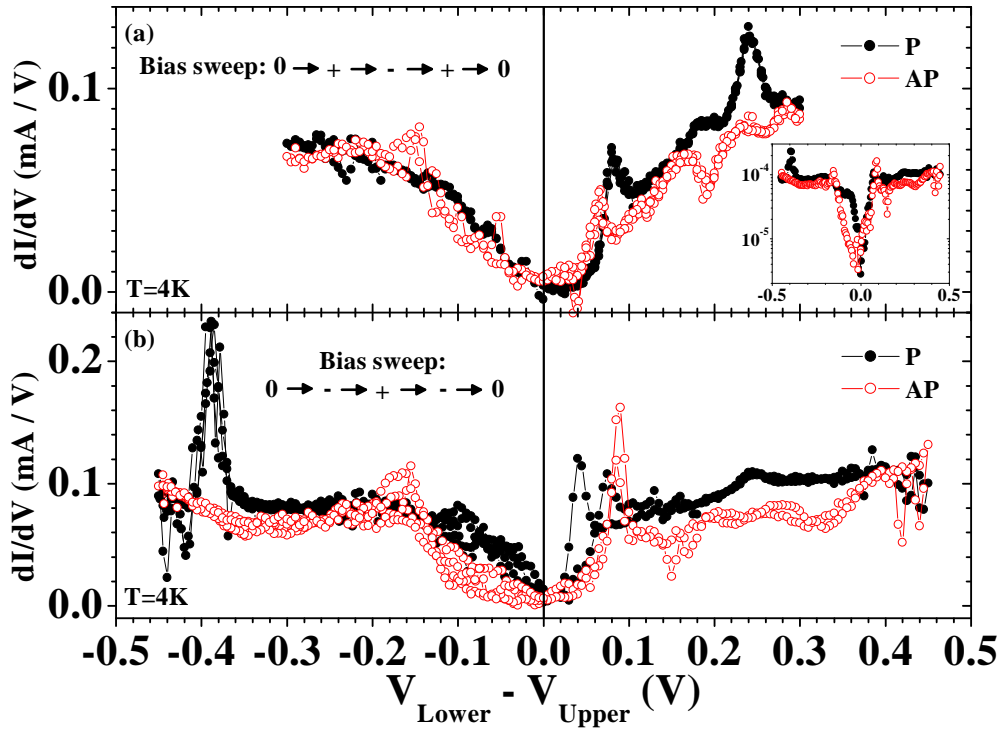
On the topic of communal living, a special thought goes to the USCA and their wonderfully progressive lifestyle project. I cherish this unique experience while studying at Berkeley, and those I grew attached to while living at Stebbins & Kingman coops: Heather, Ariella, Katie, Sam (you're in it, no protest!), Helen, Yishai, "Baby" & "Classic" Drew, Joel (putain t'es ou?), Selby, Davey, Jacqueline, Jay, Nevada, Craig, Chris. Ah Siavash, what can I say but to be grateful to count you among my most cherished friends!

Finally, I dedicate the hard sweat, the vanquished uncertainty, the epiphanies and disappointments behind this now-completed travail to my friend and companion Claudi. Let life be light-hearted, spirited and intense.

To Mom, Dad, Steve, Tom and Loubard, along with my entire family, for their support and love, in spite of the distance.

“Be the change you wish to see in the world.”—Mahatma Ghandi

For beauty if not for science...



Bias dependence of conductance at $T=4\text{K}$ in the parallel (P) and antiparallel (AP) alignments of electrode magnetizations for the LSMO (350 Å)/STO (7ML)/LSMO (100 Å) junction which yielded 1860% TMR, for two successive sweeps (a) and (b) as denoted in the figure. The inset to panel (a) shows data on a logarithmic scale.

Possible explanations: quantum well states in the top electrode, metallic inclusion in the barrier, other quantum interference effects...

Contents

1	Introduction	xv
I	Experimental context	5
2	MTJ fundamentals & concepts	7
2.1	Tunneling basics	7
2.1.1	The WKB approximation	8
2.1.2	The Jullière model	9
2.2	Defining tunneling spin polarization	11
2.2.1	Measuring spin polarization	11
2.2.2	The ferromagnetic/barrier couple	14
2.2.2.1	First hints	14
2.2.2.2	The Slonczewski model	15
2.2.2.3	Interfacial bonding and Metal-Induced Gap States	16
2.2.3	Trilayer band structure effects in MTJs	18
2.3	Bias dependence of magnetotransport	22
2.3.1	Bias voltage & barrier profile	22
2.3.1.1	Barrier profile effects	23
2.3.1.2	Magnetic interlayer exchange coupling	25
2.3.2	Elastic & inelastic tunneling processes	26
2.3.3	Density of States effects	28
2.4	Temperature dependence of TMR	29
2.5	Recent experiments	30
2.5.1	Density of states effects	30
2.5.2	Barrier profile effects	32
2.5.3	Partially and fully epitaxial magnetic tunnel junctions	33
2.5.3.1	Transition metals	34
2.5.3.2	Manganites	37
2.5.3.3	Dilute magnetic semiconductors	37

2.6	This Thesis's scientific motivations	38
2.6.1	The sign of spin polarization of Co	39
2.6.2	On the TMR bias dependence	39
2.6.2.1	A density of states interpretation	39
2.6.2.2	A junction potential profile interpretation	41
2.6.3	On the TMR temperature dependence in LSMO junctions	42
2.6.4	Spin-dependent tunneling in the model system Fe(001)/MgO(001)	42
3	Experimental techniques	43
3.1	Sample growth	43
3.1.1	La _{0.7} Sr _{0.3} MnO ₃ and SrTiO ₃	44
3.1.2	Transition metal counterdeposition	44
3.1.2.1	Sputtering	45
3.1.2.2	Molecular Beam Epitaxy	46
3.1.3	Fe/MgO samples	46
3.2	Sample patterning	48
3.2.1	Process I	48
3.2.1.1	From trilayer to junction in four steps	48
3.2.1.2	Standard Procedures	50
3.2.2	Optimizing the lithographic process for oxide heterostructures	50
3.2.2.1	High lower electrode resistances	50
3.2.2.2	Few junctions per sample	51
3.2.2.3	Trilayer chemical passivation during the etching processes.	51
3.2.2.4	Resist Conditioning	52
3.2.3	Process II: modifying the electrical contact on LSMO	53
3.2.4	Process III: more junctions of smaller size	53
3.2.4.1	Junction Design	54
3.2.4.2	Resist Conditioning	54
3.2.4.3	Sample Etching	55
3.3	Experimental considerations	55
3.3.1	Chemical state of the La _{0.7} Sr _{0.3} MnO ₃ /SrTiO ₃ , SrTiO ₃ /La _{0.7} Sr _{0.3} MnO ₃ and SrTiO ₃ /Co interfaces	55
3.3.1.1	Upper and lower LSMO/STO interfaces	56
3.3.1.2	The STO/Co interface	56
3.3.2	Transport	56
3.3.2.1	Transport measurements	57
3.3.2.2	Determining barrier heights	57

3.3.2.3	Electromigration & Junction forming	58
3.3.3	On junction irreproducibility	61
3.3.3.1	The patterning process	61
3.3.3.2	Electrostatic modifications	61
3.3.3.3	Temporal evolution of oxide junctions	61
3.3.3.4	Pinholes in the epitaxial tunnel barrier	62
3.4	Probing magnetism with XMCD	62
3.4.1	Theory of X-Ray Magnetic Circular Dichroism	62
3.4.1.1	Spin-dependent, element-specific transitions	63
3.4.1.2	The two-step model	64
3.4.1.3	The sum rules	65
3.4.2	Experimental Implications	66
 II Experiments		 67
 4 On ferromagnet/insulator interfaces		 69
4.1	Magnetotransport experiments	69
4.1.1	Nearly total spin polarization at the LSMO/STO in- terface	70
4.1.2	LSMO/I/Co experiments	71
4.1.3	The Fe/MgO(001) interface	74
4.1.3.1	Large magnetoresistance	74
4.1.3.2	Band structure effects	76
4.1.4	Summary	79
4.2	Induced Moments in the tunnel barrier	79
4.2.1	Experimental considerations	80
4.2.2	Experimental results	80
4.2.2.1	Al ₂ O ₃	81
4.2.2.2	MgO	82
4.2.3	Discussion & conclusion	83
 5 Spin-dependent tunneling spectroscopy		 87
5.1	LSMO/STO/LSMO tunnel junctions	87
5.1.1	Spin wave excitations in the low-bias regime	88
5.1.2	Intermediate bias regime	90
5.1.3	The unoccupied spin-dependent DOS of the La _{0.7} Sr _{0.3} MnO ₃ /SrTiO ₃ (001) interface	92
5.1.4	Beyond the minority gap	94
5.1.5	Summary	97
5.2	Revisiting the LSMO/STO/Co system	98

5.2.1	Magnetotransport in LSMO/STO/Co junctions	99
5.2.1.1	Spin wave excitations	99
5.2.1.2	Beyond the spin wave excitation regime	102
5.2.2	Doping with Cr to manipulate the Co spin-dependent density of states	103
5.2.2.1	Cr doping: a spin-dependent modification to the Co DOS	103
5.2.2.2	Magnetotransport results	105
5.2.2.3	An incomplete study	107
5.3	Summary	108
6	On the LSMO/STO interface T_C	109
6.1	Probing with LSMO	109
6.2	Probing with Co	111
6.2.1	Bias-dependent temperature dependence of tunneling transport	112
6.2.2	Spin wave excitations and magnetotransport	114
6.2.3	Bias and temperature dependence of TMR	116
6.2.4	Summary	118
7	Tunneling barrier effects	121
7.1	Electrochemistry of the STO/CoCr interface	122
7.1.1	Chemical state of the SrTiO ₃ / Co _{1-x} Cr _x interface	123
7.1.2	Manipulation of the CoCr/SrTiO ₃ interfacial chemistry through electromigration	125
7.1.2.1	Reversibility of the junction metastable states	126
7.1.2.2	Electrochemical activity between CrO ₂ & Cr ₂ O ₃ probed by spin-polarized tunneling	130
7.1.3	Summary	136
7.2	Interface profile & Fowler-Nordheim tunneling	137
7.2.1	Introduction	137
7.2.2	Barrier heights & magnetotransport trends	139
7.2.3	Magnetotransport above barrier heights: temperature dependence	144
7.2.4	Fowler-Nordheim tunneling and quantum well states in the barrier	146
7.2.5	Fowler-Nordheim tunneling and exchange coupling across the barrier	148
7.2.5.1	Experimental results	148
7.2.5.2	Discussion	150
7.2.6	Summary	153

7.3	On LSMO/STO/Co junctions	154
7.3.1	Barrier crystallinity	154
7.3.1.1	SrTiO ₃	155
7.3.1.2	Ce _{0.69} La _{0.31} O _{1.845}	156
7.3.2	Annealing and forming effects	157
7.3.2.1	Annealing	157
7.3.2.2	Forming	159
7.3.3	Electromigration effects	160
7.3.3.1	Resistance instability & state preparation . .	161
7.3.3.2	Ti electromigration	165
7.3.3.3	Magnetotransport features	168
7.3.3.4	On the TMR sign inversion and Fowler-Nordheim tunneling	171
7.3.3.5	Fowler-Nordheim tunneling and exchange coupling	173
7.3.4	Summary	175
8	Conclusions & perspectives	179
9	Transport Tunnel Polarisé en Spin	185
9.1	Contexte de Thèse	186
9.1.1	Introduction	186
9.1.2	Fondements du transport tunnel	186
9.1.3	Sur le degré de polarisation de spin tunnel	187
9.1.4	Sur le transport inélastique	189
9.1.5	Motivations de Thèse	190
9.2	Travail expérimental	190
9.2.1	Echantillons	190
9.2.2	Lithographie & transport	191
9.2.3	Dichroïsme Magnétique Circulaire X	192
9.3	Résultats expérimentaux	193
9.3.1	Polarisation de spin quasi totale de La _{0.7} Sr _{0.3} MnO ₃ . .	193
9.3.2	Rôle de la barrière dans l'effet tunnel polarisé en spin .	194
9.3.2.1	Transport	194
9.3.2.2	Dichroïsme Magnétique Circulaire X	196
9.3.3	Spectroscopie tunnel polarisée en spin	197
9.3.4	Sur la température de Curie amoindrie à l'interface La _{0.7} Sr _{0.3} MnO ₃ /SrTiO ₃	202
9.3.5	Effets de barrière tunnel	205
9.3.5.1	Électromigration à l'interface SrTiO ₃ /Co _{1-x} Cr _x	205

9.3.5.2	Jonctions $\text{La}_{0.7}\text{Sr}_{0.3}\text{MnO}_3/\text{SrTiO}_3/\text{La}_{0.7}\text{Sr}_{0.3}\text{MnO}_3$	207
9.3.5.3	Jonctions $\text{La}_{0.7}\text{Sr}_{0.3}\text{MnO}_3/\text{SrTiO}_3/\text{Co}$	213
9.4	Conclusions et perspectives	219
A	Bulk band structures & interfaces	223
A.1	Transition metal oxide energy bands	223
A.1.1	Crystal field model	224
A.1.2	Molecular orbital model	225
A.2	The perovskite STO	226
A.2.1	Perovskite crystal structure	227
A.2.2	The band structure of intrinsic SrTiO_3	228
A.2.3	Experimental band positions in $\text{SrTiO}_3(001)$	230
A.2.4	Phase transitions in SrTiO_3	233
A.3	Electronic structure at an interface	234
A.3.1	The Co band structure and DOS	234
A.3.2	The SrTiO_3/Co interface	234
A.3.3	A generalization	238
A.4	The band structure and DOS of LSMO	238
A.4.1	LaMnO_3 : Superexchange between $3d^4$ sites	240
A.4.2	From LaMnO_3 to $\text{La}_{0.7}\text{Sr}_{0.3}\text{MnO}_3$: the special case of double exchange	243
A.4.3	Lattice distortions, half-metallic considerations and pseudogaps	246
A.4.4	Band structure and Fermi surface of $\text{La}_{0.7}\text{Sr}_{0.3}\text{MnO}_3$	247
A.4.5	Deviations in the $\text{La}_{0.7}\text{Sr}_{0.3}\text{MnO}_3$ electronic structure	248
A.4.5.1	Deviations in oxygen stoichiometry	249
A.4.5.2	Electronic phase segregation in double exchange systems	250
A.5	The LSMO/STO(001) interface	251
A.5.1	Electronic structure	251
A.5.2	Exchange considerations between $\text{La}_{0.7}\text{Sr}_{0.3}\text{MnO}_3(001)$ and $\text{SrTiO}_3(001)$	252
A.5.2.1	The $\text{La}_{0.7}\text{Sr}_{0.3}\text{MnO}_3/\text{SrTiO}_3(001)$ interface	252
A.5.2.2	Exchange between interfaces in a $\text{La}_{0.7}\text{Sr}_{0.3}\text{MnO}_3/\text{SrTiO}_3/\text{La}_{0.7}\text{Sr}_{0.3}\text{MnO}_3(001)$ junction	254
B	Structural analysis of interfaces	257
B.1	Chemical state of the LSMO/STO(001) interface	257
B.2	Chemical state of the STO/Co interface	260

C Interlayer exchange interactions	263
C.1 The quantum well state picture	264
C.2 Spacer materials	265

Chapter 1

Introduction

To the layman, quantum-mechanical tunneling may be compared to two situations one can encounter while playing mini-golf. Who has not puttied a ball toward a small hill, only to see it roll back to your feet because not enough kinetic energy was provided to overcome the height of the hill? And how does the ball mysteriously disappear into one hole only to reappear at another? In the quantum mechanical world of uncertain positions and velocities, objects move about spatially as represented by probability waves, and interact with their surroundings as particles. When an electron - to pick a simple object, while moving within a metal, encounters an insulator - which by definition does not conduct electricity, it is most probable that it will bounce off this potential barrier in the opposite direction as would an underputted golf ball. However, the wave nature of the particle offers a more subtle description. As broached in all introductory quantum mechanical textbooks, once the oscillating wavefunction reaches the potential boundary, penetration of the barrier occurs with exponentially decaying amplitude. In the limit of macroscopic insulating distances, such penetration may be set to zero, as expected from our real-world experience. However, for ultrathin barriers, a sizeable wavefunction amplitude subsists at the other side of the barrier. The electron has effectively “tunneled” through this potential hill and, much as the golf ball, magically reappeared on the other side.

Quantum mechanical tunneling has been observed in numerous occasions. In a scanning tunneling microscope, the sensitivity of the tunneling current to the distance between a tip and a sample surface through a potential vacuum barrier has resulted in a marvelous technique to image individual atoms on a surface, and led to interesting fundamental experiments. More recently, it has become possible to take into account the conservation of electron spin through the tunneling process to enhance our vision of the quantum world. In this case, electrodes and barrier are naturally defined and therefore quite distinct. However, a solid state approach implies the challenge of designing such mesoscopic structures given merely macroscopic control. Fueled by interest in technological applications, knowledge of semiconductor growth has evolved over the past 50 years to result in the current explosion of personal computing initiated in the 80s. In this domain of solid state physics, the understanding of the tunneling phenomenon has reached considerable precision as theory has backed up experiments on fully epitaxial artificial heterostructures. However, until very recently, the study of spin-dependent tunneling in such structures has not been possible given the semiconducting nature of the materials used.

The natural approach to studying spin-dependent tunneling involves integrating ferromagnetic transition metals into metal/insulator hybrid structures. However, in contrast to the semiconductor field, the growth knowl-

edge of such structures has evolved more slowly. An early approach involved the formation of the tunneling barrier through plasma oxidation of a metal such as Al. This technique, used nearly 40 years ago to probe spin dependent tunneling effects through an Al_2O_3 barrier by means of the adjacent Al electrode in the superconducting state, was successfully reapplied in 1995 toward the study of junctions comprising two transition metal ferromagnetic electrodes. Much of this success hinged on advances in metallic layer growth techniques such as Molecular Beam Epitaxy and sputtering. The ensuing rebirth of the field has resulted in substantial performance improvements of such Magnetic Tunnel Junctions, in relation to the proper stoichiometry of the barrier, and improved quality of the metal/insulator interfaces on each side of the junction.

Nevertheless, knowledge of spin-dependent tunneling through this particular technological approach has been hindered by theoretical difficulties in modelling the amorphous barrier used in these experiments. Theoretical tracks have therefore involved describing the physics of spin-dependent tunneling mainly through vacuum or ordered barriers, in conjunction with attempts at describing the case of barrier disorder. Given the limitations of a theoretical to such imperfect systems, a need in the field has emerged concerning the experimental study of fully epitaxial magnetic tunnel junctions.

This Thesis attempts to bridge this gap between experimental and theoretical knowledge of spin-dependent tunneling in Magnetic Tunnel Junctions through the experimental magnetotransport study of partly and fully epitaxial oxide heterostructures. Chapter 2 reviews the theory of spin-dependent tunneling in solid state junctions and presents the Thesis's scientific motivations in the context of salient experiments. Chapter 3 describes sample growth conditions, and the experimental techniques of lithographic patterning and X-Ray Magnetic Circular Dichroism to measure magnetotransport properties and magnetic moments. The two techniques are thereafter applied in Chapter 4 to probe the role of the solid state tunneling barrier in promoting the electronic transmission of certain electronic wavefunctions. The main asset of our magnetotransport studies lies with the integration of the manganite $\text{La}_{0.7}\text{Sr}_{0.3}\text{MnO}_3$ into magnetic tunnel junctions. The nearly total spin polarization of this material is then used in Chapter 5 to explicitly affirm the spectroscopic nature of spin-dependent solid-state tunneling. With the knowledge gained from these bias-dependent studies, Chapter 6 investigates the origin of the manganite's depressed Curie temperature regarding transport when at the interface with a tunneling barrier. Chapter 7 describes transport experiments on magnetic tunnel junctions which utilize electromigration effects to probe the incidence of the interfacial density of states and the junction's effective potential profile on spin-dependent tunneling. In

particular, this study relates magnetotransport above the junction's barrier height to the Giant Magnetoresistance pictures of quantum well states and magnetic interlayer exchange coupling. Finally, several appendices provide additional scientific background regarding the contents of this Thesis.

Part I

Experimental context

Chapter 2

Magnetic tunnel junctions: fundamentals, pending questions & Thesis motivations

This Chapter describes the physics behind the spin-dependent tunneling phenomenon, reviews remarkable features behind this effect of band structure mismatches throughout the heterostructure, and outlines the scientific motivations behind the experimental investigations in this Thesis. In Section 2.1, we first introduce overarching aspects of the tunneling process within a simplified free electron framework which equates the insulating barrier to a simple potential step. Section 2.2 tackles the subject of transport spin polarization as understood up to the onset of this Thesis. The bias and temperature dependencies of magnetotransport on applied junction bias and temperature are broached in Sections 2.3 & 2.4 respectively. A compendium of recent experiments of relevance to this Thesis is presented in Section 2.5. Finally, Section 2.6 presents magnetotransport experiments on $\text{La}_{0.7}\text{Sr}_{0.3}\text{MnO}_3/\text{SrTiO}_3/\text{Co}$ junctions which motivated this Thesis's experimental investigations. Throughout this Chapter, special consideration is given to the case of spin-dependent tunneling from double exchange electrodes since it represents a primary axis of experimental investigation for this Thesis.

2.1 Tunneling basics

Figure 2.1 depicts the quantum mechanical tunneling process for a wavefunction traversing a metal/insulator/metal heterostructure. A tunneling current through such a junction results from the application of a bias be-

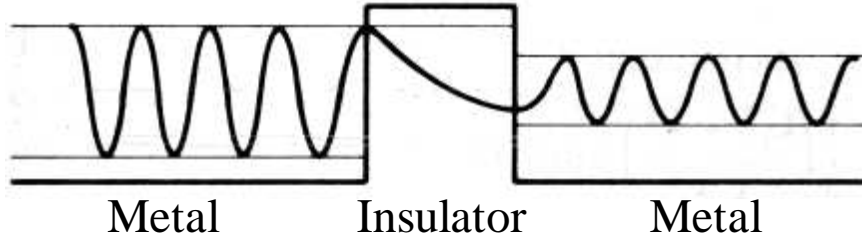


Figure 2.1: Schematic of a wavefunction within a metal undergoing quantum mechanical tunneling through a potential barrier toward another metal.

tween its metallic electrodes. At $V=0$, the Fermi levels of the two electrodes align, so that currents from either side of the junction cancel each other out. When a bias V is applied, the electrode Fermi levels shift by eV relative to one another. A phenomenological variant of the Fermi golden rule, proposed by Bardeen to explain metal/insulator/superconductor results, [1] uses a perturbation technique to describe independent wavefunctions on either side of the barrier. In this limit a barrier with infinite thickness and abrupt potential step is required. With these assumptions, the electron tunneling current $I(E)$ at given energy E from the injecting electrode (Inj) to the collecting (Col) electrode is:

$$I(V) = \int_{-\infty}^{+\infty} \rho_{Inj}(E) \rho_{Col}(E + eV) |M(E, V)|^2 f(E) [1 - f(E + eV)] dE \quad (2.1)$$

where $\rho(E)$ is the electrode density of states (DOS), $f(E)$ is the Fermi-Dirac distribution and $M(E, V)$ is the tunneling transfer matrix. Davis and MacLaren show that since applied bias may involve new unoccupied states in the collecting electrode, and modify the potential profile of the barrier, [2] this matrix element is indeed energy- and bias-dependent.

2.1.1 The WKB approximation

Much of the widely used theory to model experimental results relies on simplifications of the one-dimensional approach reflected in Equation 2.1. Indeed, the Simmons, [3] Brinkman [4] and Stratton [5] models generally used to extract barriers heights, thicknesses, and in the Brinkman framework, barrier asymmetry, all make use of the WKB approximation which holds for gradual changes in the junction potential landscape compared to the wavefunction decay length into the barrier. Given approximately equivalent length scales $\sim \text{\AA}$, the merit of this approximation is debatable. Furthermore, in enabling

an analytical solution to the transfer matrix coefficients $M(E,V)$, this approximation eliminates the electrode densities of states in the expression of tunneling conductance of Equation 2.1. [6]

Nevertheless, this approach yields some qualitative notions regarding the tunneling process. The Brinkman model considers a trapezoidal barrier of the form $\Phi(x, V) = \Phi_{Inj} + \frac{x}{d}(\Phi_{Col} - eV - \Phi_{Inj})$ where d is the barrier thickness and Φ the potential step at each interface. In the limit $V \ll \Phi$, dynamic conductance may be written as

$$\frac{G(V)}{G(0)} = 1 - \left(\frac{A_0 \Delta \bar{\Phi}}{16\bar{\phi}^{3/2}}\right)eV + \left(\frac{9A_0^2}{128\bar{\phi}}\right)(eV)^2 \quad (2.2)$$

with

$$G(0) = \frac{e^2}{h^2 d} \sqrt{2m\bar{\phi}} e^{-\frac{4\pi d}{h} \sqrt{2m\bar{\phi}}}$$

and

$$A_0 = 4\sqrt{2m} \frac{d}{3\hbar}$$

where $\bar{\phi}$ is an *average* barrier height, and $\Delta \bar{\Phi}$ the barrier asymmetry at $V=0$. Thus, in addition to the parabolic dependence of junction conductance with applied bias, this free electron model underscores the exponential dependence of the tunneling process on carrier effective mass m , barrier thickness d and height Φ as $G \propto e^{-d\sqrt{m\Phi}}$. This implies that the tunneling process is sensitive to the density of states near the Fermi level of the electron-injecting metallic electrode near the interface with the tunneling barrier.

2.1.2 The Jullière model

In 1975, Jullière applied Equation 2.1 to explain his original Tunneling Magneto-Resistance (TMR) results on Fe/Ge/Co junctions. [7] In the limit $T \rightarrow 0$, constant M and for infinitesimal disequilibrium eV , this expression reduces to

$$\frac{I}{V} \propto |M(E, V)|^2 \rho_{Inj}(E_F) \rho_{Col}(E_F) \quad (2.3)$$

Therefore, in this extensive simplification, the linearized tunneling conductance is directly related to the DOSs of the electrodes at the Fermi level. To consider spin-dependent tunneling transport, Jullière used the following definition of a ferromagnet's spin polarization:

$$P = \frac{\rho^\uparrow(E_F) - \rho^\downarrow(E_F)}{\rho^\uparrow(E_F) + \rho^\downarrow(E_F)} \quad (2.4)$$

In a picture of two spin-independent conduction channels to promote electron transfer, given the electrodes' spin polarization as defined above, and the requirement of electron spin conservation during the tunneling process, it is evident that current in the parallel and antiparallel alignments of electrode magnetizations will differ. For instance, spin \uparrow electrons will tunnel toward \uparrow (\downarrow) empty states in the parallel(antiparallel) configurations. These considerations are summarized in the schematic of Figure 2.2.

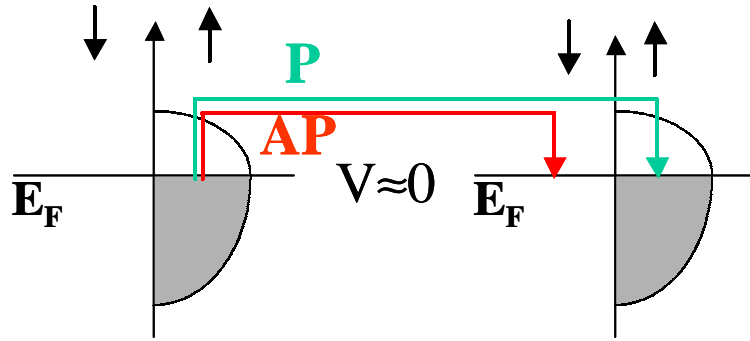


Figure 2.2: Schematic of the spin-dependent tunneling process through an insulating barrier in the special case of half-metallic electrodes when their magnetizations are aligned parallel (P) and antiparallel (AP) to one another. The process is assumed to be purely elastic, so that no mixing of spin states occurs during the process.

Using Equations 2.3 & 2.4, the tunneling magnetoresistance ratio (TMR) may be expressed as

$$TMR = \frac{I_P - I_{AP}}{I_{AP}} = \frac{R_{AP} - R_P}{R_P} = \frac{2P_{Inj}P_{Col}}{1 - P_{Inj}P_{Col}} \quad (2.5)$$

The dissociation of a ferromagnetic electrode's spin polarization from the interplay of band structures throughout the MTJ heterostructure thus represents both a practical simplification and in certain cases a limitation to a more accurate picture. Though limits to this model are increasingly becoming evident, it has nevertheless enjoyed much success in correctly predicting TMR amplitudes based on predicted and/or measured spin polarizations. We will reexamine the concept of spin polarization as applicable to MTJs in Section 2.2.

2.2 Defining tunneling spin polarization

This Section offers a rapid review of the historical concepts behind the definition, and measurement techniques, of spin polarization. For a more detailed account of the historical pitfalls behind measurements of spin polarization, we refer the interested reader to Theses by P. Seneor [8] or P. LeClair. [9] As will become clear, the overarching conceptual difficulty resulted both from the mindset described previously of decoupling a ferromagnet's spin polarization from the electronic filtering character of a tunnel barrier, and from technological limitations regarding spin polarization measurements.

2.2.1 Measuring spin polarization

The degree of spin polarization of a tunneling current originating from a ferromagnet may be generally defined as:

$$P_T = \frac{\rho^\uparrow(E_F)|M_\uparrow|^2 - \rho^\downarrow(E_F)|M_\downarrow|^2}{\rho^\uparrow(E_F)|M_\uparrow|^2 + \rho^\downarrow(E_F)|M_\downarrow|^2} \quad (2.6)$$

If the transmission matrix M is considered constant, this expression reduces to the much used Equation 2.4. However, as argued by Mazin, [10] the nature of the physical process underlying this spin polarization may result in specific dependencies of M on the Fermi velocity v_F . This is notably the case regarding the Andreev technique, for which $|M_\uparrow|^2 \propto v_F$. This technique, originally discussed by Blonder, Tinkham and Klapwijk in 1982, [11], was extended to ferromagnets [12] and used to probe the spin polarization P_C of a variety of ferromagnetic materials (see Table 2.1). [13, 14]

In the tunneling process, $|M_\uparrow|^2 \propto v_F^2$. Therefore, in the context of spin-dependent tunneling, it is more salient to consider the degree of spin polarization as measured through a technique which exploits this transport phenomenon. In 1970 Meservey and Tedrow developed the first technique to measure the amplitude and the sign of the spin-polarized tunneling probability from the ferromagnet(FM) by performing tunneling experiments on FM/Al₂O₃/Al junctions. When the temperature is lowered below the Al superconducting threshold, an energy gap opens at the Fermi level of the quasiparticle density of states, the voltage threshold of which may be spin-split by an external field. As the DOS of the superconductor represented in Figure 2.3a shows, within that narrow $2\mu_B H$ voltage window, the superconducting electrode is fully spin-polarized.

Given the conservation of spin during the tunneling process, [16] and the phenomenological dependence of conductance on the electrodes' DOS as proposed by Bardeen (see Equation 2.1), each junction conductance peak should

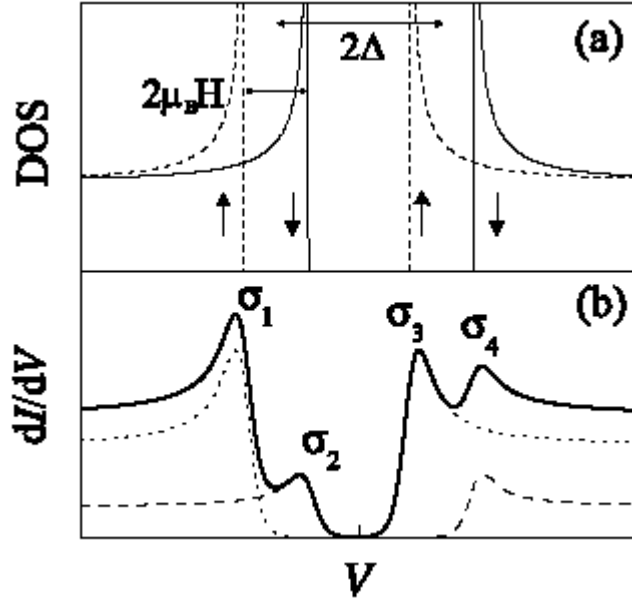


Figure 2.3: Measuring a ferromagnet's (FM) spin polarization from FM/Barrier/Superconductor tunneling experiments: (a) Zeeman-split superconductor DOS. Tunneling in a ferromagnet/insulator/superconductor junction. (b) Bias dependence of total (solid curve) and spin-resolved (dotted and dashed curves) conductances. After Meservey & Tedrow *et al.* [15]

reflect the spin conductance of the superconductor weighed by that of the ferromagnetic counterelectrode. The spin polarization P_T of the ferromagnet near E_F , as measured by this tunneling technique, is then reflected by the relative heights of the four conductance peaks σ_{1-4} as:

$$P_T = \frac{(\sigma_4 - \sigma_2) - (\sigma_1 - \sigma_3)}{(\sigma_4 - \sigma_2) + (\sigma_1 - \sigma_3)} \quad (2.7)$$

In the example of Figure 2.3b, with $\rho_{\uparrow}(E_F) = 3\rho_{\downarrow}(E_F)$, this definition of spin polarization indeed leads to $P_T=50\%$. Although the accuracy of this technique depends on additional corrections for orbital depairing and spin-orbit scattering, [15] it has been successfully used by Meservey and Tedrow, and more recently by a number of groups to obtain values of tunneling spin polarization for various FM transition metals in FM/ Al_2O_3 /Al junctions. [17–20] Table 2.1 lists the highest values P_T found for given ferromagnetic electrodes and offers a comparison with those of P_C found using the point-contact Andreev reflection technique.

A source of confusion and controversy in the field of spin-dependent tun-

	$P_T(\%)$	Ferromagnet	$P_C(\%)$ [13]
I=Al ₂ O ₃	33 [17]	Ni	46
	36 [18]	Ni ₉₀ Fe ₁₀	
	42 [17]	Co	42
	45 [18]	Fe	45
	48 [17]	Ni ₈₀ Fe ₂₀	37
	51 [17]	Co ₅₀ Fe ₅₀	
I=SrTiO ₃	55 [18]	Ni ₄₀ Fe ₆₀	
	72 [19]	La _{0.7} Sr _{0.3} MnO ₃	78
	-9.5 [20]	SrRuO ₃	51 [14]
		NiMnSb	58
	CrO ₂	90	

Table 2.1: Values of ferromagnet (FM) spin polarization P_T and P_C extracted from FM/I/Al tunneling, and point-contact Andreev reflection experiments, respectively. References are indexed therein.

neling lay with the positive sign of spin polarization observed in all experiments, even though for hard ferromagnets such as Co with $\rho^\downarrow(E_F) > \rho^\uparrow(E_F)$, a negative sign should have been observed. This technique should have provided the correct sign of spin polarization, yet in all early experiments, a positive sign was consistently observed. As we will describe below, this conceptual difficulty resulted from the use of an Al₂O₃ barrier, historically chosen due to the technological challenge of designing such FM/I/S junctions differently than with the convenient superconducting Al/insulating Al₂O₃ bilayer couple. This in turn led to the amalgam of a FM's intrinsic spin polarization to that reflected by a particular ferromagnetic/barrier couple.

Breakthrough experiments in 1999 involved the study of spin-dependent tunneling through transition metal oxide barriers which showed inverse TMR - a lower resistance in the antiparallel alignment of electrode magnetizations compared to the parallel. This observation implied a negative ferromagnet spin polarization at the interface with such a barrier. Sharma *et al.* observed inverse TMR in junctions with Ta₂O₅ and hybrid Ta₂O₅/Al₂O₃ barriers.¹ At our laboratory, magnetotransport experiments on La_{0.7}Sr_{0.3}MnO₃/SrTiO₃/Co junctions also evidenced inverse TMR. [22] Given the half-metallic nature of La_{0.7}Sr_{0.3}MnO₃ with only spin \uparrow carriers at E_F , it was argued that the inverse TMR reflected a neg-

¹An alternate explanation involves differences in the interfacial potential profiles at each interface (see Section 2.3.1.1) due to a poorer oxidation of Ta and/or differing potential barrier heights at each interface. [21]

ative sign of spin polarization of the Co counterelectrode expected from its exchange-split d bands. Further experiments on $\text{La}_{0.7}\text{Sr}_{0.3}\text{MnO}_3/\text{I}/\text{Co}$ ($\text{I}=\text{Ce}_{0.69}\text{La}_{0.31}\text{O}_{1.845}, \text{Al}_2\text{O}_3, \text{SrTiO}_3/\text{Al}_2\text{O}_3$) showed that the sign of tunneling spin polarization of a transition metal could not be dissociated from the barrier material. [23] To confirm the different transmission character of a SrTiO_3 barrier compared to Al_2O_3 , and to reaffirm the ability for the spin-dependent tunneling technique to measure the sign of a ferromagnet's spin polarization, Worledge and Geballe performed conductance measurements on $\text{SrRuO}_3/\text{SrTiO}_3/\text{Al}$ junctions. [20] As shown in Table 2.1, they found a spin polarization of -9.5% for SrRuO_3 , in agreement with the expected sign of spin polarization. A very recent report of inverse spin polarization at the $\text{SrRuO}_3/\text{SrTiO}_3$ interface through magnetotransport measurements in $\text{La}_{0.7}\text{Sr}_{0.3}\text{MnO}_3/\text{SrTiO}_3/\text{SrRuO}_3$ junctions has not only confirmed this negative spin polarization but also further confirmed the DOS interpretation of inverse TMR at low bias in the LSMO/STO/Co system. [24] Table 2.1 also references values of spin polarization found for a SrTiO_3 barrier.

These experiments demonstrate the inaccuracy of simply considering the tunneling barrier in solid state structures as a potential step. The following Sections lend support to the notion of treating the ferromagnet and the tunneling barrier as a couple, toward considering band structure effects through the entire junction trilayer.

2.2.2 The ferromagnetic/barrier couple

2.2.2.1 First hints

Since the spin dependent tunneling technique, until quite recently, always yielded a positive sign of ferromagnet spin polarization, attempts were made to explain this discrepancy. A first approach was to consider how an electron current may be spin-polarized. Electronic transport in metals is generally dominated by s electrons due to a larger delocalization and larger Fermi velocities, compared to d electrons. Through s - d wavefunction hybridization, as illustrated in Figure 2.4, it is possible to polarize the current.² However, the sign of such spin-polarized s bands is always found to be positive.

To explain the positive sign of spin polarization observed, Stearns proposed in 1977 that the spin polarized current consist of highly itinerant electrons with d character, thus providing the basis for a picture of s - d wavefunction hybridization (see Figure 2.4) underlying the overarching concept of spin-polarized currents. [26] Also, improved evanescent coupling efficiency

²This fact is far from trivial as spin-polarized currents lie at the heart of the field of spin electronics!

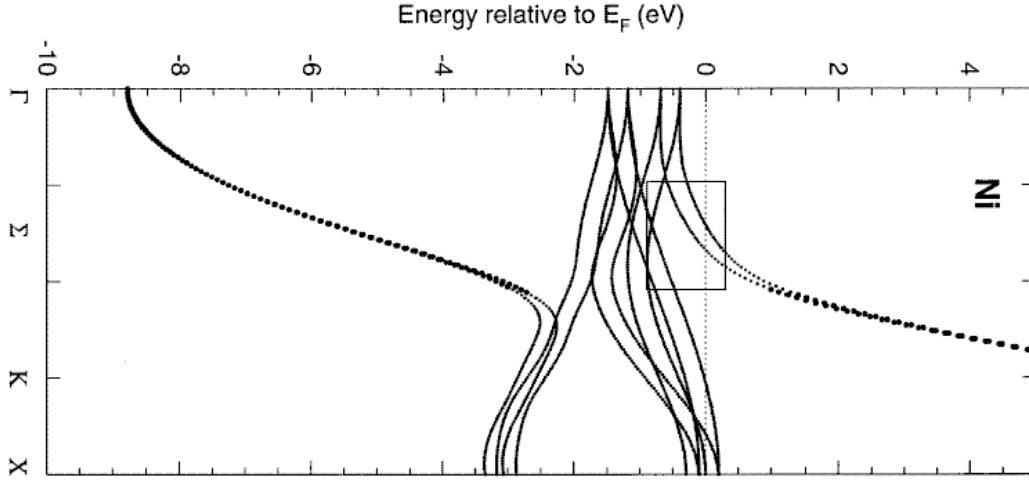


Figure 2.4: Band structure calculation of Ni. Avoided crossings between sp bands with parabolic dispersion, and flat d bands, result in spin polarized spd hybrids, which are framed as they cross the Fermi level. Note the crystal orientation dependence of such hybridization. From Himpfel *et al.* [25]

of s -character wavefunctions into the tunneling barrier, compared to wavefunctions of d -character, due to their larger orbital overlap into the barrier, could explain the experimental result. Regarding field emission, this was asserted as early as 1969 [27] and confirmed experimentally in 1976. [28] Recently, this consideration was reasserted theoretically regarding solid state tunneling. [29]

2.2.2.2 The Slonczewski model

In 1989 J. Slonczewski proposed a more rigorous tunneling framework, devoid of the WKB approximation, which introduces a degree of electronic interaction between the ferromagnet and the tunneling barrier. [30] In this model the barrier band structure isn't explicitly taken into account, so that this model best describes the case of tunneling through a vacuum barrier. This free-electron method, broached in every introductory quantum mechanics treatise, considers incident and reflected plane wavefunctions at each junction interface, and takes into account eventual overlap within the barrier. Slonczewski's model also introduces spin polarization through an exchange field which splits the chemical potential of the two spin populations. In the case of nearly normal wavefunction incidence on the tunneling barrier ($k_{\parallel} \approx 0$), and for $T \rightarrow 0$, an infinitesimal applied bias involves states near the Fermi level in the tunneling process as

$$G_{P(AP)} = G_0(1 \pm P^2) \quad (2.8)$$

where the spin polarization P of the ferromagnet/barrier couple is

$$P = \frac{k_{\uparrow} - k_{\downarrow} \kappa^2 - k_{\uparrow}k_{\downarrow}}{k_{\uparrow} + k_{\downarrow} \kappa^2 + k_{\uparrow}k_{\downarrow}} \quad (2.9)$$

and

$$G_0 = \frac{\kappa}{\hbar d} \left[\frac{e\kappa(\kappa^2 + k_{\uparrow}k_{\downarrow})(k_{\uparrow} + k_{\downarrow})}{\pi(\kappa^2 + k_{\uparrow}^2)(\kappa^2 + k_{\downarrow}^2)} \right]^2 e^{-2\kappa d} \quad (2.10)$$

In 1997 Bratkovsky extended the Slonczewski model by taking into account the electron effective mass m^* within the barrier. [31] The incidence on spin polarization as expressed in Equation 2.9 is to weigh the $k_{\uparrow}k_{\downarrow}$ factors by $(m^*)^2$.

Thus treating the quantum mechanical system in its entirety leads to a spin polarization P which involves the decay length κ of the wavefunction into the barrier. It is therefore impossible to distinguish a spin polarization which is intrinsic to the ferromagnet used. Though this result is limited to a free electron case, we will see in later Sections that this general conclusion holds even for more complex tunneling considerations. In the limit of infinite barrier height, $\kappa \rightarrow 0$ and the spin polarization P in Equation 2.9 reduces to that of Equation 2.4 used in the Jullière model. It is even possible to retain the Jullière model if one defines an effective spin interfacial spin polarization resulting from the ferromagnetic/barrier couple. Section 2.2.3 will show, however, that in fully epitaxial junctions band structure effects may need to be taken into account *throughout* the trilayer structure to account for the resulting TMR. The two interfacial spin polarizations cannot then be dissociated from one another, as premised in the Jullière model.

2.2.2.3 Interfacial bonding and Metal-Induced Gap States

With the renewal of spin-dependent tunneling through pioneering experiments by Moodera *et al.* (Massachusetts, USA) in 1995, [32] and the consistently positive values of TMR observed in magnetic tunnel junctions integrating an Al_2O_3 barrier, the question of the positive sign of observed spin polarization regardless of the ferromagnet used once again begged a satisfying explanation. Tsymbal and Pettifor argued in 1997 that different types of bonding at the interface between a FM and an insulator could lead to changes in amplitude, and even in sign, of the spin-polarized tunneling current. [33] In the case of $ss\sigma$ bonding, the s character of the FM's conduction current (see previously), with positive spin polarization, is maintained into

the barrier. In contrast, $sd\sigma$ bonding may decrease or reverse this positive sign of spin-polarized current since the spin-polarized d bands at the Fermi level carry a much larger DOS than their s counterparts.

To further probe interfacial bonding effects requires modelling the actual tunneling barrier. Yet until then the vast majority of experiments had been performed on junctions with an amorphous Al_2O_3 barrier. In comparison with theoretical investigations on ideal structures (see Section 2.2.3 hereafter), such an endeavour is both less salient since it is no longer possible to discuss tunneling in terms of wavefunctions with given electronic symmetries, as well as difficult to carry out since it is arduous to model an amorphous material. At the onset of this Thesis, Oleinik, Tsymbal and Pettifor presented results on the calculation of the moment induced on Al and O sites within a α - Al_2O_3 (0001) relaxed epilayer atop a fcc(111) Co layer. [34] While on Al sites any induced moment is virtually negligible, on O sites a negative moment is found at the first layer away from the interface. Extending into the barrier, the moment switches sign past $\approx 10\text{\AA}$. The authors argue that this eventually positive sign of O site spin polarization at E_F corresponds to that observed in all experiments reported above. The origin of this sign changes lies with the stronger s - d hybridization for minority electrons compared to majority electrons, leading to a smaller tunneling current for minority electrons. [35]

In light of the negative spin polarization of Co at the interface with SrTiO_3 in $\text{La}_{0.7}\text{Sr}_{0.3}\text{MnO}_3/\text{SrTiO}_3/\text{Co}$ junctions, Oleinik, Tsymbal and Pettifor calculated the DOS for the fcc(111) Co/ SrTiO_3 (001) [36] ideal interface. [36] In this case, the authors find an additional d - d bonding between Co and Ti of d_{xz} and d_{yz} symmetry mediated by O $2p$ states which induces both a negative spin polarization—as in the case of Al_2O_3 , along with a magnetic moment on the Ti site. This $pd\pi$ hybridization leads to antiferromagnetic coupling of Co and Ti through superexchange [37] (see Figure A.9c page 237). The authors argue that this inverted moment on the Ti site could explain the observed negative tunneling spin polarization of Co at such an interface.

In addition, virtual gap states, or Metal-Induced Gap States, which are used to explain how an electron may physically cross the insulating barrier, affect the tunneling current. They may be represented by Bloch evanescent wavefunctions with a complex wavevector κ which penetrate the insulator over several \AA . [38] As discussed by Tersoff, [39] the spectral weight of MIGS at a given energy level within the gap depends on the efficiency for metallic wavefunctions to hybridize with valence and conduction band states as evanescent MIGS states. Referring to the schematic of Figure 2.5a, the charge neutrality level (CNL) indicates the energy position within the gap with equal decay lengths. For purposes of clarity, we defer a more in-depth

discussion of this topic to Appendix A, which presents a generalized overview of the band structure of conventional and transition metal oxides (see Section A.1), and discusses MIGS considerations on such electronic structures (see Section A.3.2). Nevertheless, the key consideration lies in the comparison of electronic symmetry between the valence and conduction bands, and the position of the Fermi level relative to the CNL. For conventional insulators such as Al_2O_3 or MgO , the valence and conduction bands share the same Δ_1 symmetry, so that the CNL, which may pin the Fermi level, [39,40] lies at the center of the gap. This consideration is illustrated in Figure 2.5b for the case of MgO .

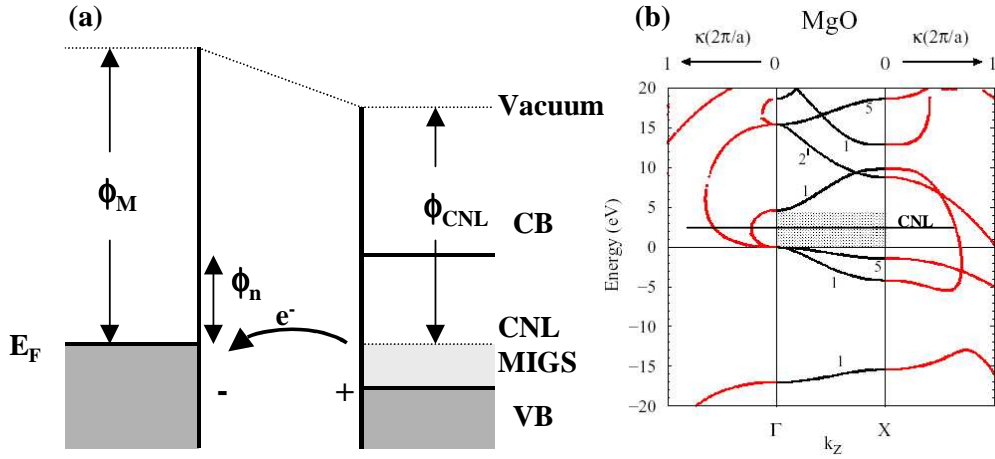


Figure 2.5: (a) Schematic band structure of MIGS at a Metal/Semiconductor interface. (b) Complex band structure of $\text{MgO}(001)$ by Bellini [41]

In the case of a direct band gap, tunneling is favored at the Γ point due to smaller κ loops joining the valence and conduction bands, compared to other k_{\parallel} points. However, if the band gap is indirect, then it is conceivable that $k_{\parallel} \neq 0$ states could be favored. [42] We will revisit these considerations in the case of a SrTiO_3 barrier with Δ_1 valence, and Δ_5 conduction, bands in Section 2.6.

2.2.3 Trilayer band structure effects in MTJs

Ever more rigorous *ab-initio* theoretical treatments have led to an increasingly rich physical picture behind the concept of tunneling spin polarization. A major advance came when the electronic symmetry of the spin carriers was taken into account. $\text{Fe}(001)$ has been an oriented material of choice to evidence such band effects from a theoretical standpoint. Indeed, while

the material has a spin polarization of 45% at E_F averaged over all electron symmetry states, the Δ_1 symmetry group presents a complete spin polarization. [43] Indeed, as shown in Figure 2.6, while the majority Δ_1 band crosses E_F along the Γ -H axis, the minority Δ_1 band lies 1.4eV above E_F at the Γ point.

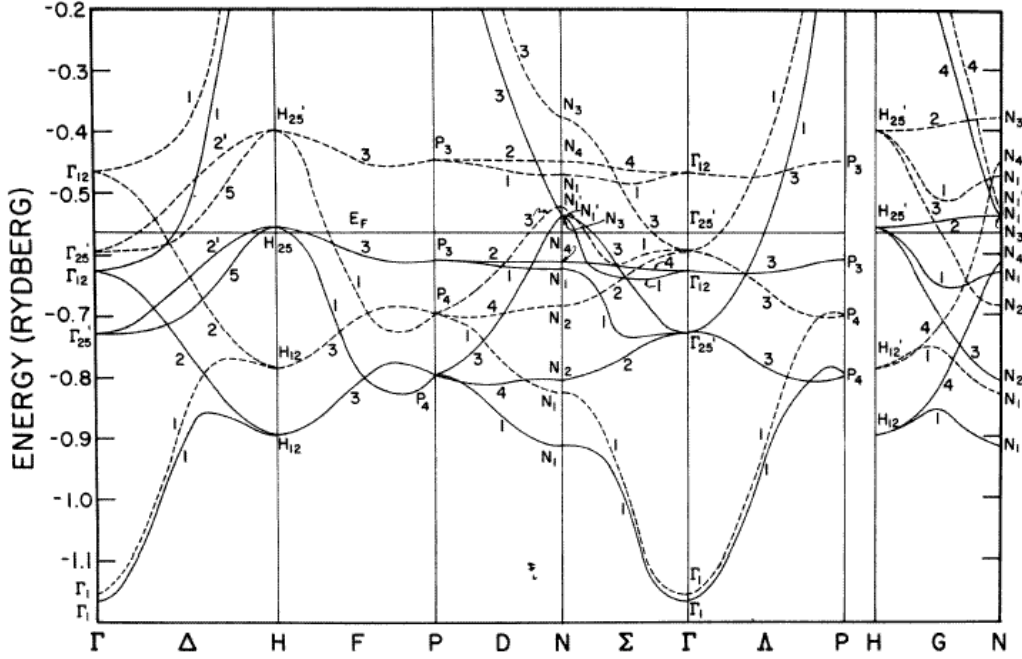


Figure 2.6: Spin polarized band structure calculation of bcc Fe. Majority (minority) bands are denoted by full (dotted) lines. From Callaway & Wang. [43]

In the case of an amorphous tunneling barrier, this total spin polarization of Fe(001) for electrons with Δ_1 symmetry does not constitute a salient feature of magnetotransport since the disordered barrier blurs any distinction between symmetry states.

On the other hand, an epitaxial barrier may *filter* electrons with a given electronic symmetry through coherent tunneling. First one must consider interfacial bonding to determine how effective wavefunction coupling into the insulator is for a given electronic state. Then, the spin-polarized density of such a state decays exponentially into the barrier according to the decay length κ set by the barrier's Metal-Induced Gap States (see above). Barriers such as MgO(001) (see Figure 2.5 previously) or ZnSe [42] promote efficient bonding and tunneling transmission of Δ_1 states, compared to other electronic symmetries. The conjunction with Fe(001) electrodes possessing

complete spin polarization of Δ_1 states at E_F is therefore apt to yield a very high TMR ratio.

The tunneling conductance through such an electrode/barrier/electrode matchup has been considered at length: first through a generic potential step, [44] then through ZnSe(001), [45] and finally through MgO(001). [46,47] Since spin-dependent tunneling results on MgO-based fully epitaxial junctions will be presented in Section 4.1.3, we review these effects in the context of this barrier.

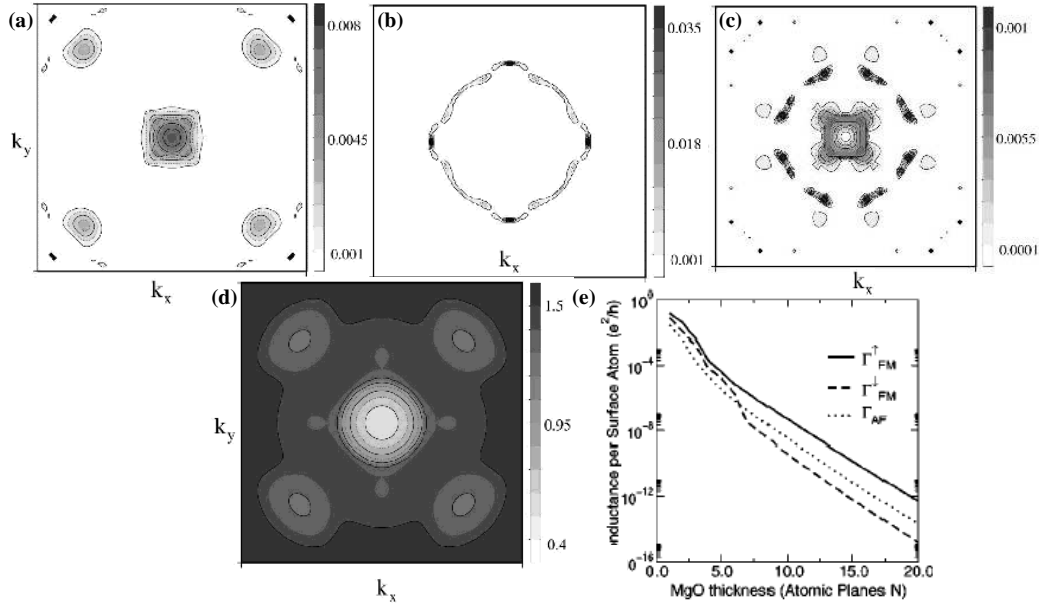


Figure 2.7: (001)-oriented Fe/MgO/Fe: junction conductance in k_{\parallel} space for (a) majority and (b) minority electrons in the parallel configuration, and (c) in the antiparallel configuration for $d_{MgO}=4ML$. (d) The smallest electron decay constant of the MgO barrier in k_{\parallel} space at the Fermi surface. (e) MgO thickness dependence of tunneling conductance for majority, minority electrons, and in the antiparallel configuration. From Mathon *et al.* [47]

Figure 2.7 presents a theoretical outlook within linear response theory by Mathon and Umerski on magnetotransport in a (001)-oriented Fe/MgO/Fe trilayer. [47] Panels (a), (b) and (c) present tunneling conductance through four atomic layers of MgO in k_{\parallel} space for majority and minority electrons in the parallel, as well as in the antiparallel state of alignment of the electrodes' magnetic moments. For this relatively small barrier thickness, majority and minority conductances in the parallel state reflect features of the majority and minority band structure of Fe(001) (not shown), while the antiparallel case combines features from each spin channel. The recurring presence in

such calculations, as an intrinsic feature, of minority states far away from the Γ point which promote nearly complete, undamped transmission through the barrier, remains somewhat puzzling from an experimental standpoint since in principle such states may shortcircuit the junction. However, as the barrier thickness increases, transmission in k_{\parallel} space through the junction is increasingly weighed by band structure effects of the barrier material itself. Panel (d) represents the mapping in k_{\parallel} space of the smallest decay constant κ , obtained by examining the lowest sheet of the complex MgO Fermi surface. For such a barrier, conductance around the Γ point is enhanced relative to other points in k_{\parallel} space, so that, past $\approx 5\text{ML}$, the transmission of minority states at in $k_{\parallel} \neq 0$ is quenched (see panel (e)). Thus, at larger barrier thicknesses, solely the dominant tunneling at the Γ point need be considered.

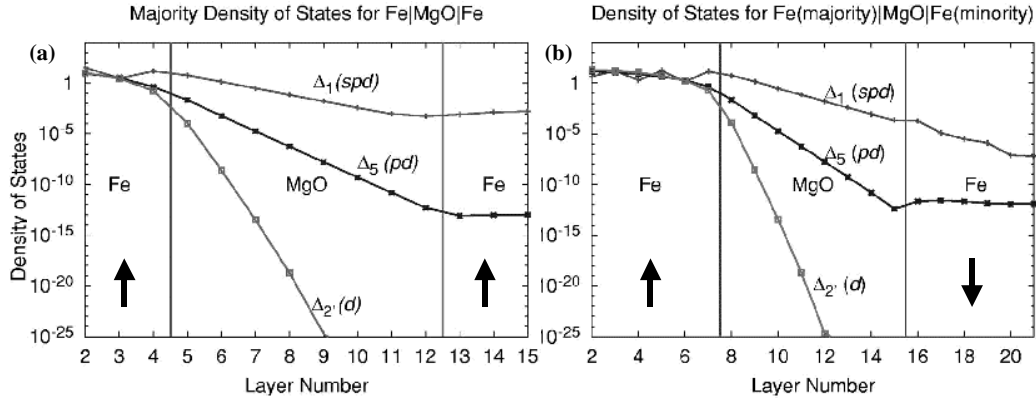


Figure 2.8: (001)-oriented Fe/MgO (8ML)/Fe: electron symmetry-resolved spin \uparrow tunneling DOS at the Γ point ($k_{\parallel}=0$) in the (a) parallel and (b) antiparallel configurations. From Butler *et al.* [46]

Figure 2.8 presents a layer Korringa-Kohn-Rostoker calculation by Butler *et al.* of the spin \uparrow electron symmetry-resolved tunneling conductance at the Γ point through a (001)-oriented Fe/MgO (8ML)/Fe trilayer. Panel (a) presents the case of a parallel alignment of electrode moments. While electrons of all symmetries approach the first Fe/MgO interface with unity DOS, evanescent wavefunction coupling (*aka* bonding) efficiency already introduces a measure of discrimination, as the density of Δ_1 states is much less affected by the onset of the interface compared to Δ_5 or $\Delta_{2'}$ states. As the states progress within the barrier, the exponential decrease is much stronger for $\Delta_{2'}$ and Δ_5 states compared to Δ_1 states, owing to a smaller decay constant κ for the latter. For $d_{\text{MgO}}=8\text{ML}$ - a reasonable barrier thickness, the transmitted density of Δ_1 states overshadows that of Δ_5 states by 10 orders of magnitude. The barrier has effectively *filtered* the tunneling current to

transmit only Δ_1 states. Notably, in the case of antiparallel alignment of the electrode moments (see panel (b)), this current of band-polarized spin \uparrow electrons enters a metallic electrode devoid of unoccupied spin \downarrow states. To these electrons, the Fe electrode constitutes an additional barrier so that, unless through some scattering process the electrons change symmetry, their DOS will continue to decay within the collecting electrode.

This example typifies how band structure effects can be put to good use in promoting large TMR ratios with transition metal electrodes. Though much attention has been placed on band structure effects using Fe(001) electrodes, for technological purposes it may be interesting to resort to others materials which possess such a spin-polarized band structure yet do not oxidize as readily (see Table 3.4). Co(110) and Ni(111) would be good candidates. [45]

It should be noted that all the above work consider the transmission of wavefunctions with bulk electronic symmetry. However, as Levy *et al.* and Wang *et al.* point out, [48, 49] the basis of eigenfunctions which describe the interface may be orthogonal to the bulk states, so that although such states are crucial in the tunneling process, they are omitted from the calculation of junction conductance.

2.3 Bias dependence of magnetotransport

We review the principal effects at play in shaping the bias dependence of TMR in a magnetic tunnel junction. Section 2.3.1 examines the incidence of the potential landscape perceived by the charge carriers. Section 2.3.2 presents the main sources of inelastic tunneling, to be contrasted with purely elastic tunneling which therefore rely on the junction electrode densities of states (see Section 2.3.3).

2.3.1 Bias voltage & barrier profile

The potential landscape of a junction is determined by the matchup of band structures across the heterostructure. Interfacial barrier heights are set by the energy difference between the effective Fermi level at a junction interface and the nearest of the valence or conduction bands. Dissimilar electrodes will result in different barrier heights at each interface. In Section 2.3.1.1, we discuss the effect of a bias voltage applied to a magnetic tunnel junction on magnetotransport through this potential landscape, particularly when reaching the Fowler-Nordheim tunneling regime above an interfacial barrier height.

Changes to the electronic character of the barrier material for electrons

injected at a given value of applied bias may lead to changes in the magnetic coupling between the two ferromagnetic electrodes as mediated by quantum well states formed in the spacer. In the Fowler-Nordheim regime, part of the barrier thickness is a metallic spacer. We therefore briefly review current knowledge of magnetic interlayer exchange coupling between ferromagnetic layers through a metallic or an insulating spacer in Section 2.3.1.2.

2.3.1.1 Barrier profile effects

As early as 1989, Slonczewski's free electron model (see Section 2.2.2.2) expressed the dependence of spin polarization in terms of the electron decay constant κ within the barrier (Equation 2.9). [30] Slonczewski shows that this expression is apt to change amplitude, and even sign, as the barrier height κ^2/k^2 is altered.

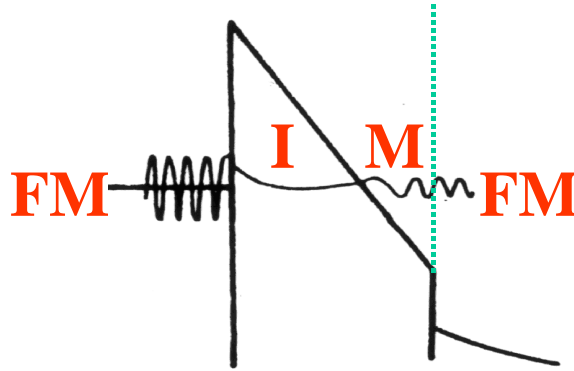


Figure 2.9: Schematic of Fowler-Nordheim tunneling above the collecting interfacial barrier height. From Wolf. [50]

A first approach to modeling the effect of applying a bias voltage to a heterojunction is to shift the Fermi levels of the two electrodes by eV while maintaining the interfacial barrier heights fixed. If the applied bias exceeds the interfacial barrier height of the collecting interface, then a Fowler-Nordheim regime of tunneling occurs. As illustrated in Figure 2.9, part of the barrier becomes metallic and may sustain wavefunction interference.

Zhang and Levy, in reviewing the various models for magnetoresistance, underlined the role that the barrier potential plays in determining the amplitude of TMR. [35] In agreement with Slonczewski, they find that even within a free electron model, changes in the detail of the potential barrier profile may affect the amplitude of TMR. Furthermore, a sizeable difference in spin-dependent scattering at each interface of the MTJ may even invert

the sign of TMR. The authors argue that such an effect may provide an alternate explanation to observations of inverse TMR in junctions with hybrid barriers such as $\text{Ta}_2\text{O}_5/\text{Al}_2\text{O}_3$ due to interfacial bonding and MIGS arguments, [51] or with a non-magnetic metallic spacer at the junction interface due to quantum well states. [52]

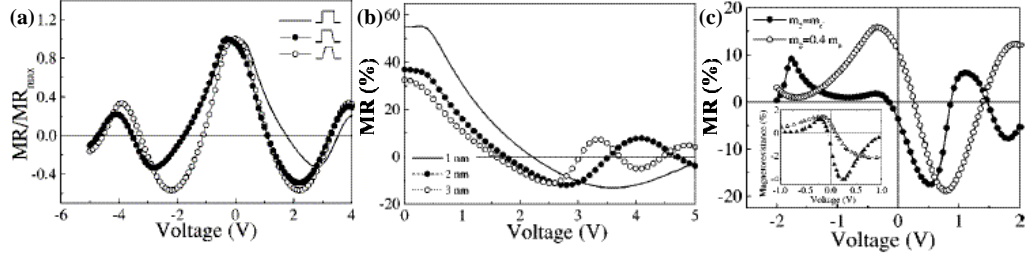


Figure 2.10: Theoretical bias response of MR of a junction with a 2eV barrier height as the potential profile is modified: (a) by changing interfacial sharpness, (b) barrier thickness, and (c) due to a much lower 0.3eV barrier height at one interface. The inset to panel (c) shows data by Sharma *et al.* on $\text{Ta}_2\text{O}_5/\text{Al}_2\text{O}_3$ junctions. [51] Where applicable, interface thickness is 0.2nm. From Montaigne *et al.* [21]

While in semiconductors the Fermi wavelength $\sim 100\text{\AA}$ implies that the electron “feels” the barrier potential step far away from the interface, in a metal it is $\sim 2\text{-}3\text{\AA}$, meaning that the spin carrier is more sensitive in the latter case to changes in the barrier potential profile of same order in real-world MTJs. It is therefore more problematic to model the potential step as abrupt in metallic MTJs compared to their semiconductive brethren. This question of the thickness of the interface, *i.e.* the lateral distance over which the potential rises to describes the barrier step, was examined by Montaigne of the Schuhl group (Nancy, France) within a free electron model. [21] As shown in Figure 2.10a, the bias dependence of TMR is influenced by the potential sharpness of the interface which *collects* the tunneling carriers. A 2nm barrier thickness was used, and where applicable a 0.2nm interface thickness which embodies a linear potential increase in going from metallic electrode to insulating barrier. The effective mass within the barrier was $m^*=0.4m_e$. While symmetric interfaces yield a symmetric TMR bias dependence, introducing an asymmetry by changing the sharpness of the interface may alter this bias dependence. Experimentally these asymmetries involve the chemical sharpness of the interface which, when improved through annealing, [53] improves the low bias value of TMR and reduces the dropoff in TMR amplitude with increasing bias.

Montaigne and coworkers also show how, at a given barrier height, the amplitude of TMR may rise with decreasing barrier thickness. Interestingly, as the barrier height is exceeded, oscillations in TMR as junction bias is further increased appear, irrespective of the ferromagnet's band structure. Rather, such oscillations result from the evolution of wavefunction interference with barrier potential profile at the metallic barrier/ferromagnet interface in this Fowler-Nordheim tunneling regime (see Figure 2.9). The period of such oscillations decreases as barrier thickness is increased as illustrated in Figure 2.10b for $m^*=0.4m_e$ and a 2eV barrier height. Davis and MacLaren also point out that lower barrier heights for a given barrier thickness result in a depressed bias dependence of TMR; and, as illustrated by Montaigne's calculations (see panel (c)), that differing barrier heights at each junction interface may lead to an asymmetry in the bias dependence of TMR. This latter fact is buttressed by calculations by Davis and MacLaren, [54] and may well explain the asymmetric TMR bias dependence in junctions with hybrid barriers. [51]

To conclude, in magnetotransport experiments on tunnel junctions, the thickness of the insulating spacer controls both the amplitude of TMR and any interlayer coupling between the two ferromagnetic electrodes. Applying a junction bias results in the presence of an electric field which is apt to modify the barrier potential. Large applied bias values may result in consequent modifications to the barrier profile probed by spin-dependent tunneling. In an intermediate bias range, the sharpness of the potential barrier step may be probed. If the applied bias exceeds a barrier height, then the diminishing effective barrier thickness and Fowler-Nordheim tunneling into the valence or conduction band of the insulator may alter spin-dependent transport and magnetic coupling between the two ferromagnetic electrodes. The intrinsic origin of both effects lies with wavefunction interference across the heterostructure.

2.3.1.2 Magnetic interlayer exchange coupling

So as to not overburden discussion, at this time we briefly present the salient points underlying magnetic interlayer exchange coupling (MIEC). A more complete discussion may be found in Appendix C.

In the late 80s it was discovered that ferromagnetic layers separated by a non-magnetic, metallic spacer align ferromagnetically (F) or antiferromagnetically (AF) depending on the thickness of this spacer, [55] promoting large changes in resistance with applied field. [56] Underlying this phenomenon of MIEC due to RKKY interactions [57–59] is the formation of quantum well states [60] within the spacer. When a quantized state crosses the Fermi level,

energy minimization results in an antiparallel alignment of ferromagnet magnetizations, leading to the observed AF coupling.

This effect has been mainly studied using metallic spacers, but may also occur through an insulating spacer. [30] Experimentally, semiconducting [61] and insulating [62] spacers have been shown to accommodate this effect. Notably, it may also occur in perovskite oxide systems, whether metallic [63, 64] or insulating as was shown regarding $\text{La}_{0.7}\text{Sr}_{0.3}\text{MnO}_3/\text{SrTiO}_3$ multilayers. [65, 66]

2.3.2 Elastic & inelastic tunneling processes

In addition to the case of elastic tunneling between occupied and unoccupied electron states on each side of the barrier, effective transmission may also occur through other mechanisms. We review here notions on inelastic tunneling through interfacial spin wave and phonon excitations, and impurity-assisted tunneling. In particular, spin waves tend to mix the two spin-independent channels.

As reviewed previously, the bias dependence of junction conductance is expected to follow a parabolic law. However, for applied bias values below $\sim 150\text{mV}$, a dip in conductance called a *zero-bias anomaly* (ZBA) occurs for junctions integrating transition metal electrodes. Theoretical and experimental investigations have attributed this ZBA to spin wave excitations at the carrier-collecting interface. [67, 68] Indeed, at a given applied bias V , electrons from the Fermi level of the injecting electrode enter unoccupied states above the Fermi level of the collecting electrode after elastic tunneling. To thermalize with their environment, these “hot” electrons may dissipate energy by emitting a magnon of energy $\hbar\omega \leq eV$. Given their bosonic distribution, the only constraint on magnon generation is the maximum energy of such spin waves sustainable by the ferromagnetic medium. This energy corresponds, within a mean field approximation to $3k_B T_C / (S + 1)$ for a transition metal with spin S and Curie temperature T_C . As illustrated in Figure 2.11a, in the case of a $\text{Co}/\text{Al}_2\text{O}_3$ interface, the cutoff appears at $\approx 140\text{mV}$, in relative agreement with this estimate if one considers a lower interface T_C for Co. Zhang *et al.* propose a somewhat modified explanation for the saturation bias of the ZBA, arguing in terms of a lower wavelength cutoff in the magnon generation spectrum due to inhomogeneities at the interface ferromagnetic matrix. [67] Thus, this phenomenon leads to a mixing of the two tunneling spin channels. Finally, it should be noted that spin wave excitations may interact in the tunneling process at both the collecting and injecting interfaces through the emission and absorption of magnons, respectively.

Spin wave generation represents a challenging topic in the case of dou-

ble exchange systems due to the half-metallic character of conduction. As discussed by Gu *et al.*, [69], long-range ferromagnetic interactions which underlie the double exchange picture lead to a 3D spectrum of interface spin wave excitations. This promotes a $V^{3/2}$ dependence of junction conductance, to be contrasted with a V dependence for transition metal electrodes. [67] The authors note that if the magnetism of the interface is different from that of the bulk, then the anisotropic spectrum will follow the standard V^2 bias dependence of conductance.

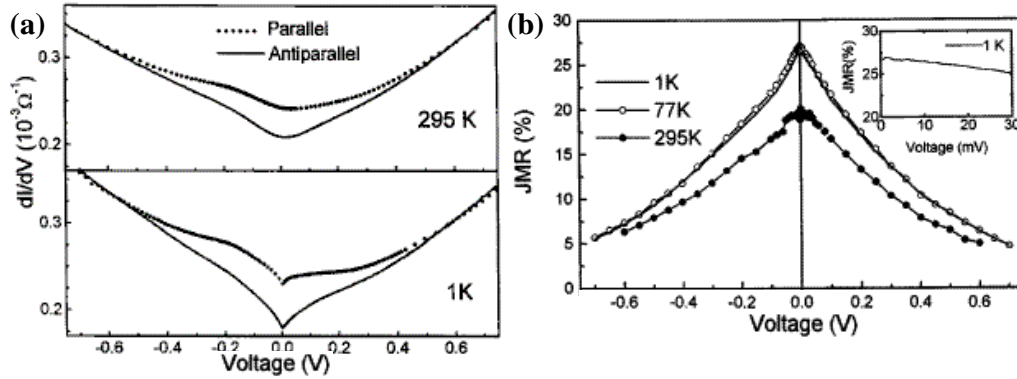


Figure 2.11: Co/Al₂O₃/Ni₈₀Fe₂₀: temperature evolution of (a) Conductance in the parallel and antiparallel configurations, and (b) JMR bias dependence. $JMR \equiv \Delta R/R_{AP}$. From Moodera *et al.* [68]

Hot electrons may also thermalize at the collecting interface through the emission of a phonon. Moodera *et al.* evidenced the activation of several OH stretching modes at the Al₂O₃ barrier interface. [68] Regarding double exchange systems, the activation of polarons may occur for electron energies ~ 200 meV. [70]

Finally, defect-assisted tunneling has been investigated by several groups. Given that $G \propto e^{-d\sqrt{m\Phi}}$, the possibility for an electron to tunnel to an intermediate state within the barrier is all the likelier if that state lies at the center of the barrier, so as to lead to sequential tunneling through only half the barrier thickness d . This leads to a doubling of the conductance logarithm, [71] as well as a stronger decrease in TMR amplitude with increasing bias and temperature. [72, 73] If two or more states are present along the effective conductive path through the barrier, phonons mediate hopping between sites. For two states, this leads to $G \sim V^{4/3}$ and $G \sim T^{4/3}$ dependencies.

The activation with applied bias of the inelastic processes described above is generally believed to account for the resulting decrease in TMR amplitude illustrated in Figure 2.11b for a Al₂O₃-based tunnel junction. In large part

this decrease has been attributed to spin wave excitations, [67, 74] though phonon and impurity-assisted tunneling may also play a role, especially above the magnon saturation energy. In particular, Bratkovsky predicts that, although magnons may decrease the TMR amplitude through mixing of the two spin-dependent conduction channels, phonon generation tends to increase the ratio. [74]

2.3.3 Density of States effects

As regards half-metallic systems, Bratkovsky has investigated the evolution of junction TMR with applied bias (see Figure 2.12. [31]) In a DOS picture, magnetotransport behavior is determined by the extent of the energy gap δ which marks the onset of the spin-polarized band absent at the Fermi level. Until $V \approx \delta$, the large TMR ratio should remain fairly constant if one discounts spin wave excitations. Past this gap, tunneling conductance in the antiparallel state increases relative to the parallel channel.

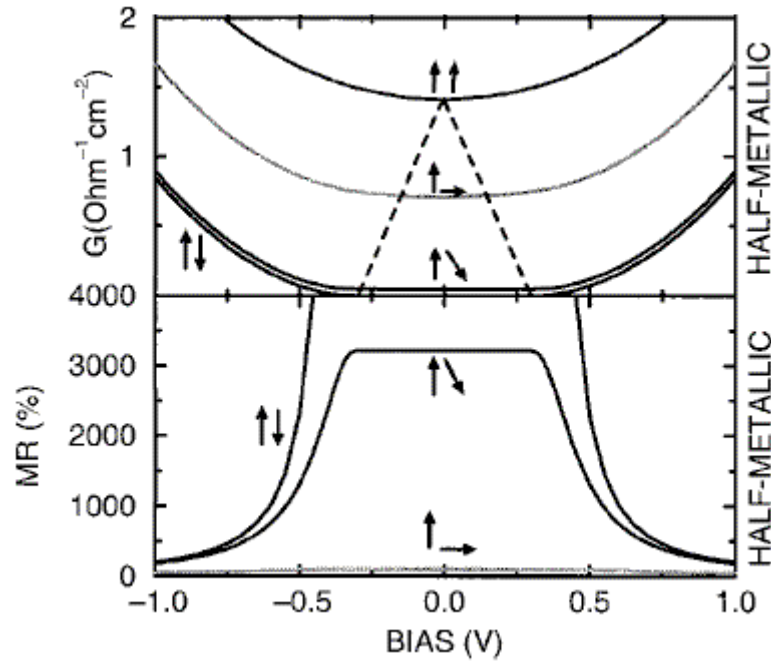


Figure 2.12: Calculation of tunneling transport between two half-metallic electrodes: (a) parallel and antiparallel conductances and (b) bias dependence of TMR.. The minority gap $\delta=0.3\text{eV}$. From Bratkovsky [31]

Also, though specific to theoretical studies on ideal junctions, it has also been argued that, since the \vec{k} wavevector of the unoccupied state is apt to

change according to the band structure above the Fermi level as probed by an increasing applied bias, this difference with the wavevector of Fermi level injecting states may be responsible for a TMR decrease. [46]

2.4 Temperature dependence of TMR

In junctions with transition metal electrodes possessing T_C values much larger than room temperature, the generally observed decrease in TMR amplitude with increasing temperature reflects in part the thermal activation of inelastic processes described above, such as magnon generation. [67] If the decrease in interfacial spin polarization and magnetization indeed result from the same mechanism of magnon activation, then, as argued by Shang *et al.* [75] and corroborated by MacDonald, [76] both should follow a $T^{3/2}$ law, *e.g.* $P(T)=P(0)(1-T^{3/2})$.

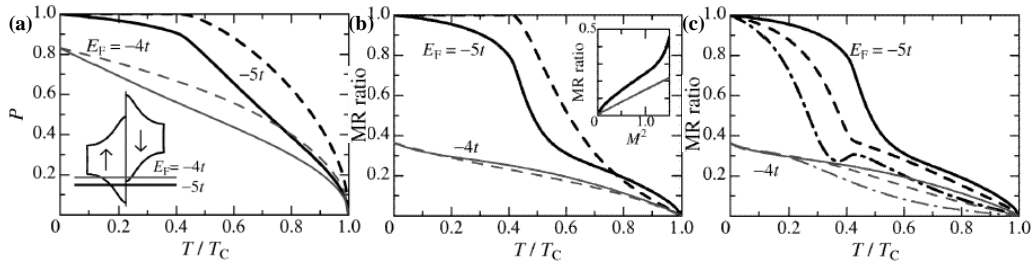


Figure 2.13: Temperature dependence within the double exchange model of (a) spin polarization, and (b),(c) MR amplitude. The inset to panel (a) illustrates the half-metallic ($E_F = -5t$) and nearly half-metallic ($E_F = -4t$) scenarii. Broken(solid) lines indicate the absence(presence) of spin fluctuations. (c): the transverse component of coupling is increased from solid to dashed to chained lines, while the longitudinal component, in the direction of transport, is fixed. From Itoh *et al.* [77]

Regarding tunneling in double exchange systems, an overriding concern is that of the increasing degree of spin fluctuations with increasing temperature. Indeed, the Hund coupling between the localized t_{2g} macrospin on the Mn site and the itinerant e_g electrons sets the spin referential of the latter. Itoh *et al.* have considered the effect of temperature on the magnetoresponse of double exchange electrodes within a MTJ. [77] Figure 2.13 presents the evolution of spin polarization, and MR ratio for various Hund coupling and spin fluctuation scenarii. In panel (a) are plotted temperature dependencies of spin polarization for half-metallic ($E_F = -5t$) and nearly half-metallic ($E_F = -4t$) cases (see inset). In addition, the authors consider the presence (solid

lines) and absence (broken lines) of spin fluctuations. Panel (b) presents the resulting evolution of MR ratio for a junction with spin polarization at each interface following the trend of panel (a). In the nearly half-metallic case, the damped MR ratio decreased in a fairly monotonic fashion toward T_C . In contrast, in the half-metallic case, the MR ratio decreases only moderately until $\sim 0.4T/T_C$, before decreasing sharply. The authors argue that this plateau reflects the persistence of the half-metallic gap until $\sim 0.4T/T_C$ (see panel (a)) as the exchange coupling decreases. This TMR plateau is enhanced as spin fluctuations lessen. Finally, panel (c) shows how this TMR plateau is diminished as transverse coupling is increased so as to promote spin flip tunneling.

2.5 Recent experiments

We discuss in this Section some experiments which were performed in approximately the same timeframe as those presented in this Thesis. Although we have categorized sets of experiments according to particular points of investigation regarding spin-dependent tunneling, in several instances the interest behind a given result overlaps into other areas within the larger picture of the field.

2.5.1 Density of states effects

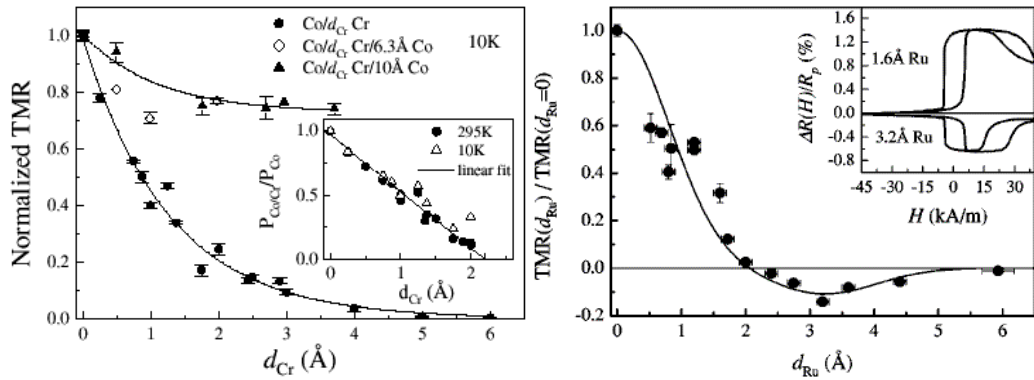


Figure 2.14: Normalized TMR at $T=10\text{K}$ for $\text{Co}/\text{Al}_2\text{O}_3/\text{Co}$ with a Cr (left) or Ru (right) interlayer at the lower junction interface. From LeClair *et al.* [78, 79]

In a quite similar spirit of investigation to ours, some ground-breaking work was presented by P. LeClair of the de Jonge group (Eindhoven, the

Netherlands) on controlled modifications to the electrode DOS and the resulting amplitude of TMR at low bias. Starting with a Co/Al₂O₃ lower interface, dusting with Cr [78] was shown to reduce TMR, while dusting with Ru [79] led to a TMR sign inversion (see Figure 2.14), in qualitative agreement with changes to the Co matrix DOS induced by the impurity (see the related Section 5.2.2.1). In the latter study, Nuclear Magnetic Resonance experiments broadly demonstrated that Ru was alloyed with Co. These studies parallel closely ours on LSMO/STO/CoCr and LSMO/STO/ALO/CoCr presented in Section 5.2.2. We point out that chemical reactions at the oxide barrier interface due to the presence of Cr, though less prevalent for ALO barriers, may nevertheless occur (see Section 7.1.2), though the Ru dusting experiments are less affected by such an argument since Ru does not oxidize as easily.

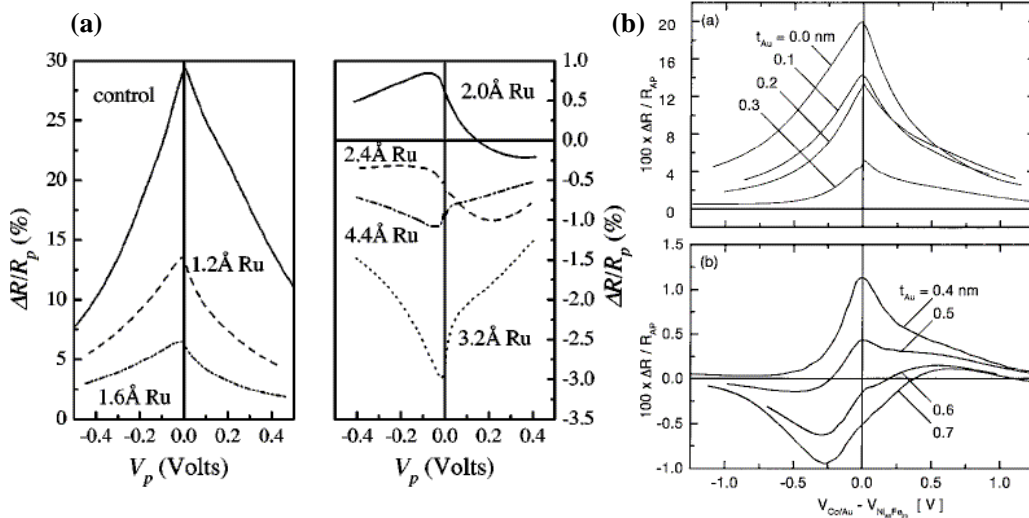


Figure 2.15: TMR bias dependence for (a) Co/Ru/Al₂O₃/Co and (b) Co/Au/Al₂O₃/Ni₈₀Fe₂₀ MTJs with increasing Ru or Au dusting interlayer thickness at the lower junction interface. From Moodera *et al.* & LeClair *et al.* [52, 79]

Interestingly, the TMR bias dependence of the Ru dusting experiments closely mirrors that found in the case of Au dusting at the Co/Al₂O₃ interface by Moodera *et al.* in 1999 (Boston, USA) (see Figure 2.15). [52] In this earlier study, the promotion of quantum well states in the intervening Au layer were argued to result in the inversion of TMR. Yet the two sets of experiments appear to offer mutually exclusive arguments, since while LeClair argues that the alloyed CoRu phase cannot promote quantum well states, Au impurities do not bring about a spin-dependent modification to Co virtual bound states.

Perhaps the best explanations for the TMR inversion and asymmetric bias dependence lie with differences in interfacial scattering and barrier potential profile at each interface of these sets of junctions. [35, 54] These arguments are backed up from theory in Section 2.3.1.1, and possibly by experiments on barrier profile effects in the upcoming Section. Regardless, it is very interesting to note that, aside from a very low amplitude, once the sign of TMR is inverted, the TMR bias dependence looks very similar to that found for a LSMO/STO/Co junction.

Recently, Xiang of the Xiao group (Delaware, USA) reported on bulk contributions to spin-dependent tunneling from transition metal electrodes. [80] The experiment involved inserting a CoFe wedge at the lower interface of a Py/Al₂O₃/Py sample. The ensuing TMR measurements on MTJs along the wedge reveal a crossover from a TMR amplitude reflecting a Py interface to a CoFe interface with a characteristic CoFe thickness of 8Å. This implies that the tunneling process samples the electrode DOS over several times the Fermi wavelength. The authors argue that this tunneling characteristic length, which is lower than the 33-55Å spin diffusion length found from GMR experiments within the Valet-Fert framework, [81] reflects conduction differences between the two systems.

2.5.2 Barrier profile effects

Asymmetries in the bias dependence of TMR have in great part been ascribed to defects in the structure arising from an inhomogeneous formation of the barrier during oxidation. Some evidence, which is particularly prevalent in TaO_x-based junctions, suggests the presence of an oxygen gradient through the ~20Å thickness of the barrier [51, 82] resulting in an asymmetric barrier profile through the thickness of the insulating layer.

The study of barrier asymmetries between one junction interface and the other may be achieved simply by varying the oxidation time of a nominal thickness of Al. In all cases the upper interface formed from the Al surface exposed to the oxygen ambient is correctly oxidized. Low oxidation times result in an underoxidized lower interface which contains metallic Al. High oxidation times result in the oxidation of the ferromagnetic electrode at the interface with the completely oxidized Al film.

Oepts of the de Jonge group (Eindhoven, the Netherlands) varied the oxidation times of a set of Co/Al₂O₃/Co junctions grown with the same thickness of Al [83], while Xiang of the Xiao group (Delaware, USA) used a wedge of Al and a fixed oxidation time to span the gamut of junction interface asymmetry on one sample. [84] Results from both groups are shown in Figure 2.16. When the oxidation time is varied from a condition of underox-

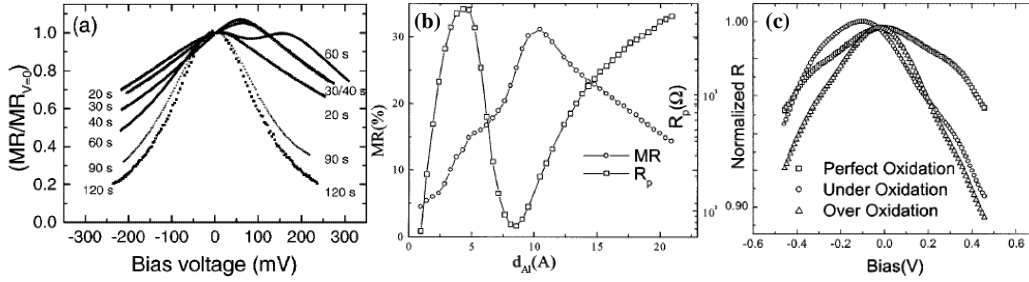


Figure 2.16: Barrier oxidation studies of the effect of barrier asymmetry on transport in MTJs: (a) on a set of junctions with identical Al thickness while varying the oxidation time, by Oepts *et al.* [83]; (b) & (c) on a set of junctions created from the same sample with a wedged Al layer, by Xiang *et al.* [84].

oxidation to one of overoxidation, the symmetry of the TMR bias dependence changes markedly. Overoxidation leads to a damping of the TMR bias dependence, and notably a drop in the $V_{1/2}$ value at which the TMR is half that at $V=0$. This illustrates the effect of spin-dependent scattering due to tunneling through an antiferromagnetic barrier formed from the oxidation of the transition metal electrode. Peaks at $V \neq 0$ occur for nearly optimal oxidation, in the direction of applied bias corresponding to electron injection toward the lower interface of interest. This oxidation state in turn influences both the interfacial barrier profile and the DOS which is to participate in the tunneling process. Given the succeeding stages of Al oxidation (see Figure 2.16b) in the process of forming the barrier, Oepts’s approach is more difficult though this issue is addressed in this study. Between the conditions of under- and overoxidation, Xiang *et al.* were able to obtain an “ideal” junction with a symmetric TMR bias dependence which they were able to fit using a modified Brinkman model (see Section 2.1.1) which iteratively takes into account the bias-dependent electrode DOS.

2.5.3 Partially and fully epitaxial magnetic tunnel junctions

Toward bridging the gap between theory and experiment, several groups have also performed spin-dependent tunneling measurements on partially and fully epitaxial magnetic tunnel junctions integrating transition metal electrodes, manganites or dilute magnetic semiconductors.

2.5.3.1 Transition metals

To evidence the influence of the ferromagnetic electrode's band structure on spin-dependent tunneling, LeClair et al. presented a transport comparison of two Co/Al₂O₃/Co junctions differing in the quality of the lower electrode crystallinity. [85]. The conductance asymmetries varied as the lower electrode crystallinity was changed from polycrystalline hcp to a fcc(111) texture. By eliminating any bias symmetry in the junction conductance when tunneling toward the fcc electrode, LeClair succeeded in isolating the incidence of fcc crystallinity on conductance, as corroborated by theory.

Yuasa of the Suzuki group (Tsukuba, Japan) has also focused on the impact of electrode crystallinity and barrier thickness in Fe/Al₂O₃/FeCo junctions. [86] When switching the crystalline orientation of the lower Fe electrode from bcc (100) to (110) to (211), Yuasa *et al.* observe sizeable differences in the amplitude of TMR - but not the sign, and some structure in this amplitude for a given orientation as the barrier thickness is increased from 12Å to 30Å. The authors do not provide an explanation for the damping of the TMR bias dependence with increasing barrier thickness. Such damping could be explained by impurity-assisted tunneling for larger barrier thicknesses.

A series of two tunneling studies by this research group focused on quantizing the electrode thickness and the impact on magnetotransport. While not entirely novel, [52] these studies provide fairly clearcut results. Nagahama *et al.* first investigated the Cr (001) /Fe (n ML) /ALO/FeCo system. Figure 2.17 summarizes their results. Oscillations in the differential conductivity appear once a parabolic background has been subtracted (Figure 2.17a). These oscillations in dI/dV_{osc} appear only when electrons from FeCo probe Fe states above E_F , not the reverse, and shift towards larger bias as Fe thickness is decremented (Figure 2.17b). The authors ascribed these oscillations to quantum well states formed in the Fe ultrathin layer and bound by the barrier on one side and by a Cr 0.9eV Δ_1 gap on the other. [87] In a 1D quantum well, decreasing the width of the well will increase the quantized energy level responsible for the conductance peak, as observed. The weakness of the oscillatory effect may arise from the lack of an efficient nesting feature in the Fe Fermi surface and the difficulty to set up spin-polarized QWS in magnetic thin films.³

In a subsequent study on Co(001)/Cu (n ML)/ALO/FeNi MTJs summarized in Figure 2.18, Yuasa et al. reverted to the more familiar epitaxial fcc

³Since for Cr(001) neither Δ_1 band crosses E_F , an additional conceptual difficulty lies with understanding how such states which result in conductance oscillations due to confinement within the Fe layer contribute to transport through the entire heterostructure. Effective conduction may involve additional points in the Brillouin zone.

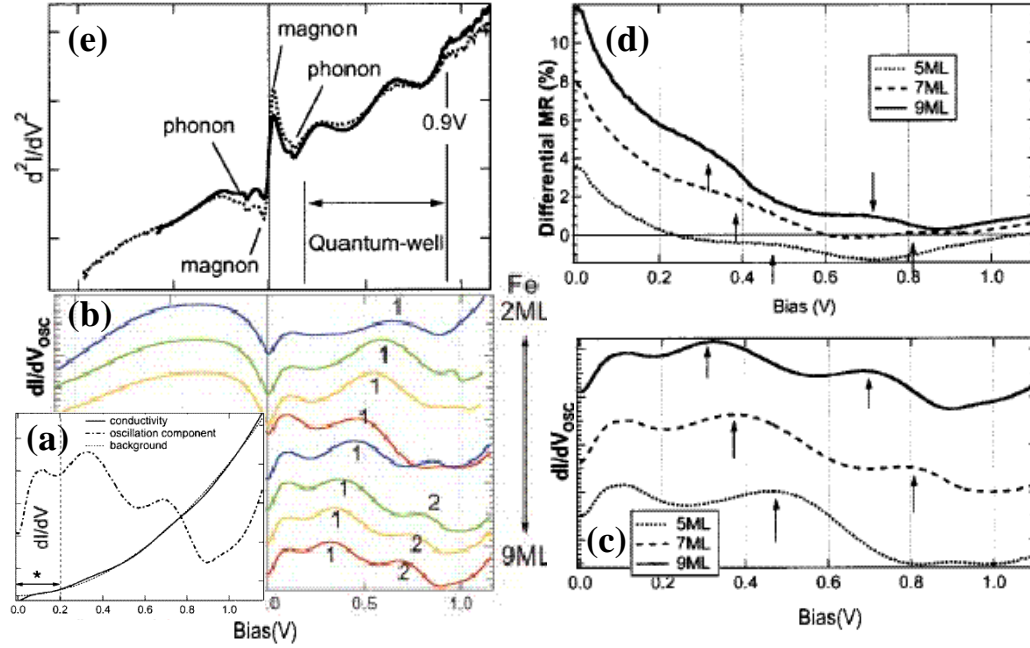


Figure 2.17: Magnetotransport experiments on Cr(100)/Fe(n ML)/Al₂O₃/FeCo MTJs: (a) Oscillatory component dI/dV_{osc} of differential conductivity once a parabolic background has been subtracted ($n=9$ ML); (b) Evolution of dI/dV_{osc} as n is varied from 9ML to 2ML in integer steps; (c) and (d) compare bias-dependent features of dI/dV_{osc} and differential TMR, respectively, for three Fe thicknesses; (e) d^2I/dV_{osc}^2 for P and AP magnetic configurations shown in solid and dashed lines, respectively ($n=9$ ML). The oscillations disappear above 0.9 V. From Nagahama *et al.* [86]

Co/Cu(001) system (panel (a)) to evidence the influence of quantum well states (QWS) at a junction interface on magnetotransport properties. As introduced in Section 2.3.1, quantum confinement of spin \downarrow electrons at a Co/Cu interface due to band mismatch may promote the formation of QWS in the Cu layer (panel (b)) for electrons which satisfy constructive interference given the spanning wavevectors at the Fermi surface (panel (c)). In this case one interface is replaced by the tunnel barrier - which of course provides confinement, allowing spin-polarized tunneling currents to probe these states. In conjunction with separate experiments on metallic Co/Cu multilayers, the authors show how the spanning wavevector at the belly of the Cu(100) Fermi surface, which gives rise to antiferromagnetic interlayer exchange coupling for $d_{Cu}=10\text{\AA}$, reverses the sign of spin polarization at that interface due to the

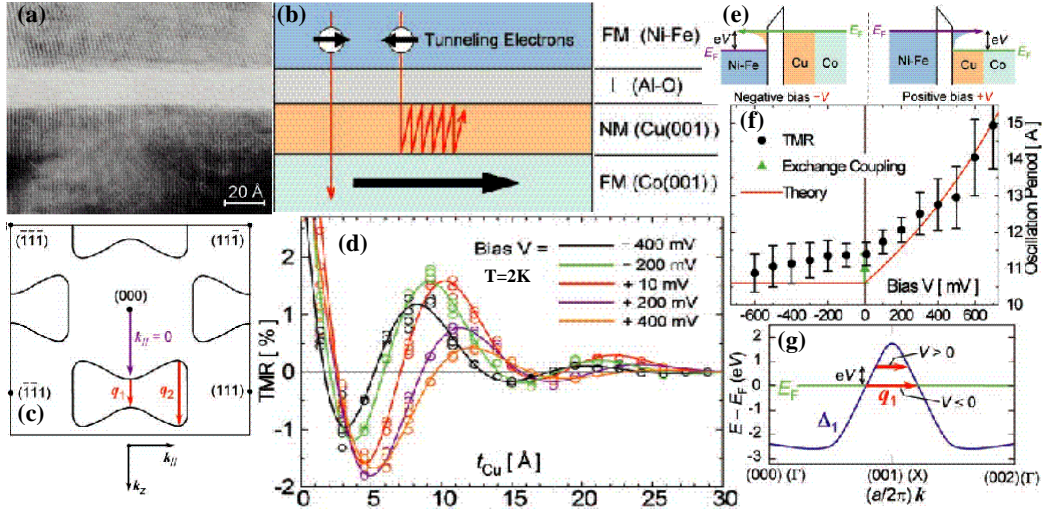


Figure 2.18: Magnetotransport experiments on $\text{Co}(001)/\text{Cu}(n \text{ ML})/\text{Al}_2\text{O}_3/\text{Fe}_{80}\text{Ni}_{20}$ MTJs: (a) TEM cross-section; (b) Transport schematic for both spin channels; (c) Fermi surface of *fcc*-Cu annotated with nesting features in the direction of electron propagation; (d) Evolution of TMR with increasing Cu thickness for several applied biases; (e) Direction of electron propagation; (f) Bias dependence of the TMR oscillation period inferred from (d) (circles), to be compared with a theoretical estimation (line) obtained from the energy dispersion of the Cu Δ_1 band along the direction of propagation(g). Positive biases probe Cu energy levels above E_F , shortening the scattering vector in the Cu Fermi surface nesting feature, thereby increasing the oscillation period. From Yuasa *et al.* [88]

Fermi level crossing of a Cu quantum well state in 10\AA Cu thickness intervals (panel (d)). As applied bias is increased, the tunneling current probes Cu states above E_F (panel (e)), and the oscillation period of TMR with Cu thickness increases (panel (f)) as the spanning wavevector decreases in amplitude beyond the Fermi surface (panel(g)). This very impressive experiment does lack a quantitative evaluation of the quantum well states energy levels within a phase accumulation framework - a difficult proposition at the time of this writing given a lack of experiments on phase shifts at the $\text{Cu}/\text{Al}_2\text{O}_3$ interface. Nevertheless, calculations of diffusive transport through such a heterostructure provide reasonably similar results. [89]

Of the fully epitaxial systems with transition metal electrodes which have been proposed, only the Fe/MgO system has yielded appreciable results. Aside from experiments presented in Chapter 4.1.3, [90] a very recently published report by Faure-Vincent *et al.* of the Schuhl group (Nancy, France)

offers evidence for band structure spin polarization effects in Fe/MgO/Fe MTJs, with TMR ratios reaching 100% in excess of predictions within a Jullière model of the spin polarization of Fe at the Fermi level. [91]

2.5.3.2 Manganites

Several groups have performed spin-dependent tunneling experiments using manganite electrodes with half-metallic double exchange conduction. Jo utilized uniaxial anisotropy to obtain very stable antiparallel alignments between $\text{La}_{0.7}\text{Ca}_{0.3}\text{MnO}_3$ electrodes and over 700% TMR using a NdGaO_3 barrier, [92] paving the way for magnetization reversal experiments. [93]

The group of K. Dörr (Dresden, Germany) studied junctions with LSMO and $\text{La}_{0.7}\text{Ce}_{0.3}\text{MnO}_3$ electrodes sandwiched between a STO barrier. The latter manganite oxide was recently discovered by that group to be an electron-doped system. The resulting magnetotransport studies yielded a positive TMR, [94] in agreement with the sign of spin polarization of the carriers, and irrespective of the differing nature of the carriers between the two electrodes. This result put to rest any question regarding the incidence of differing charge carriers on the interpretation of magnetotransport results in LSMO/STO/Co junctions.

2.5.3.3 Dilute magnetic semiconductors

The study of dilute magnetic semiconductors, [95] and their integration into spin electronic devices, is gathering momentum, with a promise of facilitated technological applications given the current state of the semiconductor industry, and a potential for progress on the fundamental physics of spin-dependent tunneling. Growth control at the monolayer level allow the tailoring of heterostructures, band structures effect in conventional semiconductor heterostructures are well understood, while the long spin diffusion lengths in semiconductors promote new spin-dependent transport experiments. In turn, ideas such as magnetic interlayer exchange coupling are being applied to this new class of materials. At the time of this writing, the origin of ferromagnetism and spin-dependent transport in such systems is still a topic of debate.

As regards the field of magnetic tunnel junctions, a landmark experiment reported by Tanaka and Higo in 2001 involved spin-dependent tunneling measurements on $\text{Ga}_{1-x}\text{Mn}_x\text{As}/\text{GaAs}/\text{AlAs}/\text{GaAs}/\text{Ga}_{1-y}\text{Mn}_y\text{As}$ for Mn doping $x=3.3\%$ and $y=4.0\%$. [96] The GaAs insertion layers are used to prevent Mn diffusion into the AlAs tunneling barrier. In addition to the exponential dependence of resistance on barrier thickness, TMR ratios reaching 75% were

observed at $T=8\text{K}$, with a barrier thickness dependence of the TMR ratio reflecting k_{\parallel} conservation during the tunneling process.

Mattana within our research group investigated the potential for long spin diffusion lengths in semiconductors to promote new spin-dependent transport behavior in heterostructures. The insertion of a non-magnetic 50\AA -thick GaAs layer within a magnetic tunneling structure such as that above did not result in damping of the TMR amplitude. [97] Mattana *et al.* argue that spins accumulate within the GaAs spacer due to injection through a first tunneling process from the ferromagnetic electrode. The ensuing splitting of the chemical potential within the spacer, which does not decay as rapidly compared to a non-magnetic metal, is detected electrically by a second, sequential tunneling process toward the second ferromagnetic electrode.

2.6 This Thesis's scientific motivations

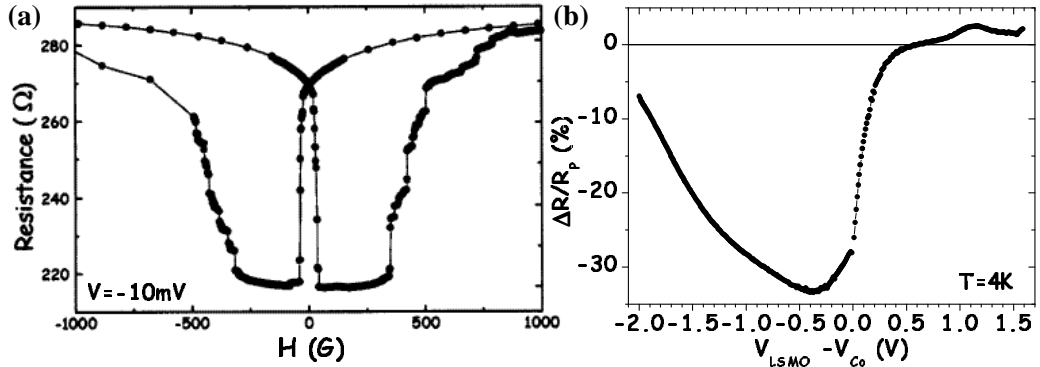


Figure 2.19: Magnetotransport experiments on $\text{La}_{0.7}\text{Sr}_{0.3}\text{MnO}_3/\text{SrTiO}_3/\text{Co}$ junctions: (a) $R(H)$ loop at $V=-10\text{mV}$ and (b) bias dependence of TMR at $T=4\text{K}$. From de Teresa *et al.* [22]

At the heart of the experimental motivations for this Thesis were the initial magnetotransport results obtained in late 1998 on $\text{La}_{0.7}\text{Sr}_{0.3}\text{MnO}_3/\text{SrTiO}_3/\text{Co}$ junctions shown in Figure 2.19. In stark contrast to Al_2O_3 -based junctions, such junctions yield an *inverse* TMR at low bias: resistance in the antiparallel state is lower than that in the parallel state (panel (a)). LSMO is known to have a positive, nearly total spin polarization (see Sections A.4.3 & 5.1 for theory and experiment) Therefore, within a density of states picture described by the Jullière model (Equation 2.5), the inverse TMR implies that the signs of spin polarization of $\text{La}_{0.7}\text{Sr}_{0.3}\text{MnO}_3$ (LSMO) and Co are opposite. Thus, in this experiment the

spin polarization of Co is negative as determined by the spin analysis of the half-metallic LSMO electrode. Furthermore, the bias dependence of TMR for such a junction departs significantly from the then-usual monotonic TMR decrease with applied junction bias found for Al_2O_3 -based junctions (see Figure 2.11b on page 27).

2.6.1 The sign of spin polarization of Co

This experiment will have paved the way toward a unified understanding of spin-dependent tunneling. Indeed, as described in previous Sections, the positive sign of spin polarization found for all transition metals through spin-dependent tunneling experiments, defied the knowledge of a negative spin polarization at the Fermi level resulting from exchange-split d bands in the case of Co (see Figure 2.20). Much thinking focused on the electronic character of the spin-polarized electrons, and their tunneling transmission through the barrier. However, the nature of the barrier was overlooked as the insulator was merely considered a step in the junction's potential landscape. To gain more insight into the role of the barrier, we performed LSMO/I/Co magnetotransport experiments to examine the role of the barrier I. To probe the model of induced moments on atomic sites within the barrier material described by Oleinik *et al.* (see Section 2.2.2.3 and hereafter), [34,36] we also performed XMCD experiments to measure this induced moment. This axis of research is presented in Chapter 4.

2.6.2 On the TMR bias dependence

The research work in this Thesis was strongly guided by a spectroscopic picture of tunneling, whereby a direction of applied bias probes both the density of states and the potential profile of the interface which collects the charge carriers. While both quantities appear in the expression of tunneling conductance (see Equation 2.1), the latter's influence is more subtle. This framework underlies many discussions on experimental results presented hereafter.

2.6.2.1 A density of states interpretation

Figure 2.20 presents the original interpretation of the bias dependence of TMR for LSMO/STO/Co junctions in terms of the electrodes' densities of states. When electrons states near the Fermi level E_F of LSMO tunnel towards unoccupied Co states, *i.e.* for $V \leq 0$, the TMR amplitude increases from -28%, and may reach -38% at a bias $V \sim -0.4\text{eV}$ before decreasing again. As shown in panel (b), this TMR peak reflects spin-polarized probing of a

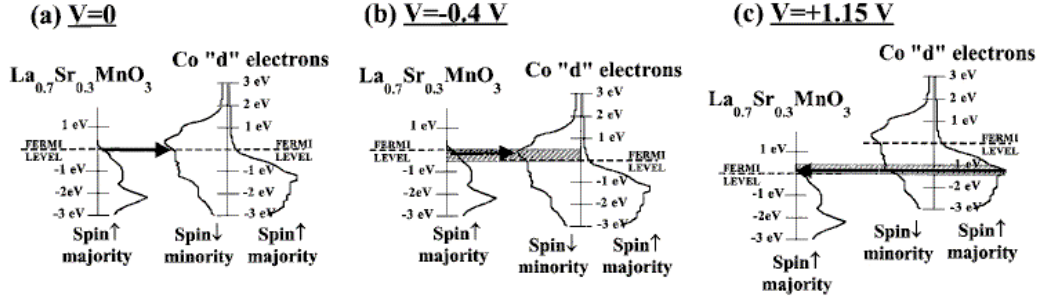


Figure 2.20: Density of states interpretation of the bias dependence of TMR in LSMO/STO/Co junctions. From de Teresa *et al.* [22]

peak in the Co unoccupied DOS. Notably, this Co DOS was found for a fcc(111) surface, [98] which has been shown to be different from that at an interface. [23] Owing to the textured nature of the Co counterelectrode, the shift in peak bias position from sample to sample could reflect a sampling of the Co DOS in various crystalline orientations. [98]

At negative bias, does the TMR peak reflect a Co DOS feature, possibly convoluted over several crystalline orientations? Towards an answer to this question, an extensive investigation of LSMO/STO/CoCr and LSMO/STO/ALO/CoCr systems was undertaken. Doping with Cr modifies the Co matrix DOS above E_F and should thus affect the TMR bias dependence given these DOS considerations. This investigation is detailed in Section 5.2.2.

In a DOS picture, the rapid decrease of TMR at low positive bias could be attributed to a vanishingly low gap in the LSMO minority DOS. As discussed in Section A.4, this gap is at the origin of the half-metallic nature of this manganite and its high spin polarization. This possible absence of a gap would be in agreement with several theoretical results [99, 100] but direct experimental verification is lacking. Section 5.1 investigates the unoccupied DOS of LSMO through two spectroscopy techniques: Spin-Polarized Inverse Photoemission and spin-dependent tunneling from another LSMO electrode in LSMO/STO/LSMO MTJs. It is shown therein that the rapid decrease in TMR when tunneling toward a LSMO electrode arises from the generation of spin wave excitations, while LSMO indeed has a minority gap $\delta=0.38\text{eV}$ as confirmed through these two techniques on our samples.

After falling rapidly, the TMR at positive bias then tapers out before dipping again, and switches sign for this junction at $V=0.7\text{V}$. As shown in Figure 2.20c, the TMR sign inversion at $V\sim 0.7\text{V}$ towards positive TMR was ascribed to a Co occupied DOS feature at $E-E_F=-0.7\text{eV}$. Likewise, the TMR

peak at $V=1.1\text{eV}$ was explained in terms of a peak in the Co DOS at that energy value below E_F . This argument supposes that electrons well below E_F may contribute significantly to tunneling transport compared to those close to E_F , even while their position much below E_F leads to an altogether higher perceived barrier height. Indeed, the transmission coefficient depends exponentially on barrier height, so that the probability for electrons 100meV below E_F to tunnel through a 1eV barrier (defined as the energy difference between the bottom of the conduction band and the electrode Fermi level) is already down to 25% of that for electrons at E_F . Thus it is fairly improbable that the Co DOS at $E < E_F - 0.3\text{eV}$ contributes to tunneling. Other arguments must be raised to explain the inversion and peak.

2.6.2.2 A junction potential profile interpretation

The other paradigm to explain the bias dependence of TMR takes into account the junction's effective potential landscape perceived by the charge carriers when traversing the heterostructure. The relevant theory was presented in Section 2.3.1.1, and experiments described in Section 2.5.2. This potential landscape is shaped by a number of effects. Firstly, the band structure of STO may differ in our ultrathin barrier layers [101] compared to bulk. This band structure may also be altered due to non-stoichiometry. This topic, illustrated in Figure A.5b on page 231, is covered in Section A.2.3.

In addition, the asymmetric Co/STO and STO/LSMO interfacial barrier heights, resulting from the different nature of the two electrodes, may account for the asymmetric bias dependence of TMR. Given the 5eV Co work function, [102] Robertson and Chen expect a 0.8eV Schottky barrier height at the Co/STO(001) interface. [103]⁴ Furthermore, the electron affinity of SrTiO_3 is 2.6eV , [105] while that of the similar double-layered perovskite $\text{La}_{1.2}\text{Sr}_{1.8}\text{Mn}_2\text{O}_7$ is 3.56eV . [106] Consequently, if band bending hasn't pushed the Fermi level within the conduction band throughout the $\sim 30\text{\AA}$ thickness of the STO barrier, we expect a larger (lower) electron (hole) barrier height at the Co/STO, rather than at the STO/LSMO, interface. Interface defects caused by poor control of the Co/STO chemistry may alter the effective Schottky barrier height. [40]

This complex description of the junction profile hinders a comparison with experimental data. It is therefore more salient to probe the incidence of *relative* changes to such a potential landscape on magnetotransport. These considerations lie at the heart of careful transport experiments on LSMO/STO/LSMO and LSMO/STO/ $\text{Co}_{1-x}\text{Cr}_x$ junctions, presented in

⁴This height may vary with the STO crystal orientation. [104]

Chapter 7 which are aimed at understanding the role of barrier profile on the bias dependence of TMR. The interpretation of such changes in the junction magnetotransport response in terms of electromigration is confirmed through experiments on modifying the chemistry of the SrTiO₃/CoCr interface so as to reproducibly change the sign of spin polarization. These forming experiments are presented in Section 7.1.2.

2.6.3 On the TMR temperature dependence in LSMO junctions

While the half-metallic nature of La_{0.7}Sr_{0.3}MnO₃ may be harnessed to probe spin-dependent tunneling from a fundamental standpoint, the original attraction for this compound lay with the potential for a large magneto-response at room temperature. However, until now, no manganite-based tunneling device operating at room temperature has fulfilled initial expectations. Such setbacks have been usually attributed to the electronic detail of the manganite/insulator interface, and in particular to the effect of symmetry breaking on the robustness of ferromagnetism at this interface. Chapter 6 explores the incidence of the tunneling transport phenomenon itself on the electronics properties of the LSMO/STO interface in LSMO/STO/LSMO and LSMO/STO/Co junctions.

2.6.4 Spin-dependent tunneling in the model system Fe(001)/MgO(001)

The Fe/MgO system provides a unique opportunity to test some of the more forward-thinking notions on spin-dependent tunneling, notably that of an effective spin polarization resulting from band structure interplay between Fe(001) and MgO(001). The special character of this system was described from a theoretical standpoint in Section 2.2.3. In Section 4.1.3 we describe the first reported magnetotransport experiments on fully epitaxial MgO-based junctions.

Chapter 3

Experimental techniques

This Chapter describes the experimental conditions used to obtain magnetotransport and X-Ray Magnetic Circular Dichroism results presented afterwards. Section 3.1 details the techniques used to grow samples presented in this Thesis, along with structural characterizations. The author was assisted by other members of our research group and by other groups in this respect. Section 3.2 presents the series of technological processes used to pattern trilayer samples into junctions for transport measurements. The author was responsible for all technological steps of junction patterning, as well as transport measurements. Section 3.3 raises some important points regarding sample characterization and transport in our junctions. Finally, Section 3.4 discusses the theory of X-Ray Magnetic Circular Dichroism as an experimental tool to probe magnetism.

3.1 Sample growth

This Section presents the experimental techniques used to grow the samples used in our magnetotransport measurements. Four distinct growth chambers were used. Our laboratory is equipped with a Pulsed-Laser Deposition (PLD) system (operated by E. Jacquet, J.-P. Contour and R. Lyonnet), which was used to grow our $\text{La}_{0.7}\text{Sr}_{0.3}\text{MnO}_3$ and SrTiO_3 oxide layers (see Section 3.1.1). To deposit transition metal counterelectrodes, we resorted to sputtering (operated by A. Vaurès) or Molecular Beam Epitaxy (operated by J. Humbert) systems (see Section 3.1.2). Finally, samples with a MgO barrier and Fe electrodes were grown in a combined sputtering-PLD system operated by C. Martínez-Boubeta within the A. Cebollada group in Madrid (see Section 3.1.3).

3.1.1 $\text{La}_{0.7}\text{Sr}_{0.3}\text{MnO}_3$ and SrTiO_3

$\text{La}_{0.7}\text{Sr}_{0.3}\text{MnO}_3$ (LSMO) thin films were grown on SrTiO_3 (001) substrates by pulsed laser deposition (PLD). A frequency tripled Nd:YAG laser ($\lambda=355$ nm) was focused on a stoichiometric target of LSMO. The films were deposited at a temperature of 700°C under 350 mtorr O_2 (*i.e.* molecular) pressure. Where applicable, ultrathin SrTiO_3 (STO) and thin LSMO layers were deposited immediately afterwards in these experimental conditions. Unless indicated otherwise, the thickness of the SrTiO_3 layer is 27.3\AA for all reported samples. Once deposition has ended, the oxygen pressure is raised to 300 torr and maintained at this value during cooldown to 500°C . Below this temperature, a full atmosphere of O_2 was introduced into the chamber. While our laboratory has separately established that the growth of STO under such partial pressure conditions impacts the dielectric properties of STO thin films [107], the presence of oxygen during growth and cooldown is necessary in order to obtain LSMO films with the correct oxygen stoichiometry.

At $T=700^\circ\text{C}$, LSMO grows cube-on-cube onto SrTiO_3 , in a strained fashion due to the 0.9% lattice mismatch. J.L. Maurice, R. Lyonnet and F. Pailoux have shown that our LSMO films remain strained up to 100nm. [108] Unless noted otherwise, $\text{La}_{0.7}\text{Sr}_{0.3}\text{MnO}_3$ films are 350\AA -thick, and STO tunnel barriers are 27.3\AA -thick. For more details, the interested reader may refer to reference [109] and to R. Lyonnet's PhD Thesis, [110] which was entirely dedicated to the optimization of growth conditions for the manganite and a boon for this Thesis.

Our laboratory has accrued extensive knowledge into the growth of manganite heterostructures which has resulted in LSMO/STO/LSMO junctions yielding 400% TMR at $T=4\text{K}$. [111] Reported in 1997, this early result reflects the crystal quality and abrupt interface of these samples, as illustrated by the High-Resolution Transmission Electron Micrograph (HRTEM) of Figure 3.1. Possible monolayer deviations in the thickness of the ultrathin STO layer result from atomic steps at the STO substrate which propagate through the 350\AA LSMO film. [112]

3.1.2 Transition metal counterdeposition

To obtain hybrid junctions with LSMO manganite and transition metal electrodes, a LSMO/STO bilayer grown as described above is transferred to either a sputtering system or a Molecular Beam Epitaxy (MBE) system. The transfer is performed in air, with temporary storage in a O_2 or N_2 environment.

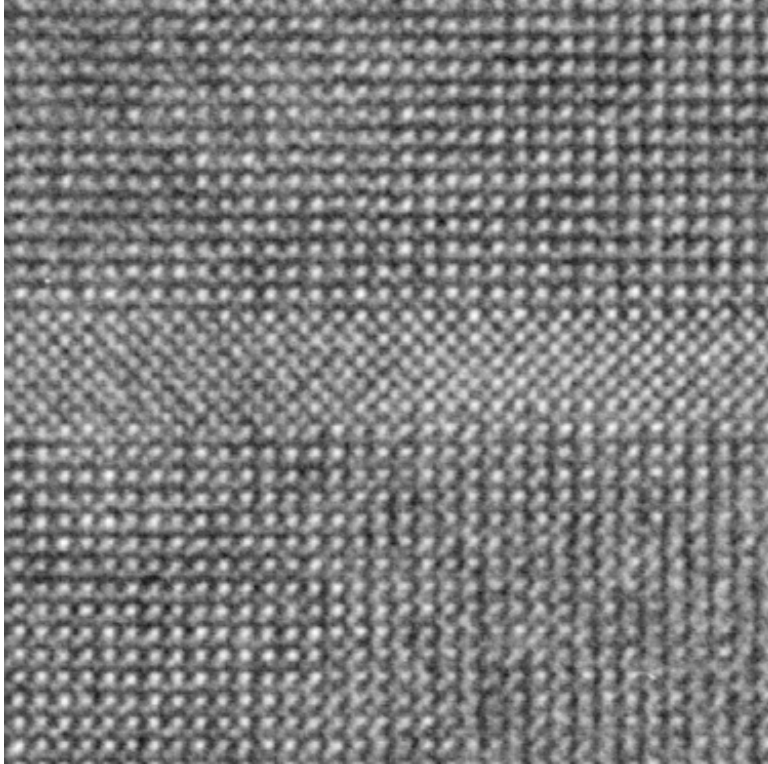


Figure 3.1: HRTEM of a STO barrier sandwiched between LSMO layers in this fully epitaxial constrained heterostructure. MnO_2 columns within LSMO, which exhibit bright contrast, are separated by the 3.905\AA STO lattice spacing. Picture by J.-L. Maurice.

3.1.2.1 Sputtering

To complete the LSMO/STO bilayer with a Co/CoO/Au multilayer, both a Alcatel A610 and a Plassys sputtering systems were used (by A. Vaures), with a base pressure of $2 \cdot 10^{-8}$ torr (high vacuum). In general, no treatment of the STO surface is performed prior to the deposition of the counterelectrode at room temperature. Co is deposited in a Ar working pressure of $2 \cdot 10^{-3}$ torr in RF mode at a $\sim 2\text{-}3\text{\AA}/\text{s}$ rate. During the course of this Thesis, our laboratory acquired the latter system, so that some of the later samples were completed using it.

Sputtering involves the formation of a plasma of a rare earth gas such as Ar. The ionized atoms are then accelerated toward a target which has been polarized. This bombardment leads to the ejection of atoms on the target, which are apt to coat the sample. This method implies a degree of incorporation of the rare earth element into the deposited layer. To increase

the effective deposition rate, the magnetron technique may be used: a magnetic field crated by permanent magnets deflects the sputtering ions, creating preferential etch sites on the target.

One advantage to using a sputtering approach is the ability to form CoO by oxidizing the Co layer - similarly to Al below, so as to promote exchange coupling between ferromagnet and antiferromagnet, and a much larger coercive field for the Co layer toward a better-defined antiparallel alignment of the two magnetic layers in an applied magnetic field. Unless noted otherwise, a so-called LSMO/STO/Co junction consists of the oxide bilayer described previously, capped with Co(150Å)/CoO(25Å)/Au(150Å).

To form the Al₂O₃ barrier where necessary, a layer of Al is first deposited, in similar experimental conditions to those of Co, then oxidized with a O₂ plasma - with equal partial pressures of Ar and O. Applied power is 25W and the oxidation time is optimized for the given Al film thickness to yield optimal oxidation. Interestingly, it was discovered that replacing Ar with a heavier rare earth element such as Kr leads to the formation of an insulating Al₂O₃ tunnel barrier of higher electrical quality, leading to larger magnetoresistance ratios. [113]

3.1.2.2 Molecular Beam Epitaxy

LSMO/STO bilayers may also be capped by Molecular Beam Epitaxy (MBE). In addition to a much better base pressure ($\sim 10^{-10}$ torr, *i.e.* ultra high vacuum), the lower kinetic energy of the atoms evaporated from a heated crucible onto the sample surface, and the generally lower deposition rate ($\sim 0.5\text{\AA}/\text{s}$) allow the growth of layers of higher crystalline quality. We used this growth method in particular to deposit Co_{1-x}Cr_x conterelectrodes. The very good stability of this deposition technique enabled, through the individual calibration of the Co and Cr cells, a good degree of control over the Cr concentration x in our Co films.

3.1.3 Fe/MgO samples

FeCo/MgO/Fe epitaxial structures were grown on GaAs(001) in a combined sputtering/laser ablation system with a base pressure of $2 \cdot 10^{-9}$ torr. A MgO buffer layer is used as an interdiffusion barrier with good electrical insulation characteristics. This prevents the incorporation of As from the substrate into the Fe bottom electrode - an important precaution since, in a subsequent step, the MgO barrier is grown at 400°C in order to obtain good crystallinity. Fe layers were deposited by triode sputtering with an Ar pressure of $3 \cdot 10^{-4}$ torr at a rate of $0.3\text{\AA}/\text{s}$. Optimal deposition temperatures were 400°C for

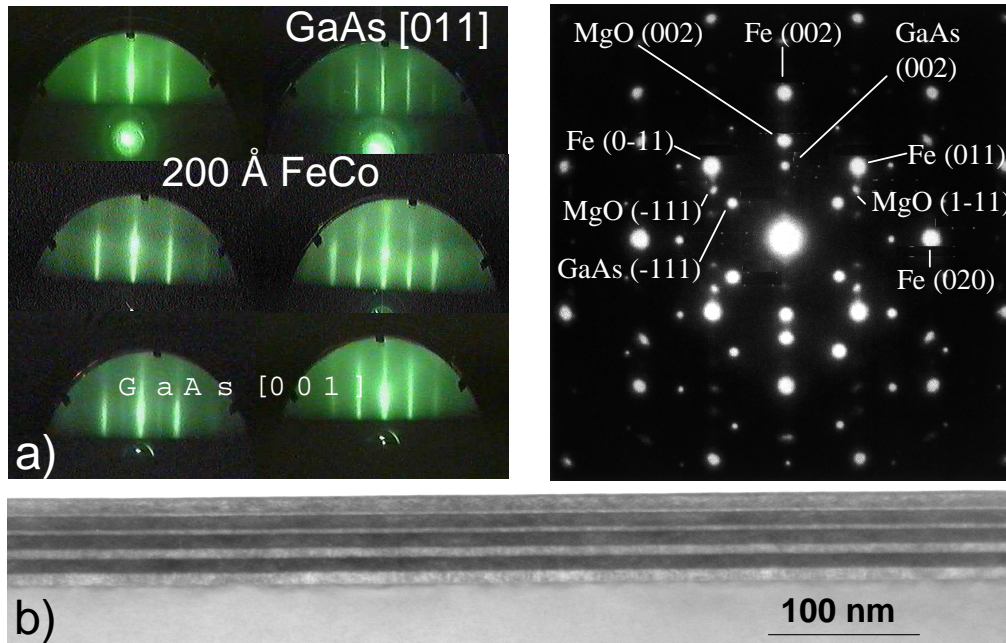


Figure 3.2: Growth of Fe/MgO/Fe multilayers: (a) RHEED pictures at each state of growth, (b) Cross-section TEM picture of a Fe/MgO multilayer and (c) electron diffraction of the entire cross-section. TEM picture by F. Güell.

the MgO, RT for FeCo top electrode and RT plus annealing at 400°C for the Fe bottom electrode. This low-temperature deposition and subsequent annealing process leads to an optimal Fe electrode in terms of crystallinity, continuity and interface sharpness.

Figure 3.2 illustrates the high quality of such samples. Panel (a) shows RHEED patterns for a typical $\text{Fe}_{50}\text{Co}_{50}/\text{MgO}/\text{Fe}$ structure. $\text{Fe}_{50}\text{Co}_{50}$ and Fe layers are bcc-structured with sharp diffraction lines for both azimuths. Similar information about epitaxial quality could be concluded from the MgO barrier pattern. Further x-ray diffraction symmetric and asymmetric scans confirm that the whole structure is epitaxial with lattice parameters close to bulk values. Panel(b) shows a [110] cross section Transmission Electron Microscopy (TEM) image from a test structure - dark regions correspond to the Fe layers while the lighter regions reflect the MgO layers. Continuous and good crystal quality MgO films with sharp interfaces are obtained all the way down to the thinnest 20Å oxide layer. As shown in panel (c), the electron diffraction pattern for a selected area of the TEM image illustrates the orientation relationship $\text{Fe}(100)[001] // \text{MgO}(100)[110]$ and is indicative of the crystallinity and high quality of the structure.

3.2 Sample patterning

This Section describes the technological procedure used to pattern trilayer samples into junctions. In order to perform electrical measurements through a specified surface of the trilayer stack on the as-grown sample, several lithography steps are required. The first two steps define the junction and the lower electrode, while the last two provide for electrical contacts above and below the structure. In an effort to optimize the junction quality of the oxide heterostructures under study, the technical parameters for this process have evolved during the course of this thesis. Initial transport studies were performed using a process originally designed for junction heterostructures with transition metal electrodes (process I: Section 3.2.1). In section 3.2.2, we will point out those technical and quantitative aspects of the process which have evolved to produce processes II and III.

3.2.1 Process I

3.2.1.1 From trilayer to junction in four steps

Step I The first process step defines the junction mesas or pillars in the trilayer structure. Thus the mask used consists of dark junction areas on a clear background, so that once the resist is exposed and developed, only those areas on the sample are covered with resist so as to be preserved from the first etching substep. Once the lithographic substep is completed, the sample is etched down beyond the upper electrode to either the barrier or the lower electrode layer, defining trilayer mesas or pillars.

Step II The second process step defines the lower electrode area. Thus the mask used consists of dark electrode areas on a clear background, so that once the resist is exposed and developed, only those areas on the sample are covered with resist so as to be preserved from the second etching substep. Once the lithographic substep is completed, the sample is etched down to the substrate.

Electrical passivation To avoid shortcircuiting the pillar when contacting the lower and upper portions, the sample is covered with a thick (2500Å) layer of Si_3N_4 . Though we have not tried other insulators, it is possible that using an oxide such as SiO_2 , because the sputtering substep is performed in an oxygen ambient, could constitute a more suitable passivator for oxide heterostructures.

Step III The third process step defines openings in the passivating layer through which to perform electrical contacts on the junctions and lower electrodes. Thus the mask used consists of light areas on a dark background, so that once the resist is exposed and developed, only those areas of passivating insulator to be removed are exposed, while the rest of the sample is covered with resist. Once the lithographic substep is completed, the sample is etched reactively to remove the desired patterns of the passivating layer. In the case of Si_3N_4 , the reactive gas used is SF_6 . A low-power O_2 etching step may be used to clean the surface before etching.

Step IV The fourth process step defines the electrical circuitry atop the structure needed to contact the junction mesas and bottom electrodes. Once insulated and developed, the open portions of the resist define the electrical paths. The sample is then coated with a bilayer of $\text{Ti}(500\text{\AA})/\text{Au}(1500\text{\AA})$, and the remaining resist removed by liftoff. Only in those areas with no resist at the end of the lithographic substep does the metallization overlayer remain. The success of the liftoff hinges on the correct definition of a hardened top portion of the resist layer which develops at a slower rate than the standard underlying resist and thus defines an overhang along all lithographic edges. This overhang provides shadow during the metallization process so as to leave exposed portions of the resist which may subsequently be attacked by acetone and yield the desired liftoff.

Substeps	Conditions	
Primer	5000rpm	30s
Resist	5000rpm	30s
Hardening using furnace	85°C	30 min
Exposure	$\lambda = 365\text{nm}$	35 $\text{mJ}\cdot\text{cm}^{-2}$
Development	MF319	Optical Control (80s)
Rinse	deionized water	180s, + N_2 dryoff

Table 3.1: Shipley S1813 photoresist conditioning for Steps I, II and III.

These steps define the original process (Process I) designed by François Moutaigne during his PhD Thesis. [114] Table 3.1 presents the technical specifications regarding resist conditioning for Steps I-III, while Table 3.2 details those regarding Step IV. The only immediate change brought to this process when carried over to oxide heterostructures consisted in depositing only Au electrical contacts to avoid any LSMO interface deoxygenation from Ti.

Substeps	Conditions	
Primer	5000rpm	30s
Resist	5000rpm	30s
Hardening using hotplate	90°C	1 min
Desensitization	chlorobenzene	10 min
Hardening using furnace	85°C	20 min
Exposure	$\lambda = 365\text{nm}$	90 $\text{mJ}\cdot\text{cm}^{-2}$
Development	MF319	150s
Rinse	deionized water	180s, + N ₂ dryoff

Table 3.2: Shipley S1813 photoresist conditioning for Step IV.

3.2.1.2 Standard Procedures

Sample preparation A good contact with the lithographic mask needed to ensure the correct definition of the desired motifs requires clean, smooth sample and substrate surfaces. Depending on the hardness of the substrate, it is worthwhile to scratch away any protrusions which could impede an even contact with the mask over the sample area. This technique was used in the case of STO given that our samples were pegged to the sample holder in the PLD chamber with silver paste. To protect the sample surface during this operation, a thick ($2.5\mu\text{m}$) layer of resist may be spun and annealed a short time (30"). Cleaning the sample surface using the standard procedure is recommended.

Sample cleaning To clean our samples, subsequent ultrasonic baths of acetone and propanol for 1 to 3 min are used. The sample is then dried thoroughly in a flux of N₂. A precursor step of trichloroethylene close to the vapor point may be used to remove any wax if used.

3.2.2 Optimizing the lithographic process for oxide heterostructures

The original process as applied to our oxide heterostructures produced several inconveniences and a few problems. This Section discusses some issues with sample processing with regards to our oxide samples.

3.2.2.1 High lower electrode resistances

Process I yielded junction devices with a manganite lower electrode of high resistance which could induced current-crowding effects. [115] This issue was

partly corrected in Process II through a redesign of the lithography masks to achieve a lower contact resistance.

This high resistance also results from the use of a *non-neutralized* ion gun to etch the samples in Steps I and II. To evacuate any accumulated charge, the sample is mounted with W clips to a grounded plate. While more elegant a solution compared to wet etching since it is materials-independent, charge accumulation was more problematic for $\text{La}_{0.7}\text{Sr}_{0.3}\text{MnO}_3$ with lower conductivity than a transition metal, so that the slow etch rate resulted in long etch times and thus in sample heating beyond the lower limit $T \sim 85^\circ\text{C}$ for LSMO deoxygenation and diminished conduction. In addition, the etching control was achieved using Auger analysis so that, owing to the small size of our samples, it was sometimes difficult to ensure that the $I \sim 20\text{mA}$ electron beam did not impinge upon a junction - with undesirable effects. This issue was corrected in Process III by resorting to a water-cooled *neutralized* ion gun with Secondary Ion Mass Spectroscopy.

3.2.2.2 Few junctions per sample

The main experimental difficulty laid with the limited number of junctions produced by the original masks: 3 junctions on an area of $5 \times 5 \text{ mm}$. Owing to homogeneity limitations during sample growth by PLD, we were restricted to $10 \times 10 \text{ mm}$ samples, $10 \times 7 \text{ mm}$ of which could be used to lithography 6 junctions at most. Given the time-intensive nature of sample preparation and junction elaboration, the sometimes poor statistic of working junctions implied repeating certain investigations a number of times. This issue was corrected in Process III.

3.2.2.3 Trilayer chemical passivation during the etching processes.

Electrical defects in the barrier may also result from the lithographic process itself. Many oxides such as STO may react with water or solvents and thus should be protected from water during lithography so as to prevent any possible shortcircuiting of the 20\AA barrier through the exposed flanks of the mesa.

Such contamination may occur between lithographic steps I and II, once the mesa has been defined. The resist used to define the mesa in Step I may be left on the junction, to be removed in a last O_2 etch during Step III. After an intervening step to deposit 800\AA of Si_3N_4 is then carried out, lithographic step II is performed, and a reactive ion etch used to lay the lower metallic layer bare for conventional etching.

The incidence of this procedure on junction performance was not fully

verified and for STO barriers the base process appeared to work. Nevertheless, at this juncture and considering overall junction statistics (see the preceding section 3.2.2), systematic application of this procedure may prove worthwhile. This procedure was implemented systematically for MgO-based junctions, but the low statistics of working junctions implies that this issue may not be the limiting factor in junction performance. Finally, junctions incorporating the double perovskite $\text{Sr}_2\text{FeMoO}_6$ as an electrode benefited from this chemical passivation procedure given the extreme reactivity of that compound to water.

3.2.2.4 Resist Conditioning

The resist layer in a given lithographic step may be conditioned in a variety of ways depending on the subsequent treatment the resist must then endure while carrying out that step of the process. The choice of resist, its thickness, the annealing time at a given temperature, the annealing method (by hotplate or oven), the development procedure and other post-development treatments all play a role in ensuring that the resist both fulfill its role as a mask and be removed at no expense to the heterostructure.

In the original process, Shipley S1813 is used throughout all steps. S1813 has a typical annealing temperature of 90°C , and a polymerization temperature of at most 130°C . The fast etch rate of transition metals allows for etch times which do not result in a temperature increase of the sample above the polymerization temperature of the S1813 resist. However, given the 3-5 fold reduction in etch rate for LSMO compared to that of a transition metal, initial lithographic processes sometimes resulted in polymerized resists, especially atop the smallest junctions. Thus for the etching steps I & II the S1813 resist was replaced with Shipley SPR 700 1.2, which has a higher polymerization temperature of 150°C .

A compromise must be reached regarding the thickness of the resist layer. A thicker layer will be easier to remove after any ion-etching step which may heat up and polymerize the resist surface. However the lower spinning rate used to obtain a thicker layer produces taller resist edge effects, especially at the sample corners, which can result in a poorer contact with the mask. This consideration is secondary with large samples, but becomes important with our 10×10 mm PLD-grown samples. It is possible to avoid this effect by either spinning the sample while applying the resist, or by letting the resist flow over the sample edge before spinning. The latter option may compound the problem by allowing for resist to go under the sample, which must then be removed once hardened from the annealing substep. And neither option really ensures a consistent process, though working junctions have resulted

from resorting to them.

3.2.3 Process II: modifying the electrical contact on LSMO

Process I was originally designed for junction heterostructures with transition metal electrodes. Since the Ar etching steps and the SF₆ reactive ion etching step don't prevent the creation of an ohmic contact with the Ti/Au circuitry, contacting the lower electrode is done directly once the upper electrode and barrier overlying the contact area have been etched away. Thus, only the trilayer area defining the junctions themselves is preserved in Step I, while the electrical contact is taken directly on the lower electrode.

However, the use of an oxide electrode such as LSMO led us to redesign this electrical contact. Indeed, the omission of Ti from the circuitry layer in Step IV results in poor bonding between LSMO and Au contacts. In addition, the aforementioned etching steps I, II and III degrade the LSMO surface stoichiometry by creating oxygen vacancies. This leads to a high contact resistance with the bottom electrode which impedes a quantitative measurement of junction resistance in 4-point geometry due to current inhomogeneities in the junction pillar. [115]

To circumvent these issues, Process II was designed to contact the bottom electrode through the overlaying structure. The resistance measured across the lower electrode is comprised of two macroscopic 1 mm² junctions in addition to the electrode itself. The design concept assumed that these macro-junctions would contribute a negligible magnetoresistive signal compared to that of the junction under study. This revised process produces electrode resistances which overall are at least one order of magnitude lower than junction resistances, as well as a MR signal well below junction MR. Thus any current crowding effects [115] in the junction pillar are avoided and little stray MR signal is introduced into the junction MR response. To accomplish these changes, Step I is modified so as to leave the lower electrode contact areas protected from the etch.

3.2.4 Process III: more junctions of smaller size

Process III was designed to address the recurring issue of junction statistics in our studies as discussed above. The main design goals were thus to increase the number of junctions produced from a given PLD-grown sample - of small size, and to decrease the size of these junctions to increase junction quality. This process takes more actively into consideration the oxide nature

of our heterostructures by endeavoring to mitigate all forms of sample heating during the etching processes. The design of this Process resulted from a collaboration between A. Anane and the author on both the design of the masks and the evolution of the lithographic process.

3.2.4.1 Junction Design

To obtain results given a poor statistic of working junctions, the process was improved. Processes I and II yielded 3 junctions for 5 x 5 mm of sample area with sizes ranging from 80 μm^2 to 1960 μm^2 . The new set of lithographic masks produces 144 junctions for 6 x 6 mm of sample area, in sizes ranging from 2 μm^2 to 4096 μm^2 , with and without shape anisotropies. In a first iteration, rectangular junctions were designed with the shape anisotropy axis perpendicular to the bottom electrode axis. This design aspect may lead to difficulties in obtaining an antiparallel alignment, and was corrected in a minor revision. This revision also lowered the maximum junction area while multiplying the number of junctions at very low area which have consistently produced better results.

3.2.4.2 Resist Conditioning

To obtain features on the order of 1-2 μm , the lithography process was revised. A switch from Shipley S1813 to SPR700 1.2 resist was made since the latter can withstand larger temperatures (130°C→150°C) before polymerizing. This in turn allows the definition of smaller resist features which could still be lifted using the appropriate solvent.

Substeps	Conditions	
Primer	4000rpm	30s
Resist	4000rpm	30s
Hardening using furnace	85°C	30 min
Exposure	$\lambda = 365\text{nm}$	35 mJ.cm ⁻²
Flank improvement using hotplate	105°C	1 min
Development	MF319	Optical Control (35s)
Rinse	deionized water	180s, + N ₂ dryoff
Water removal using hotplate		
Further hardening	110°C	30s

Table 3.3: Shipley SPR700 1.2 photoresist conditioning for Steps I and III.

Table 3.3 outlines the substeps used to condition the resist for Steps I and III where high definition is required. For Steps II and IV, the conventional

Process may be used (see Tables 3.1& 3.2).

3.2.4.3 Sample Etching

Another substantial improvement in the patterning process laid with resorting to a water-cooled sample holder, in conjunction with a *neutralized* ion gun. This feature is essential to avoiding charge accumulation on the sample surface when etching oxide heterostructures with poorer electrical conductivity than conventional metals.

To further minimize any heating, the sample is mounted onto the water-cooled sample holder by means of a paste with high thermal conductivity though little electrical conductivity. Initial tests at the time of writing are to ascertain the incidence of grounding the sample on the properties of the LSMO electrode and junctions, supposing that the beam isn't totally neutralized.

Compared to our previous technique, the net result of cooling the sample during a neutralized etch is to substantially lower LSMO lower electrode resistivities toward values on par with those of as-deposited films. [116]

In addition, our neutralized ion gun is equipped with a Secondary Ion Mass Spectrometer so as to permit a nearly real-time monitor on the evolution of sample etching through the various multilayers by accumulating data on specific elements.

3.3 Experimental considerations

This Section describes some important experimental considerations regarding our magnetic tunnel junction heterostructures. Section 3.3.1 briefly discusses the chemical state of the interfaces in LSMO/STO/LSMO and LSMO/STO/Co junctions. Section 3.3.2 presents our magnetotransport measurement technique and discusses possible electromigration effects through our oxide films.

3.3.1 Chemical state of the $\text{La}_{0.7}\text{Sr}_{0.3}\text{MnO}_3/\text{SrTiO}_3$, $\text{SrTiO}_3/\text{La}_{0.7}\text{Sr}_{0.3}\text{MnO}_3$ and SrTiO_3/Co interfaces

During the course of this Thesis, J.L. Maurice at our laboratory has overseen and taken part in an extensive characterization of manganite trilayer structures. This Section describes the salient results of this High-Resolution Transmission Electron Microscopy (HRTEM) and Electron En-

ergy Loss Spectroscopy (EELS) study, with a particular focus on interfaces in LSMO/STO/LSMO and LSMO/STO/Co junctions. A more in-depth discussion of results is presented in Appendix B.

Several HRTEM pictures have been shown above to illustrate the epitaxial quality and abruptness of our heterostructures. The EELS technique involves sweeping an electron beam across the interface, with $\approx 7\text{\AA}$ resolution, in 3\AA steps. The resulting energy loss spectra provide information on the electronic environment of a given element with spatial resolution, thereby permitting a chemical and electronic analysis of the interface.

3.3.1.1 Upper and lower LSMO/STO interfaces

To assess any disruption of the manganite's electronic properties due to symmetry breaking at the interface, a series of EELS studies on the upper and lower interfaces in LSMO/STO/LSMO junctions was conducted. [117, 118] No shift in the $\text{Mn}^{3+}/\text{Mn}^{4+}$ ratio governing the double exchange mechanism was found at either the lower or upper interface. However, these studies show that the two interfaces aren't exactly identical. Indeed, the variation in the elemental profiles across each interface differ somewhat.

3.3.1.2 The STO/Co interface

As pointed out previously, a transfer in air occurs between the deposition of STO and Co. It is therefore important to characterize the chemical state of the STO/Co interface. HRTEM studies evidence the presence of a monolayer of foreign oxide at this interface. Subsequent EELS experiments performed at the STO/Co interface [119] provide evidence for the presence of a 4-10 \AA -thick layer of Co in an oxygen environment which resembles CoO. However, HRTEM pictures show that the oxide layer isn't continuous, so that we expect tunneling transport to occur through the metallic inclusions in such a layer.

Finally, it should be noted that the 350mtorr oxygen ambient used to deposit the SrTiO_3 barrier layer may lead to a possible oxygen gradient. [120] This could affect the chemical profile of these interfaces.

3.3.2 Transport

This Section describes our experimental apparatus to perform transport measurements, and discusses possible electromigration effects in our oxide heterostructures.

3.3.2.1 Transport measurements

Our lithographic processes permit electrical contacts at each end of the lower electrode, as well as two contacts atop the junction mesa. These contacts enable the use of a four-point measurement geometry. Given the spectroscopic nature of our tunneling investigations, we performed measurements in a voltage source mode. To this end, a Keithley 2400 has been mainly used.¹ Although this sourcemeter only provides a $650\mu\text{V}$ resolution on applied bias, it integrates this function with current measurement so as to offer a complete solution.

In our four-point measurement geometry, a bias is applied between the lower electrode and junction contact, and current is measured between the other lower electrode contact and the second junction contact. Since the actual measurement reflects only the overlap of current lines between the two sets of contacts, only the junction mesa is probed through this technique.

3.3.2.2 Determining barrier heights

Most experimental investigations on magnetic tunnel junctions resort to WKB models such as those of Simmons, [3] Brinkman [4] or Stratton, [5] to extract barrier height, thickness, and asymmetry (Brinkman) from I-V characteristics. However, as argued by Sun, [121] these widely used models do not take into account the variety of physical effects at play in manganite-based tunnel junctions.

Other techniques may be used. As argued by Rottländer *et al.*, [122] the premise behind evaluating barrier heights by examining the evolution of I-V curves at one temperature relative to another is that the increasing thermal energy $k_B T$ will allow electrons injected toward the collecting interface at an applied bias nearing the interfacial barrier height to tunnel all the more predominantly. A peak in $\frac{I(T)-I(T_0)}{I(T_0)}$ for P and AP configurations at a given value of applied bias V therefore indicate the presence of a tunneling barrier of height $\Phi = eV$. In the limits of low spin-dependent scattering and high spin polarization of the tunneling current, this premise may be generalized to reflect spin-dependent features of the entire heterostructure as well. For instance, a DOS feature in the spin \downarrow channel probed by a spin \uparrow current will be enhanced with temperature as other processes intermix the two spin channels. We have adopted this simple, physical approach to characterizing our barrier heights throughout this Thesis.

¹In some instances, a Keithley 236 with higher current sensitivity was also used.

3.3.2.3 Electromigration & Junction forming

This Section describes the manifestation of junction forming under an applied bias. Since the voltage drop occurs predominantly across the tunnel barrier, any electromigration from the resulting electric field is apt to occur at the interfaces as well as across the tunnel barrier. We first discuss general electromigration considerations, and then consider such forming effects on the STO/ferromagnet interface. Finally, we outline how this effect, generally considered to adversely affect magnetotransport measurements, may in fact be harnessed as an additional parameter to probe spin-dependent solid state tunneling.

Generalities In the domain of ferroelectrics, much attention has been placed on the performance of perovskites such as BaTiO_3 or $\text{Pb}(\text{Zr}, \text{Ti})\text{O}_3$ (PZT). Destined for use in memories among possible applications, these materials must retain their virgin characteristics, such as remanent polarization after applying an electric field in alternating directions, over the course of many cycles. However, microstructural changes to these thin films over the course of cycling (10^4 to 10^7) degrade their performance. [123] An overarching cause of such “fatigue” lies with the consequences of electron injection on domain states within the ferroelectric, and the modification of the electronic potential step at the electrode/ferroelectric interface. Fatigue has also been attributed to the redistribution within a perovskite thin film of defects such as oxygen vacancies, [124] though the predominance of effects at play have not been fully understood at this time. [123] More recent studies show that, in the process of cycling, oxygen is not released from the perovskite, [125] while the process of oxygen electromigration alone does not explain the observed fatigue, as reported from isotopical profile studies of PZT films subjected to cycling. [126] Nevertheless, it appears that oxygen vacancies in such oxide structures appear to dominate any electromigration considerations. [127] Finally, according to Stolichnov *et al.*, [128] charge accumulation also controls dielectric breakdown in perovskites, so that time spent at a given bias is just as important as the amplitude of bias applied in determining dielectric resiliency under voltage stress. In the particular case of SrTiO_3 , oxygen vacancy diffusion occurs with a very small $\sim 1\text{eV}$ enthalpy of activation. [126]

The above electromigration studies are performed using perovskite thin films subjected to an electric field $\sim 10^5\text{V/cm}$. In contrast, voltage biases reaching 1V and more are applied across our $\approx 30\text{\AA}$ SrTiO_3 barriers, resulting in a $\sim 10^6\text{V/cm}$ electric field. Forming must therefore be taken into account when performing bias-dependent studies on magnetic tunnel junctions.

Element	Oxide	Enthalpy (kcal/mol)
Ni	NiO	-101
Co	CoO	-104
Fe	FeO	-122
Zn	ZnO	-152
Cr	Cr ₂ O ₃	-170
Ta	Ta ₂ O ₅	-180
Ti	TiO ₂	-212
Al	Al ₂ O ₃	-252
Mg	MgO	-272

Table 3.4: Enthalpy of oxide formation for selected elements at T=300K. Thus, MgO oxidizes most readily in contrast to Ni. From [129]

Oxide stability Possible electrochemical changes to an oxide are predicated on its stability through a low enthalpy of formation. Table 3.4 lists the enthalpy of oxide formation for remarkable elements. Thus Mg readily oxidizes in contrast to Ni. This implies that Al₂O₃ tunnel barriers are not as sensitive to forming effects.

Also, the integration of certain ferromagnets (FM) such as Fe as electrodes in magnetic tunnel junctions are more likely to yield a transition metal oxide at the ferromagnet/barrier interface with possibly undesirable consequences on magnetotransport. Consequently, using a counterelectrode which contains Fe may also lead to a more unstable junction than one with Co alone. This trend was empirically observed at our laboratory, as LSMO/STO/FM with FM=Fe,FeCr,FeNi exhibited more electrical instability and evolving history-dependent magnetotransport properties. [130] Such effects underscore accrued forming processes at the STO/FM interface when the FM has a low enthalpy of oxide formation.

This explanation was independently corroborated by Sun *et al.* on LSMO/STO/FM (FM=Fe,Co_{0.8}Fe_{0.2}) junctions. [131] The authors observe electrical instabilities, leading to hysteretic behavior after applying a large bias (typically V=0.5V) and to differing signs of tunneling magnetoresistance from junction to junction on the same sample. In addition, a persistent junction resistance creep was observed even at low applied bias. It is important to mention that in their work the STO/FM interface is also exposed to air during transfer, so that a O₂ plasma etch of the SrTiO₃ surface was performed to remove any contaminants.

In spite of the large electric fields applied across our STO barriers in our junctions, in general the junction remains stable up to applied bias values

$\sim 1\text{V}$ when LSMO or Co counterelectrodes are used. Beyond this value, some partly reversible forming may sometimes occur. The history of the junction also factors into the heterostructure's electrochemical stability. As a dramatic example, LSMO/STO/FM junction with FM=CoCr exhibit electrochemical instability at moderately large applied bias values ($\sim 0.5\text{V}$). We have also tried Sun *et al.*'s sample growth procedure and etched the STO surface with a O_2 plasma to remove contaminants before Co counterdeposition. Junctions measured on such samples indeed exhibit resistance creep and generalized junction electrical instabilities.

Electromigration as a tool If the experimental investigation purports to explain magnetotransport properties in terms of a heterostructure as grown nominally, then such electromigration effects represent an experimental nuisance. If, on the other hand, the experiment takes into account such electrochemical changes to the heterostructure, then the effect may be harnessed as a tool to probe interfacial effects such as changes to the density of states or to the sharpness of the interfacial profile. Also, since such electromigration effects through the junction represent a form of spatial doping, it is possible to relate such effects to changes in the junction's chemical potential, and thus investigate repercussions on transport. The effect of modifying the stoichiometry of STO and LSMO on band structure is described in Appendix A.

As experimental work in this Thesis has progressed, the inclusion of possible electromigration effects into an understanding of magnetotransport has led to a very compelling physical picture. Beyond first results on LSMO/STO/FM (FM=Fe,FeNi,FeCr), [130] the study using FM=CoCr, designed to probe the effect of DOS modifications on the bias dependence of TMR (Section 5.2.2), evidenced a recurring issue with junction electrical instability. Careful experimentation described in Section 7.1.2 on such junctions shows how electromigration may be used to affect the chemical state of the STO/CoCr interface so as to control magnetotransport properties of the junction. The instability of LSMO/STO/Co junctions processed from samples with an etched STO surface was utilized to prepare junction states which remain stable at low temperature. The junction's magnetotransport properties may then be examined in each state and related to electrochemical changes to the junction's effective potential profile for that state (Section 7.3.3). Similarly, electromigration effects at very large bias ($|V|=3\text{V}$) were used in otherwise stable LSMO/STO/LSMO junctions with a similar intent (Section 7.2.2).

3.3.3 On junction irreproducibility

During the course of investigating the magnetotransport properties of junctions with perovskite materials, and in particular SrTiO₃ barriers, it has become clear that it is not possible to reproduce R·A products from sample to sample. This degree of junction irreproducibility may have multiple origins.

3.3.3.1 The patterning process

Despite the evolutions described above to mitigate any damage to the oxide heterostructure, it is possible that certain aspects of the technological steps need further amelioration. Since heating may damage the LSMO layer, an effort was undertaken to minimize all forms of sample heating. However, the definition of small resist features which may withstand the ensuing etching substep requires hardening in a furnace. Notably, the metallization process (Step IV) we have used clearly heats up the sample, though the temperature remains below the 130°C polymerization temperature of the S1813 resist.

3.3.3.2 Electrostatic modifications

Whether during the initial electrical contacting, or when the sample is mounted or removed from the holder, the junction may be subjected to electrostatic discharges. As noted above, this may affect junction chemistry. When possible, precautions are taken to eliminate or mitigate any such effects, whether when contacting the junction to the sample holder or when placing the sample holder on the measuring stage. It has become clear, nevertheless, that contacting can modify junction resistance. Also, a junction will be affected by removal and reinsertion from the measuring stage.

3.3.3.3 Temporal evolution of oxide junctions

We have witnessed on a number of occasions how sample curing with the passage of time may affect in a positive manner the electrical characteristics of LSMO/STO/FM junctions. While still quite qualitative at the time of this writing, we may state with reasonable certainty that: junctions which are allowed to “rest” regularly during the lithographic cycle tend to exhibit R·A products amenable to tunneling transport measurements; and that junctions measured just after completing the lithographic patterning may display an enhanced tendency toward quite low R·A products. Finally, junction characteristics, measured immediately after patterning, appear to improve with time. To shore up these statements, we provide the following anecdotal evidence: samples patterned over 3-5 weeks tend to exhibit good electrical

characteristics. This trend appears to be enhanced by reoxygenation steps in an air furnace at 85°C for several days, particularly after the first two etching steps. Samples patterned in 4 days (Process II) were shortcircuited, but after a span of nearly one year showed decent magnetotransport characteristics. This last fact was independently confirmed on a separate set of samples using Process III.

A mechanism which may underlie these observations is the degree of electrochemical activity for such all-oxide junctions, combined with the fact that SrTiO₃ may pump oxygen from the La_{0.7}Sr_{0.3}MnO₃ layer so as to reduce the number of defects in the tunneling barrier. This could explain why such temporal effects haven't been reported in junctions integrating the more stable Al₂O₃ barrier.

3.3.3.4 Pinholes in the epitaxial tunnel barrier

As opposed to an amorphous tunnel barrier formed through the oxidation of a metal, an epitaxial barrier will naturally contain defects. A Conducting Tip Atomic Force Microscope scan across the surface of a STO(001)//LSMO(350Å)/STO(27.3Å) sample has shown the presence of very localized hotspots (diameter $\sim 40\text{\AA}$) in the tunnel barrier for which resistance falls by several orders of magnitude. [132] It is supposed that these hotspots, when present across a macroscopic junction, may channel most of the tunneling current. This physical picture points to an *effective* surface area in the junction instead of the nominal one.

3.4 Probing magnetism with X-Ray Magnetic Circular Dichroism

This Section presents a succinct description of the X-Ray Magnetic Circular Dichroic effect and its utilization as a tool to probe magnetism on a very small scale.

3.4.1 Theory of X-Ray Magnetic Circular Dichroism

The rotation of the axis of electromagnetic oscillations which have interacted with a magnetic material, discovered through transmission experiments by Faraday in 1848, [133] and 30 years later by Kerr through reflection experiments, [134] have led to a flurry of techniques to probe magnetic behavior. Today Magneto-Optic Kerr Effect setups utilizing lasers represent a convenient tabletop apparatus, but the concept has also led to the development of

more refined and elaborate techniques to offer insight into magnetic behavior with astounding precision. Once a tool of advances in weaponization, synchrotrons have become an invaluable asset to the larger research community. From the first handheld cyclotron developed by O.E. Lawrence in Berkeley, CA (USA) in the late 1930s to the future SOLEIL synchrotron in France, refinements over the generations have led to gargantuan facilities which can provide a coherent, very intense source of electromagnetic radiation. Electrons are accelerated in circular fashion so as to emit X-Rays. Tangential to the ring are beamlines which channel the X-Ray emission for use by endusers to probe a property of their sample.

3.4.1.1 Spin-dependent, element-specific transitions

By definition, XMCD is the difference between the absorption spectrum for left-circularly and right-circularly polarized light - with helicity $+\hbar$ and $-\hbar$ as per Feynman's definition, [135] for a magnetic field applied along the incident photon axis. The interaction of a circularly polarized photon of energy 10eV-30keV with an atom primarily causes scattering processes and photoelectric absorption. Scattering processes may be elastic (Compton) or inelastic (Raman), while the photoelectron absorption process involves the transition of a core electron to a higher lying state or to the continuum, followed by deexcitation processes. Figure 3.3 summarizes the effect described hereafter.

According to the composition rules for spherical harmonics described in the Wigner-Eckart theorem:

$$\Delta s = 0 \quad \Delta l = \pm 1 \quad \Delta j = 0, \pm 1 \quad \Delta m = \pm 1 \quad (3.1)$$

$\Delta s = 0$ implies the conservation of spin between initial and final states of the transition. The total absorption cross-section, in the dipole approximation, is then given by the summation over all initial and final states of the transition probability following the Fermi Golden rule:

$$\sigma(\hbar\omega) = 4\pi^2\alpha\hbar\omega \sum_{i,f} |\langle f | \vec{\epsilon} \cdot \vec{r} | i \rangle|^2 \cdot \delta(E_f - E_i - \hbar\omega) \quad (3.2)$$

where $\alpha \approx 1/137$ and ϵ is a unitary plane electromagnetic wave. Since $E_f - E_i$ is a quantity which is specific to each element, tuning the incident photon energy $\hbar\omega$ to this transition energy yields an element-specific probe of spin-dependent electronic transitions occurring within the penetration thickness of the incident photon.

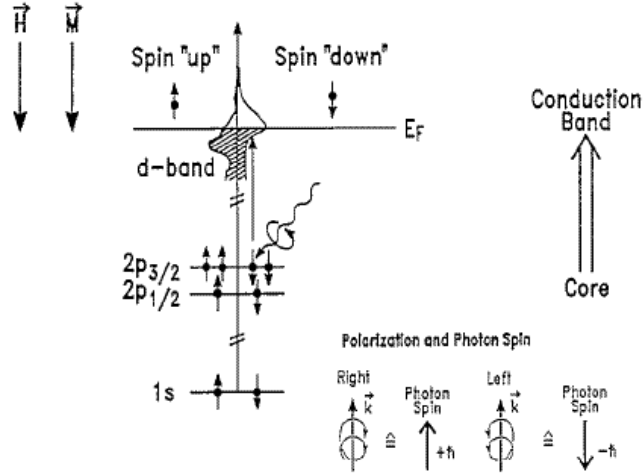


Figure 3.3: Schematic of the photoelectron absorption process between spin-orbit split $2p$ bands and valence $3d$ bands in a transition metal. The efficiency of X-ray absorption due to a circularly polarized photon beam reflects the spin imbalance created at the Fermi level crossing the valence $3d$ band by the photoelectrons.

3.4.1.2 The two-step model

XMCD may be viewed as a two step process. The first involves the emission of a photoelectron at an atomic site which has interacted with a photon. We shall focus on $p \rightarrow d$ transitions within a $3d$ transition metal element. The core level $2p$ band is split into $2p_{3/2}$ and $2p_{1/2}$ initial substates by the spin orbit interaction. Transitions from such initial states to empty states in the $3d$ valence band above E_F are termed the L_3 and L_2 edges, respectively. Due to the spin orbit interaction, these initial substates are no longer pure spin states but are coupled to the orbital moment, so that \vec{l} and \vec{s} are parallel and antiparallel at the L_3 and L_2 edges, respectively. When a left circularly polarized photon transfers its angular momentum $+\hbar$ to a L_3 substate, the probability of transition is greater for spin \uparrow states since \vec{l} , \vec{s} and $+\hbar$ are all parallel. Likewise, at the L_2 edge, since \vec{s} and $+\hbar$ are antiparallel, this edge will promote the transition of mainly spin \downarrow electrons. In a similar fashion, the incidence of right-circularly polarized light at each of the two edges will create an equal amount of photoelectrons at each edge but of opposite spin.

The second step concerns the final state of the transition. Since the $3d$ valence band is exchange-split, there is an unequal density of unoccupied final states (*i.e.* holes) to reach in each photoelectron spin channel. For a hard ferromagnet such as Co, there are more minority states than majority states

at E_F . Therefore, as the helicity of the incoming photon is changed from left- to right- circularly polarized light, absorption will increase at the L_3 edge since it favors spin \uparrow transitions, and decrease at the L_2 edge since it favors spin \downarrow transitions. In this sense, the valence d band acts as a spin analyzer of the photoelectric absorption process, setting the conversion efficiency of spin \uparrow and \downarrow transitions at each edge given its exchange splitting.

The experimental measurement of photoelectron absorption occurs either through fluorescence (*i.e.* detecting the photon resulting from radiative recombination of electron and hole), or through the collection of emitted electrons from the Fermi level crossing the valence $3d$ band. We have worked in this latter total electron yield mode. The electron yield is $\sim e^{-z/\lambda_e}$ where λ_e is the electron escape depth. X-Ray Absorption Spectra (XAS) may be then taken with the magnetic field and photon helicity alternately in parallel and antiparallel configurations, which we define as the positive and negative phase, respectively. In practice it is possible to switch either, so that four spectra may be acquired.

3.4.1.3 The sum rules

In 1992, Thole *et al.* proposed the first magneto-optic sum rule to be applied to circular dichroism in the x-ray regime of radiation. [136] This rule enables a direct evaluation of the average expectation value of the ground state of the momentum operator L_Z acting on the shell receiving the photoelectron final state. One year later, Carra *et al.* proposed the second sum rule to extract the spin momentum operator L_Z and magnetic dipole operator T_Z . [137] The following sum rules take into account refinements to initial theory, and discard the small $2p \rightarrow 4s$ contribution to absorption to consider only the predominant $2p \rightarrow 3d$ transition: [138, 139]

$$\frac{\int_{j^+ + j^-} (I^{-1} - I^{+1}) d\omega}{\int_{j^+ + j^-} (I^{-1} + I^{+1} + I^0) d\omega} = \frac{\langle L_Z \rangle}{ln_h} \quad (3.3)$$

$$n_h = 2(2l + 1) - n$$

$$\frac{\int_{j^+} (I^{-1} - I^{+1}) d\omega - \frac{l}{l-1} \int_{j^-} (I^{-1} - I^{+1}) d\omega}{\int_{j^+ + j^-} (I^{-1} + I^{+1} + I^0) d\omega} = \frac{2}{3n_h} (\langle S_Z \rangle + \frac{2l+3}{l} \langle T_Z \rangle) \quad (3.4)$$

where I^{-1}, I^{+1} and I^0 denote the normalized absorption cross-sections for left-circularly, right-circularly and linearly polarized photons. j^+ and j^-

refer to the L_3 and L_2 absorption edges. From these sum rules, the following magnetic moments may be determined:

- the orbital magnetic moment: $m_L = -\frac{\mu_B}{\hbar} \langle L_Z \rangle$
- the spin magnetic moment: $m_S = -\frac{2\mu_B}{\hbar} \langle S_Z \rangle$
- the magnetic dipole moment: $m_T = +\frac{\mu_B}{\hbar} \langle T_Z \rangle$

Since these rules involve differences between integrals over the L_3 and L_2 edges, spectra need to include stable baselines at each end which are reproducible from scan to scan.

3.4.2 Experimental Implications

We will discuss specific details on sample design when presenting results. Nevertheless, the above description of the theory underlying the XMCD effect brings to light the following basic consideration when designing samples: the $\approx 30\text{\AA}$ electron escape depth, when working in total electron yield mode, sets certain sample design constraints to fully utilize the element specificity of the technique.

Part II
Experiments

Chapter 4

Ferromagnet/Insulator interfaces probed by spin-dependent tunneling and synchrotron radiation

This Chapter presents two experimental approaches to verifying ideas on the role of the barrier material in spin-dependent solid state tunneling. The first approach is to utilize the spin-analyzing properties of the manganite $\text{La}_{0.7}\text{Sr}_{0.3}\text{MnO}_3$ with nearly total spin polarization [116] to probe other barrier types, in conjunction with experiments on MgO-based fully epitaxial magnetic tunnel junctions (see Section 4.1). The second approach regards the picture of magnetic moments induced within the paramagnetic tunnel barrier at the interface with a ferromagnet, developed by Oleinik, Tsymbal and Pettifor [34, 36], which purports to explain the positive and negative signs of spin polarization of ferromagnets at the interface with Al_2O_3 and SrTiO_3 barriers. Such a picture may be explicitly verified through X-Ray Magnetic Circular Dichroism studies on carefully designed samples (see Section 4.2).

4.1 Magnetotransport experiments

Through a set of spin-dependent transport experiments, we discuss in this Section the electronic character of solid state tunneling through various barrier materials. In Section 4.1.1 we present evidence for the nearly total spin polarization of the $\text{La}_{0.7}\text{Sr}_{0.3}\text{MnO}_3$ when at the interface with SrTiO_3 . This half-metallic character of transport is then used in a spin-analysing manner

to probe the role of the barrier in solid state tunneling (see Section 4.1.2). Finally, Section 4.1.3 presents experiments on band structure effects in fully epitaxial junctions with MgO barriers.

4.1.1 Nearly total spin polarization at the LSMO/STO interface

The key advantage of integrating a manganite such as $\text{La}_{0.7}\text{Sr}_{0.3}\text{MnO}_3$ into magnetic tunnel junctions is the purported half-metallic nature of transport in this oxide through double exchange conduction. However, the 88% of tunneling spin polarization for a manganite, reported by Jo *et al.*, has been the highest reported value. [92] Such a result leaves room for doubt regarding half-metallicity, especially as Nadgorny *et al.* have evidenced [140] the presence of minority states at E_F in $\text{La}_{0.7}\text{Sr}_{0.3}\text{MnO}_3$ through point contact Andreev reflection.¹

We have synthesized a STO(001)//LSMO (350 Å) / STO (27.3 Å) / LSMO (100Å)/Co (125Å)/CoO(25Å)/(Au 150Å) heterostructure through pulsed-laser deposition and sputtering for the oxide perovskites and metals, respectively. The metals were deposited at room temperature. In counterdepositing Co to be pinned by the succeeding CoO through antiferromagnetic exchange coupling, we intended to increase the coercive field of the top LSMO layer so as to promote a better antiparallel (AP) state during magnetotransport measurements.

The sample was then patterned into junctions using lithography Process III. As shown in Figure 4.1 through a R(H) loop taken at T=4K on $V_{DC}=1\text{mV}$ for a $64 \mu\text{m}^2$ junction, the tunneling magnetoresistance (TMR) may reach 1860%. From the Jullière model, and taking $P_1=P_2$, this value leads to a spin polarization of $P=95\%$. Simple considerations imply that this very high spin polarization of the LSMO/STO(001) interface may be *nearly total*. Indeed, this value represents only an average for the upper and lower interfaces which, though very similar, we know are not identical (see Section A.5). In addition, as discussed hereafter, the TMR ratio decreases immediately with increasing applied bias. Therefore, resorting to zero-bias AC lock-in measurements at lower temperatures should yield increased ratios. Nadgorny *et al.*, using the Andreev reflection technique, had evidenced the presence of minority states at E_F . [140] As explained in Section 2.2.1, the spin polarization measured through this technique takes into account a transmission factor $M \propto v_F$, whereas in tunneling $M \propto v_F^2$. Since in

¹This technique does not measure the same degree of spin polarization as the tunneling effect. See Section 2.2.1

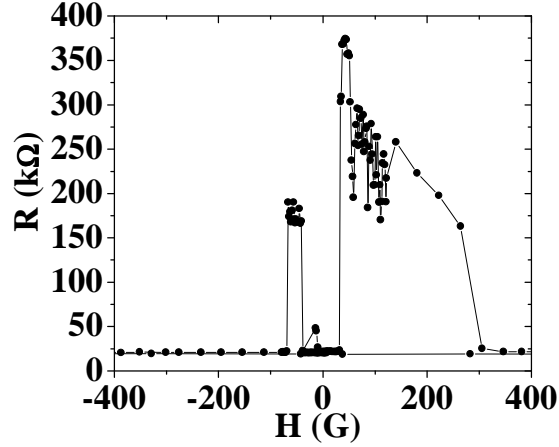


Figure 4.1: LSMO/STO/LSMO magnetotransport at $T=4\text{K}$. Junction A with area $64\mu\text{m}^2$: $R(H)$ loop at $V_{DC}=1\text{mV}$.

$\text{La}_{0.7}\text{Sr}_{0.3}\text{MnO}_3$ $v_F^\uparrow \gg v_F^\downarrow$, it isn't surprising to find a larger degree of spin polarization from tunneling. Thus, this result affirms the nearly total tunneling spin polarization of $\text{La}_{0.7}\text{Sr}_{0.3}\text{MnO}_3$.

The eventual antiparallel alignment of such a junction's magnetic electrodes depends on factors such as junction shape anisotropy respective to the lower electrode anisotropy, eventual dipolar fields caused by overetching into the lower electrode during junction mesa definition, and the additional uniaxial anisotropy induced by CoO pinning. As shown above, we have difficulty in obtaining a good antiparallel alignment over the field range promoted by CoO pinning. This difficulty is to be contrasted with the well-defined AP plateaux for $\text{La}_{0.7}\text{Ca}_{0.3}\text{MnO}_3/\text{NdGaO}_3/\text{La}_{0.7}\text{Ca}_{0.3}\text{MnO}_3$ junctions in the (110) orientation due to manganite uniaxial anisotropy as reported by Jo. [92] Nevertheless, we believe we have obtained a fully antiparallel configuration in this case. Indeed, the 35G-wide resistance plateau during the positive-to-negative field sweep lies approximately half the resistance of the 10G-wide plateau obtained during the negative-to-positive field sweep. We think that this first plateau with evidently stable micromagnetism represents a 90 degree alignment of electrode magnetizations.

4.1.2 LSMO/I/Co experiments

This Section describes a set of magnetotransport measurements on LSMO/I/Co junctions, where $I=\text{Ce}_{0.69}\text{La}_{0.31}\text{O}_{1.845}$, Al_2O_3 , $\text{SrTiO}_3/\text{Al}_2\text{O}_3$ and TiO_2 . The inverse TMR obtained on LSMO/STO/Co

was interpreted as resulting from the negative d -band spin polarization of Co evidenced through favorable d -character tunneling due to interfacial bonding and MIGS in the case of SrTiO₃ (see theoretical and experimental Sections 2.2.2.3 on page 16, & 2.6 on page 38). To confirm this interpretation, we have tried other barrier materials.

La_{0.7}Sr_{0.3}MnO₃ (350Å) thin films were grown on SrTiO₃ (001) in standard growth conditions described in Section 3.1.1. The epitaxial growth of SrTiO₃, lattice-matched Ce_{0.69}La_{0.31}O_{1.845} [141] and TiO₂ [142] is then performed in the same growth conditions, after which a Co counterelectrode is deposited in a separate chamber by MBE. In the case of the composite SrTiO₃/Al₂O₃ barrier, an ultrathin Al layer was deposited onto the SrTiO₃ surface, and thereafter etched with a O₂ plasma to form the Al₂O₃ barrier. Co was immediately deposited atop this freshly formed barrier. The samples were then patterned into magnetic tunnel junctions thanks to lithographic Processes I and III.

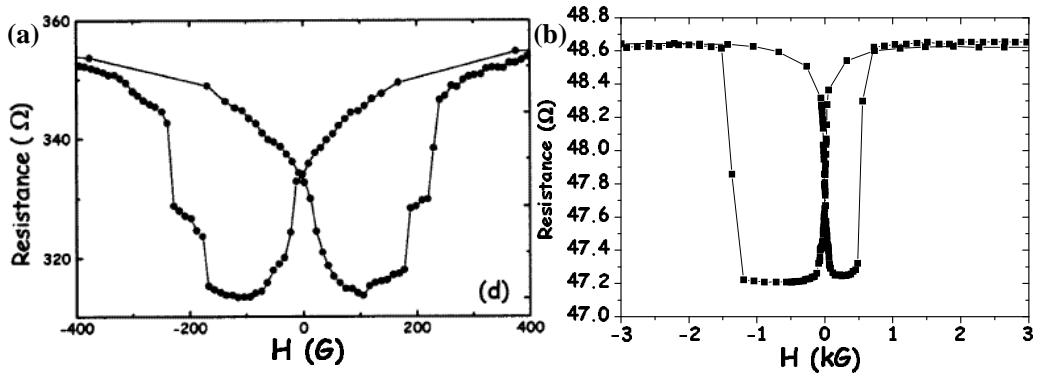


Figure 4.2: LSMO/I/Co: $R(H)$ loops at $V=10\text{mV}$ for (a) $I=\text{Ce}_{0.69}\text{La}_{0.31}\text{O}_{1.845}$ and (b) $I=\text{TiO}_2$. The asymmetric loop found in the case of TiO₂ reflects AF pinning by CoO atop the Co layer.

Figure 4.2 presents $R(H)$ loops taken at low temperature and low applied bias for LSMO/I/Co ($I=\text{Ce}_{0.69}\text{La}_{0.31}\text{O}_{1.845}$ (30Å), TiO₂ (30Å)). As shown in panels (a) and (b), spin-dependent tunneling between LSMO and Co through either Ce_{0.69}La_{0.31}O_{1.845} or TiO₂ result in an inverse TMR. According to the Jullière model, and the spin analyzing capability of LSMO with $P\approx+1$, this implies a negative spin polarization (P) at the Co/barrier interface for these two barrier types. These results buttress an interfacial bonding and MIGS picture since these barriers possess a d -type conduction band typical of transition metal oxides (see Section A.1) which result in d - d interfacial bonding and conduction band MIGS of d character, so as to promote the negative d -band spin polarization of Co in the tunneling transmission.

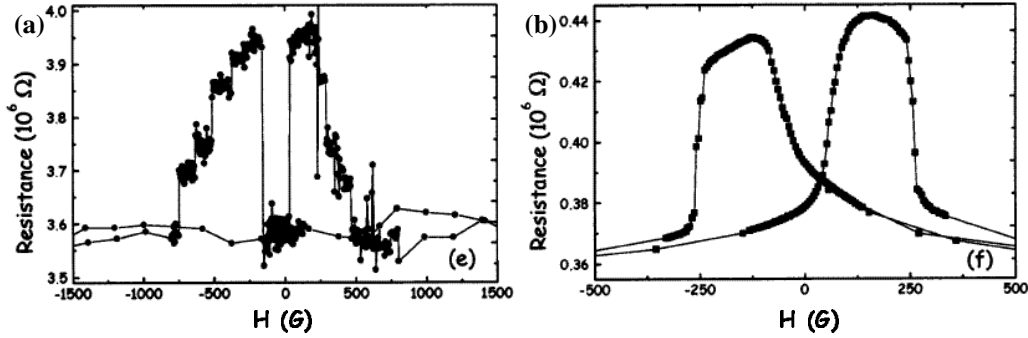


Figure 4.3: LSMO/I/Co: $R(H)$ loops at $V=10\text{mV}$ for (a) $I=\text{Al}_2\text{O}_3$ and (b) $I=\text{SrTiO}_3/\text{Al}_2\text{O}_3$.

To discern whether the inverse TMR observed for a LSMO/STO/Co junction results from an interface or trilayer band structure effect, we have also tried Al_2O_3 and $\text{SrTiO}_3/\text{Al}_2\text{O}_3$ barriers. Figure 4.3 presents $R(H)$ loops taken at low temperature and low applied bias for junctions with an Al_2O_3 (30\AA) or a SrTiO_3 (10\AA)/ Al_2O_3 (15\AA) barrier. In both cases the TMR is normal, so that the $\text{Al}_2\text{O}_3/\text{Co}$ interface is solely responsible for this positive TMR. This indicates a positive sign of spin polarization at the $\text{Al}_2\text{O}_3/\text{Co}$ interface. This set of magnetotransport data thus reveals the importance of taking into account the ferromagnet/barrier couple when considering spin-dependent tunneling. In addition, the insight provided by these results [23] will have led to the harmonization of the picture of solid state tunneling. Indeed, by attributing the positive sign of ferromagnet (FM) spin polarization obtained through the spin-dependent tunneling technique (with FM/ $\text{Al}_2\text{O}_3/\text{Al}$, see Section 2.2.1) to the incidence of the barrier type on this conduction process, these results reaffirmed the capability for this technique to indeed measure the sign of FM spin polarization given a tunneling barrier which may promote the d -band character of this P. This outlook has been verified by Worledge *et al.* who measured the correct negative spin polarization of SrRuO_3 by means of the spin-dependent tunneling technique through a SrTiO_3 barrier. [20] More akin to our experiments, Takahashi *et al.* have also observed a negative sign of SrRuO_3 spin polarization at the interface with SrTiO_3 through spin-dependent tunneling measurements on $\text{La}_{0.7}\text{Sr}_{0.3}\text{MnO}_3/\text{SrTiO}_3/\text{SrRuO}_3$ magnetic tunnel junctions. [24]

4.1.3 The Fe/MgO(001) interface

This Section describes a set of measurements on fully epitaxial MgO(001)-based magnetic tunnel junctions. As described in Section 2.2.3, the interest behind spin-dependent tunneling between Fe(001) electrodes through a MgO(001) barrier lies with band structure spin polarization effects across the trilayer. This research axis resulted from a collaboration with the group of A. Cebollada (Madrid, Spain) and his graduate student C. Martínez-Boubeta. Within the framework of a Franco-Spanish Picasso project, this group synthesized the samples, while our participation involved junction patterning and magnetotransport measurements. Section 4.1.3.1 presents initial results on tunneling through a MgO barrier, while Section 4.1.3.2 investigates the electronic character of tunneling transmission in the Fe/MgO system with spin-dependent tunneling measurements on fully epitaxial Fe/MgO/FeCo(001) and LSMO/STO/MgO/Fe magnetic tunnel junctions.

4.1.3.1 Large magnetoresistance

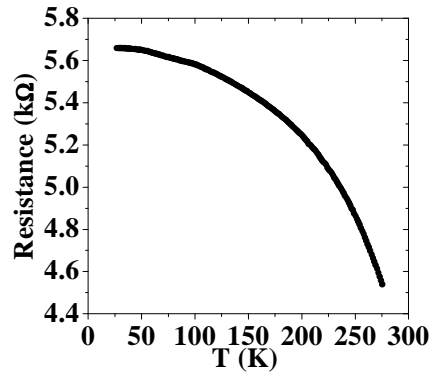


Figure 4.4: Fe/MgO/FeCo: temperature evolution of junction resistance.

A Fe(200Å)/MgO(20Å)/FeCo(250Å) trilayer grown epitaxially onto MgO(001)-buffered GaAs(001) was processed by optical lithography using Process II. The differing Fe and FeCo electrodes were chosen so as to ensure different coercive fields toward a good antiparallel alignment of the electrode moments. Here we present results obtained on a tunnel junction of area $80 \mu\text{m}^2$. Transport measurements were performed in 4-point voltage source mode ($V+ = \text{Fe}$). The resistance of the Fe electrode is more than 100 times smaller than the junction resistance, thus ruling out any significant contribution from geometrical effects. [115] As shown in Figure 4.4, the resistance of our MTJ (at $V=+10 \text{ mV}$) saturates below 50 K and then decreases slowly by

about 25% between 50 K and 300 K. This is a typical temperature dependence in which intrinsic tunneling transport processes have given way above 50 K to additional thermally-assisted processes. The temperature dependence of non-linear $I(V)$ curves places [122] the barrier height at $\Phi=0.9\text{eV}$. Simmons' model [3] yields $\Phi=1.1\text{eV}$ for a barrier thickness $d\sim 15\text{\AA}$, in good agreement with previous transport studies using epitaxial MgO(111) by Kiyomura *et al.*, [143] and polycrystalline MgO by Moodera *et al.*, [144] who both report $\Phi=0.9\text{eV}$ using this method. If we compare this value to half that of the 5.5 eV MgO band gap calculated for an ultra-thin layer, [46] the difference may be due to metal-induced gap states in the MgO barrier [42] although we can not completely rule out the presence of stoichiometric and/or thickness inhomogeneities in the insulating film. A somewhat higher value of Φ has been reported by Wulfhekel *et al.* through STM measurements in which both the MgO and the vacuum barriers are taken into account. [145]

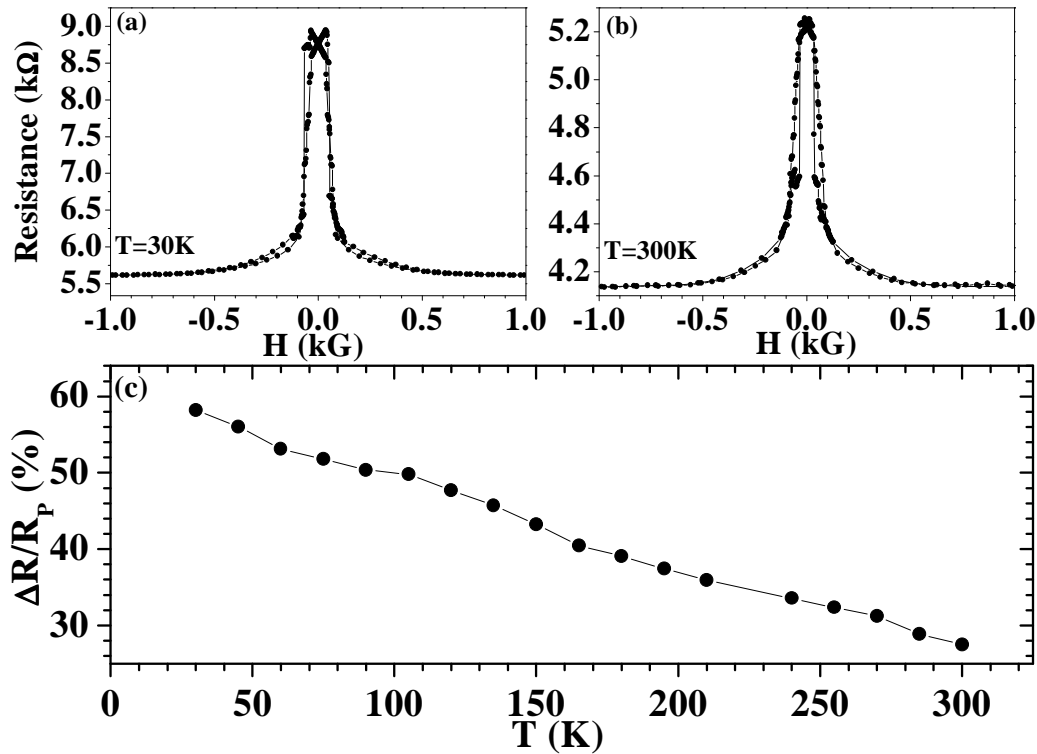


Figure 4.5: Fe/MgO/FeCo: $R(H)$ loops at (a) $T=30\text{K}$ and (b) $T=300\text{K}$; and (c) temperature dependence of TMR.

Figure 4.5a shows a $R(H)$ cycle taken at $T=30\text{K}$ for an applied bias of $V=+10\text{ mV}$. We find a TMR $(R_{AP}-R_P)/R_P=+60\%$. The rise in resistance

to the antiparallel (AP) state in a decreasing field before reaching $H=0$, and more generally the symmetry of the $R(H)$ curve around $H=0$, was initially interpreted as resulting from overmilling into the bottom Fe electrode during the junction mesa definition, thus creating a stray field-induced antiparallel state.

As temperature increases, the TMR decreases in almost linear fashion to 27% at 300K (panels (b) and (c)). The origin of this sizeable decrease in TMR amplitude with increasing temperature, which has been broadly reproduced by very recent experiments on Fe/MgO/Fe epitaxial MTJs by Faure-Vincent *et al.*, [91] is not understood at the time of this writing, though it could involve a reduction of barrier Δ_1 band filtering due to thermally-assisted processes.

Yuasa *et al.* have studied Fe/Al₂O₃/FeCo tunnel junctions with (100), (110) and (211)-oriented single-crystal electrodes and amorphous Al₂O₃ yielding up to 40% TMR for the (211) orientation but only 13% for the (100) orientation. [146] Yuasa *et al.* ascribed this weak TMR to a small (7%) spin polarization of the calculated density of states (DOS) at the (100) surface of Fe. The 60% TMR we find for Fe(100) demonstrates that the spin polarization of tunneling electrons can not be directly correlated with the spin-polarized DOS of a free metal surface, but depends on the actual electronic structure of the barrier/electrode system and can be quite different for Fe(100)/Al₂O₃ and Fe(100)/MgO(100) interfaces. It is therefore coincidental that the low-temperature TMR value is in agreement with expectations from Jullière's expression (Equation 2.4) when using $P_{Fe} = 45\%$ and $P_{FeCo} = 51\%$ - obtained through the spin-dependent tunneling technique with Al₂O₃ barriers (see Table 2.1). As explained below, such a junction could have yielded a larger TMR amplitude at lower applied bias and temperature. This would have confirmed the band structure origin of the effective spin polarization in this system.

4.1.3.2 Band structure effects

As described in the previous Section 4.1, a given metal-oxide interface favors a particular spin polarization and electronic character of the tunneling current. Co/Al₂O₃ interfaces result in a positive polarization which, in an oversimplified picture, can be ascribed to a predominant tunneling of *s*-character electrons due to Co-O chemical interactions at the interface. [34]. We now extend this discussion to the Fe/MgO interface.

We present a bias dependence study of the TMR obtained for our Fe/MgO/FeCo junction in Figure 4.6. The TMR decreases almost² sym-

²The slight asymmetry could reflect somewhat different barrier heights at each inter-

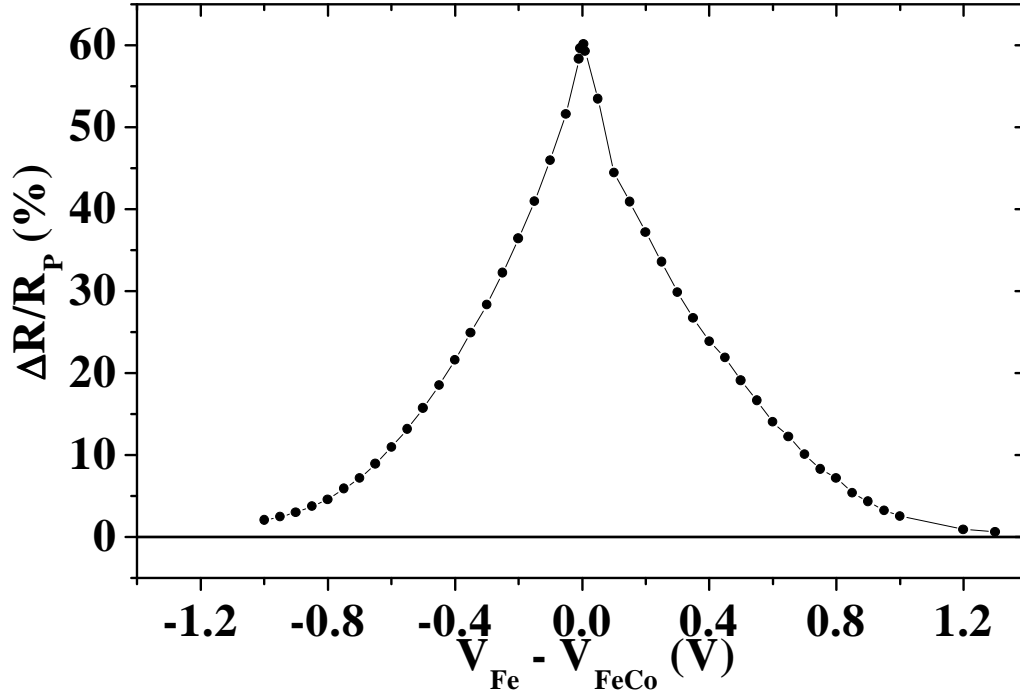


Figure 4.6: Fe/MgO/FeCo: bias dependence of TMR at T=30K from R(H) loops.

metrically from a value of 60% at $V=+10$ mV to nearly 0 around 1.4V. This result is confirmed with 2 mV-resolved $I(V)$ curves taken in the parallel and antiparallel states. This monotonic TMR decrease with applied bias is very similar to that found for a junction with a Al_2O_3 barrier. In the case of MgO, calculations show a Δ_1 electronic symmetry of predominant transmission. [46] This symmetry group includes s , p_z and d_{z^2} orbital characters. In amorphous barriers, instead of electron symmetries one can only speak in terms of orbital character. In Al_2O_3 s -character transmission is observed (see Section 2.2.2.3). [34] Therefore, to the extent that a comparison is possible, calculations and experiment point to the same character of predominant transmission. Given the similar Δ_1 electronic character of the valence and conduction bands for Al_2O_3 and MgO, one may expect a similar picture of interfacial bonding and Metal-Induced Gap States for the two barriers (see Figures 2.5 & 2.8).

The predominant transmission (*e.g.* filtering) in MgO(001) of electronic states with Δ_1 symmetry, coupled with the presence of only Δ_1^\uparrow states at the Fe(001) Fermi level, leads to a positive sign of spin polarization

face. [54]

due to such band structure effects, despite the fact that, as pointed out by Butler *et al.*, [46] the spin polarization at the Fe/MgO(001) interface is negative. To determine whether standard spin polarization or band structure effect drive magnetotransport, we used the spin-analysis properties of the half-metallic $\text{La}_{0.7}\text{Sr}_{0.3}\text{MnO}_3$ with $e_g \uparrow$ conduction to determine the sign of spin polarization at the Fe/MgO interface. Through the sample growth capabilities of both laboratories, we synthesized a $\text{La}_{0.7}\text{Sr}_{0.3}\text{MnO}_3$ (350Å)/ SrTiO_3 (11.7Å)/ MgO (33.6Å)/ Fe (50Å) fully epitaxial [147] sample.

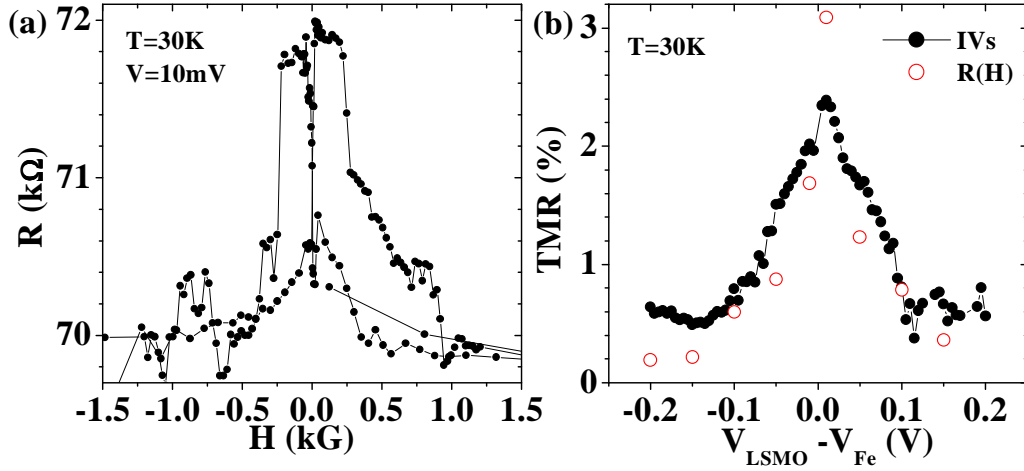


Figure 4.7: LSMO/STO/MgO/Fe: $R(H)$ at $V=+10\text{mV}$, and (b) bias dependence of TMR at $T=30\text{K}$ from IV data and $R(H)$ loops.

Figure 4.7 presents magnetotransport results at $T=30\text{K}$ on a $80\mu\text{m}^2$ junction patterned using Process II. As shown in the $R(H)$ taken at $V=+10\text{mV}$, the TMR is positive, lending credence to a band structure spin polarization of positive sign at the Fe/MgO interface. The bias dependence of TMR, shown in panel (b), exhibits the similar decrease around $V=0$ found above, thus reinforcing a picture of Δ_1 tunneling for the Fe/MgO ferromagnet/barrier couple. Beyond these salient considerations, it may seem puzzling that the amplitude of TMR is so low. This effect may well result from sample preparation conditions, which involve the growth of Fe at 400°C without the oxygen ambient needed to prevent oxygen desorption in the LSMO thin film. Indeed, electrode resistance was over twice that usually found. It is also possible that a wavefunction electronic asymmetry between the two ferromagnetic electrodes is responsible for this low amplitude.

4.1.4 Summary

The results obtained on LSMO/I/Co (I=Ce_{0.69}La_{0.31}O_{1.845}, Al₂O₃, SrTiO₃/Al₂O₃, TiO₂) demonstrate that the inverse TMR observed in LSMO/STO/Co junctions reflect solely *d-d* interfacial bonding at the Co/STO interface and MIGS considerations for this barrier type. The sign of P_{Co} at the interface with other transition metal oxide barriers also reflects similar band structure effects. In addition, the Δ_1 electronic symmetry of tunneling electrons through a MgO(001) barrier was demonstrated both through the magnetotransport response in Fe/MgO/FeCo(001) and in LSMO/STO/MgO/Fe(001) fully epitaxial magnetic tunnel junctions, as expected given the complex band structure of MgO(001).

The interpretation of these results does not take into account possible barrier profile effects, which have been shown to influence the amplitude and even the sign of TMR. [21] It is therefore quite useful to note a very recent report of inverse TMR measured for the La_{0.7}Sr_{0.3}MnO₃/SrTiO₃/SrRuO₃ system. [24] This sign of TMR is in agreement with the positive and negative degrees of tunneling spin polarizations for La_{0.7}Sr_{0.3}MnO₃ and SrRuO₃ respectively. In this particular case, given the fully epitaxial nature of the junction, no extrinsic effects can be invoked to explain the result. The reliance of all these measurements on the spin-analyzing property of the half-metallic La_{0.7}Sr_{0.3}MnO₃, while a definite asset, also bring to question the effect of the double-exchange *d*-character (e_g spin \uparrow) DOS on spin-dependent tunneling in such systems. It may be interesting to perform measurements on more conventional junctions with composite barriers, such as Co/Al₂O₃/SrTiO₃/Co in the spirit of experiments performed by Sharma *et al.*, [51] or perhaps utilizing a SrRuO₃ electrode with itinerant ferromagnetism.

4.2 Induced Moments in paramagnetic tunnel barriers

The predicted influence of junction interfacial bonding and Metal-Induced Gap States on spin-dependent solid state tunneling offers a very compelling model to describe the effect of barrier material on the electronic character of the tunneling current. According to Oleinik *et al.*, [34, 36] predictions arising from this physical picture include the appearance of a magnetic moment induced on the barrier's interfacial layer resulting from proximity to a ferromagnetic electrode, through a direct or indirect ferromagnetic exchange mechanism. To test the concept, we performed X-Ray Magnetic Circular Dichroism experiments at the European Synchrotron Radiation Facility

(ESRF) on samples with Al_2O_3 and MgO barriers, grown using processes which have yielded working magnetic tunnel junctions with good characteristics. [90,148] The MgO samples were grown in the same conditions as those of the previous Section (see sample growth in Section 3.1.3), while the others were grown by A. Vaurès at our laboratory.

4.2.1 Experimental considerations

Experiments were performed at the ESRF's ID8 beamline operated by the group of N. Brookes, where we were assisted by P. Bencok and S. Dhesi. A more detailed explanation of the X-Ray optics which compose their beamline may be found on the group's web site. [149] The particularity of their beamline is the ability to apply magnetic fields up to $H=70\text{kG}$ at liquid helium temperatures while switching the helicity of the incoming photon beam with $\approx 100\%$ polarization. The energy resolution $\Delta E/E \sim 2 \cdot 10^{-4}$ at 850eV , so that their setup is well adapted to the XMCD study of transition metals.

The theory underlying the XMCD technique has been described in Section 3.4.1. Since our measurements are in total electron yield mode, the electron escape depth requires that the material to be probed not lie below $\sim 30\text{-}50\text{\AA}$ of the sample surface. This implies that the ferromagnet/barrier interface to be probed must lie near the surface of the sample stack. Finally, we are looking for an interface effect, so that this element-specific technique needs to be applied to ultrathin barrier layers which may yield an appreciable interfacial signal.

To test predictions by Oleinik *et al.* regarding an induced moment at the $\text{Co}/\text{Al}_2\text{O}_3$ interface on the O site of the barrier, we performed XMCD experiments on the following sample: $\text{Si} // \text{Ta}(50\text{\AA}) / \text{Co}(150\text{\AA}) / \text{Al}_2\text{O}_3 \text{ wedge} / \text{Co}(30\text{\AA}) / \text{Au}(20\text{\AA})$. The Al_2O_3 wedge was sputtered from a stoichiometric target, so that the lower interface is properly oxidized throughout the wedge. In a similar spirit, we also endeavored to detect an induced moment on the O site of a MgO barrier. Given the pulsed-laser deposition growth of MgO, no wedge capability could be utilized to probe a barrier thickness dependence of the induced moment. Therefore, the experiment was conducted on several samples individually grown with varying MgO thickness.

4.2.2 Experimental results

We now present our experimental findings on the detection of an induced moment within the tunneling barrier through the XMCD technique. For all scans, $H=\pm 3\text{T}$ and $T=5\text{K}$.

4.2.2.1 Al_2O_3

The sample under consideration, Si // Ta(50Å) / Co(150Å) / Al_2O_3 wedge / Co(30Å) / Au(20Å), consisted of an Al_2O_3 wedge 30mm long and with a final thickness of 30Å. Since the photon beam width is $10 \times 50 \mu\text{m}^2$, a measurement will probe a particular thickness of the barrier wedge with very high precision. We first present results for $d_{\text{Al}_2\text{O}_3} \approx 3\text{Å}$. For this wedge thickness, we surmise that any signal covers the entirety of the 30Å-thick Co overlayer, as well as a very small portion of the Co layer below the Al_2O_3 layer.

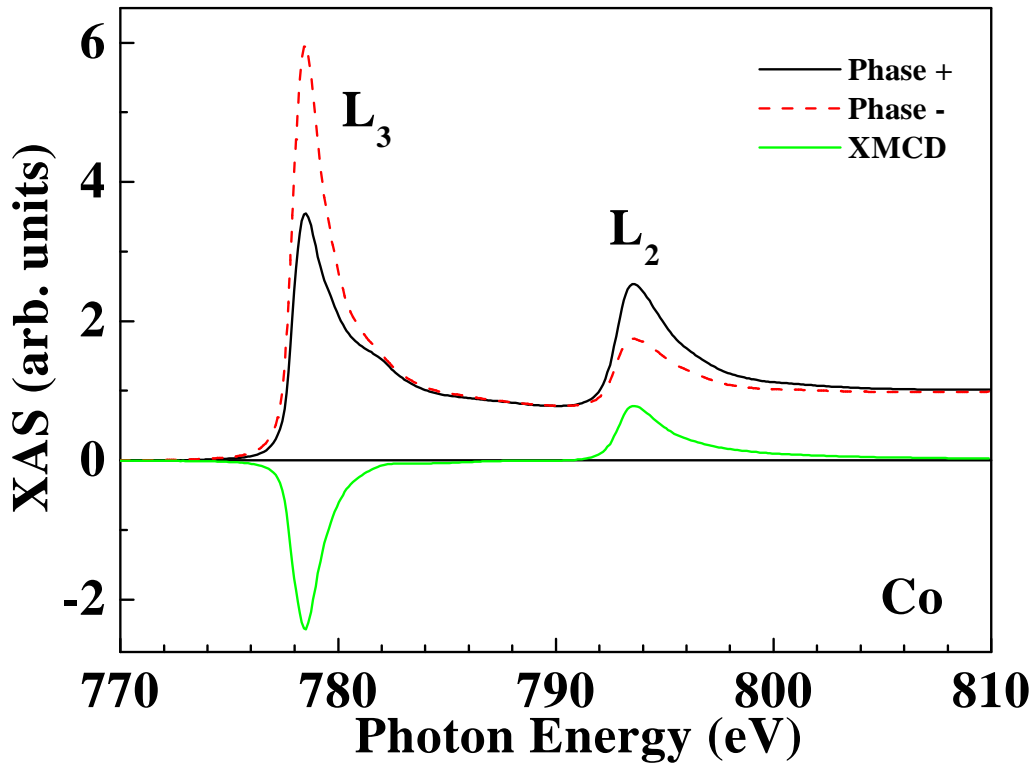


Figure 4.8: Si//Ta(50Å)/Co(150Å)/ Al_2O_3 ($3 \pm 1\text{Å}$)/Co(30Å)/Au(20Å): X-ray absorption spectra (XAS) for the positive and negative phases, and the resulting XMCD spectrum, at the Co $L_{3,2}$ edges at $T=5\text{K}$. No corrections have been made.

Figure 4.8 presents X-ray absorption spectra (XAS) at the Co L edge for parallel and antiparallel alignments of photon helicity and magnetization, along with the resulting dichroic signal. As expected, Co exhibits sizeable dichroism at the $L_{3,2}$ edges of opposite sign as described previously, with no sign of peak splitting indicative of oxidation within the 0.2eV resolution of the experiment. From the sum rules, the spin and orbital moments are

$1.64\mu_B/\text{atom}$ and $0.15\mu_B/\text{atom}$, in good agreement with the calculated values $1.63\mu_B/\text{atom}$ and $0.12\mu_B/\text{atom}$. [150]

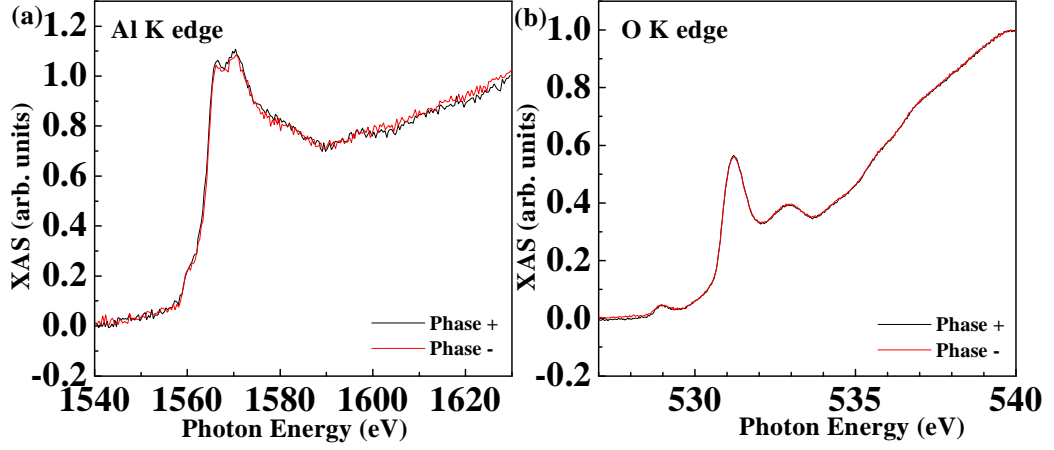


Figure 4.9: Si//Ta(50Å)/Co(150Å)/Al₂O₃ (3±1Å)/Co(30Å)/Au(20Å): X-ray absorption spectra (XAS) for the positive and negative phases, at the (a) Al K edge and (b) O K edge at T=5K. No corrections have been made.

Figure 4.9 presents X-ray absorption spectra (XAS) at (a) the Al K and (b) the O K edges for positive and negative phases. No dichroism was observed at either edge.

To verify this negative result, we repeated the same experiment on a thicker part of the wedge. Figure 4.10 presents X-ray absorption spectra (XAS) at the Al K edge for $d_{\text{Al}_2\text{O}_3} \approx 7\text{\AA}$. The slight difference observed between phase-shifted XAS spectra closely mirrors the derivative of the XAS scan, and therefore cannot be attributed to dichroism. No dichroism was observed at the O K edge (data not shown).

4.2.2.2 MgO

Figure 4.11 presents XAS spectra at the Fe L edge on the following sample: MgO(001)//MgO(100Å)/Fe(250Å)/MgO(10Å)/Fe(20Å)/Pt(20Å). No sign of peak splitting indicative of oxidation is present, while from the sum rules, the spin and orbital moments of Fe are $2.19\mu_B$ and $0.03\mu_B$ per atom, within the error bar of bulk value of $2.25\mu_B$ and $0.08\mu_B$ per atom. [150] We surmise that this signal arises from both the Fe overlayer and a small portion of the Fe layer below the 10Å MgO layer.

Figure 4.12 presents XAS spectra at (a) the Mg K edge and (b) the O K edge of the same sample. Regarding Mg, the difference between the XAS

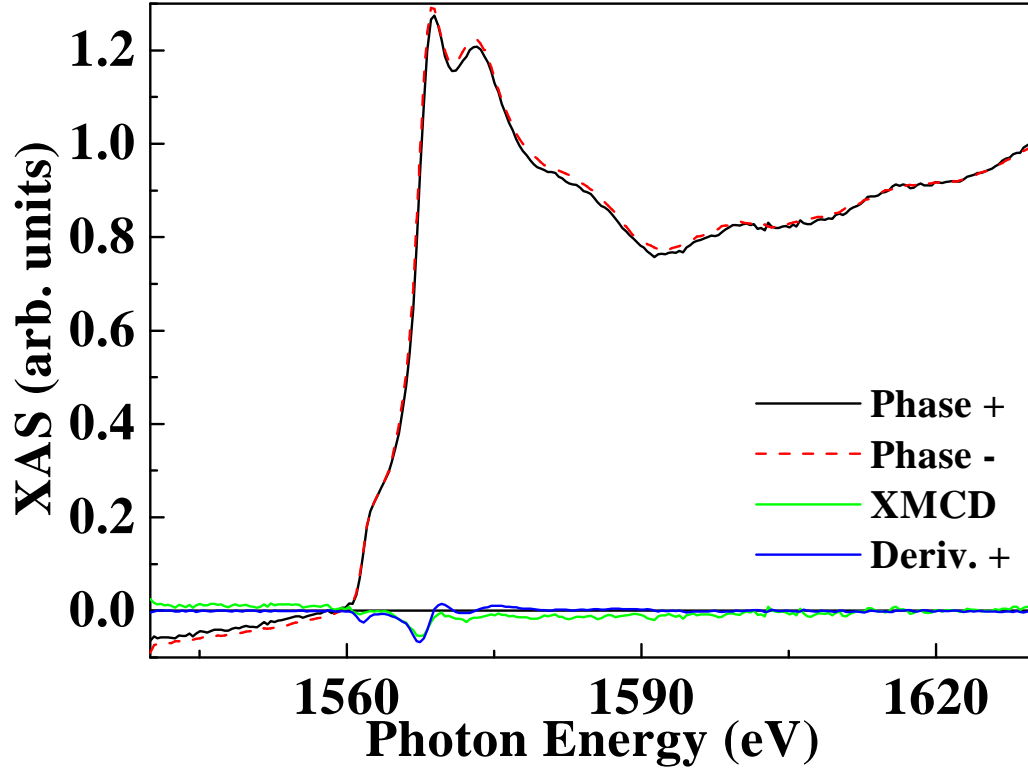


Figure 4.10: Si//Ta(50Å)/Co(150Å)/Al₂O₃ (7±1Å)/Co(30Å)/Au(20Å): X-ray absorption spectra (XAS) for the positive and negative phases, at the Al K edge at T=5K. No corrections have been made.

spectra is quite similar to the derivative of one spectra, so that it cannot be attributed to dichroism. Regarding O, this spectra differs somewhat from that found for Al₂O₃, probably due to the different electronic environments of O in the two samples. No dichroism is present at the O K edge.

4.2.3 Discussion & conclusion

Evidently, the results presented above do not provide an affirmative answer to the question of induced moments on elemental sites within tunneling barriers due to contact with a ferromagnet. Both sets of samples show strongly magnetic, non-oxidized transition metals at the interface with the barrier to be probed. However, the XAS data and any resulting XMCD signal at the absorption edges of the barrier materials show no reliable dichroic data.

Our experiments to detect an induced moment within tunneling barriers mainly focused on elements such as Mg, Al and O with only K and L shells.

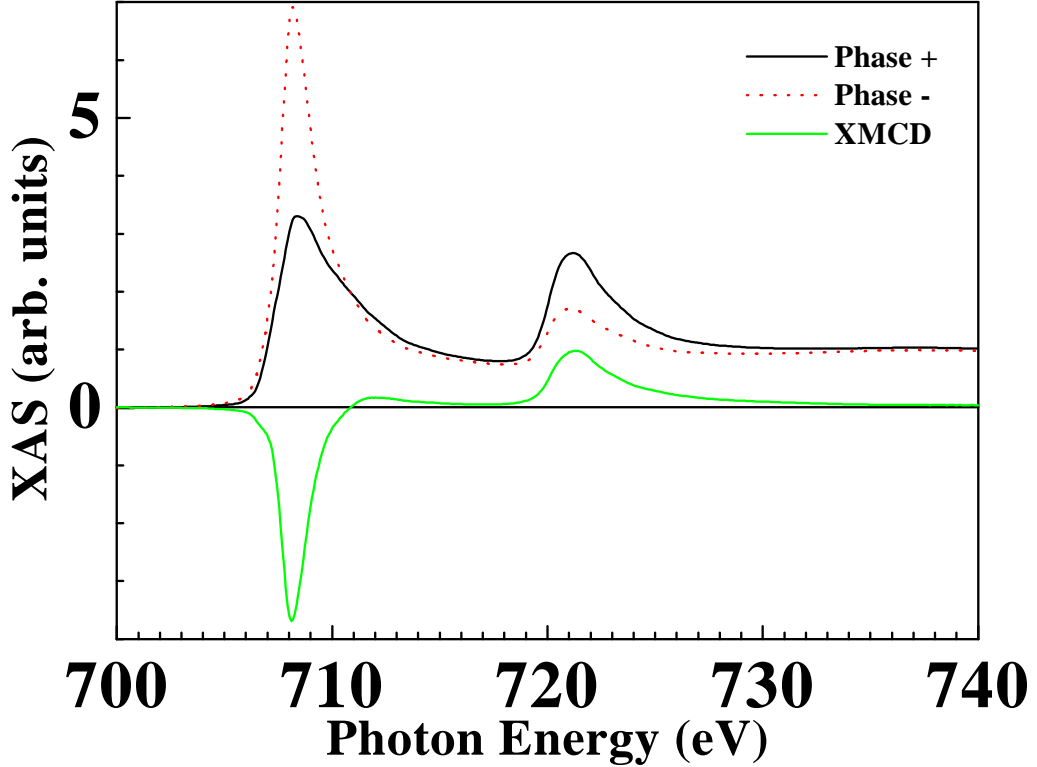


Figure 4.11: MgO(001)//MgO(100Å)/Fe(250Å)/MgO(10Å)/Fe(20Å)/Pt(20Å): X-ray absorption spectra (XAS) for the positive and negative phases at $T=5\text{K}$ at the Fe L edge. No corrections have been made.

Beamline ID8 at the ESRF implements a monochromator which provides the highest flux in the 850eV range so as to probe L edges in 3d transition metals. While the photon flux drops quite a bit at these edges, and the $2p \rightarrow 4s$ transitions are not as probable as the usual $2p \rightarrow 3d$, the good signal-to-noise ratio on individual scans presented above, even for Al, validate our experimental conditions. We of course accumulated spectra, to no avail.

At the Co/Al₂O₃ interface, covalent bonding between the O 2p and the Co 3d orbitals was calculated [34] to lead to an induced magnetic moment of $\approx 0.07\mu_B$ on the O site. In the case of Co-Al bonding, these calculations predict a smaller induced moment. Regarding the Fe/MgO interface, Fe was calculated to induce a $\approx 0.2\mu_B$ moment on the O site. [151] In this latter case, the epitaxial nature of our sample placed the experiment in quite ideal conditions to verify the calculation. In a separate experiment on the similar beamline ID12, Pellegrin *et al.* measured a 1.6% dichroic signal at the O K edge for La_{0.7}Sr_{0.3}MnO₃, [152] associated with a calculated $0.08\mu_B$ moment

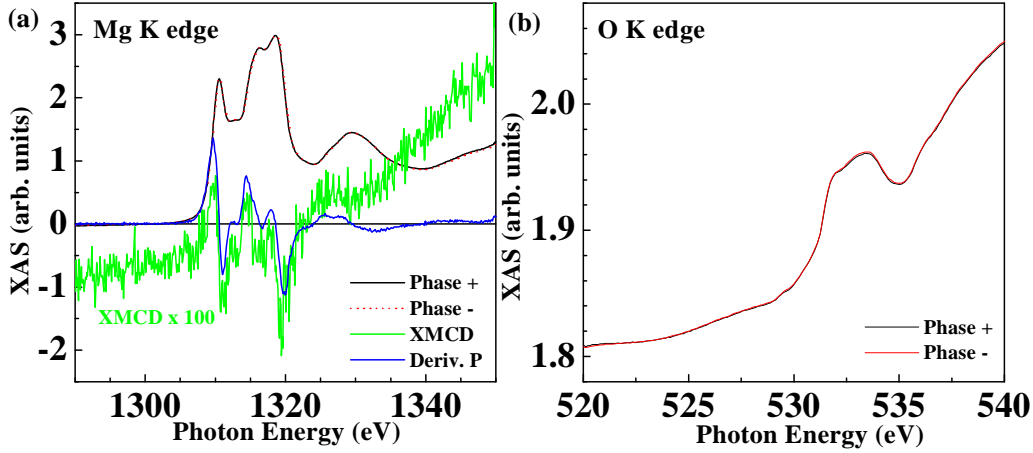


Figure 4.12: MgO(001)//MgO(100Å)/Fe(250Å)/MgO(10Å)/Fe(20Å)/Pt(20Å): X-ray absorption spectra (XAS) for the positive and negative phases at $T=5\text{K}$, at (a) the Al K edge, and at (b) the O K edge. No corrections have been made.

on the O site induced by hybridization. [153] Our experiment should therefore have been sensitive to an induced moment of $\sim 0.05\mu_B$, though it compounds the difficulty of measuring an induced moment along a 2D plane and not within a magnetic environment.

This experiment could have been better suited to the study of induced moments on $3d^0$ transition metal sites within a tunneling barrier. The case of Ti within SrTiO₃ would correspond to such a scenario, and has been studied theoretically by Oleinik *et al.* regarding a fcc Co(111)/SrTiO₃(100) interface. [36] We performed the XMCD measurement on a SrTiO₃(001)//La_{0.7}Sr_{0.3}MnO₃(350Å)/SrTiO₃(7.8Å)/Co(30Å)/Cu(20Å) sample. However, as we discovered during the experiment, harmonics generated by the undulator providing this beamline with synchrotron radiation resulted in overlapping absorption edges between Ti and Co, impeding any determination of an eventual moment on the Ti site.

It is difficult to profess conclusions based on negative results. Further experiments are therefore required to confirm or infirm the predictions based on this model. It would seem, nevertheless, that the overall experiment was performed in appropriate conditions on good samples, but that no induced moment was observed.

Chapter 5

Spin-dependent tunneling spectroscopy in $\text{La}_{0.7}\text{Sr}_{0.3}\text{MnO}_3$ -based tunnel junctions

This Chapter presents spin-dependent transport results in LSMO/STO/LSMO and LSMO/STO/Co junctions with an aim to explicitly affirm the spectroscopic nature of spin-dependent tunneling. In Section 4.1.1, we presented spin-dependent tunneling evidence affirming the transport half-metallic nature of $\text{La}_{0.7}\text{Sr}_{0.3}\text{MnO}_3$. We now utilize this nearly total spin polarization to probe salient features in the electrodes' interfacial densities of states. Section 5.1 presents and discusses results on LSMO/STO/LSMO junctions, notably in the context of an independent assessment of the unoccupied LSMO density of states through Spin-Polarized Inverse Photoemission Spectroscopy. In light of this newfound understanding, Chapter 5.2 reassesses spin dependent transport in the LSMO/STO/Co system.

5.1 LSMO/STO/LSMO tunnel junctions

This Section describes our experimental knowledge of magnetotransport in $\text{La}_{0.7}\text{Sr}_{0.3}\text{MnO}_3/\text{SrTiO}_3/\text{La}_{0.7}\text{Sr}_{0.3}\text{MnO}_3$ (LSMO/STO/LSMO) magnetic tunnel junctions (MTJs). We pursued this research axis with a double purpose. The first was to reassess predictions of manganite half-metallicity (see Section A.4.3) in light of previously reported experimental evidence. Furthermore, the conjunction of a fully epitaxial MTJ along with electrodes

possessing a very high spin polarization should advance the state of the research field given the necessity for such experiments to mirror theoretical investigations on ideal systems.

Figure 5.1 shows the bias dependence of TMR for Junction B of area $2 \times 6 \mu\text{m}^2$. For clarity the data have been normalized to the 350% value found at $V_{DC} = -10\text{mV}$. In the first of three distinguishable bias regimes, the TMR amplitude decreases as junction bias is increased, to about $\pm 100\text{mV}$ where it begins to level off. This dramatic drop may result from spin wave generation, [67,68] and therefore does not embody a DOS effect. In the intermediate bias range $100\text{mV} < |V| \lesssim 400\text{mV}$, the TMR amplitude shows a much lessened decrease. Finally, in the high bias regime for $|V| > 0.4\text{V}$, the TMR decreases rapidly again and switches signs for one direction of applied bias, reaching -8%. This asymmetry in our transport results with respect to bias, especially noticeable in this high bias regime, probably reflects a slight difference in the chemical structure of the upper and lower LSMO/STO interfaces in our junctions as observed [118] by Electron Energy Loss Spectroscopy. We will discuss the magnetotransport response at large bias and possible asymmetries in Chapter 7.

5.1.1 Spin wave excitations in the low-bias regime

Figure 5.2 presents the temperature evolution of junction electrical response at low bias. As shown in panels (a) and (b) for the parallel and antiparallel states, a conductance dip is present at low bias. This zero-bias anomaly (ZBA), of bias extent 50-100mV, has been reported to occur in junctions with transition metal electrodes MTJs [67, 68, 154] and been attributed to spin wave excitations at the interfaces. This explains the decrease in TMR amplitude within this bias range. As discussed in Section 2.3.2, the double exchange nature of conduction promotes a $V^{1/2}$ signature of spin wave generation in the second derivative of junction current to be contrasted with a linear response regarding conventional transition metal electrodes. As shown for the parallel state in panel (c), this signature subsists past $T=200\text{K}$, though quite weakened past 150K.

Inspection of the second derivative (panels (c) and (d)) reveals a non-linear response around $V=0$. In contrast to the linear response expected within a standard spin wave model, this $|V|^{1/2}$ dependence marks the signature of spin wave generation within a double exchange framework which predicts a 3D spectrum. [69] This results from the long-range nature of the double exchange conduction process. Thus, tunneling from a double-exchange electrode need not be a purely interfacial process as for a transition metal electrode. Since spin-pairing may occur between bulk and interfacial sites

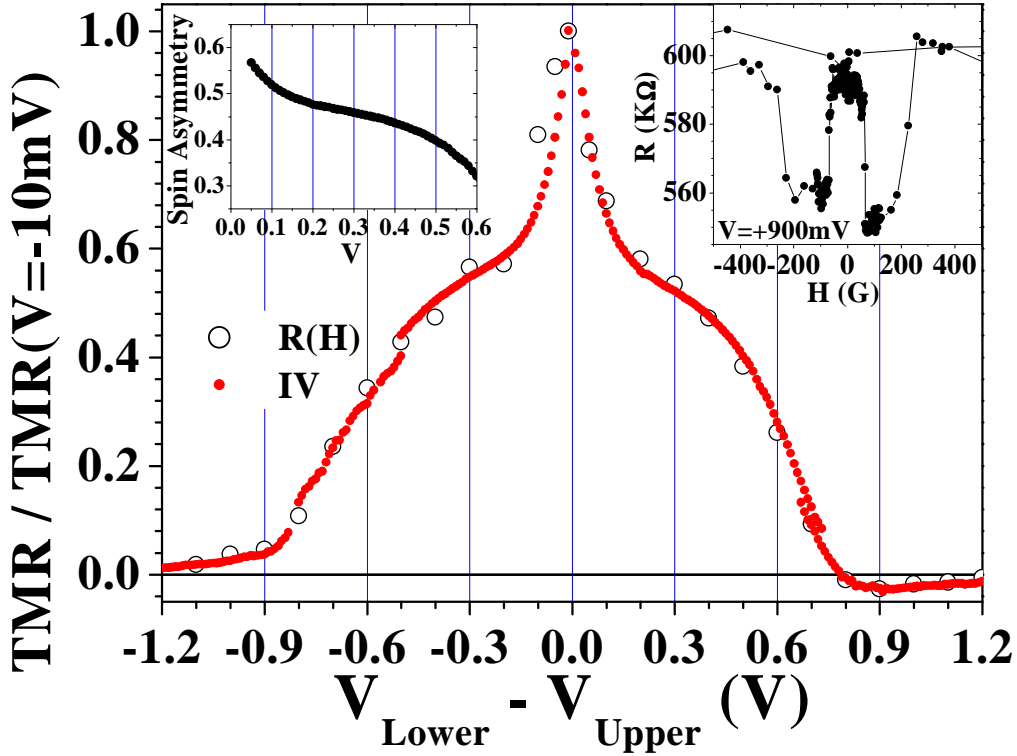


Figure 5.1: LSMO/STO/LSMO, Junction B: Bias dependence of TMR at $T=4\text{K}$. Left-hand inset: bias dependence of spin asymmetry (see text). Right-hand inset: $R(H)$ loop at $V=+900\text{mV}$ showing -8% TMR.

subject to double exchange conduction, [155] such an effect may be expected. The decrease in non-linearity of d^2I/dV^2 as temperature is increased, toward a linear behavior at $T=210\text{K}$, could reflect the transition to a more interfacial nature of tunneling as carrier localization begins to dominate transport past the manganite's $T_C/2$ [156].

It is interesting to note that, beyond $V=150\text{mV}$, while the conductance derivative is virtually constant in the antiparallel state between $T=4\text{K}$ and $T=70\text{K}$ (panel (d)), in the parallel state the conductance derivative decreases past $T=40\text{K}$, and in doing so changes slope. This implies changes in the relative weight of both conduction channels with increasing temperature as thermal mixing of the two spins channels begins to occur. This could explain the increased slope of the TMR plateau beyond this low-bias regime. The electronic origin of such a difference in temperature-dependent behavior may lie with the difference in wavefunction symmetry across the heterojunction: in the parallel state e_g wavefunctions match up across the barrier, while in the antiparallel state an e_g wavefunction from the injecting electrode matches

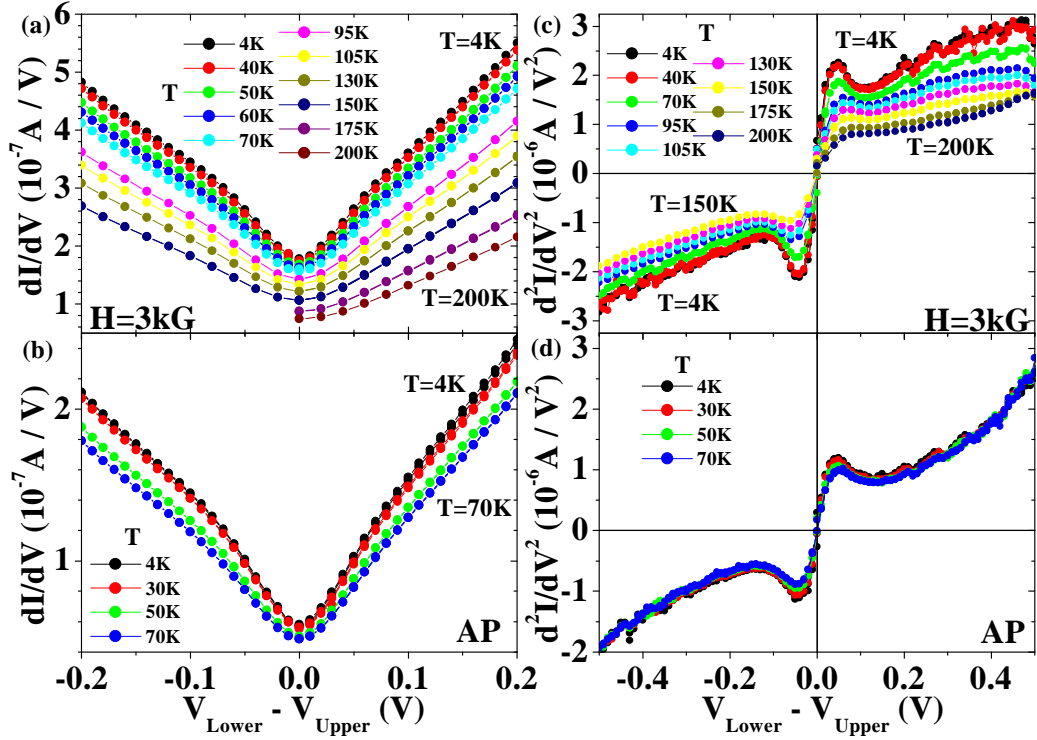


Figure 5.2: LSMO/STO/LSMO, Junction C: Temperature evolution of (a)/(b) first and (c)/(d) second derivatives of I-Vs in the parallel/antiparallel states.

up with a t_{2g} wavefunction from the collecting electrode.

5.1.2 Intermediate bias regime

The dramatic TMR decrease stemming from inelastic scattering at low bias is then followed by a much more moderate decrease over the intermediate bias range $100\text{mV} < |V| \lesssim 400\text{mV}$. The slowdown in TMR decrease with applied bias then changes trends beyond an inflection point at $V \simeq \pm 0.3\text{V}$, and the TMR decreases more rapidly thereafter. The spin asymmetry $\Delta_{spin} = (I_P - I_{AP}) / (I_P + I_{AP}) = P^2$ (see left-hand inset of Figure 5.1a) confirms the fairly constant evolution of P^2 over this bias range.

Materials with intrinsic half-metallic character are endowed with a density of states crossing the Fermi level consisting of only one spin band. In LSMO this band consists of $e_g \uparrow$ carriers. An energy gap therefore exists between E_F and the bottom of the nearest spin \downarrow band with t_{2g} electronic character. In a purely DOS picture, this LSMO minority gap may be probed

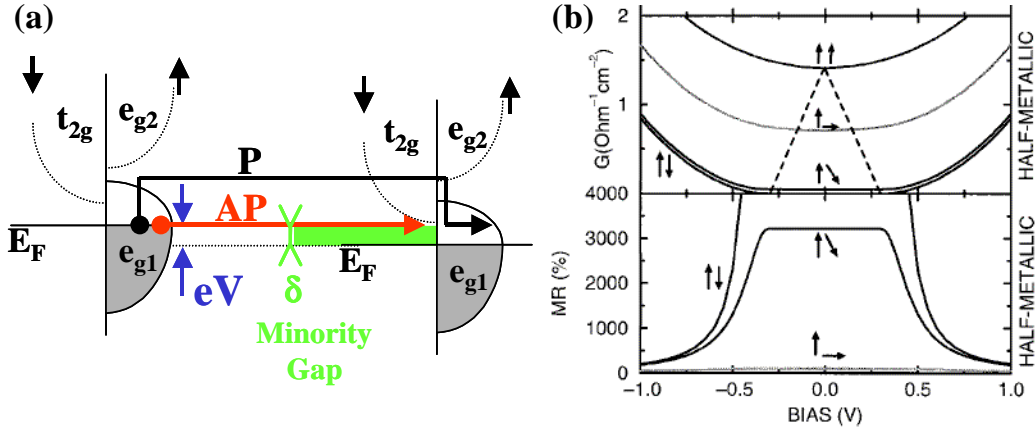


Figure 5.3: Tunneling between half-metals with a gap in the spin-dependent DOS: (a) schematic of the two ideal conductance channels in the parallel (P) and antiparallel (AP) configurations. (b) Theoretical conductance (top panel) and TMR (bottom panel) for a half-metallic gap $\delta=0.3\text{eV}$. From Bratkovsky. [31]

by spin-dependent tunneling from another LSMO electrode as schematized in Figure 5.3a. Given the 95% spin-polarization reported above for the LSMO/STO/LSMO system, our experimental conditions may be deemed close to those depicted, such that the P & AP configurations respectively probe the spin \uparrow & \downarrow density of states of the collecting electrode. Bratkovsky applied this picture toward performing calculations of tunneling magneto-transport between half-metals with a minority gap $\delta=0.3\text{eV}$. [31] As the top panel of Figure 5.3b shows, while conductance G_P in the parallel state increases in quadratic fashion, G_{AP} only rises once the minority gap δ is reached and exceeded. One therefore expects the TMR to remain constant within the bias range $0 < V < \frac{\delta}{e}$, as calculated in the bottom panel of Figure 5.3b.

We argue that Bratkovsky's analytical DOS approach to the bias dependence of spin-dependent tunneling between half-metals is reproduced by our experimental data on LSMO/STO/LSMO junctions. As discussed previously, the sharp drop in TMR amplitude in the low-bias regime results from spin wave excitations generated at the collecting interface. The incidence of such magnon generation events on total conductance is lessened beyond the extent of the magnon excitation spectrum, which we have identified as spanning $\hbar\omega_{Max} \approx \pm 100\text{meV}$. Aside from this inelastic scattering contribution at low bias, the TMR bias dependence is thus broadly constant from zero bias up to $V \simeq \pm 0.3\text{V}$, in agreement with Bratkovsky's theoretical predictions. [31] The inflection point at $V \simeq \pm 0.3\text{V}$ and the renewed decrease in TMR am-

plitude reflect the onset of tunneling into the LSMO minority t_{2g} band. An inspection of tunneling conductances, shown in Figure 5.4, reveals how G_P , which reflects the spin \uparrow tunneling channel between the two half-metallic electrodes, increases linearly within the bias range $100\text{mV} < V < 600\text{mV}$. In contrast, G_{AP} departs from this progressive increase around $V \simeq 0.3\text{V}$. As expected and predicted (see Figure 5.3), this is consistent with tunneling beyond the minority gap and into the $t_{2g} \downarrow$ band of the collecting electrode. From the conductance derivatives shown in Figure 5.4c, a more quantitative value of $\delta = 350\text{meV}$ can be attributed to the LSMO minority gap at the lower interface as probed by spin-polarized tunneling. Interestingly, these features aren't as obvious regarding the upper interface (see inset of Figure 5.4a). The antiparallel conductance does appear to rise before the parallel one at negative biases, but not as decisively, and at a somewhat larger $\delta = 400\text{mV}$ value. Qualitatively, the interfaces show similar magnetotransport behavior. We attribute the quantitatively different minority gaps to slight differences in the electronic structure of each interface.

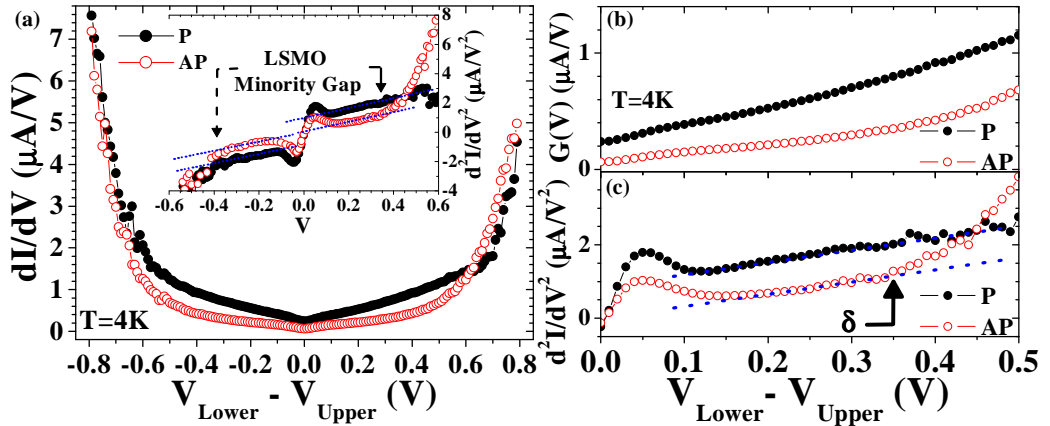


Figure 5.4: Tunneling between half-metals with a gap in the spin-dependent DOS: LSMO/STO/LSMO, Junction B: (a) Conductance $(dI)/(dV)$ in the parallel (P: closed circles) and antiparallel (AP: open circles) configurations. Inset: Second derivative of current showing the LSMO minority gap at each interface. (b) & (c) Closeups of data at positive bias.

5.1.3 The unoccupied spin-dependent DOS of the $\text{La}_{0.7}\text{Sr}_{0.3}\text{MnO}_3/\text{SrTiO}_3(001)$ interface

Through a collaboration with R. Bertacco of the "Politecnico di Milano", an independent experimental determination of the unoccupied density of

states of $\text{La}_{0.7}\text{Sr}_{0.3}\text{MnO}_3$ at the interface with SrTiO_3 was conducted by spin-polarized inverse photoemission (SPIPE) spectroscopy. Figure 5.5a shows results for such an interface: the $380 \pm 30 \text{ meV}$ energy difference in metallic onset between the spin \uparrow and \downarrow channels reflects the minority gap between E_F and the onset of the $t_{2g} \downarrow$ band as probed by this technique. A schematic in panel (b) of the manganite's density of states around E_F describes this minority gap. This value is close to $\delta = 400 \pm 30 \text{ meV}$ found for a $\text{La}_{0.7}\text{Sr}_{0.3}\text{MnO}_3$ surface through this technique. [157]

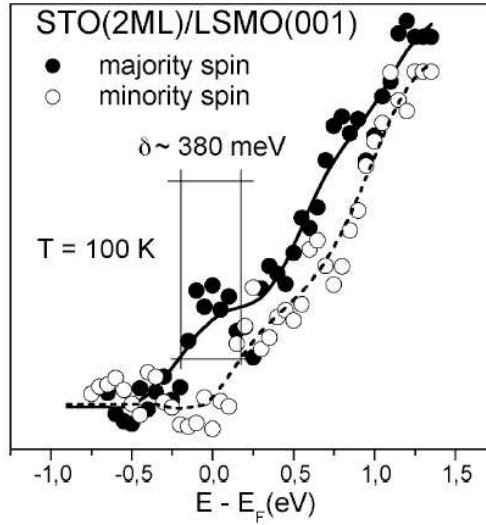


Figure 5.5: SPIPE experiment on a $\text{STO}(001)//\text{LSMO}/\text{STO}(2\text{ML})$ sample revealing the spin-polarized DOS of the LSMO/STO interface at $T=100\text{K}$. The 0.38eV energy difference in metallic onset between the spin \uparrow (closed circles) and \downarrow (open circles) channels reflects the minority gap in this half-metallic compound.

Section A.4.3 (p. 246) discusses the existence of such a gap. Depending on the theoretical approach considered, reported bulk values for the LSMO minority spin band gap range from 0.6eV [158] to 0 [99]. The value $\delta = 0.35\text{eV}$ we have observed through SPIPE and TMR experiments, given the surface/interface sensitivity of these techniques, reflects the LSMO/STO interface rather than the LSMO bulk electronic structure. Bandwidth reduction, Anderson localization of the lowest energy levels and electronic disorder resulting from symmetry breaking could thus account [159] for this *effective* ¹ gap observed.

¹These results don't rule out the presence of a very low density of localized minority states in the gap. B. Nadgorny *et al*, [140], private communication 2002.

5.1.4 Beyond the minority gap

As the applied bias is increased beyond the minority gap, the TMR amplitude begins to decrease more rapidly and may change signs for one direction of applied bias, reaching -8% at $V=+900\text{mV}$ (see right-hand inset of Figure 5.1a). Interestingly, the TMR sign change lies very close to a sharp rise in junction conductance, which occurs at positive and negative biases, and for both P and AP alignments (see Figure 5.4a). This spin-independent feature is attributed to a potential barrier which, once exceeded, leads to this sharp rise. As discussed in Section A.2, the band structure of SrTiO_3 may promote low electron and high hole barrier heights totalling the band gap.

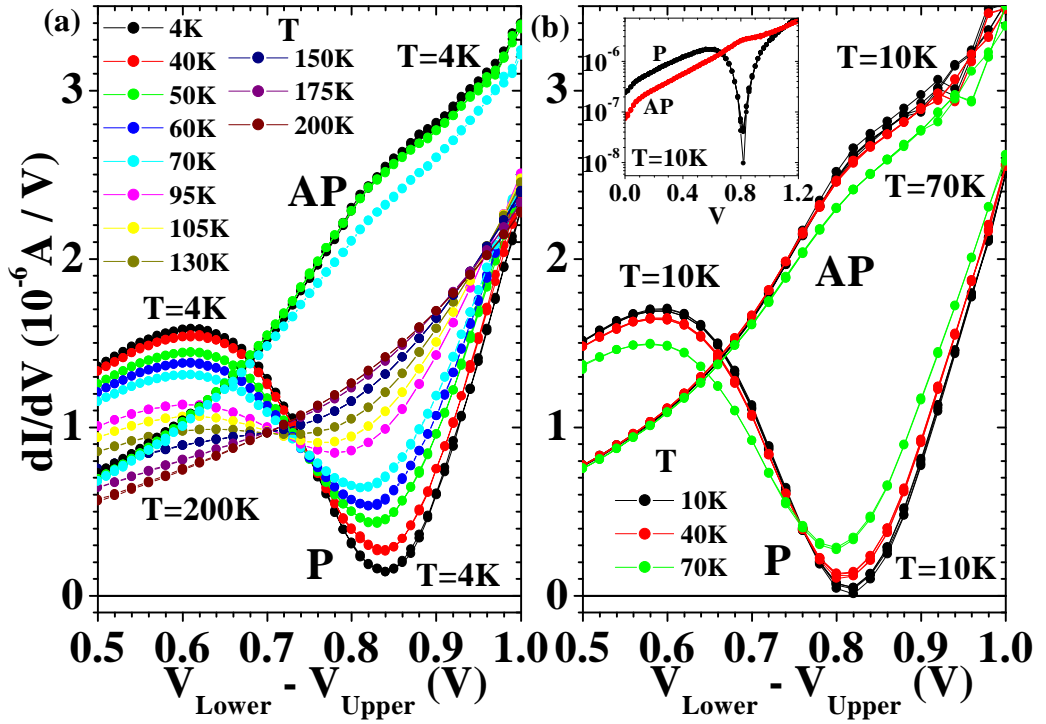


Figure 5.6: LSMO/STO/LSMO, Junction C: temperature evolution of junction conductance in the parallel (P) and antiparallel (AP) states for (a) $V_{\text{Desc}} = +10\text{mV}$ and (b) $V_{\text{Desc}} = +3\text{V}$. AP Data at $T=4\text{K}$, 50K and 70K is represented in panel (a). The inset to panel (b) presents $T=10\text{K}$ P and AP data on a logarithmic scale. All bias sweeps are represented.

However, if a junction's barrier heights lie at larger values, it is possible to further probe electrode density of states effects before barrier profile effects become prevalent. Figure 5.6 presents the temperature evolution of conductance in the parallel (P) and antiparallel (AP) states for junction C,

200 μm away from junction B and also of area $2\times 6\mu\text{m}^2$. Increasing and decreasing bias sweeps attest to junction resiliency and to the intrinsic nature of data presented here. Panels (a) and (b) show data on the same junction which has endured slight modifications to its structure due to voltage stress resulting from cooldown at an applied bias V_{Desc} .² As the data for $V_{Desc}=+10\text{mV}$ shows (panel (a)), beyond $V\approx+0.6\text{V}$ conductance in both states changes markedly. In the P state, after saturating at this point conductance G_P drops dramatically, to a minimum at $V=+0.82\text{V}$ at about the value $G_P=1.8\times 10^{-7}$ A/V found at $V=0$. Beyond this minimum, G_P rises sharply again. In the AP state, the increase in junction conductance G_{AP} quickens past $V=+0.6\text{V}$, and produces a local maximum at $V=+0.82\text{eV}$ before converging with G_P at higher bias values (not shown here).

These features are illustrated even more spectacularly from data taken after cooling down at $V_{Desc}=+3\text{V}$. As panel (b) and its inset show, G_P at $V=0.82\text{V}$ drops to $G_P=4\times 10^{-8}$ A/V, nearly one order of magnitude lower than $G_P=1.8\times 10^{-7}$ A/V found at $V=0$. Inspection of conductances at $V=+0.82\text{V}$ yield differential TMR ratios reaching -98.5% in three instances and one at -99.6%, at the threshold of *total* differential TMR.

This highly spin-polarized feature diminishes as temperature increases, to disappear between $T=175\text{K}$ and $T=200\text{K}$. However, while the AP peak only diminishes beyond $T=40\text{K}$ due to thermally-assisted tunneling processes, the P dip lessens immediately with increasing temperature. If this feature had reflected a barrier-induced TMR oscillation, [21] then the peak and dip in G_{AP} and G_P would have evolved similarly, decreasing beyond $T=40\text{K}$. However, this is not the case, so that a DOS explanation should be considered.

Figure 5.7 presents a DOS interpretation of the above effect. The nearly extinguished conductance in the parallel configuration at $V=0.82\text{V}$ implies that each spin-dependent conduction channel is effectively blocked. Since at this energy level the collecting electrode may provide empty spin \downarrow states, the absence of a conductance in this spin channel implies that no spin \downarrow states are present in the injecting electrode. Beyond our explicitly demonstrated value $P_{LSMO} > 95\%$ mentioned previously, this measurement confirms that $P_{LSMO} \rightarrow +1$, and represents the strongest statement yet as to the ideally half-metallic nature of the $\text{La}_{0.7}\text{Sr}_{0.3}\text{MnO}_3/\text{SrTiO}_3$ interface.

The second implication regards the spin \uparrow conduction channel. Since spin \uparrow states are present at the Fermi level of the injecting electrode, this means that at $E-E_F=0.82\text{eV}$ there are no empty spin \uparrow states. We at-

²As detailed in Section 7.2, electromigration effects may occur due to applying a bias V_{Desc} during cooldown on an otherwise stable junction, leading to modifications in the stoichiometry of the junction's interfaces and barrier.

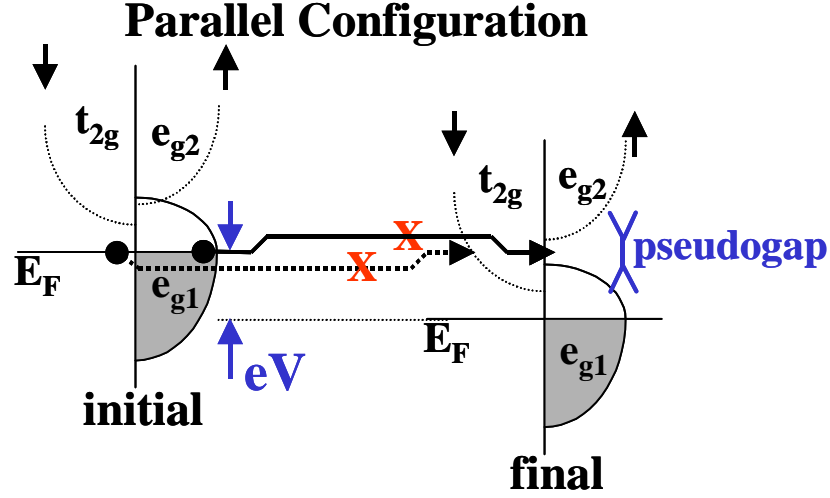


Figure 5.7: Scenario of a splitting in the e_g^\uparrow band manifold due to a rotation of the MnO_6 octahedra at the LSMO/STO interface to define a pseudogap between d_{z^2} and $d_{x^2-y^2}$ subbands: schematic explaining the nearly extinguished tunneling conductance between LSMO electrodes in the parallel configuration at $V \approx +0.8\text{V}$.

tribute this nearly completely spin-polarized feature to a pseudogap in the e_g manifold of the lower LSMO/STO interfacial DOS. As discussed in Sections A.4.3 & A.4.5, distortion of the manganite's cubic cell to tetragonal symmetry lifts the degeneracy between d_{z^2} and $d_{x^2-y^2}$ subbands. A schematic of tunneling toward such a DOS is presented in Figure 5.7. As shown in Figure A.13 (page 246), the calculations of Pickett and Singh reveal a gap in the spin \uparrow manganite DOS which lies at $V \sim 0.8\text{eV}$ above E_F , in excellent agreement with our experimental data.

This distortion of the LSMO cubic cell results from two factors. The first is the cubic to tetragonal phase transition of SrTiO_3 as temperature decreases below $T=105\text{K}$. This explains how the G_P dip decreases so much between $T=4\text{K}$ and $T=105\text{K}$, as the gap closes and differential TMR drops (see inset to Figure 7.15a). Yet the conductance dip subsists at $T=130\text{K}$, to only disappear between $T=175\text{K}$ and $T=200\text{K}$. Since LSMO in our samples is grown epitaxially constrained onto $\text{SrTiO}_3(001)$, the resulting tetragonal distortion of the LSMO cell should be reflected by the conductance dip at all temperatures which promote metallic conduction of double exchange nature. This both explains how the feature subsists above $T=105\text{K}$, and pegs a qualitative value $T_C/2 \sim 175\text{K}$ to the effect observed. [156] Since the T_C of

our interfaces rarely exceed $T=300\text{K}$, and given the bulk $T_C=350\text{K}$ of our films, this implies that either we are probing not *interfacial*, but *bulk* DOS features through magnetotransport at this bias value; and/or that at this value of applied bias, spin wave excitations contribute to a very small part of overall conduction processes, so that critical temperatures aren't affected by this possible disruption of electronic properties (see Chapter 6).

At the time of this writing we do not understand the exact origin of this corresponding peak in the G_{AP} . We surmise that, given the absence of available spin \uparrow states at that energy level, spin wave excitations present at low bias could eventually³ place the electron in an available spin \downarrow state, thereby increasing effective conductance. The decrease in this peak's amplitude with increasing temperature doesn't begin past $T=40\text{K}$, so that an explanation in terms of manganite electronic properties is indeed required.

5.1.5 Summary

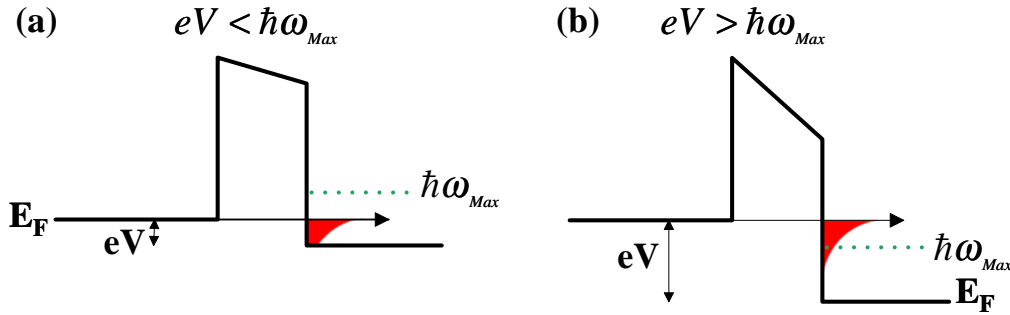


Figure 5.8: Schematics depicting the (a) low-bias regime dominated by magnon excitations and the (b) intermediate bias regime for which the influence of magnon excitations on the total tunneling current is lessened. The transition from one bias-dependent tunneling regime to the other occurs at the energy extent $\hbar\omega_{Max}$ of the magnon excitation spectrum.

These experiments on LSMO/STO/LSMO magnetic tunnel junctions underscore the influence of spin-polarized density of states effects on the tunneling process. Of prime importance is the notion that the spin polarization of a tunneling current, while decreased due to spin wave excitations in the low bias-regime, may retain its degree of spin polarization at bias values for which the energy of the hot electrons injected at the collecting interface exceeds the magnon excitation spectrum (see Figure 5.8). For bias values in

³At this applied bias, spin wave excitations contribute little to overall conduction.

excess of the magnon excitation spectrum $\hbar\omega_{Max}$, it is possible to observe salient spin-polarized features in an electrode's unoccupied density of states through spin-dependent tunneling. In the particular case of LSMO at the interface with STO, a minority gap $\delta=0.35\pm 0.05\text{eV}$ as probed by this technique was independently confirmed through Spin-Polarized Inverse Photoemission spectroscopy to lie at $\delta=0.38\pm 0.03\text{eV}$. This *quantitative* comparison of the minority gap amplitude with that found through the confirmed technique of Spin-Polarized Inverse Photoemission underscores the spectroscopic character of spin-dependent tunneling between ferromagnetic electrodes in a fashion seen up to now only in junctions with a superconducting electrode. [13, 15]

The clarity in interpreting our transport results is due to the use of a nearly fully spin-polarized electrode to probe a salient feature in the DOS of a counterelectrode. This condition is reaffirmed with great emphasis through the measurement of a nearly extinguished conductance in the parallel configuration. Beyond the 95% spin polarization explicitly measured at the LSMO/STO interface, this observation shows that $P_{LSMO/STO} \rightarrow +1$, thus strongly affirming the ideally half-metallic nature of the LSMO/STO interface.

5.2 Revisiting the bias dependence of TMR in LSMO/STO/Co junctions

This Section revisits tunneling in the LSMO/STO/Co system. The main difference with the LSMO/STO/LSMO system is that now only one electrode is subject to double exchange conduction. Therefore, we may utilize the STO/Co interface with a T_C much higher than that probed by our measurements to investigate spin wave excitations and other phenomena at the LSMO/STO interface with lower T_C .

Figure 5.9 represents the bias dependence of TMR for a LSMO/STO/Co junction. Since the original interpretation of this asymmetric bias dependence entirely in terms of the Co density of states (see Figure 2.20 and accompanying text), [22] our understanding has evolved considerably. It has become clear from theoretical and pragmatical considerations on tunneling that for a given direction of applied bias V , electrons injected from the Fermi level occupy empty states at $E=E_F + eV$ in the collecting electrode. This description of tunneling spectroscopy, which was applied previously for LSMO/STO/LSMO junctions, can now be used to understand the LSMO/STO/Co system. In LSMO/STO/LSMO junctions, the TMR drop at low bias was attributed to spin wave excitation. Past this low-bias

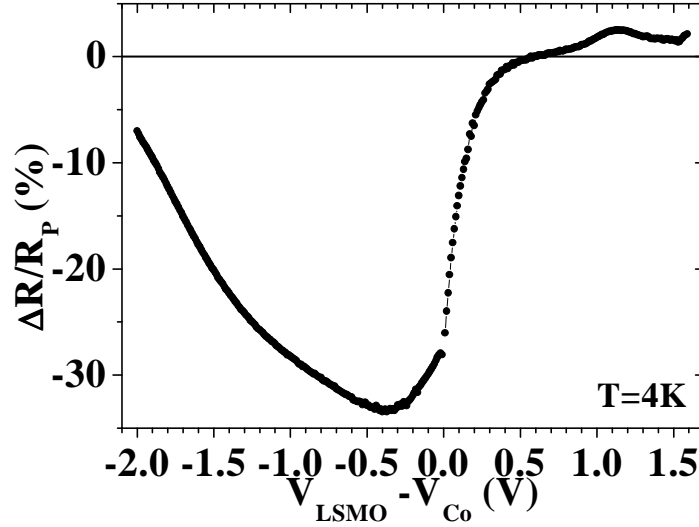


Figure 5.9: LSMO/STO/Co: bias dependence of TMR at $T=4\text{K}$.

regime, the TMR decrease lessened. As shown in Figure 5.9, when electrons are injected from Co toward the collecting LSMO/STO interface in a LSMO/STO/Co junction ($V > 0$), a fairly similar bias dependence of TMR ensues. Section 5.2.1 discusses spin-dependent tunneling in this system. At negative applied bias values, electrons from LSMO probe the Co unoccupied density of states. This picture was argued to account for the peak in the inverse TMR. To investigate the influence of the Co density of states in this system, we present results on LSMO/STO/CoCr junctions in Section 5.2.2.

5.2.1 Magnetotransport in LSMO/STO/Co junctions

We discuss in Section 5.2.1.1 the interfacial tunneling regime at low bias overshadowed by spin wave excitations. We then broach intrinsic electrode behavior at bias values beyond the magnon excitation spectrum in Section 5.2.1.2.

5.2.1.1 Spin wave excitations

LSMO/STO/Co junctions are also subject to magnon generation in the low bias regime. Figure 5.10 presents the magnetotransport response of a stable junction. As illustrated in panel (a), zero bias conductance anomalies (ZBA) are present in both the parallel (P) and antiparallel (AP) configurations of the alignments of electrode magnetizations. The anomaly extends $\sim 100\text{mV}$ about zero bias, and while broadly symmetric in the AP state, is much more pronounced in the P state when injecting toward LSMO.

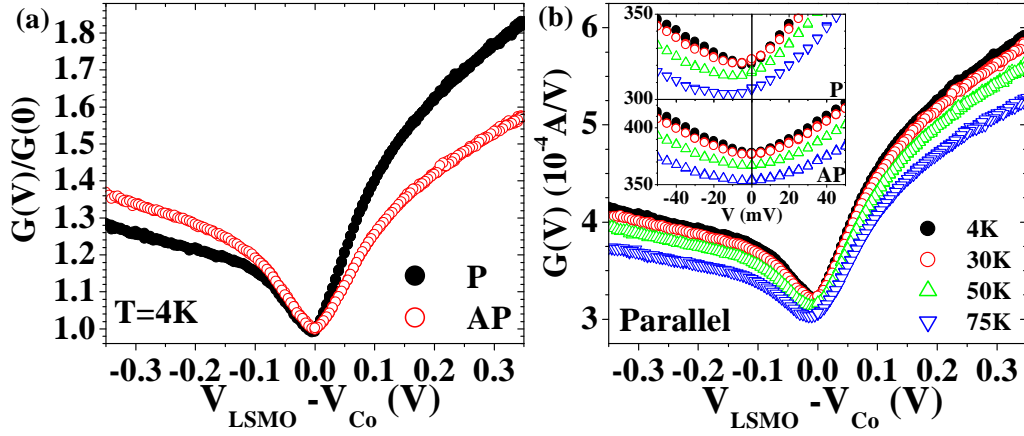


Figure 5.10: Magnetotransport measurements on a stable LSMO/STO/Co junction (Al_{2232}) of area $48\mu\text{m}^2$: temperature dependence of (a) conductance in the parallel (P) and antiparallel (AP) states at $T=4\text{K}$. (b) Temperature dependence of P conductance for several temperatures. The inset represent closeups of the low bias P & AP conductance.

This observation supports the picture of a negative degree of spin-polarized states at the Co/STO interface which tunnel toward the half-metallic LSMO electrode with majority states. Indeed, in the antiparallel alignment with lower resistance, Co minority states tunnel toward LSMO majority states. Thus the tunneling conduction of Co majority states is permitted through spin flip at the LSMO/STO interface. Since for Co $\rho^\downarrow(E_F) > \rho^\uparrow(E_F)$, the incidence of spin wave excitations on conductance is minor. In contrast, in the parallel alignment with higher resistance, tunneling conduction of the more numerous Co minority states occurs through spin flip. Thus spin wave excitations generated with applied bias promote a much larger zero-bias anomaly (ZBA) as observed. This result is opposite to that found when tunneling through an Al_2O_3 barrier (*e.g.* Figure 2.11 on page 27), even though the interfaces subject to spin wave excitations carry the same sign of spin polarization. This difference underscores the sign of spin polarization of the injecting electrode. While for Al_2O_3 junctions, the sign of P is positive, at the interface with SrTiO_3 this sign is indeed negative.

For $V < 0$, as LSMO majority states tunnel toward Co, the amplitude of the ZBA is very similar for both P and AP configurations. In this direction of applied bias, the behavior of the ZBA isn't as clear. At the time of this writing we do not understand the slightly larger ZBA in the AP configuration, in contradiction with $\rho^\downarrow(E_F) > \rho^\uparrow(E_F)$ for for Co.

The differing nature of conduction between Co and LSMO also leads to a

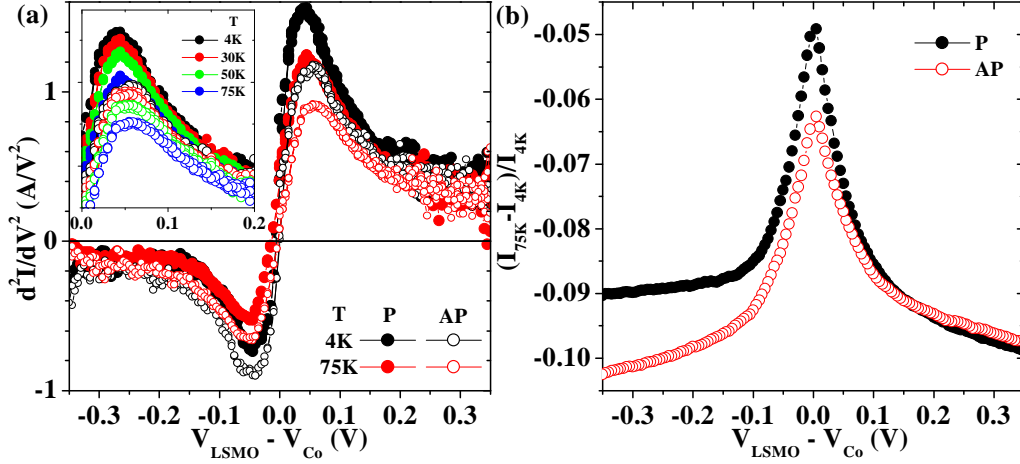


Figure 5.11: Magnetotransport measurements on a stable LSMO/STO/Co junction (Al_{2232}) of area $48\mu\text{m}^2$: (a) second derivative of current in the parallel (closed circles) and antiparallel (open circles) The inset represents a closeup of data for a larger temperature set. (b) Evolution of junction current with temperature in the parallel and antiparallel states.

different response of the second derivative of junction current. Referring to panel (a) of Figure 5.11, the non-linear response at low bias resulting from magnon excitation is more prevalent at the LSMO/STO interface compared to the STO/Co interface. An overarching reason lies with the much lower $T_C = 360\text{K}$ for $\text{La}_{0.7}\text{Sr}_{0.3}\text{MnO}_3$ compared to Co. It is therefore much harder to excite spin waves in the ferromagnet with the larger T_C . Furthermore, at the LSMO/STO interface, the amplitude of the non-linear response is higher in the parallel state compared to the antiparallel state; while at the STO/Co interface, an opposite response is observed. This further underscores DOS effects at the two interfaces with opposite signs of spin polarization. Finally, the decrease in non-linearity indeed occurs beyond $T=40\text{K}$ (compare data at 4K, 30K and 50K in the inset to Figure 5.11) as thermally-assisted spin flip processes begin to mix the two spin channels. As shown in Figure 5.11b, in the P configuration, this mixing leads to an relative increase in conductance which is higher in the P configuration compared to AP since more Co spin \downarrow states participate in the tunneling process. It will prove interesting to assess the origin of other temperature-dependent magnetotransport behavior in light of this effect.

A secondary effect may be noted in Figure 5.10, regarding the temperature evolution of the conductance minimum shown in the inset to panel (b). While in the antiparallel state no bias shift of this minimum is observed,

the minimum in the parallel state, already at -5mV for $T=4\text{K}$ and $T=30\text{K}$, shifts to -15mV at $T=50\text{K}$ and $T=75\text{K}$. Such conductance minima at $V \neq 0$ have been ascribed to a combination of differing evolutions of the densities of states for spin \uparrow and spin \downarrow electrons, as well as to differing barrier heights at each interface. [160]

5.2.1.2 Beyond the spin wave excitation regime

In LSMO/STO/LSMO junctions, once the applied bias exceeded the cutoff in the magnon generation spectrum, it became possible at low temperature to probe highly spin-polarized features of the collecting electrode DOS (see Section 5.1.2). We now apply this methodology to LSMO/STO/Co junctions. Since the spin polarization of Co isn't total, a straightforward approach isn't possible.

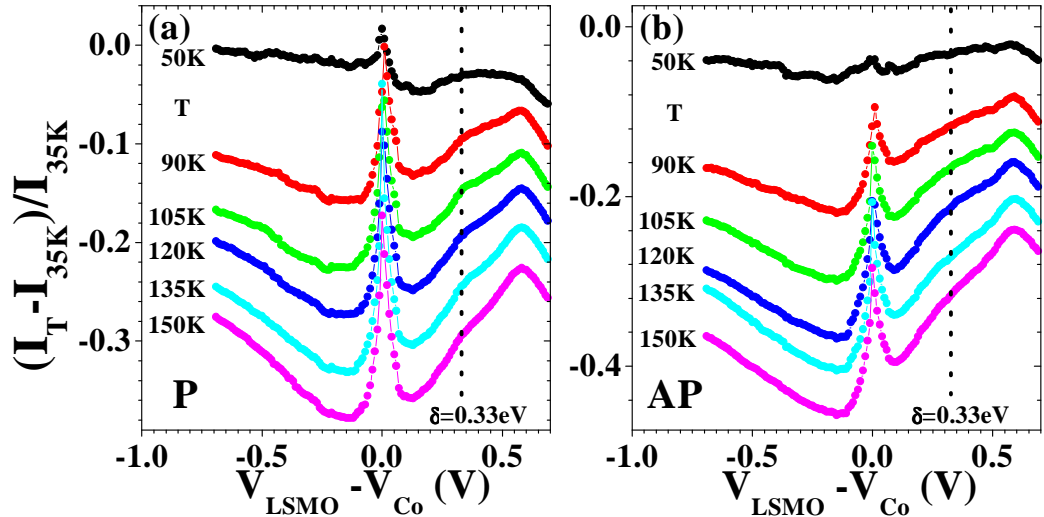


Figure 5.12: LSMO/STO/Co: temperature evolution of I-Vs in the (a) parallel (P) and (b) antiparallel (AP) configurations between $T=50\text{K}$ and $T=150\text{K}$ relative to $T=35\text{K}$.

Figure 5.12 presents the temperature evolution of I-V characteristics between 50K and 150K relative to 35K in the parallel (P) configuration (panel (a)) and antiparallel (AP) configuration (panel (b)). The peak at $V=+600\text{mV}$, present in both P and AP data, reflects a spin-independent feature which we discuss later. As shown by the guide to the eye, a spin-dependent feature appears at $V=+330\text{mV}$. It is noticeably more marked in the parallel configuration.

In this direction of applied bias, electrons from the Co electrode probe the LSMO unoccupied DOS. The bias position of this feature corresponds to that of the LSMO minority gap $\delta \approx 350\text{meV}$ found in Section 5.1.2. Since the spin polarization of Co is not total, a spin-polarized feature probed by the spin-polarized current from this electrode will appear in both the P and AP channels. Nevertheless, this feature is more marked in the P channel since the larger number of Co spin \downarrow states which probe the LSMO minority gap will lead to a larger increase in junction current. This is to be compared to the antiparallel case for which the smaller number of Co spin \uparrow states probe the LSMO minority gap, leading to a more diffuse increase, as observed.

5.2.2 Doping with Cr to manipulate the Co spin-dependent density of states

To confirm the spectroscopic origin of the inverse TMR peak observed when LSMO states at E_F probe the Co unoccupied DOS, we have performed a controlled manipulation of this DOS through Cr doping of the Co counter-electrode and investigated the incidence on the bias dependence of TMR.

5.2.2.1 Cr doping: a spin-dependent modification to the Co DOS

From a DOS standpoint, alloying a $3d$ metal with another $3d$ metal may induce two classes of behavior. If the atomic number of the impurity element is close to that of the matrix element, then the spin-polarized d -bands of the matrix element are merely shifted toward the position of those of the impurity element, by a proportion related to the doping value. This explains the increase in Fermi level spin polarization for FeCo alloys compared to either Fe or Co, as summarized in Table 2.1.

If the value ΔZ for the difference in atomic number between matrix and impurity elements is large, or if the impurity level lies near the end of the matrix d band, then the change in potential created by the impurity cannot be fully screened by the matrix atoms surrounding it. s - d wavefunction hybridization between the two species leads, for impurity concentrations lower than 10%, to the creation of *virtual bound states* (VBS). The number of states, and therefore the extent of the induced DOS modification, depend on impurity concentration.

Experience at our lab on the CoCr alloy within the framework of Carole Vouille's Thesis on the GMR effect, [161] and more precisely her work on modifying the ratio γ/β of interface and bulk spin-dependent scattering parameters to affect the sign of GMR in Co/Cu multilayers, [162] led us to retain this alloy for our study. $\Delta Z=3$ for CoCr, thus satisfying the criteria for

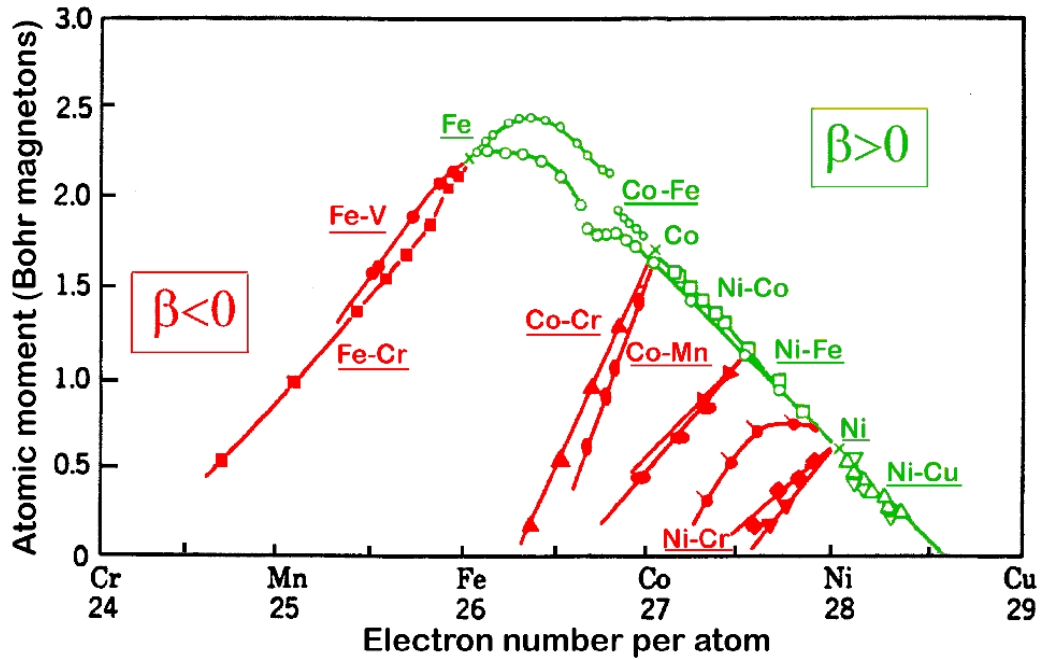


Figure 5.13: Slater-Pauling diagram of the average atomic moment for several series of $3d$ transition metal alloys.

a VBS description of a strong DOS modification induced by doping. Owing to the antiferromagnetic nature of Cr, the magnetic moment of Cr impurities antialigns itself to that of Co atoms forming the matrix. A first consequence is that the magnetic moment of the $\text{Co}_{1-x}\text{Cr}_x$ alloy is diminished with respect to Co, and vanishes for $x \sim 0.2$, as shown in the Slater-Pauling diagram of Figure 5.13. This diagram summarizes the evolution of the magnetic moment of various binary $3d$ alloys as a function of average atomic mass, and covers the two scenarios for doping outlined above. A second consequence is the increase in the coercive field of the CoCr thin film, which may be appreciated in Figure 5.14 representing $M(H)$ loops for LSMO/STO/ $\text{Co}_{1-x}\text{Cr}_x$ trilayers of constant $\text{Co}_{1-x}\text{Cr}_x$ layer thickness but increasing x .

The effect of this reduction in magnetic moment may be understood when comparing the spin-dependent total DOSs for Co [98] and CoCr [163] (see Figure 5.15). Doping Co with Cr depletes d^\uparrow states below E_F to form the VBS above E_F . The VBS peak lies at $E \sim E_F + 0.8\text{eV}$, and extends about 1eV from that energy value. This modification of the *unoccupied* DOS may be probed by the spin-dependent tunneling process from a LSMO electrode with nearly total spin polarization to those unoccupied states at $E = E_F + eV$, where V denotes the applied junction bias.

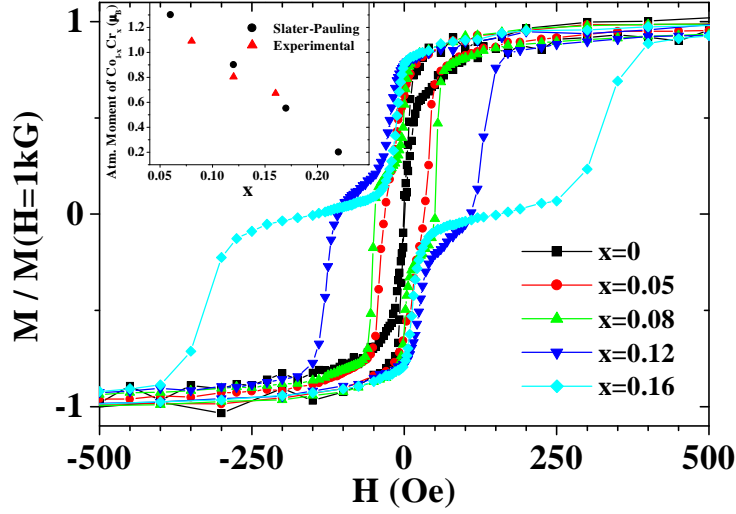


Figure 5.14: Magnetization loops at $T=20\text{K}$ of LSMO (350\AA)/STO (7ML)/ $\text{Co}_{1-x}\text{Cr}_x$ (150\AA). An increase in Cr concentration x leads to an increase in $\text{Co}_{1-x}\text{Cr}_x$ film coercivity and to a better-defined antiparallel plateau. Inset: a comparison between Slater-Pauling data (Figure 5.13) and experiment.

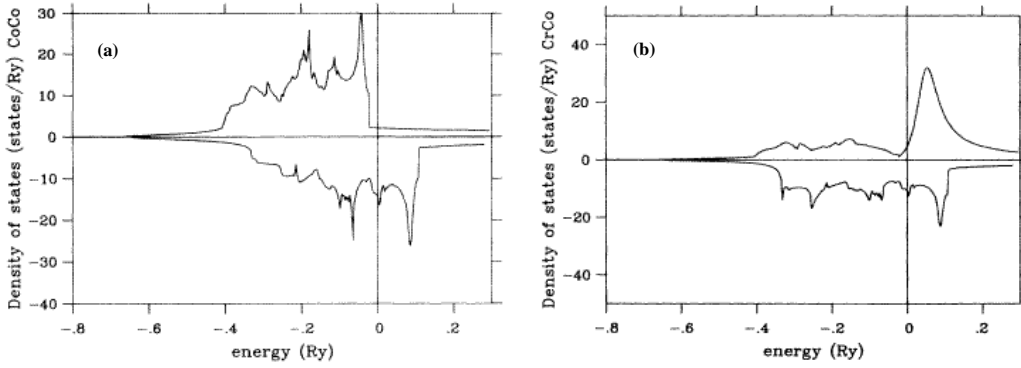


Figure 5.15: Calculation of the spin-dependent density of states of (a) Co, (b) on the site of a Cr impurity. From Stepanyuk *et al.* [163]

5.2.2.2 Magnetotransport results

Due to the s - d wavefunction hybridization between Co and Cr which underlies the VBS, both an impurity-localized d -character and a delocalized s -character modification of the Co DOS induced by Cr doping may be investigated. As detailed in Sections 2.2.2.3, 2.6 & 4.1.2, LSMO/STO/Co and LSMO/STO/ALO/Co junctions probe the d and s characters of the Co

interfacial DOS resulting from d - d and s - d wavefunction coupling at the interface with SrTiO₃ (STO) and Al₂O₃ (ALO) insulators respectively. In this spirit we have investigated LSMO (350 Å)/STO (7 ML)/CoCr(150 Å) and LSMO/STO (2ML)/ALO (10 Å) / CoCr (150Å) junctions of increasing Cr concentration. Samples were capped with 50-150Å of Au.

Figure 5.16 summarizes our findings for this multi-sample study. The TMR amplitude for the bias dependence of the various junctions was normalized to the value found at $V=+20$ mV so as to allow a comparison between junctions of the relative TMR change resulting from the DOS modifications. This bias value was considered to constitute a reference for all samples since in that direction of applied bias, CoCr electron states near E_F are sampling the LSMO unoccupied DOS, itself a reference throughout all samples. This argument supposes that the Cr VBS influence on the Fermi level DOS be minor, but regardless the close overlap between curves at all positive bias values appears to validate this scaling procedure. Thus the DOS modification from Cr doping may be appreciated at negative bias values, for which LSMO states near E_F tunnel toward CoCr unoccupied states.

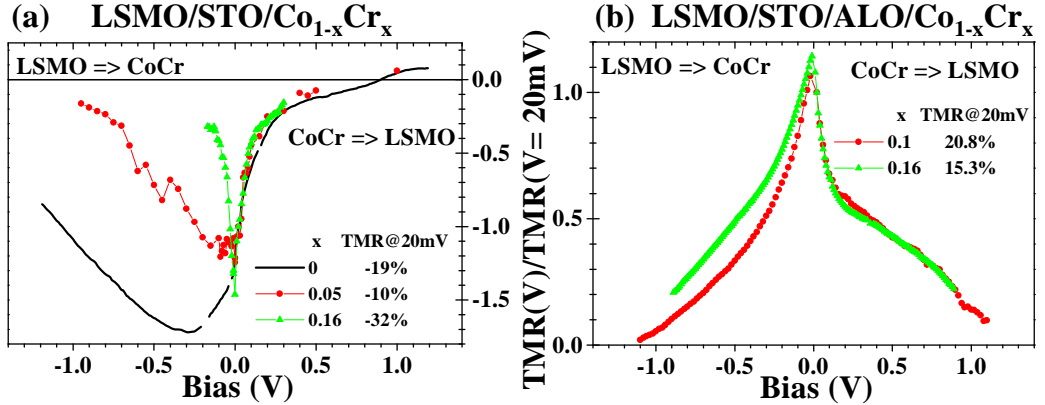


Figure 5.16: Normalized TMR bias dependence for: a) LSMO/STO/Co_{1-x}Cr_x and b) LSMO/STO/ALO/Co_{1-x}Cr_x junctions taken at 30K. TMR values at low bias are shown in the legend. Arrows indicate the direction of electron transport. See text for an explanation of the normalization procedure.

From the left-hand panel of Figure 5.16 representing LSMO/STO/CoCr data taken at $T=30$ K, Cr doping clearly alters the bias dependence of TMR when probing CoCr unoccupied states. In comparison to the curve for $x=0$, Cr doping, though it doesn't necessarily decrease the TMR amplitude ob-

served at low-bias⁴, does induce a drastic reduction in the relative TMR amplitude. The inverse TMR peak appears to have both decreased in amplitude and been shifted towards $V=0$. In a DOS interpretation, this behavior results from a competition between the Co d -band spin \downarrow DOS peak at $E \sim E_F + 0.3\text{eV}$ and the spin \uparrow VBS located at $E \sim E_F + 0.8\text{eV}$ which spans 1eV. As Cr concentration increases, the energy width of the Cr VBS as well as its amplitude increase. This results in an effective decrease of the spin polarization arising from the Co $d \downarrow$ band. One may attain a clearer understanding by referring to Figure 5.17's schematic of the s, d and VBS contributions to the total spin-dependent DOS.

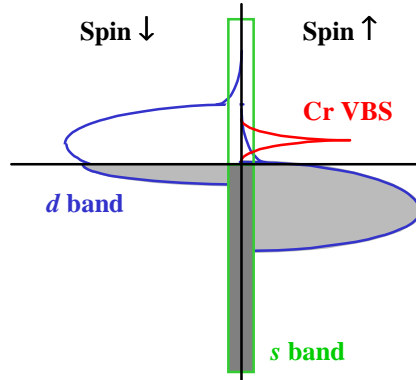


Figure 5.17: Schematic representation of the spin-dependent density of states of the $\text{Co}_{1-x}\text{Cr}_x$ dilute alloy.

As represented in the right-hand panel of Figure 5.16, an opposite though attenuated trend may be inferred in the case of LSMO/STO/ALO/ $\text{Co}_{1-x}\text{Cr}_x$. The slight increase in the relative TMR amplitude at negative biases when Cr concentration is increased, from $x=0.1$ to $x=0.16$, could reflect the more diffuse s -character of the Cr VBS, both in energy and in state density. Referring to the CoCr schematic of Fig 5.17, the positive Co spin polarization induced at the interface with Al_2O_3 [34] is thereafter increased by the VBS contribution of spin \uparrow states, thus explaining the relative increase in TMR with Cr doping when probing the CoCr unoccupied states.

5.2.2.3 An incomplete study

In order to compare junctions from one sample to another, it is desirable to grow the samples and process the junctions in the same run. Unfortunately,

⁴Please refer to Section 7.1.2 for an explanation of this trend in our junctions.

such stringency in the experimental conditions of this study could not always be maintained, because in several instances samples did not yield any result. An obvious problem was one of junction statistics: lithographic processes I and II produced only 3-6 junctions per sample. In addition, a change of sputtering systems used to produce the ALO insulating layer impaired a conclusive end to the study of LSMO/STO/ALO/CoCr samples, even though we had figured that by overoxidizing the deposited Al we could attain the same quality Al_2O_3 as that produced in the former sputtering system. Yet magnetotransport results show that structures grown in the two sputtering systems are different. We were thus unable to complete the study with a $x=0$ reference curve for the LSMO/STO/ALO/CoCr study despite numerous tries.

5.3 Summary

This Chapter presented experimental results which evidence the role of the spin-dependent density of states on the tunneling process. A set of experiments on LSMO/STO/LSMO and LSMO/STO/Co junctions have shown how the electrode densities of states manifest themselves within, and beyond, the magnon excitation bias regime. In particular, a comparison with the established spectroscopy technique of spin-polarized inverse photoemission has confirmed the spectroscopic nature of solid state spin-dependent tunneling. Magnetotransport experiments on LSMO/I/CoCr junctions aimed to confirm the spectroscopic interpretation of the TMR bias dependence in LSMO/STO/Co system at negative applied bias. The set of bias-dependent TMR results obtained may be successfully interpreted in terms of a controlled modification of the Co DOS through Cr doping. However these results assume a nominal STO/CoCr interface with no chemical activity. We reassess transport in this system from an electrochemical viewpoint in Section 7.1.

Chapter 6

On the origin of the depressed transport Curie temperature at a manganite/barrier interface

An impediment to integrating manganite materials into tunneling devices operating at room temperature lies with what has been reported as a diminished Curie temperature at the interface with the tunneling barrier. This decrease has been argued in terms of disruptions in the oxide's electronic properties at the interface. This Chapter discusses the temperature dependence of TMR in LSMO/STO/LSMO and LSMO/STO/Co junctions, with an aim to understanding the conduction mechanisms which affect the effective spin polarization at the LSMO/STO interface. In Section 6.1, we first present results on LSMO/STO/LSMO junctions, which probe one LSMO/STO interface using another LSMO/STO interface. In Section 6.2, we isolate contributions from only one LSMO/STO interface by probing with a STO/Co interface possessing a much higher Curie temperature.

6.1 Probing with LSMO

Figure 6.1a presents the temperature dependence of tunneling spin polarization at the LSMO/STO interface, obtained within the Julliere model (see Equation 2.5) from TMR values garnered thanks to $R(H)$ (see inset) at several temperature values in LSMO/STO/LSMO junctions. Difficulties in maintaining a proper antiparallel alignment impede a very accurate determination of the evolution of TMR with increasing temperature, though the trend of a rapid decrease of TMR with increasing temperature is clear. On one junction, a 30% value was found at $T=250K$, while 12% remain at

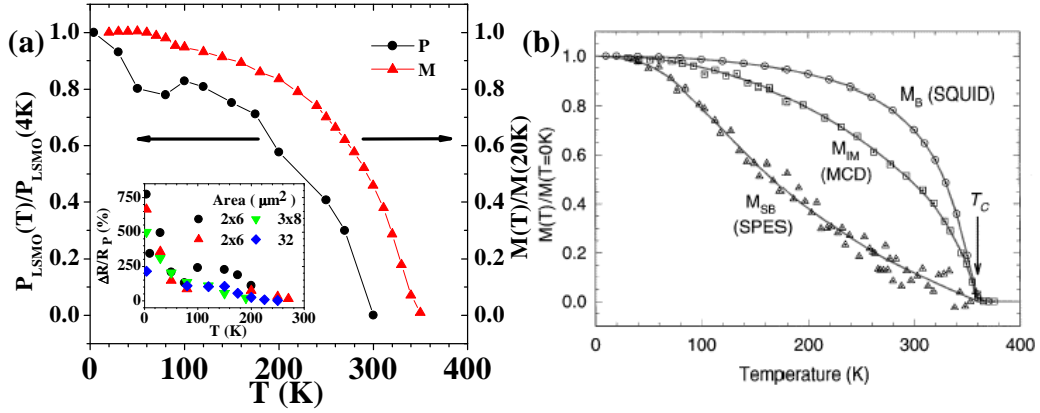


Figure 6.1: LSMO/STO/LSMO: (a) Temperature evolution of normalized $P_{LSMO}(V=10mV)$ and sample magnetization, obtained from $R(H)$ at increasing temperature on a set of junctions (see inset). (b) Temperature dependence for $La_{0.7}Sr_{0.3}MnO_3$ of bulk magnetization, surface magnetization (XMCD) and surface spin polarization (spin-polarized photoemission) from Park *et al.* [164].

$T=270K$.

As the comparison with the bulk LSMO magnetization shows, the evolution of $P_{LSMO}(T)/P_{LSMO}(4K)$ with increasing T follows the same trend as $M(T)/M(20K)$. As argued by Shang *et al.*, [75] both $P(T)$ and $M(T) \propto (1 - \alpha T^{3/2})$ in the case of transition metal electrodes, while a similar relation was found regarding double exchange electrodes. [165] Therefore, this comparison clearly underscores the similar evolutions of the manganite's spin polarization and interfacial magnetizations with that of the bulk film. In contrast, Park *et al.* had found a markedly different temperature dependence of LSMO surface spin polarization as probed by photoemission (see Figure 6.1b), which he had ascribed to symmetry breaking effects at the surface. [164] Comparing both results, two remarks can be made. Firstly, these results were performed on a surface and an interface, so that the electronic properties at the latter boundary are not subject to contamination. Secondly, while Park's spectroscopic technique reveals the intrinsic electronic structure of the interface, our spectroscopic technique through spin-dependent tunneling involves additional factors related to the transport nature of our experiment. One is related to the incidence of the double exchange conduction mechanism on the ferromagnetic properties at such an interface. As argued by Filipetti and Pickett, [155] spin pairing at the manganite interface may lead to enduring ferromagnetism at the interface due to the double exchange

conduction mechanism. This could explain why in our tunneling experiments we witness a temperature evolution of TMR which is similar to that of the bulk magnetization.

Interestingly, the T_C obtained from P_{LSMO} is lower than the bulk T_C . In addition, the evolution of this spin polarization does not follow that expected from spin-dependent tunneling between half-metallic electrodes subject to double exchange conduction. As calculated by Itoh *et al.*, [77], the spin polarization should remain fairly constant up to $0.4T_C$ (see Figure 2.13a on page 29). Both effects may be attributed to the incidence of an additional conduction process on the electronic properties of the manganite/barrier interface, that of spin wave excitations in the low-bias regime ($V=+10\text{mV}$) used to perform the measurement. We also examined the temperature dependence of P_{LSMO} at bias values exceeding the magnon energy cutoff, but the same trend is observed (data not shown). The reason for this is that we are using one LSMO interface to probe another, so that it is impossible to eliminate this spin wave contributions to this determination of $P_{LSMO}(T)$. The following Section presents results using the Co/STO interface - which is more insensitive to spin wave excitations, to probe the LSMO/STO interface.

6.2 Probing with Co

Since magnon generation occurs only up to a cutoff bias value $\sim 150\text{mV}$ (see Section 2.3.2), beyond such a value of applied bias, tunneling may be relatively unaffected by such spin wave excitations, and thus reflect magnetotransport properties more intrinsic to the junction electrodes. In LSMO/STO/LSMO junctions, this allowed us to probe spin-dependent DOS features of the manganite collecting the current, such as the half-metallic minority gap. In that study, most measurements were performed at low temperature so as to avoid the incidence of spin fluctuations at either interface on magnetotransport. [77] However, in LSMO/STO/Co junctions, Section 5.2.1.1 showed how magnon generation was much more difficult at the STO/Co interface due to this ferromagnet's high T_C . It is therefore possible to independently probe the effect of spin fluctuations at the LSMO/STO interface by studying the temperature dependence of magnetotransport at an applied bias for which the tunneling current is unaffected by spin wave excitations.

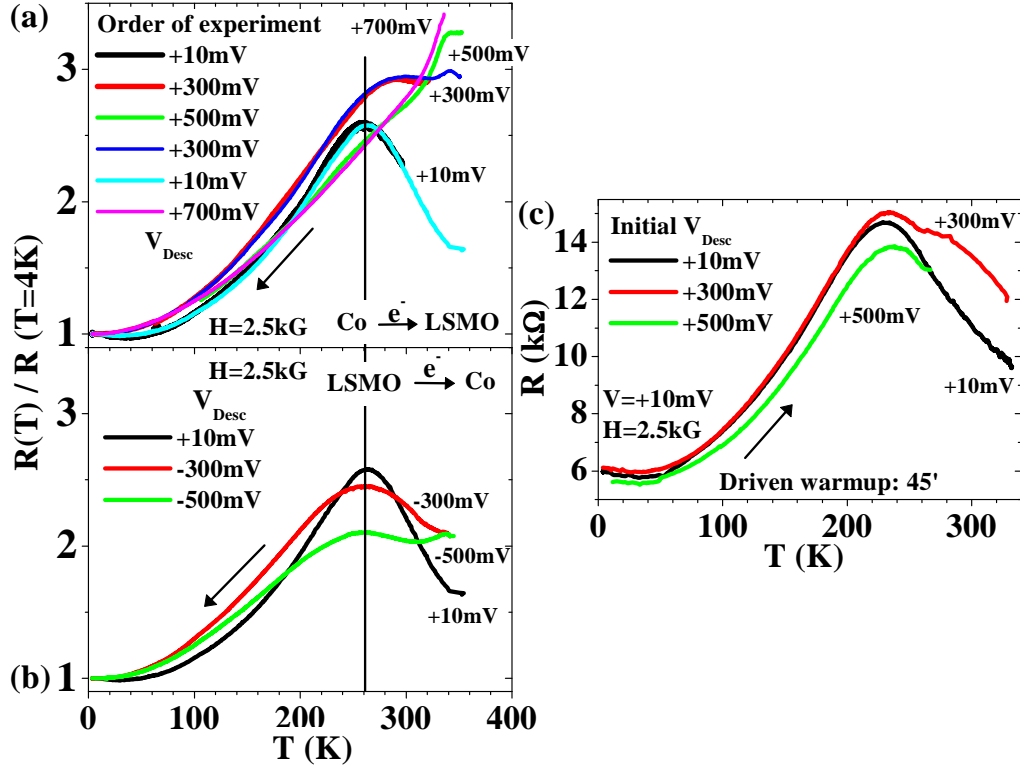


Figure 6.2: LSMO/STO/Co: temperature dependence of resistance within and beyond the spin wave excitation regime for electrons injected (a) toward LSMO and (b) toward Co. Resistances are normalized to the value found at $T=4K$. (c) Junction resistance at $V=+10mV$ during a 45 minute driven warmup after cooling down at V_{Desc} .

6.2.1 Bias-dependent temperature dependence of tunneling transport

Figure 6.2 presents a study of the temperature evolution of resistance for a representative LSMO/STO/Co junction of area $80\mu m^2$ patterned on sample Al1531. Panel (a) shows the evolution with decreasing temperature of junction resistance for several positive applied bias values V_{Desc} , which correspond to electron injection from the Fermi level of the Co electrode toward unoccupied states of LSMO across the STO barrier under electric stress. Once at low temperature, the bias applied to the junction never exceeded $\pm 500mV$, save for the last measurement performed at $V_{Desc}=+700mV$. A cooldown was first performed at $V_{Desc}=+10mV$. The resistance peak for this low bias was found to occur at $T \sim 260K$. Subsequent measurements at

$V_{Desc}=+300\text{mV}$ and $V_{Desc}=+500\text{mV}$ reveal a change in the temperature dependence of resistance of the junction. Indeed, the peak at 260K appears somewhat shifted toward higher temperatures, while a second peak appears at $T=340\text{K}$. This second peak is especially prevalent at the higher bias value. Following these measurements, additional cooldown sequences were performed at $V=+300\text{mV}$ and $V=+10\text{mV}$ to confirm the stability of these temperature-dependent resistance features.

Similarly, cooldown measurements were performed at several negative bias values, which correspond to electron injection from the LSMO Fermi level toward unoccupied Co states. As may be appreciated in panel (b), no temperature shift was observed in the resistance peak at 260K as V_{Desc} was ramped negatively from 10mV to -300mV and -500mV. Furthermore, while at positive biases this peak was eclipsed by that at 340K, for negative biases this peak dominates any signal at 340K. This remark is especially obvious in the case of $V=\pm 300\text{mV}$, wherein no peak at 340K could be observed at negative bias while at positive bias this peak is as prevalent as that at 260K.

Panel (c) underscores the stability of the junction during these succeeding cooldown sequences at varyingly large bias values. Indeed, the junction retains broadly the same resistance value at $T=4\text{K}$ regardless of V_{Desc} . Furthermore, measurements of junction resistance at $V=+10\text{mV}$ while the junction is then forcibly warmed up in 45 minutes by means of a nearby resistor reveal no shift of the resistance peak.¹ Finally, all these measurements were performed at the same value $H=2.5\text{kG}$ of applied magnetic field, so that the interpretation of these results cannot arise from external field-induced modifications to the electronic structure of the manganite.

To assess the possible incidence of the junction barrier profile on these effects, Figure 6.3a presents the temperature evolution of IVs in the parallel (P) and antiparallel (AP) states. A clear, spin-independent peak at $V=+0.6\text{V}$, associated with a sharp spin-independent rise in junction conductance (see panel (b)), underscores the effect of exceeding the tunneling barrier height. The inset to panel (b) presents the temperature dependence of junction resistance at $V_{Desc}=+500\text{mV}$ and $V_{Desc}=+700\text{mV}$ once a linear background has been subtracted. Both measurements reflect the dominant peak at $T=340\text{K}$, but at $V_{Desc}=+500\text{mV}$ the peak at $T=260\text{K}$, though weak, is still visible. For a value $V_{Desc}=700\text{mV}$ which exceeds the barrier height, only the peak at $T=340\text{K}$ is visible.

¹The fact that the peak consistently occurs at the lower temperature value of $\sim 230\text{K}$, compared to the peak found at $T=260\text{K}$ during cooldown, reflects the non-equilibrium nature of such a warmup procedure due to a probable temperature gradient within the cryostat between the sample and the thermocouple on the sample holder. This warmup procedure is to be opposed to thermalization over many hours.

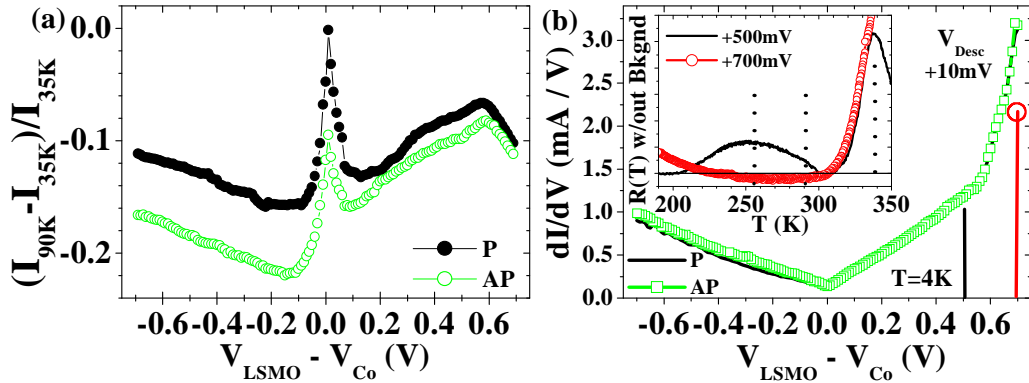


Figure 6.3: LSMO/STO/Co: temperature evolution of IVs in the parallel (P) and antiparallel (AP) configurations between 35K and 90K. (b) Junction conductance in the parallel (P) and antiparallel (AP) states at $T=4\text{K}$. Inset: temperature dependence of junction resistance for applied bias values below ($V=+500\text{mV}$) and above ($V=+700\text{mV}$) the STO hole barrier height. A linear resistance background has been subtracted.

6.2.2 Spin wave excitations and magnetotransport

The observation of a resistance peak in the range $250\text{K} < T < 300\text{K}$ has consistently been a feature of tunneling measurements on LSMO/STO/Co junctions for $V=+10\text{mV}$. Since tunneling is sensitive to the ferromagnet/barrier interfacial DOS and electronic structure, this peak has been usually attributed to the interfacial manganite's metal-insulator transition, and represents a measure of the quality of the interface.

We argue that the second peak at $T=340\text{K}$ reflects the expected Curie temperature of the bulk film. Indeed, at this value $x=0.3$ of Sr doping, the T_C of LSMO is $\sim 360\text{K}$. Due to the 0.9% in-plane lattice expansion resulting from growth onto $\text{SrTiO}_3(001)$, the T_C of our 350\AA -thick films has been observed at slightly lower values in the $340\text{K}-350\text{K}$ range. [166]

Why is this second peak appearing in the $R(T)$ measurements? Why does it dominate the other peak? We propose that the first peak at $T=260\text{K}$ reflects the disruption of the interface's electronic properties due to spin wave excitations at the interfaces in the low-bias regime. Beyond this regime, the second peak at $T=340\text{K}$ reflecting the intrinsic electronic property of the interface becomes more prevalent. Once tunneling transport exceeds the barrier height, interfacial contributions to tunneling, including those from magnons, become negligible in proportion of the total current compared to that resulting from Fowler-Nordheim tunneling.

As described theoretically (see Section 2.3.2) and experimentally (LSMO/STO/LSMO: Section 5.1.1; & LSMO/STO/Co Section 5.2.1.1) we have seen that in the low bias regime spin wave excitations affect the tunneling process through the emission and absorption of magnons at the collecting and injecting interfaces. The high T_C of Co results in a more difficult magnon excitation and absorption process. On the other hand, since for LSMO $T_C \approx 350\text{K}$, the disruption of ferromagnetic order due to ambient magnons is more likely.

As shown experimentally (LSMO/STO/LSMO: Section 5.1.2; & LSMO/STO/Co Section 5.2.1.2), the probing of fully spin-polarized DOS features at the collecting interface beyond this cutoff imply the persistence of a highly spin-polarized current in spite of the spin wave excitations. In the above experiments, the peak at $T=260\text{K}$ becomes dwarfed in amplitude by that at $T=340\text{K}$ for $V>0$, corresponding to hot electron injection at the LSMO/STO interface at an applied bias beyond the $\sim 100\text{mV}$ cutoff in the magnon excitation spectrum at that interface. However, that a more "bulk" signal comes to dominate an "interfacial" one here is not merely the result of exceeding the barrier height, since this trend occurs below the barrier height.² The relevant mechanism is therefore one of suppression of the weight magnon generation plays in the tunneling process beyond this cutoff. The implication is then that the peak at $T=260\text{K}$ reflects the disruptive influence of spin wave excitations on a metal-insulator transition at the LSMO/STO interface at $T=340\text{K}$.³

For $V<0$, electrons are injected from the LSMO Fermi level toward Co unoccupied states as hot electrons. In this case the peak at $T=260\text{K}$ remains prevalent at all values of V_{Desc} . This is to be expected since electrons at the LSMO/STO interface are always injected from E_F , and are therefore subject to spin wave excitations, specifically the absorption of ambient magnons. [67] The peak at $T=340\text{K}$ does appear with increasing V_{Desc} , though it is much more subdued than at positive V_{Desc} (*e.g.* compare data at $V_{Desc} = \pm 300\text{mV}$). This behavior may result from spin-pairing effects which drive ferromagnetism at the LSMO/STO interface thanks to the double exchange conduction process. [155].

²We state without proof that these results could also reflect exceeding a lower, $\sim 50\text{-}100\text{meV}$ *electron* barrier height at the LSMO/STO interface. Please refer to experimental Sections 7.2.2 & 7.3.3 and to Appendix A.2.3 for relevant discussions of this consideration.

³...with all the implications in terms of manganite integration into room-temperature devices.

6.2.3 Bias and temperature dependence of TMR

The departure from a magnon-limited ferromagnetic response at the LSMO/STO interface for applied bias values exceeding the magnon excitation spectrum should affect the temperature dependence of TMR.

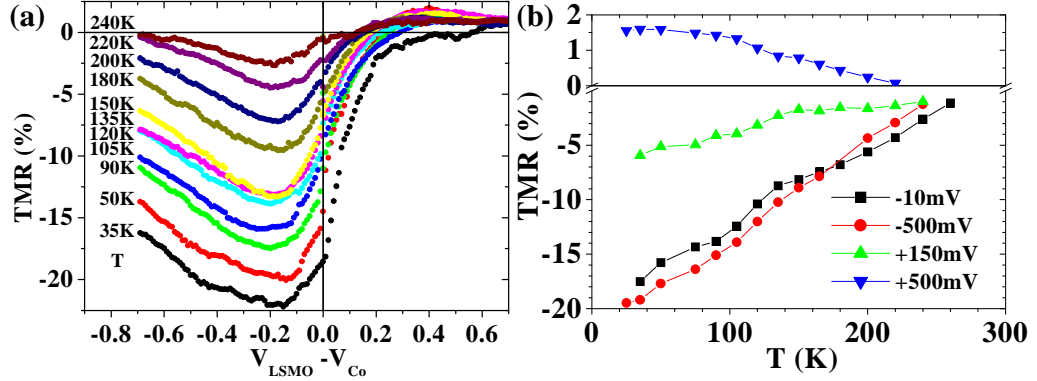


Figure 6.4: Bias and temperature-dependent TMR response of a LSMO/STO/Co junction ($\text{Al}_{15}\text{31:A}=80\mu\text{m}^2$): (a) evolution of the TMR bias dependence with temperature and (b) temperature evolution of TMR at remarkable bias values.

Figure 6.4 presents the tunneling magnetoresistance ($\text{TMR}=\Delta R/R_P$) response of our representative nominal LSMO/STO/Co junction as bias and temperature are varied. Panel (a) presents the bias dependence of TMR for a set of temperatures ranging from 35K to 240K, *i.e.* just below the interface $T_C \sim 260\text{K}$. At $T=35\text{K}$, the TMR at low bias is around -18%. At negative biases this value may rise to -22% at $V \simeq -200\text{mV}$. This peak in inverse TMR amplitude is broadly constant over the temperature range explored, though it appears that the peak position shifts to lower biases above 90K. Sections 7.3.2 & 7.3.3 further discuss this trend.

At positive biases, the TMR drops rapidly, but once the magnon excitation regime is exceeded at $V \leq 150\text{mV}$, the decrease lessens. Notably, the change in sign of TMR at $T=35\text{K}$ occurs at the tunneling barrier height $\Phi=0.6\text{eV}$.

The effect of interfacial and bulk LSMO contributions to magnetotransport may be appreciated in panel (b) of Figure 6.4, which presents the temperature dependence of TMR at remarkable values of applied bias. In the bias range $-500\text{mV} < V < 0$ the TMR decreases in fairly monotonic fashion, to disappear at the temperature corresponding to the LSMO interface $T_C \sim 260\text{K}$. This behavior mimics that found by Park through photoemission experiments on the spin polarization of the $\text{La}_{0.7}\text{Sr}_{0.3}\text{MnO}_3$ surface. [167] At $V=+150\text{mV}$

- an intermediate bias value beyond the initial spin-scattered bias region, this decrease lessens past 150K as other effects come to dominate, such as perhaps the increased LSMO carrier localization beyond this temperature.

However, while at $V=-500\text{mV}$ the TMR signal exhibits a monotonic decrease characteristic of a LSMO interfacial contribution - similarly to that at $V=-10\text{mV}$, the temperature dependence of TMR at $V=+500\text{mV}$ shows a plateau until $T\sim 100\text{K}$ before decreasing.⁴ In this temperature range, the decrease arises mainly from inelastic tunneling processes above 50K. Nevertheless, the TMR at 90K has only decreased 8% at $V=+500\text{mV}$ relative to that at 35K, compared to 20% and 30% drops for $V=-10\text{mV}$ and $V=+150\text{mV}$, respectively. We argue that the monotonic decrease in TMR for $-500\text{mV} < V < +150\text{mV}$ reflects the influence of spin wave excitations at the LSMO/STO interface, which occur more easily given the manganite's $T_C=350\text{K}$. Once the contribution of spin wave excitations at this interface to transport may be neglected, for $V>+150\text{mV}$, the temperature dependence of TMR reflects other processes. We neglect the possible magnon absorption at the STO/Co interface in this temperature range, and focus on considerations inherent to the double exchange electrode. As shown in Figure 2.13 (page 29), Itoh *et al.* calculate that, without taking into account spin wave excitations, the TMR of a tunnel junction with double exchange electrodes should remain constant until $T=0.4T_C$, beyond which the decreasing exchange coupling results in the disappearance of the half-metallic gap, and leads to a decrease in TMR. If we use $T_C=260\text{K}$, then the onset of spin fluctuations occurs at $T=100\text{K}$. In this sense, the the TMR plateau below $T=100\text{K}$ for $V=+500\text{mV}$ may reflect the negligible influence of spin wave excitations in this temperature range for this value of applied bias.

It is surprising that we should use the value of T_C which reflects spin wave excitations to understand the temperature dependence of TMR at a bias value where such excitations may be neglected. This contradiction may reflect a more subtle interplay between all these aspects of spin electronics at the LSMO/STO interface, possibly mediated by the aforementioned spin-pairing of a manganite interface to bulk layers through double exchange conduction. [155] Beyond $V=+150\text{mV}$, one expects to find a TMR signal at $T>260\text{K}$. We performed $R(H)$ loops at $V=+500\text{mV}$ and $V=+700\text{mV}$ at temperatures beyond the interface $T_C\sim 260\text{K}$. A low-field, symmetric magnetoresistance of 0.1% could be observed at $T=270\text{K}$ for $V=+700\text{mV}$, reflecting some low-field ordered spin-dependent response, as opposed to $V=-10\text{mV}$ which only showed noise (data not shown). However, the coercive fields did not correspond at all to the $H_C\approx 10\text{G}$ expected of LSMO, nor could the loop

⁴This behavior is reproduced in Figure 7.32 on page 172 with 3% TMR amplitudes.

be consistently explained in terms of the successive magnetization reversal of the LSMO and Co electrodes. Since the TMR at $T=35\text{K}$ only reached $+1.5\%$, it is possible that such a measurement was impeded by noise at higher T . Section 7.3.3.4 presents a similar dataset on another junction for which electromigration effects are argued to modify the effective potential profile of the junction. TMR plateaux are found to span $0.4T_C$, where $T_C=300\text{K}$, beyond the value found at low bias.

6.2.4 Summary

The above experimental results point to the differing magnetotransport behaviors of magnetic tunnel junctions in a low-bias regime dominated by spin wave excitations, and one at larger bias values wherein intrinsic features of the magnetic electrodes may be probed. Such a picture had already been painted through magnetotransport experiments on LSMO/STO/LSMO junctions described in the above Section 5.1, which evidenced the manganite minority gap beyond a bias regime of spin wave excitations. However, in those experiments, tunneling is always taking place from one LSMO/STO interface, leading to a depressed Curie point for the transport spin polarization at the LSMO/STO interface. In the case of LSMO/STO/Co junctions, the higher T_C of Co made it possible to investigate the incidence of the transport technique on ascertaining the tunneling spin polarization at the LSMO/STO interface. In particular, we've shown that the monotonic decrease in TMR amplitude with increasing temperature, found when the LSMO/STO interface is involved in the tunneling process ($-500\text{mV} < V < +150\text{mV}$), evolves to describe a plateau for $T < 100\text{K}$, *i.e.* once the increase in exchange coupling with decreasing temperature has lifted the $2g^\downarrow$ band from E_F so that half-metallicity ensues. Thus the lower T_C of manganites when at the interface with tunneling barriers mainly⁵ results from the generation of spin waves which disrupt the electronic properties of the material. In this case the interface T_C was pegged to 260K . However, beyond the spin wave excitation regime, a dominant resistance peak appears at $T=340\text{K}$ reflecting the LSMO bulk T_C . This implies that it is possible to involve the intrinsic electronic properties of a manganite/barrier interface for bias values exceeding the magnon excitation regime. Studies at much lower applied bias than the $V=+10\text{mV}$ should confirm this explanation of the depressed transport Curie temperature at a manganite/barrier interface by evidencing a shift of the resistance peak to higher temperatures as fewer magnons disrupt the

⁵For the sake of completeness, we point out that the evolution in the TMR temperature dependence as positive bias is increased could also result from entering a ballistic regime after exceeding the low SrTiO_3 electron barrier height.

electronic properties at the interface.⁶ This discovery should have important consequences regarding the design of room-temperature spin electronic devices which integrate manganite ferromagnetic oxides with otherwise low interface T_C values.

⁶This behavior was indeed observed. [168]

Chapter 7

Tunneling barrier effects

This Chapter endeavors to single out barrier profile effects present in a magnetic tunnel junction's bias-dependent response. As noted in Section 2.3.1, exceeding a barrier height through the application of a sufficiently high bias results in a Fowler-Nordheim tunneling regime. The injection, for instance, of electrons into the barrier's conduction band may lead to interference effects through wavefunction reflection at the metallic barrier/ferromagnet collecting interface. This notion has been advanced in theoretical descriptions of tunneling and confirmed to some extent by experiments. Separately, magnetic interlayer exchange coupling between ferromagnetic layers has been shown to occur not simply through non-magnetic metallic spacers - whether a conventional metal or a metallic oxide, but also through insulating layers. Oscillations in this coupling occur with the evolving spacer thickness as it accommodates the formation of quantum well states. To the extent that this second effect also involves wavefunction interference, the two effects share common traits. We propose to unify the two physical pictures by considering the effect of spin-dependent tunneling transport above a barrier height in terms of wavefunction interference and changes to the coupling between the junction's ferromagnetic electrodes.

In this sense an understanding of, and a form of control over, the junction's effective barrier profile, are needed to probe such effects. As described in Section 3.3.2.3, electromigration effects are apt to occur in such heterostructures, especially when reactive elements are present. Section 7.1 presents a set of experiments on $\text{La}_{0.7}\text{Sr}_{0.3}\text{MnO}_3/\text{SrTiO}_3/\text{Co}_{1-x}\text{Cr}_x$ MTJs which demonstrate electrochemical activity at the CoCr interface due to forming effects involving the highly reactive Cr. Section 7.2 presents a comprehensive set of experiments on a fully epitaxial $\text{La}_{0.7}\text{Sr}_{0.3}\text{MnO}_3/\text{SrTiO}_3/\text{La}_{0.7}\text{Sr}_{0.3}\text{MnO}_3$ magnetic tunnel junction. Profile modifications are effected through somewhat irreversible electromigration for

large applied bias values in an otherwise stable heterostructure. We consolidate these findings with experiments on $\text{La}_{0.7}\text{Sr}_{0.3}\text{MnO}_3/\text{SrTiO}_3/\text{Co}$ junctions (Section 7.3). Section 7.3.1 discusses the effect of barrier crystallinity on magnetotransport. Section 7.3.2 investigates the effect of annealing and junction forming on the magnetotransport of remarkable junctions, while Section 7.3.3 presents results on one junction with an electrical instability induced by the trilayer deposition process. The resulting reversible electro-migration processes enable a controlled study of the bias-dependent magnetotransport response while changing the effective barrier profile and possibly affecting the interfacial densities of states.

7.1 Electrochemical activity at the STO/CoCr interface

This Section presents the evolution of an investigation into electrode DOS effects on the tunneling current through magnetotransport experiments on doping the Co electrode in LSMO/STO/Co and LSMO/STO/ALO/Co junctions with Cr. Our initial intent was to utilize the spin-dependent DOS modification that the Cr impurity introduces into the Co matrix to further investigate DOS effects on the magnetotransport properties of this type of junction. Section 5.2.2 presented results in the framework of this research axis. However, as readily apparent from Table 3.4, introducing Cr in a junction electrode will tend toward an unstable Metal/Barrier interface. Though somewhat mitigated in the case of Al_2O_3 interfaces, the issue is quite prevalent for SrTiO_3 barriers, and at the heart of our difficulties in drawing definite conclusions from the CoCr DOS modification study. Indeed, relative to LSMO/STO/Co junctions, LSMO/STO/CoCr junctions always exhibited some degree of electrical instability. An intrinsic reason for this difference in instability lies with the relative miscibility of elements across both interfaces. The lower heat of formation of Al_2O_3 ($\sim -1700\text{kJ/mol}$) relative to CrO_2 ($\sim -600\text{kJ/mol}$), Cr_2O_3 ($\sim -1200\text{kJ/mol}$) or Cr_3O_4 ($\sim -1500\text{kJ/mol}$) implies a fairly stable ALO/CoCr chemical interface. [169] On the other hand, the heats of formation of SrO and TiO_2 are very comparable to that of CrO_2 , so that a STO/CoCr interface may undergo reduction-oxidation, thus changing its chemical state.

Section 7.1.1 presents microstructural evidence for the segregation and oxidation of Cr at the STO/CoCr interface. We utilize the resulting electrochemical instability in Section 7.1.2 to manipulate the chemical character of the CoCr/Barrier interface in a *controlled* manner. In the proper con-

ditions, the direction of oxygen electromigration induced by a sufficiently high electric field applied to the barrier region may favor either a CoCr or a CrO₂ metallic layer at the interface with the effective tunneling barrier. Due to this *forming* of the junction interface, the resulting sign of TMR may be respectively negative or positive as expected from DOS considerations, while the amplitude may reach or exceed 40%.

7.1.1 Chemical state of the SrTiO₃ / Co_{1-x}Cr_x interface

To investigate the chemical state of the STO/CoCr interface, TEM slices were prepared by Patricia Prod'homme and Jean-Luc Maurice. Figure 7.1 presents a HRTEM picture of a LSMO/STO/Co₈₄Cr₁₆ trilayer sample (Al1689) from which a junction yielded data for x=0.16 doping value (see Figure 5.16). Similarly to the HRTEM of a LSMO/STO/Co junction (see Figure B.5), a nanometric layer with lighter contrast appears at the STO/CoCr interface.

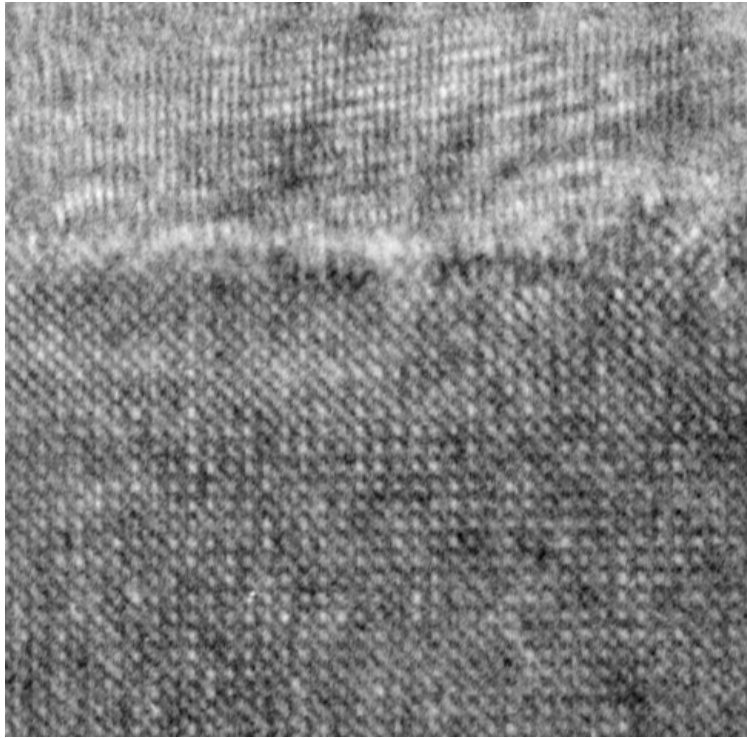


Figure 7.1: HRTEM image of a LSMO/STO/Co₈₄Cr₁₆ trilayer (Al1689). MnO₂ columns in the lower La_{0.7}Sr_{0.3}MnO₃ layer are expanded to the 3.905Å STO lattice spacing. Picture by Patricia Prod'homme.

To identify the nature of this nanolayer, this slice was then examined¹ by Electron Energy Loss Spectroscopy (EELS) at $T=300\text{K}$ Figure 7.2a shows an elemental profile starting from within the STO barrier and through the STO/CoCr interface into bulk CoCr. Data for Ti, Cr and Co are represented. As revealed by the ratio Cr/Co, a segregation of Cr to the interface has occurred, while in the bulk of the $\text{Co}_{84}\text{Cr}_{16}$ film a lower-than-expected ratio is found. Such a deviation from nominal stoichiometry has previously been observed [170] in CoCr films as temperature is raised past $\sim 400\text{K}$, and may occur at a surface. [171] While the as-deposited interface may not exhibit such segregation,² TEM slice preparation involved heating the sample to $T=400\text{K}$, which may explain this result. Nevertheless, junction preparation also involves heating to about that temperature (*e.g.* ion milling in Steps I and II, or metallization in Step IV of the lithography), so that the result is relevant to our magnetotransport studies.

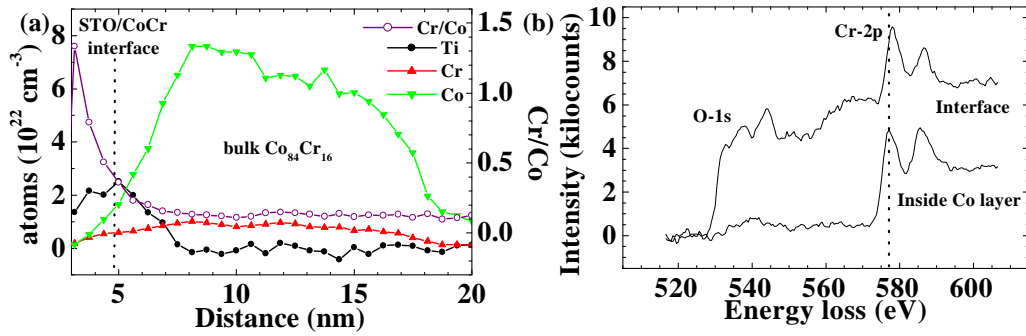


Figure 7.2: EELS analysis of the chemical state of the $\text{STO}/\text{Co}_{84}\text{Cr}_{16}$ interface of sample A11689. (a) Elemental profile starting from the STO barrier and through the Cr-segregated interface to bulk CoCr. (b) Energy Loss profiles at the Cr-2p edge revealing an oxidized state of Cr at the interface compared to bulk CoCr.

Figure 7.2b shows energy loss scans taken at the interface and within the bulk CoCr layer. Absent in the case of Co, a shift in the Cr-2p peak to higher energies for the interfacial scan reveals that Cr at the interface is oxidized. [169] Indeed, the aforementioned increase in Cr concentration at the interface cannot explain this increase in peak position since for pure Cr the 2p peak (EELS technique) is at $\sim 575\text{eV}$ - for Co, 579eV . [172] An increase of $\sim 1\text{eV}$ between the Cr 2p peaks of CrO_2 and/or Cr_2O_3 was reported using

¹This work resulted from a collaboration with D. Imhoff and C. Colliex of the Université Paris-Sud Orsay

²The CoCr counter-electrode was deposited by MBE at 300K . As such adsorbed atoms during deposition have low kinetic energy -compared to the case of sputtering.

EELS experiments. [173] Also, a study using the similar technique of X-Ray Photoelectron Spectroscopy (XPS) indicates a 0.5eV energy increase of the Cr $2p_{3/2}$ binding energy from Cr_2O_3 to CrO_2 . [174] Thus the $\sim 1\text{eV}$ shift found in our EELS study points to the formation of either CrO_2 and/or Cr_2O_3 at the STO/ $\text{Co}_{84}\text{Cr}_{16}$ interface, though we cannot distinguish between the two. It is indeed quite likely that the oxidation state of Cr may reach that in Cr_2O_3 (Cr_{3+}) at the interface with STO since any incoming oxygen electromigration from LSMO and STO (see Section 3.3.2.3) will increase the oxidation state from that of CrO_2 (Cr_{2+}). In Section 7.1.2 we examine how this interface instability may be used to probe DOS effects.

7.1.2 Manipulation of the CoCr/SrTiO₃ interfacial chemistry through electromigration

Junction instability when Cr is introduced into the Co electrode underscores the chemical activity at the STO/CoCr interface. It is possible to affect the chemical state of the STO/CoCr interface through electromigration. Section 3.3.2.3 presented some experimental illustrations of oxygen diffusion in perovskites. As alluded to in the literature on electromigration considerations in oxide fuel cells, [175] chromium may also participate in this process. This Section showcases the incidence of electromigration effects on the magnetotransport properties of LSMO/STO/CoCr junctions. The multiphase STO/CoCr interface consists of Cr oxide (see Section 7.1.1), and possibly CoCr_2O_4 (a ferromagnetic insulator) or CoO , though no chemical shift at this interface was found for Co. Thus the actual tunnel barrier may consist of SrTiO_3 , Cr_2O_3 , as well as CoCr_2O_4 and CoO . Since these barriers allow more efficient evanescent transmission of d -character wavefunctions through a conduction band with this electronic character (see Section A.1), the positive sign of spin polarization of LSMO implies that the sign of the counterelectrode's spin polarization will determine the ensuing sign of TMR. We remind the reader that all magnetotransport results adopt the following convention: LSMO is biased positively with respect to CoCr. As such, a positive bias induces an electric field across the barrier which may promote electromigration of anionic species from CoCr to STO, while a negative bias will enable diffusion in the reverse direction. A complementary trend is expected of cationic species.

More than one dozen LSMO (350Å)/STO (7ML)/ $\text{Co}_{1-x}\text{Cr}_x$ (150Å) / Au (150Å) samples with Cr concentrations x in the range 0.04 to 0.2 were grown and processed into junctions by lithography processes I,II & III. We will present experiments on representative junctions from three samples which il-

illustrate the effect of electromigration on the magnetotransport properties of this system. Junctions A ($x=0.08$, $A=80\mu\text{m}^2$) and B ($x=0.16$, $A=314\mu\text{m}^2$), of larger area, exhibit an instability between a STO/CoCr chemical state (State I) of lower resistance with a negative spin polarization, achieved by applying a positive bias; and a high-resistance state (State II) associated with a mixed or positive spin polarization - though of low amplitude, achieved by applying a negative bias. Switching between states is a fairly reversible current-mediated process (see Section 7.1.2.1). Junction C, with a area $A=12\mu\text{m}^2$ reduced thirty-fold and a high $x=0.2$ Cr concentration, offers more insight into the electrochemical activity of cationic and anionic species at the STO/CoCr interface with large TMR amplitudes of both signs. The change in sign of TMR is interpreted as originating from a metallic CoCr or half-metallic CrO_2 interface with negative and positive spin polarizations, respectively. Such effective metallic interfaces result from the electric-field directed electromigration of species at the STO/CoCr interface (see Section 7.1.2.2).

7.1.2.1 Reversibility of the junction metastable states

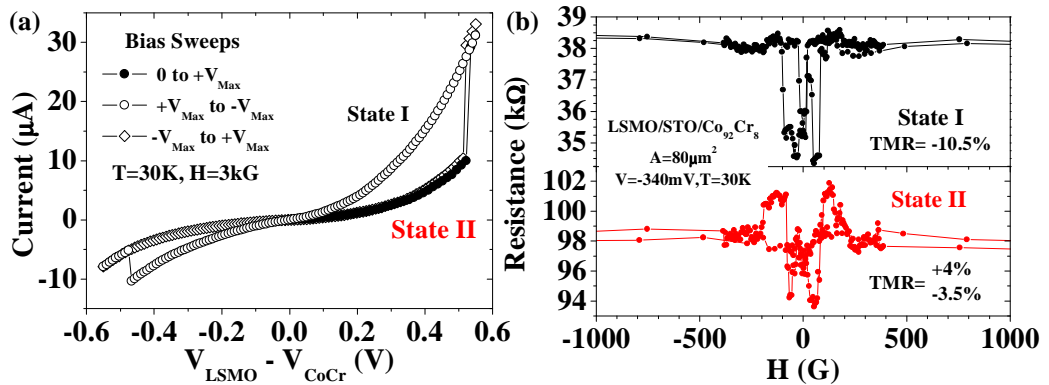


Figure 7.3: Sample A: LSMO/STO/ $\text{Co}_{92}\text{Cr}_8$ junction of surface area $80\mu\text{m}^2$. (a) Two junctions states are created from current *vs* voltage sweeps (in voltage mode). (b) $R(H)$ loops at $V=-340\text{mV}$ in each of the two junction states. For clarity, the IV curves are displayed with fewer points than the 2mV step used.

Figure 7.3a presents current-voltage sweeps (in voltage mode) on a LSMO/STO/ $\text{Co}_{92}\text{Cr}_8$ junction of surface area $80\mu\text{m}^2$ (Junction A). Prior to this measurement, a negative bias of $V=-0.55\text{V}$ had been applied. Therefore, beginning from $V=0$, the IV sweep reflects the high resistance of State

II (closed squares). Beyond a critical bias, junction current jumps to a higher value, reflecting the low resistance of State I. Upon reaching $+V_{Max}$, the applied bias is then swept from zero to negative values (open circles). Beyond a second critical bias, junction resistance increases as the junction switches again to State II. Finally, junction bias is continuously swept from $-V_{Max}$ to $+V_{Max}$, the junction switches once more to State I. The overlap of successive bias sweeps reflecting the same state emphasizes the degree of reversibility. In fact, such a sweep was repeated well over 100 times on this junction, though beyond 40 runs the critical bias value began to increase from $+350\text{mV}$ to eventually beyond the maximum bias value $V_{Max}=+550\text{mV}$. The junction resistance creep toward higher values reflects the partly irreversible behavior of such switching, and suggests an electrochemical migration interpretation involving both anionic and cationic species. A typical set of resistance values at $V=-50\text{mV}$ is $70\text{k}\Omega$ for State I and $250\text{k}\Omega$ for State II. Figure 7.3b shows $R(H)$ loops taken at $V=-340\text{mV}$ in both states. The set of $R(H)$ loops at this bias value was selected because it clearly illustrates the magnetotransport response of the junction: while State I exhibits inverse TMR as expected of CoCr, State II is composed of a mix of inverse and normal TMR, both of low amplitude. Interestingly, the field value $H \simeq 100\text{G}$ at which the CoCr layer flips magnetization direction in State I is also associated in State II with a rise in resistance from the inverse TMR to the positive TMR situation. The positive TMR of State II occurs within the range $100 < H < 200\text{G}$. Other bias values yield similar, if not as clear-cut, behavior with possible field direction asymmetries (see Figure 7.5 hereafter).

An increase in Cr concentration x leads to an increased tendency for junction electrical instability. We surmise that this is due to the larger proportion of Cr atoms present at the interface to participate in electrochemical processes. While in sample A $x=0.08$, in sample B $x=0.16$. After cooldown, the junction with area $80\mu\text{m}^2$ showed a positive TMR of amplitude $+4\%$ at $V=+10\text{mV}$, reflecting a virgin State II (data not shown). The junction next to it of area $314\mu\text{m}^2$ exhibited a State I with an impressive $\Delta R/R_P=-35\%$ amplitude of inverse TMR at $V=+10\text{mV}$ (see Figure 7.4a). This difference illustrates possible inhomogeneities in Cr concentrations at the STO/CoCr interface across the sample compounded by considerations on the active area of the junction.³ Given usual values of $\sim 20\%$ TMR at low bias for a Co counterelectrode, and the tendency for the d -band spin polarization of Co to decrease with Cr doping (see Section 5.2.2.1), this high amplitude cannot

³Junction areas as defined through lithography are not representative of the active junction area, which is constrained by STO barrier hotspots in conjunction with the filamentary conduction of LSMO. See Section 3.3.3.4.

be explained by DOS considerations. It may instead reflect a shift of the Ferromagnet/Insulator interface away from the contaminated STO interface to a CoCr/Cr₂O₃ interface of better chemical quality.⁴

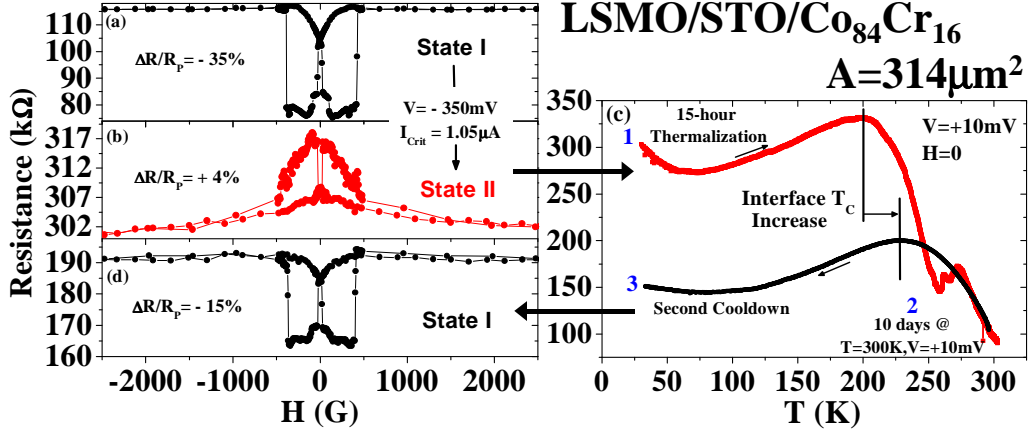


Figure 7.4: Sample B. History of a $314\mu\text{m}^2$ LSMO/STO/Co₈₄Cr₁₆ (Al1689) junction: $R(H)$ loops at $V=+10\text{mV}$ depicting (a) State I and (b) State II. (c) Thermalization to $T=300\text{K}$ and forming at $V=+10\text{mV}$ lead to an increase in LSMO interface T_C and (d) a return to State I with -15% TMR at $V=+10\text{mV}$.

Upon applying a bias $V=-350\text{mV}$, the junction resistance at $V=+10\text{mV}$ increases by a factor of three and the junction displays a clearly positive TMR associated with State II. The return to the parallel state of resistance for an applied field corresponding to the coercive field of the Co₈₄Cr₁₆ layer (see Figure 7.4b) in both junction states underscores the ferromagnetic coupling between the hard CoCr layer and the adjacent ultrathin alloy. The former drives the overall magnetization reversal while the latter determines the sign and amplitude of TMR. This effect is not clear-cut in junction A (see Figure 7.3b), possibly because the lower Cr concentration, though segregated at the interface, doesn't permit a homogeneous interface. Thus a part of the active junction area may consist of Co-rich CoCr which promotes the initially negative TMR. Flipping the CoCr electrode magnetization reverses interfacial CoCr moments, while Cr-segregated interfacial regions, which underwent oxidation to CrO₂,⁵ have yet to flip.

As shown in Figure 7.4c, Junction B was allowed to thermalize to room temperature over 15 hours and form at $V=+10\text{mV}$ for ten days. The junction

⁴As described in Section 3.1.2, the STO surface is exposed to air during trilayer growth.

⁵... so as to explain the sign of TMR if not the amplitude, but Junction C takes care of this issue with +40% TMR.

was subsequently cooled down again. As evidenced from the inverse TMR found at low bias (see Figure 7.4d), the junction has recovered State I. Since no sizeable resistance change occurred during the 10-day forming of the junction, we conclude that the return of the STO/CoCr interface to a chemical order reflecting State I occurred with rising temperature, as illustrated by the resistance instability beyond 250K during thermalization. The increase in LSMO interface T_C between States II and I underscores the oxygen electromigration activity - from LSMO (and STO) toward CoCr, in extending the Cr oxide thickness. This picture of the formation of State II from State I explains both the observed resistance increase and the creation of a Cr oxide with a lesser degree of oxidation (such as CrO_2) due to the oxygen gradient. The low amplitude of observed TMR may reflect the presence of both CrO_2 and CoCr which contribute spin polarizations with opposite signs.

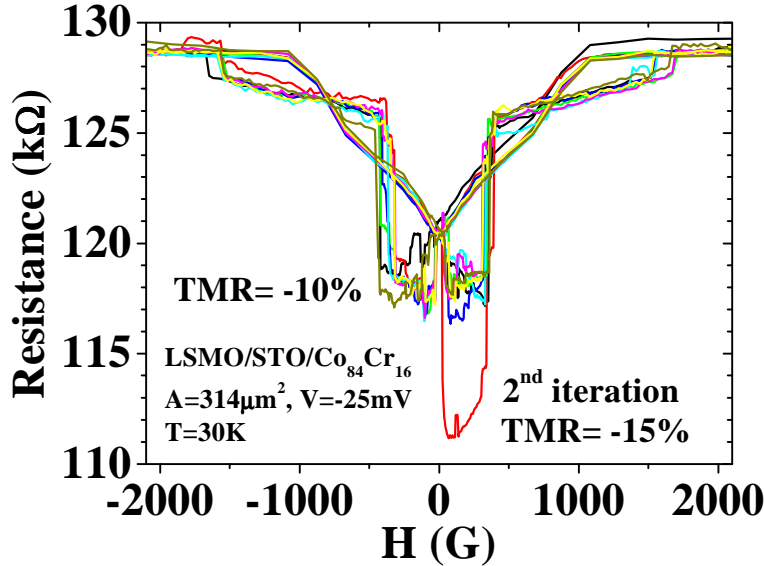


Figure 7.5: Sample B: LSMO/STO/ $\text{Co}_{84}\text{Cr}_{16}$ junction of surface area $314\mu\text{m}^2$. Iterative set of eight $R(H)$ loops in State I.

In the footsteps of Junction B's aforementioned history, Figure 7.5 presents a series of eight $R(H)$ loops from junction B at $V=-25\text{mV}$, taken successively with 5 minute time lapses between measurements. Each loop required approximately 15 minutes to complete, so that the slow magnetization reversal process could explore a wider range of behaviors. The appearance of an occasional loop with an asymmetric TMR behavior between positive to negative and negative to positive magnetic field sweeps underscores the influence of magnetic anisotropies at the STO/CoCr interface. The difference

in shape of the antiparallel plateaux attests to this hypothesis. The sample was cooled down in a positive applied field $H=1500\text{G}$, which drives the antiferromagnetic ordering of any interfacial Cr_2O_3 below its Néel temperature. Such ordering tends to minimize exchange energy at the interface by aligning the interfacial Cr_2O_3 moments parallel to those of the field-driven CoCr layer adjacent to it. As a result, the parallel states at positive and negative applied magnetic fields may be different. Indeed, the parallel state at positive field values is described by a parallel alignment of the ferromagnetic electrodes' moment with the Cr_2O_3 interfacial moment. At negative field values, moments of both electrodes are anti-aligned with respect to the Cr_2O_3 interfacial moment. This change in magnetic configuration between positive and negative H_{Max} may thus result in differing resistance values, as well as the possibility for antiparallel states of different extent depending on the state of the Cr_2O_3 interfacial moment with respect to the adjacent CoCr layer.

7.1.2.2 Electrochemical activity between CrO_2 & Cr_2O_3 probed by spin-polarized tunneling

As illustrated in samples A and B, the observation of a clear State II is aided by a larger concentration of Cr which may segregate at the STO interface to form Cr oxide phases. Limiting the formation of several phases in a given junction state by decreasing the junction area will enhance the TMR signal observed in each State. We now present results on sample C, a LSMO/STO/ $\text{Co}_{80}\text{Cr}_{20}$ junction of area $12\mu\text{m}^2$ defined by Process III.

Initial measurements taken at $T=4\text{K}, V=1\text{mV}$ after cooldown with $H=1500\text{G}$ show an ill-defined virgin state (see Figure 7.6) which evolves toward State II as the junction is subjected to a positive current. This may be interpreted as either arising from the reduction of a CoCr oxide induced by oxygen electromigration from the STO/CoCr interface to the LSMO/STO bilayer. Since Cr may oxidize more readily than Co, this reduction would lead to an interface consisting of metallic Co or CoCr and CrO_2 at the interface with Cr_2O_3 . Thus reduction of Cr_2O_3 to CrO_2 across a fraction of the total Cr_2O_3 thickness would place a metallic system with positive spin polarization at the interface with the effective tunneling barrier. Since $P_{LSMO} > 0$ the TMR would be positive.

At $V=+10\text{mV}$, the junction showed $+9\%$ TMR. After several measurements spanning $V=\pm 700\text{mV}$, a final $R(H)$ loop at $V=+600\text{mV}$ left the junction in State I with $\text{TMR}=-10\%$ at $V=+1\text{mV}$. The applied bias was then ramped up to $V=+850\text{mV}$, corresponding to $I_{Max}\sim 350\mu\text{A}$. No resistance jump was observed. As before, this positive current led to a return to State

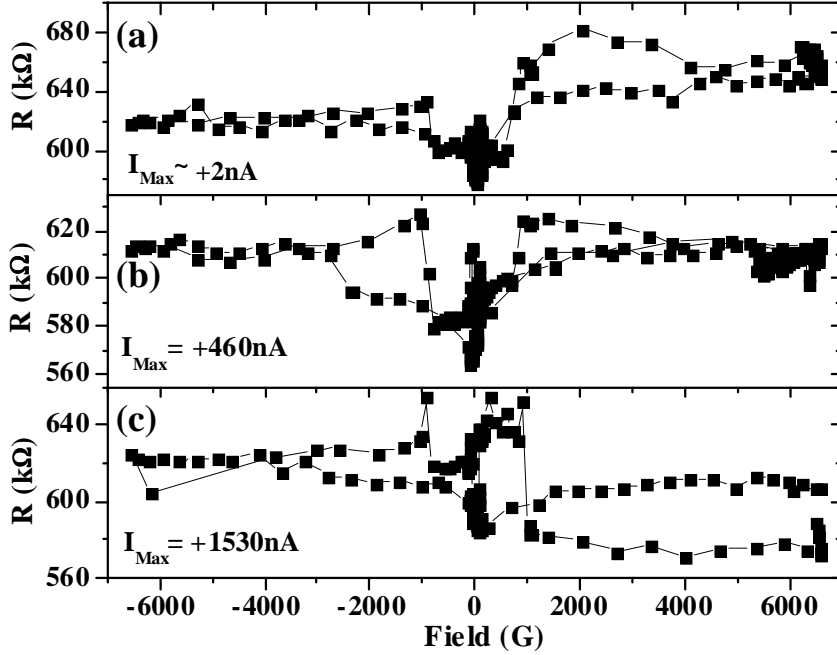


Figure 7.6: Sample C: LSMO/STO/Co₈₀Cr₂₀ junction of area $12\mu\text{m}^2$. First $R(H)$ loops of a at $T=4\text{K}$ and $V=+1\text{mV}$, with a history of injected current $I_{Max} =$ (a) $+2\text{nA}$, (b) $+460\text{nA}$ and (c) $+1530\text{nA}$.

II, with TMR amplitude $+12\%$ as shown in the top panel of Figure 7.7. Interestingly, the magnetic behavior of the junction changed little as bias was thereafter ramped down toward $V=+1\text{mV}$. While comparable in current amplitude, the loop measured at $V=-1\text{mV}$ illustrates how poorly the parallel and antiparallel states are defined when electron flow occurs from LSMO to Co.⁶ A second loop was immediately taken to confirm the anomaly (open symbols, middle panel). As negative current is increased almost tenfold, the magnetic behavior of the junction returns to that expected by the coercive fields of the LSMO ($H_C \sim 10\text{G}$) and Co₈₀Cr₂₀ ($H_C \sim 1000\text{G}$).

The following explanation may account for this asymmetry with current direction of the magnetic behavior. As argued in this and preceding Sections, possible chemical disorder, as well as the ultrathin nature, of the CrO₂ layer may lead to a weakened ferromagnetic state. Current-mediated effects notwithstanding, this ferromagnetism is enhanced through ferromagnetic coupling with the CoCr bulk. However, the high $x=0.2$ doping con-

⁶This observation reflects the chemical state of the STO/CoCr junction interface at this particular point in the experiment.

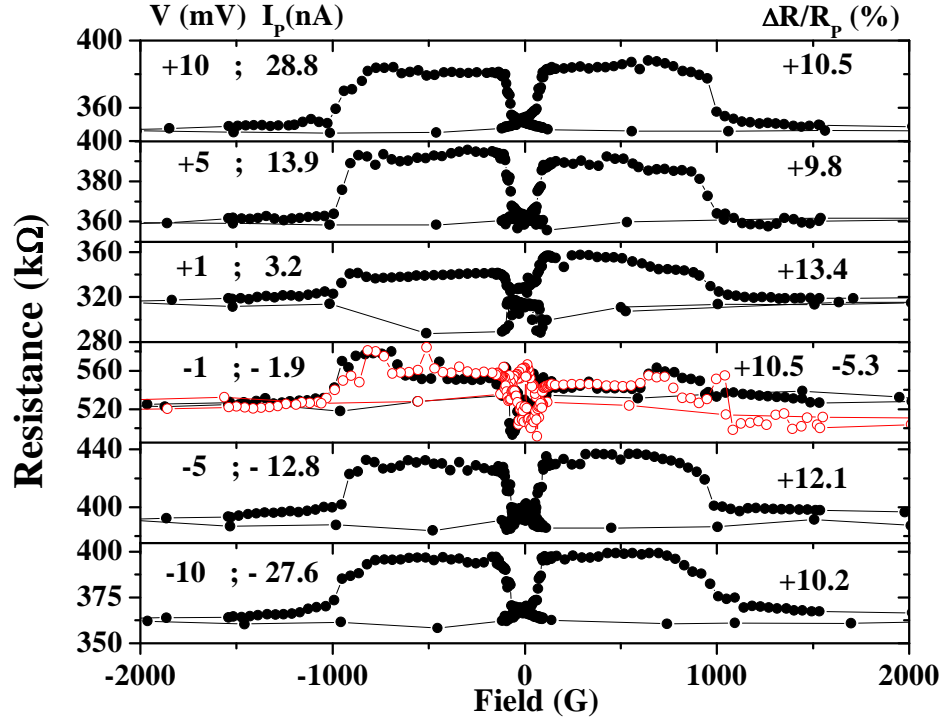


Figure 7.7: Sample C: LSMO/STO/CoCr₈₀Cr₂₀ junction of area $12\mu\text{m}^2$. $R(H)$ loops at $T=4\text{K}$ in State II with $\text{TMR}\sim-10\%$ after a current ramp-up to $I_{Max}\sim+350\mu\text{A}$, obtained from top to bottom. The second $R(H)$ loop with open symbols displayed in the middle panel was taken right after the one with closed symbols.

centration of Cr leads to an almost compensated Co moment and a very small global magnetization of the CoCr film. Thus current-induced magnetic ordering of the CrO₂ nanolayer may control the magnetic behavior of the junction, perhaps by increasing the local carrier concentration to improve metallic (and therefore magnetic) behavior. [155] Since the current through the sample is of similar amplitude for $V=\pm 1\text{mV}$, the key factor in driving the asymmetry is the tunneling probability. As electrons impinge on the CrO₂ nanolayer from the CoCr bulk, only a small fraction actually tunnel through the barrier, while most scatter off and remain near the interface, *i.e.* within the CrO₂ nanolayer, as they renew attempts to tunnel. Thus, for $V=+1\text{mV}$, the increased electron concentration may ameliorate the magnetic behavior of the interfacial CrO₂ nanolayer. However, for $V=-1\text{mV}$, the carrier concentration of the CrO₂ nanolayer is only increased due to the actual tunneling current, which is orders of magnitude lower than that carried by metallic

conduction. Thus the magnetic behavior of the junction is poorly defined as shown in the middle panel of Figure 7.7. Indeed, closure of the $V=-1\text{mV}$ loop at negative applied field values occurs at a higher value $H>1000\text{G}$ than for the other $R(H)$ loops.

After several measurements were performed at $V=\pm 10\text{mV}$, $R(H)$ loops were taken at $V=+500\mu\text{V}$ (and then eventually at $V=-500\mu\text{V}$), as negative current was ramped up by way of IV curves. No obvious accidents in the IV curves occurred, yet the ensuing resistances measured at low bias did change as presented in Figure 7.8a. Resistance in the antiparallel state remained fairly constant while that in the parallel state dropped, leading to enhanced TMR values for $I_{Max} \gtrsim 3.6\mu\text{A}$ which reach +50% (see panel (b)). Such a high value of normal TMR for a LSMO/STO/Co-type system - and the limitations of our counterelectrode growth procedure, may only be explained as resulting from the formation of a material with very high spin polarization. The consistency of the above discussion on $\text{CrO}_2/\text{Cr}_2\text{O}_3$ electrochemical considerations, and the half-metallic nature of CrO_2 with majority carriers, supports the picture of a State II defined as LSMO/STO/ Cr_2O_3 / CrO_2 /CoCr with normal TMR of unusually large amplitude. Again, as discussed in Section 7.1.2.1, the higher amplitude of TMR could result from a shift of the junction interface away from STO surface contaminants during sample preparation.

While in this State II of high quality, the sign of applied bias was changed from $V=+500\mu\text{V}$ to $V=-500\mu\text{V}$ with an intent to gain more information about the magnetic state of the STO/CoCr interface as argued above (see Figure 7.8). As illustrated in Figure 7.8, upon increasing the forming current, the antiparallel resistance and TMR amplitudes between $R(H)$ loops taken at $V=\pm 500\mu\text{V}$ are similar. We conclude that it is thus relevant to compare the two sets of data.

The trend of synthesizing States I and II in junctions A, B and C has thus far been to respectively apply positive and negative currents of low amplitude. Electrochemical arguments have mainly centered around oxygen, but Cr may also be taken into account. The fact that these species migrate in opposite directions of applied bias; coupled with the location of the Cr and O sources on either side of the STO/CoCr interface, and the strong reactivity of Cr with O; leads to a *chemical sharpening* of the Cr_2O_3 interfacial layer with little to no CrO_2 for positive applied biases. The resulting State I with inverse TMR may then be ascribed to an effective LSMO/STO/ Cr_2O_3 /CoCr junction. Similarly, negative bias values will promote a *chemical blurring* of the Cr_2O_3 interfacial layer as oxygen electromigrates toward CoCr while Cr diffuses toward STO, leading to a reduced CrO_2 nanolayer at the interface with CoCr. The resulting State II with normal TMR may then be ascribed

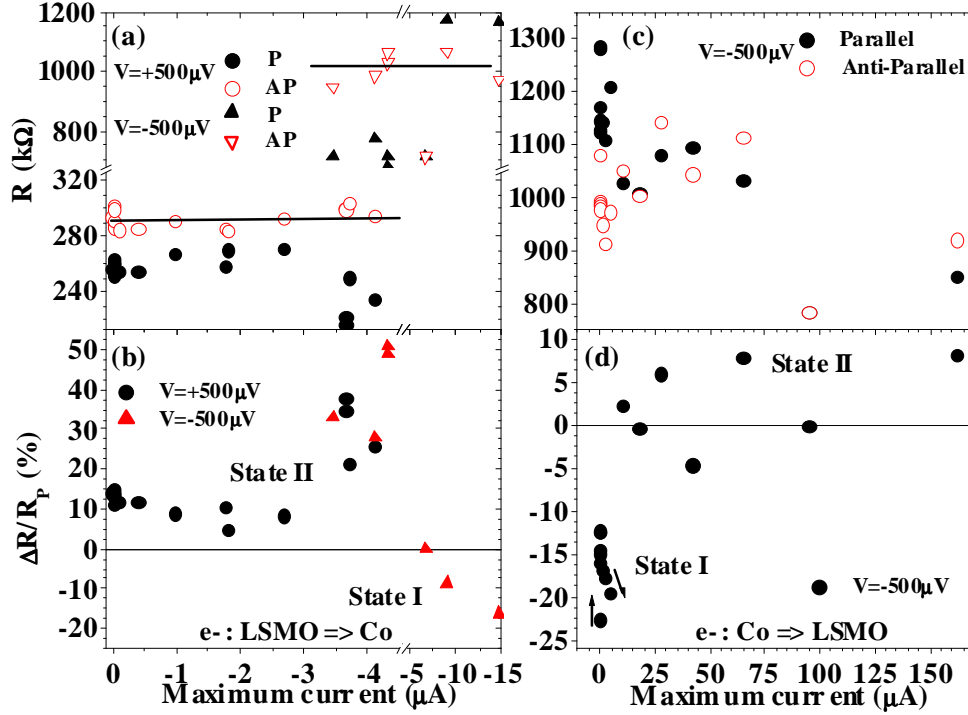


Figure 7.8: Sample C: LSMO/STO/CoCr₈₀Cr₂₀ junction of area 12 μm². Evolution of junction resistances R_P and R_{AP} taken at $V = \pm 500 \mu\text{V}$ just after negative (a), then positive (c) forming currents. Panels (b) and (d) present the associated TMR values.

to an effective LSMO/STO/Cr₂O₃/CrO₂/CoCr junction. The success, for this latter case, in reducing Cr₂O₃ to CrO₂ while Cr electromigration from the CoCr source toward the Cr₂O₃ layer, lies in the larger electromigration rates of O compared to Cr. This is due, at least qualitatively, to the larger ionic radius of O.

Nevertheless, State I may be obtained from State II given a further increase in negative current amplitude. In this higher range of barrier-applied electric field values, other species at the STO/CoCr interface with a higher enthalpy of oxide formation, such as Co may participate in the electromigration process. Oxygen may further diffuse into the CoCr electrode, yielding Co oxides such as CoO or CoCr₂O₄. The effective junction interface becomes one between CoCr and a set of insulating oxides such as CoO or CoCr₂O₄, then Cr₂O₃ before the STO and LSMO nominal oxide layers. Since all these barriers may efficiently transmit d-character electrons (see Section A.1), so as to reflect the d-band spin polarization of the counterelectrode, the synthesis of such a junction interface would lead to an inverse TMR as in State I,

though with a much larger resistance owing to the extended barrier thickness. This is indeed what is observed in panels (a) and (b) as negative current is increased from ~ 5 to $15 \mu\text{A}$.

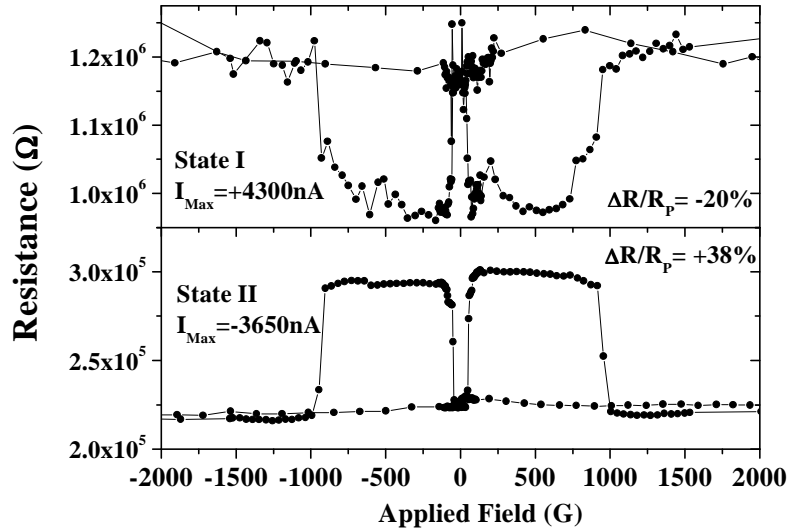


Figure 7.9: Sample C: LSMO/STO/CoCr₈₀Cr₂₀ junction of area $12 \mu\text{m}^2$. R(H) loops at $V = +500 \mu\text{V}$ in junction States I and II.

The oxidation of Co or a Co alloy described above represents a form of relative electrochemical irreversibility given the low reactivity of Co with O. Therefore, large electric fields - as represented by the maximum tunneling current amplitude, will be required to reduce any Co oxides. As shown in panels (c) and (d) of Figure 7.8, positive currents one order of magnitude larger were required to switch the junction from State I to State II. The larger resistance of this final State II compared to that presented in panel (a) further illustrates the irreversibility considerations presented above. The key to reversibility lies in limiting the number of electrochemical reactions present given the applied electric field used to generate the State change. This may be achieved by working below the electrochemical threshold of the second-most reactive species. Figure 7.9 presents the most stable, symmetric R(H) loops representative of States I & II with high TMR which were obtained during the course of studying junction C. As noted the maximum currents used to obtain these States are not at the extreme end of the current range studied. As negative current was increased beyond this State II, though the TMR did increase, the junction also developed a high-field MR indicative of a newly-formed magnetic anisotropy, possibly resulting from the first stages of Co oxidation throughout the interface area. Also, the magnetic behavior of

the junction improved as the junction in State I was subjected to increasing positive currents (panels (c) and (d) of Figure 7.8). It is possible that in this range of applied electric fields only oxygen electromigration is activated, with a tendency to reduce any CoO. No reliable bias dependence of TMR could be obtained to confirm or infirm these spin-dependent characteristics of the magnetic tunnel junction.

7.1.3 Summary

The magnetotransport investigation of LSMO/STO/CoCr and LSMO/STO/ALO/CoCr junctions was originally motivated by the intent to confirm the density of states interpretation of the TMR bias dependence in LSMO/STO/Co junctions. A controlled spin-dependent modification of the Co density of states through Cr doping was aimed at changing this bias dependence in an expected way. To a large extent, the results obtained corroborate this interpretation. The inverse TMR peak, attributed to a Co density of states feature, was shown to shift toward lower bias positions with increasing Cr concentration due to the effect of Cr doping on the d-band density of states at the STO/CoCr interface. A complementary trend was observed in the case of the ALO/CoCr interface.

However, all junctions processed from samples with CoCr counterelectrodes exhibited electrical instabilities that led to changes in the junction's resistance and magnetotransport response at low applied bias. The low enthalpy of Cr oxide formation was argued to account for this instability. Notably, the possible presence of antiferromagnetic materials composing the effective STO/CoCr interface could in turn explain the collapse of the inverse TMR peak with increasing Cr concentration. This idea was strengthened by Transmission Electron Microscopy and Electron Energy Loss Spectroscopy experiments on one sample which displayed the presence of a segregated Cr oxide at the STO/Co₈₄Cr₁₆ interface. This evidence naturally led to a reexamination of such experiments in an electromigration picture.

The forming experiments on LSMO/STO/CoCr presented above underscore the complex chemical state of such junctions prepared through an exposure to air of the STO surface before transition metal counterelectrode deposition. While for a conventional Co counterelectrode, the high enthalpy of Co oxide formation leads to a weakened influence of interfacial contaminants, introducing Cr leads, through segregation toward and reaction with contaminants, to a more complex interface. The low enthalpy of Cr oxide formation enables the electromigration process of both oxygen and chromium species to promote in a *controlled* manner an effective metal/barrier interface with opposite signs, though consequent amplitudes, of spin polarization

as probed by the half-metallic LSMO electrode. To our knowledge, these experiments represent the first reported case of such dramatic tailoring of a junction's magnetotransport response through electromigration effects. Additional work needs to be undertaken to more completely understand the microscopic transformations that the junction undergoes through this process. Such work would help address issues with possible electrochemical changes in effective barrier thicknesses and active areas (*e.g.* pinholes in the barrier), which these experiments have not come to terms with. A more comprehensive understanding of this effect should allow the harnessing of an otherwise cumbersome feature in oxide-based magnetic tunnel junctions toward device considerations. Eventually, it would be interesting to witness such electromigration effects on biased sample slices visualized through Transmission Electron Microscopy.

7.2 Interface profile & Fowler-Nordheim tunneling in $\text{La}_{0.7}\text{Sr}_{0.3}\text{MnO}_3 / \text{SrTiO}_3 / \text{La}_{0.7}\text{Sr}_{0.3}\text{MnO}_3$ junctions

In Section 4.1.1, we presented magnetotransport results on a $\text{La}_{0.7}\text{Sr}_{0.3}\text{MnO}_3 / \text{SrTiO}_3 / \text{La}_{0.7}\text{Sr}_{0.3}\text{MnO}_3$ junction (Junction A) which exhibited over 1800% at $V=1\text{mV}$ and $T=4\text{K}$. In Section 5.1 we presented bias-dependent data from Junctions B& C to illustrate the spectroscopic nature of spin-dependent tunneling between ferromagnets. This Section presents a comprehensive dataset on Junction C of area $12\mu\text{m}^2$. Due to difficulties in maintaining an antiparallel alignment, AP data up to only 70K will be shown. Changes to the barrier profile thanks to junction forming are performed through a cooldown sequence while applying a bias $|V_{Desc}|$ which was varied between 10mV and 3V.

7.2.1 Introduction

Figure 7.10 presents an overview of junction C's magnetotransport properties for an applied bias during cooldown $V_{Desc}=+10\text{mV}$. In similar fashion to junction B, the TMR bias dependence, shown in panel (a), exhibits a large decrease at low bias which spans the bias extent of the zero-bias conductance anomaly (see panel (a)). A much more moderate decrease then ensues. Past an inflection point at $V \approx \pm 0.3\text{V}$, the TMR decreases again. As temperature is increased from $T=4\text{K}$ to $T=70\text{K}$, the slope of this plateau increases, due to mixing of the two spin-dependent conduction channels which blurs the

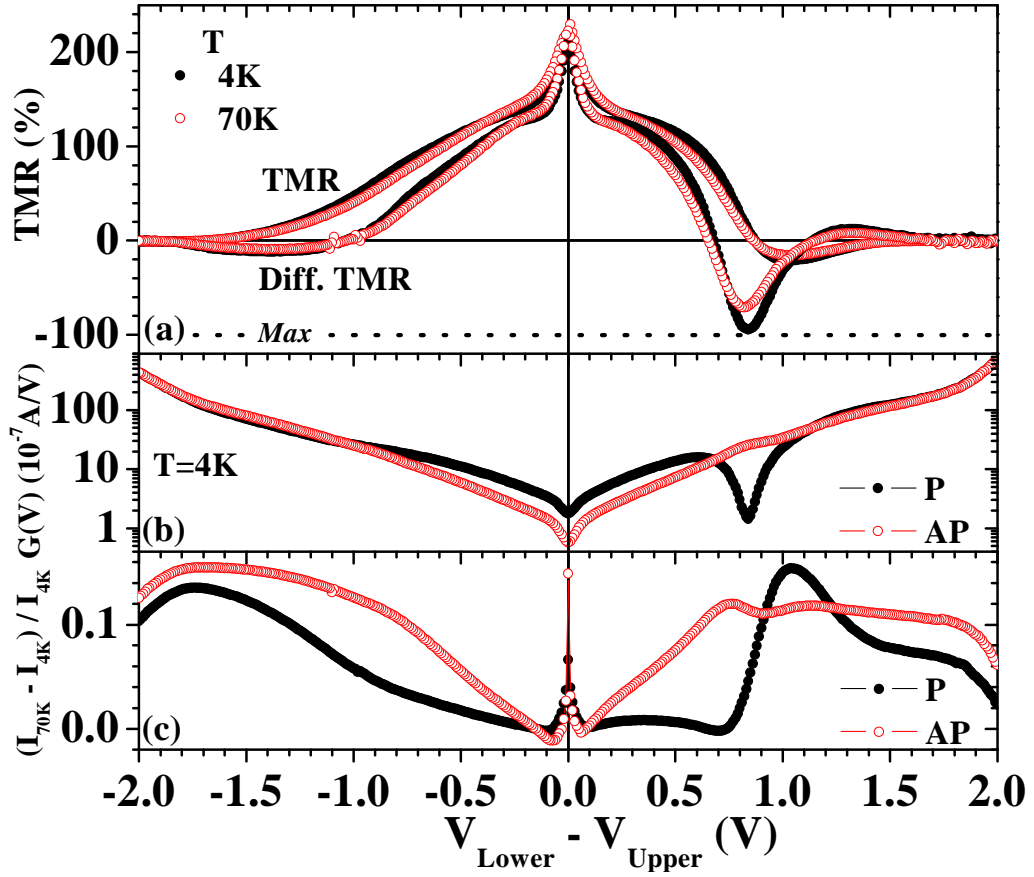


Figure 7.10: LSMO/STO/LSMO, Junction C: Magnetotransport properties for $V_{Desc}=+10\text{mV}$. (a) Bias dependence of TMR (calculated from $I(V)$, in closed circles) at $T=4\text{K}$, and differential TMR ($dI(V)/dV$; open circles) at $T=4\text{K}$ and $T=70\text{K}$. (b) Conductances ($\equiv dI/dV$) in the parallel (P) and antiparallel (AP) states at $T=4\text{K}$. (c) Evolution of IVs in the parallel (P) and antiparallel (AP) states at $T=70\text{K}$ relative to $T=4\text{K}$. Diff TMR $\equiv (dI_P/dV - dI_{AP}/dV)/dI_{AP}/dV$

spin-polarized LSMO minority gap feature (see associated diff. TMR). Beyond the minority gap, the bias dependence of TMR at positive and negative bias begin to differ significantly. We will argue that this difference reflects dissimilarities between the two LSMO/STO interfaces, such as stoichiometric considerations, chemical sharpness and spatial extent of the potential step. We will focus the remainder of this overview on positive data since it presents the most remarkable properties. Nevertheless, these features find their equivalent at negative biases, albeit at different values and with differing amplitude. It is important to note the resiliency of this junction under

voltage stress, as illustrated by the overlap of data as bias is smoothly swept through the entire bias range explored in this dataset up to $|V|=2V$.

Beyond $V=+0.6V$, a strongly spin-polarized feature appears in the unoccupied DOS of the lower electrode, as characterized by the sharp conductance drop in the parallel channel. As reflected by the differential $TMR \equiv (G_P - G_{AP})/G_{AP}$, this feature is almost fully spin-polarized. At the origin of the quickened decrease in TMR past this bias value, this dramatic decrease in spin \uparrow DOS reflects, as argued in Section 5.1.4, a splitting of the $e_g \uparrow$ manifold due to tetragonal distortions induced by oxygen non-stoichiometry (see Sections A.4.3 & A.4.5). Our experiment also shows how this pseudogap in the spin \uparrow DOS is probed by a nearly fully spin-polarized current.

Barrier profile effects also play an important role in affecting the magnetotransport properties of the LSMO/STO/LSMO junctions. As reflected by both panels (b) and (c) of Figure 7.10, spin-independent features at $V \approx \pm 1.8V$ lead to a large conductance increase and produce a peak in the relative evolution of junction current with temperature. We attribute these features to the interfacial hole barrier heights. Although only somewhat evident from this magnetotransport overview, a similar spin-independent feature lies at $V=+1.1V$. We attribute it to the electron barrier height at the lower interface. Exceeding this electron barrier height results in an oscillation of differential TMR near $V=+1.3V$.

We now present and discuss data in terms of these general conclusions regarding magnetotransport in the LSMO/STO/LSMO system. In particular, in Section 7.2.2 we make use of oxygen electromigration considerations introduced in Section 3.3.2.3 which, as demonstrated in Section 7.3.3, arise through the cooldown of a junction while applying a bias V_{Desc} , and affect the barrier potential profile through doping changes in oxygenation (see Section A.2.3). Section 7.2.3 examines the incidence of these salient features in the junction's potential landscape on magnetotransport. Finally, Sections 7.2.4 % above ϕ_{MIEC} examine magnetotransport in the Fowler-Nordheim regime of tunneling above barrier heights from quantum well state and magnetic interlayer exchange coupling pictures, respectively.

7.2.2 Barrier heights & magnetotransport trends

As illustrated in Figure 7.11, the manganite's DOS pseudogap feature results in an inversion of TMR which reaches -20%. Beyond the pseudogap, the TMR exhibits a series of sign inversions. This TMR oscillation is highly reproducible as attested by the $R(H)$ loops presented for several values of applied bias. Notably, even at $V=+3V$, resistance has only decreased to $8k\Omega$.

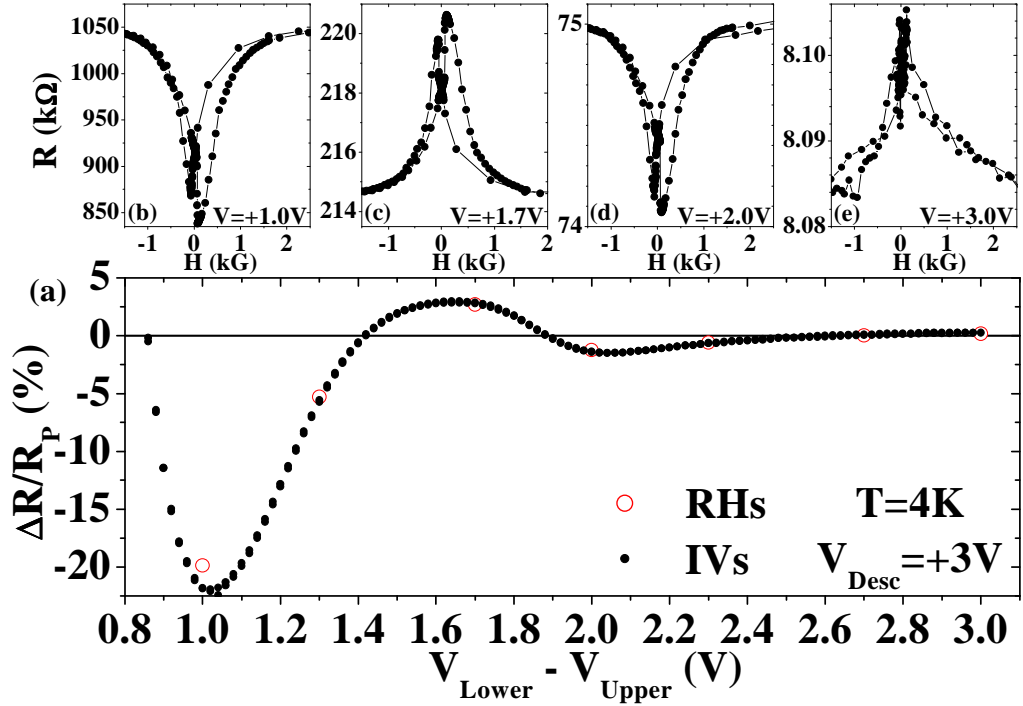


Figure 7.11: LSMO/STO/LSMO, Junction C in $V_{\text{Desc}}=+3\text{V}$ state: (a) bias dependence of TMR at $T=10\text{K}$ from IV data, confirmed by $R(H)$ loops at (b) $V=+1\text{V}$, (c) $V=+1.7\text{V}$, (d) $V=+2\text{V}$, and (e) $V=+3\text{V}$.

Since this resistance value remains about one order of magnitude larger than that of our lower electrode at this temperature, no current crowding effects are at play here to falsify the amplitude of TMR. [115]

To understand this oscillatory response of magnetotransport, a careful evaluation of junction barrier heights is necessary. We first focus on the more salient magnetotransport results obtained after cooldown at $V_{\text{Desc}}=+3\text{V}$. Figure 7.12 presents a comparison between junction conductance (panel (a)), the temperature evolution of bias-dependent junction current (panel (b)), and the bias dependence of TMR and differential TMR⁷ (panel (c)). The large increase in overlapping junction conductances in the parallel (P) and antiparallel (AP) states at $V \approx +1.6\text{V}$ and $V \approx -1.4\text{V}$ mark the onset of the hole barrier heights Φ_U^h & Φ_L^h at the upper and lower LSMO/STO interfaces, respectively. The position of these barrier heights are confirmed by the spin-independent peaks at those values in the temperature evolution of junction

⁷As is the case throughout this Thesis, MR is measured relative to the parallel configuration. Positive MR may therefore be infinite, while inverse MR may reach -100%.

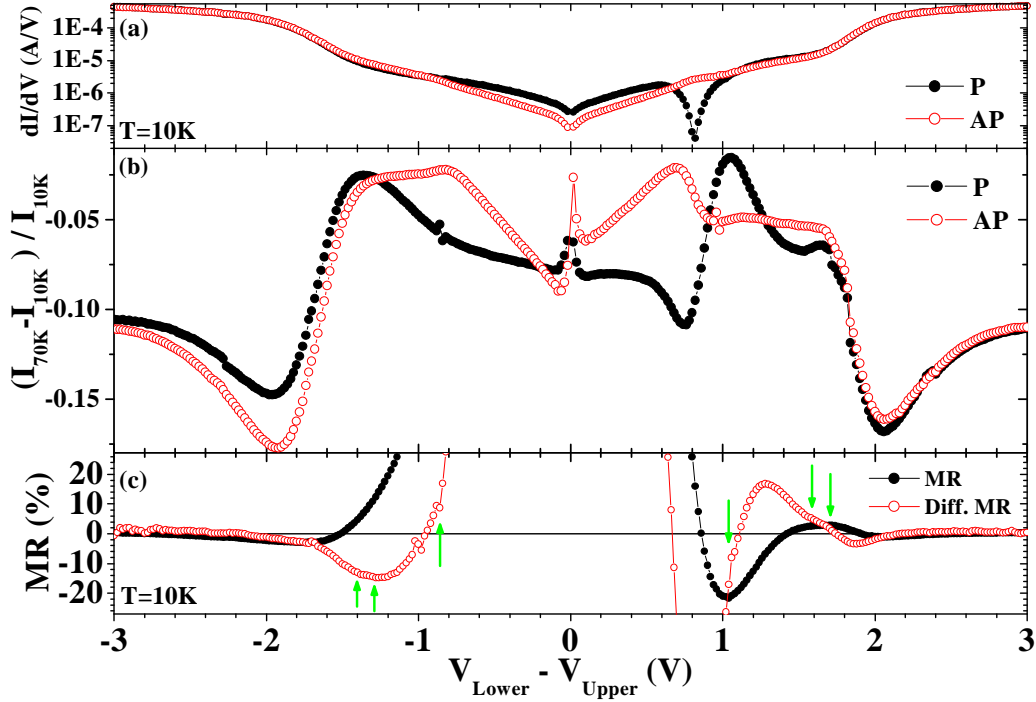


Figure 7.12: LSMO/STO/LSMO, Junction C in $V_{\text{Desc}}=+3\text{V}$ state: (a) conductance at $T=10\text{K}$ in the parallel (P) and antiparallel (AP) configurations. (b) Temperature evolution of IVs in the P and AP configurations between 10K and 70K. (c) Closeup at low amplitude of the bias dependence of TMR and differential TMR. $\text{Diff TMR} \equiv (dI_P/dV - dI_{AP}/dV) / dI_{AP}/dV$

current.

The consequence of exceeding the electron barrier heights is also reflected in panel (b), although not as strikingly as for the hole barrier heights. We suppose that this reflects the hole-limited nature of transport in LSMO. We may assign the lower electron barrier height Φ_L^e to a spin-independent peak at $V \approx +1.05\text{V}$ in panel (b).⁸ The value of the upper electron barrier height $\Phi_U^e \approx 0.9\text{eV}$ may be deduced from the other three barrier height values assuming a constant STO band gap throughout the barrier.

As discussed by Wolf, [50] and more recently by Montaigne *et al.*, [21] exceeding a tunneling barrier height will lead to wavefunction interference

⁸The $\sim 50\text{mV}$ separation between peak positions in the P and AP configurations reflects the slight error made by using these bias-convoluted measurements as a spectroscopic tool. Nevertheless, the pseudogap feature at $E - E_F \approx 0.8\text{eV}$, which decreases in amplitude with rising temperature, masks this subtle feature entirely, so that resorting to equivalent conductance data is not an option.

effects which alter the junction's magnetotransport response. The effect of reaching these barrier heights on magnetotransport is most clear in the differential MR as it does not convolute the effect over applied bias in the way that TMR does. Indeed, reaching $\Phi_U^h \approx 1.6\text{eV}$ results in a clear change in the oscillation of differential TMR at $V=+1.6\text{V}$. A similar break in the differential TMR trend occurs at $V=-1.4\text{V}$ at Φ_L^h (see following Figures for more compelling closeups of same data). A careful examination of the trend of differential TMR near the barrier-attributed peaks in the temperature-relative IV curves of panel (b) reveal the presence of not one but a pair of kinks in the curve. For instance, the peak at $V \approx +1.6\text{V}$ is associated with kinks in the differential TMR at $V=+1.52\text{V}$ and $V=+1.68\text{V}$. We surmise that this reflects the *sharpness* of the interfacial profile. To be consistent we will attribute an average value 1.6eV to the onset of this upper hole barrier height. Similarly, kinks at -1.29V and -1.40V circumscribe the onset of Φ_L^h , which we peg at -1.35eV .

	V_{Desc}	+10mV	+3V	-3V
Lower Interface	Electron 1 (V)	+0.98	+0.94	+1.01
	Electron 2 (V)		+1.06	
	Hole 1 (V)	-1.86	-1.29	-1.45
	Hole 2 (V)		-1.4	
	Average Φ_L^e	0.98	1.0	1.01
	Average Φ_L^h	1.86	1.35	1.45
	STO band gap E_g (eV)	2.84	2.35	2.46
	Φ^e/E_g (%)	34.5	42.5	41
Upper Interface	Electron 1 (V)	-1.09	-0.9	-1.05
	Electron 2 (V)			
	Hole 1 (V)	+1.83	+1.52	+1.45
	Hole 2 (V)		+1.68	
	Average Φ_U^e	1.09	0.9	1.05
	Average Φ_U^h	1.83	1.6	1.45
	STO band gap E_g (eV)	2.82	2.5	2.5
	Φ^e/E_g (%)	38.6	36	42

Table 7.1: LSMO/STO/LSMO, Junction C: Electron and hole barrier heights in $V_{Desc}=+10\text{mV}$ and $V_{Desc}=+3\text{V}$ states. The entry for $V_{Desc}=-3\text{V}$ corresponds to a separate run discussed in Section 7.2.5.

A similar assessment of barrier heights may be performed for the $V_{Desc}=+10\text{mV}$ state, using Figure 7.10 (page 138) and Figure 7.14. The

results are presented in Table 7.1. Notably, we rely on the more precise kinks in differential TMR to obtain averaged values for all barrier heights. Also, the STO band gap of $\approx 2.8\text{eV}$ found for the virgin $V_{Desc}=+10\text{mV}$ state of the 27.3\AA thin film compares very favorably to the bulk 3.2eV STO band gap. As may be expected from the nanoscopic characterization of the lower and upper interfaces in such a structure (see Section B.1), the somewhat different electronic structure at each interface results in the presence or not of a pseudogap, and in differences in the inversion behavior of MR. All quantitative changes may be linked to such differences, yet in many ways both interfaces offer qualitatively similar behavior if we suppose that the upper interface in this particular junction is of higher quality. This could explain how the differential MR plateau at $|V| \sim 0.3\text{V}$ is flatter (see Figure 7.10) when probing this interface with electron spectroscopy at negative applied bias, or how this upper interface probes the pseudogap at the tetragonally distorted manganite at the lower interface for positive applied bias. It may also explain how positive bias values beyond Φ_U^h results in MR oscillations reflecting junction response at an interface of high quality.

The differing values for barrier heights from experiments between one V_{Desc} state and another reveal changes induced by the electric field across the tunneling barrier. The reduction in effective STO band gap may reflect some damage to the barrier induced by the increase in V_{Desc} and maximum applied bias. Assuming the validity of discussing changes in oxygen concentration within the STO barrier given the all-oxide nature of the junction, the increase in V_{Desc} at positive values promotes oxygen electromigration towards the lower interface. Thus, relative to the effective band gap, the Fermi level should rise at the upper interface, and fall at the lower interface. These electromigration considerations of Fermi level changes are confirmed by the electron and hole barrier heights extracted at both interfaces for evolving values of V_{Desc} . As shown in the Table, when going from $V_{Desc}=+10\text{mV}$ to $V_{Desc}=+3\text{V}$, the rise in the Fermi level at the upper interface is reflected by a decrease in the electron barrier height Φ^e 's proportion of the STO band gap E_g from 38.6% to 36%. At the lower interface, the fall in the Fermi level is confirmed by a corresponding increase from 34.5% to 42.5% of the total band gap.

These data all reflect the fact that, for a given interface, $\Phi^e < \Phi^h$, *i.e.* that the Fermi level lie above the midpoint in the band gap. This fact is corroborated by a similar position of the charge neutrality level - which may pin the Fermi level, in the calculated complex band structure of SrTiO_3 (see Figure A.8 on page 236 and accompanying text).

Figure 7.13 summarizes the effect of cooling down at V_{Desc} on junction characteristics by comparing the junction's magnetotransport response to

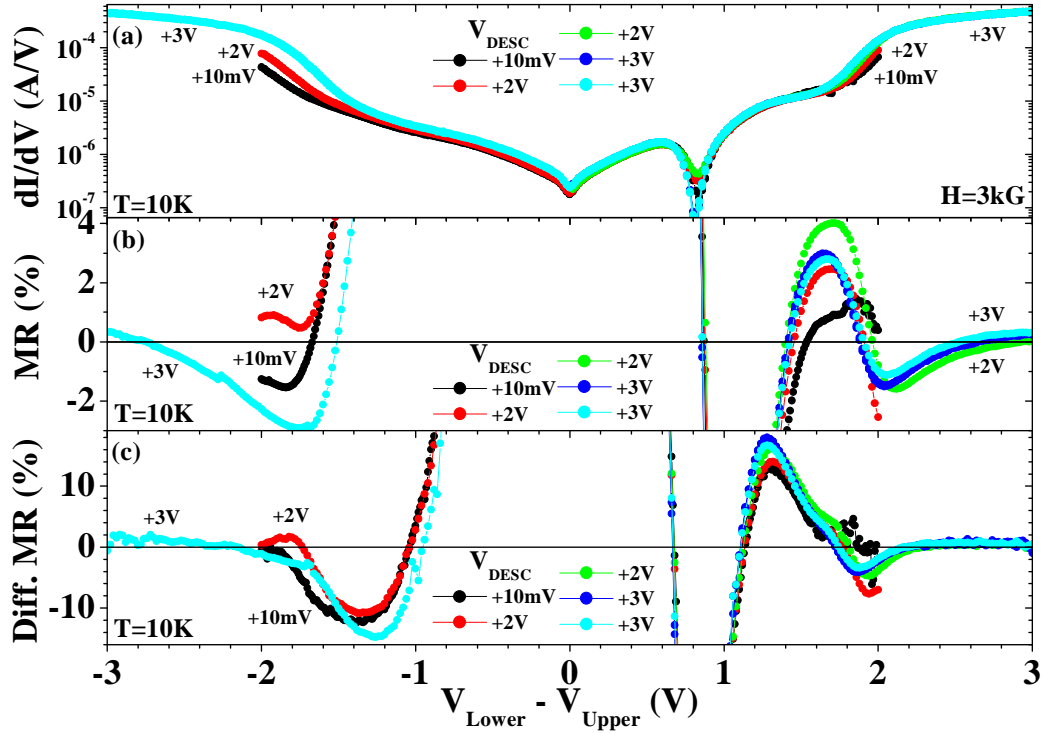


Figure 7.13: LSMO/STO/LSMO, Junction C: Influence of V_{Desc} on (a) junction conductance in the parallel state, and the bias dependence of (b) MR and (c) differential MR.

conductance curves at given V_{Desc} states. As the experiment progressed, states were measured in order of increasing V_{Desc} . The first $V_{Desc}=+2V$ data extended to only $V=\pm 2V$, while the second included $V\rightarrow+3V$. Likewise, first $V_{Desc}=+3V$ data extended to only $V=-2V$, while the second included $V\leftarrow-3V$. Changes in the potential landscape of the junction, evident from comparing conductances and detailed in Table 7.1, lead to changes in the amplitudes and zero-crossing bias positions of TMR and differential TMR. We discuss these changes in Section 7.2.4.

7.2.3 Magnetotransport above barrier heights: temperature dependence

The junction barrier heights affect the temperature dependence of magnetotransport. Figures 7.14 & 7.15 present the temperature evolution of TMR and differential TMR in the $V_{Desc}=+10mV$ and $V_{Desc}=+3V$ states.

Though the magnetotransport response is more salient at positive bias,

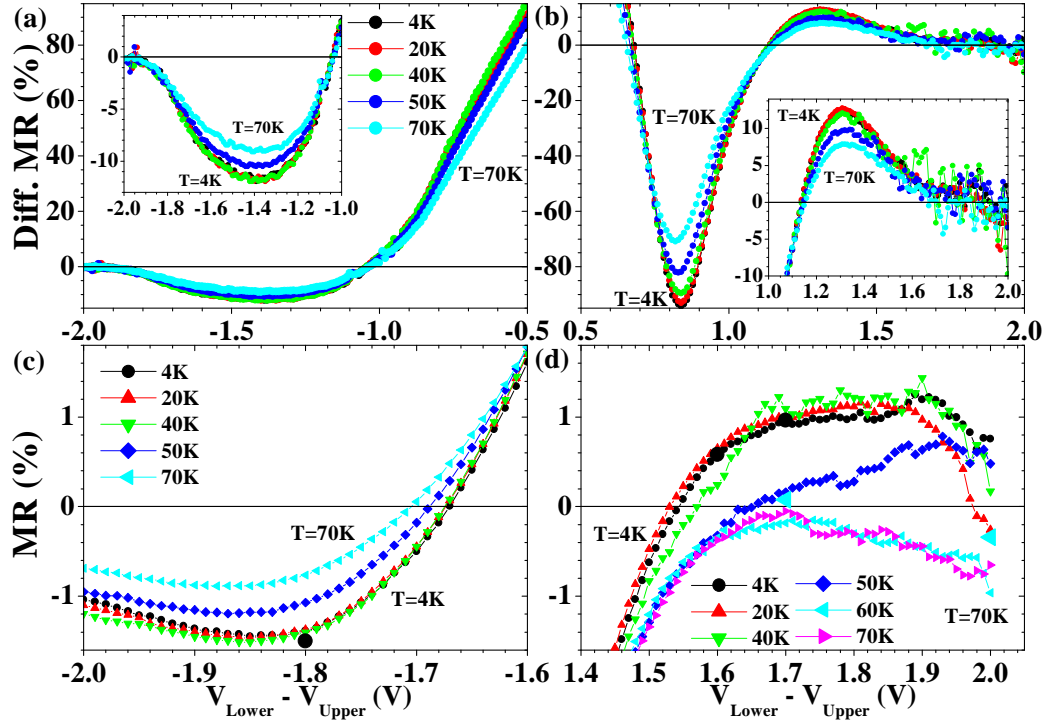


Figure 7.14: LSMO/STO/LSMO, Junction C in the $V_{Desc}=+10\text{mV}$ state: closeups of the bias dependence of differential MR and MR at (a),(c) negative and (b),(d) positive bias values, as temperature is varied between $T=4\text{K}$ and $T=70\text{K}$. The insets provide further closeups. Large symbols correspond to R(H) measurements of TMR.

the following description applies to both bias directions, regardless of the junction's V_{Desc} state. As temperature increases, the sign change of differential TMR does not shift bias position. This may be expected given that the actual barrier heights are unlikely to change in this temperature range. Rather, changes in the effective profile may be appreciated from the bias dependence of TMR, which convolutes the thermal contribution to transport. Thus, near the barrier height, a departure in the TMR trend should be observed. As the electron barrier height is reached, the ensuing TMR oscillation changes period as the zero-amplitude crossing occurs for larger bias values with increasing temperature. This trend increases markedly in going from $T=40\text{K}$ to $T=70\text{K}$. Similarly, the second change in TMR oscillation period due to reaching the hole barrier height is itself affected by temperature, with the zero-amplitude crossing occurring at lower bias values, especially as T is increased from 40K to 70K . An oscillation of differential TMR defined by nodes at these two bias points is observed to decrease in amplitude as

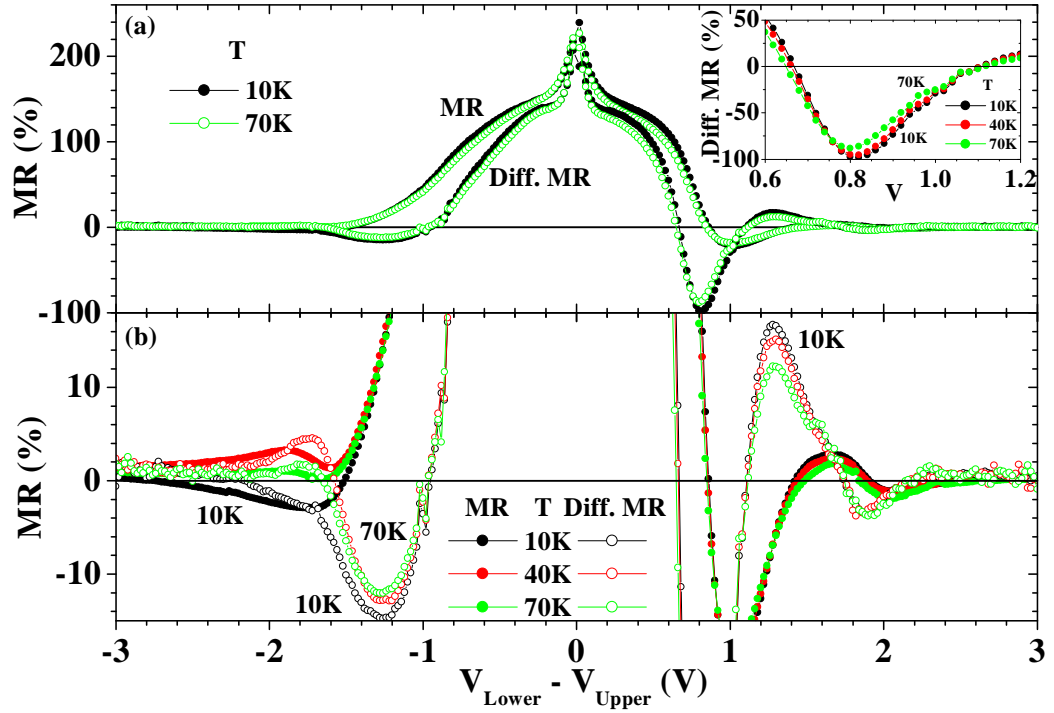


Figure 7.15: LSMO/STO/LSMO, Junction C in $V_{Desc}=+3V$ state: (a) bias dependence of TMR and differential TMR at $T=10K$ and $70K$. The inset to panel (a), and panel (b), are closeups of panel (a) for $T=10K$, $40K$ and $70K$.

temperature is increased past $T=40K$.

7.2.4 Fowler-Nordheim tunneling and quantum well states in the barrier

Upon applying a voltage bias, the electric field across the barrier, which shifts the Fermi levels of the two ferromagnetic electrodes relative to one another, distorts the barrier profile. When the applied bias reaches an interfacial potential barrier height, the Fermi level of the injecting electrode has lined up with the top of the potential step at the collecting interface. Above this potential step lies an electronic band of the insulator. A further increase in bias then injects electrons across an insulating portion of the barrier as well as a metallic portion, toward the collecting electrode. This describes the Fowler-Nordheim tunneling regime, wherein wavefunction reflection at the barrier conduction band/ferromagnet interface leads to interference effects. [21, 50] A similar case may be made of holes with respect to the hole barrier height separating the barrier's Fermi level and valence band. The two cases differ

notably in that this metallic spacer is unoccupied regarding conduction band injection and occupied regarding valence band injection.

The experimental results described above all point to a kink in the trend of differential TMR past either the hole or electron barrier heights, which leads to oscillations of differential MR as well as MR. Many sign changes were observed in what we deem to be a magnetotransport response of high quality thanks to an oftentimes excellent signal-to-noise ratio - in spite of the non dynamic conductance measurements, as well as reasonably large MR amplitudes throughout the oscillatory behavior. In particular, we may distinguish differing periods and damping constants between the oscillations above the electron, and hole, barrier heights, respectively. Qualitatively, this reflects different nesting wavevectors of holes and electrons in SrTiO₃ (001) as well as different effective masses of the two charge carriers.

In this sense transport above a barrier height resembles inserting a non-magnetic layer between the barrier and the ferromagnetic electrode. As illustrated in Figure 2.18 (page 36), introducing a non-magnetic spacer at a tunnel junction interface leads to an oscillation of the TMR sign as quantum well states (QWS) modulate spin-dependent transport. [52,88] Indeed, shifts in the energy position of the QWS occur as the thickness of the spacer which promotes them is varied. Within the physical picture of GMR, AF interlayer coupling occurs when the energy level of the QWS crosses the Fermi level. When applied to a tunneling system, this promotes a magnetotransport oscillation which may result in a sign inversion of MR, and similar decreases in the amplitude of the oscillations with increasing temperature.

The first novelty in our experiment is that the non-magnetic spacer is in fact a portion of the barrier itself, which is of perovskite nature. The material involved, SrTiO₃, satisfies the Fermi surface nesting requirement (see Section A.2.2). Furthermore, evidence of QWS in perovskites has been provided through the observation of magnetic interlayer exchange coupling (MIEC) between La_{0.7}Ba_{0.3}MnO₃ through a LaNiO₃ spacer. [63] MIEC has also been observed through insulating STO layers. [65]

The second novelty in our experiment is that the change in non-magnetic spacer thickness results directly from the bias voltage applied across the barrier. Therefore, the sole parameter of applied bias probes spin-dependent features relative to E_F , yet also controls the spacer thickness, upon which depend the QWS energy levels. As shown in Figure 7.13, oxygen electromigration considerations through V_{Desc} and maximum applied bias offer a separate handle on the evolution of spacer thickness with applied bias by modifying the effective barrier profile. These modifications includes shifts in the Fermi level position within the barrier band gap, changes to the amplitude of this band gap and transformations of the interface sharpness. As

discussed in Section, increasing V_{Desc} leads to a more diffuse potential profile. Figure 7.13 shows how this change also results in an increase in the oscillation periods. The link between these two trends is confirmed theoretically by Montaigne *et al.* (see Figure 2.10 on page 24). [21]

7.2.5 Fowler-Nordheim tunneling and exchange coupling across the barrier

In the introductory Section 2.3.1 and its complement in Appendix C, we described the link between the concepts of quantum well states and oscillations in the magnetic interlayer exchange coupling. As demonstrated in the previous Section, exceeding a tunneling barrier height leads to the formation of quantum well states which modulate the amplitude of TMR. It is therefore natural to expect changes in the magnetic interlayer exchange coupling between the two ferromagnets.

7.2.5.1 Experimental results

Experimental evidence is provided through measurements on Junction C in a separate run. Figure 7.16 presents an introductory assessment of the junction's characteristics for $V_{Desc}=+3V$ and $V_{Desc}=-3V$ states. Comparing to Figure 7.13, one notes that the two $V_{Desc}=+3V$ states possess different barrier heights and interface sharpnesses. This may result from electrostatic effects due to sample handling between runs. A subsequent cooldown sequence at $V_{Desc}=-3V$ appears to modify the junction state back to one resembling the first set of experiments. Indeed, conductance increases are more abrupt. This may reflect possible improvements to the interfaces, as the TMR amplitude doubles to 250% at $V=+10mV$ as found in the first measurement run. Furthermore, the hole barrier heights, as described by the onset of conductance increase, appear to have increased at the upper interface and decreased at the lower interface. This is consistent with a STO doping picture of oxygen electromigration toward the upper interface due to $V_{Desc}=-3V$.

As described previously, these changes in barrier height and interface sharpness modify the oscillation periods of TMR (see Figure 7.17). From the now-standard tryptic comparison in Figure 7.16 between the bias dependencies of junction conductance, temperature-relative current and MR/differential MR, we extract nearly identical values of 1.05eV and 1.45eV for the electron and hole barrier heights at each interface, corresponding to a 2.5eV barrier band gap. These values may be compared in Table 7.1 to those obtained previously.

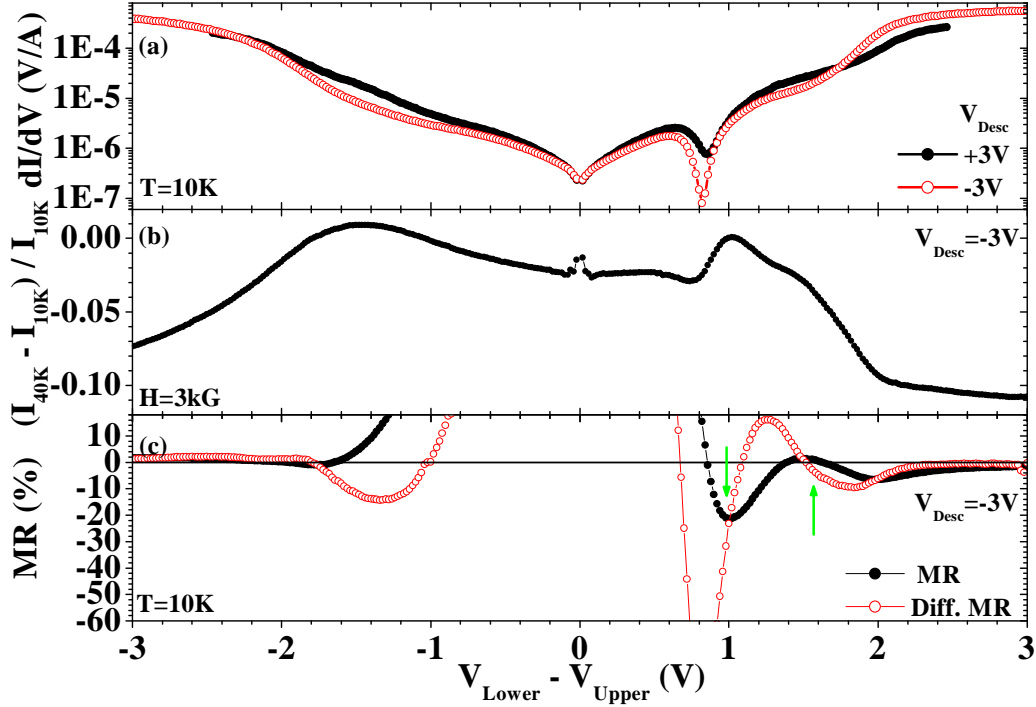


Figure 7.16: LSMO/STO/LSMO, Junction C on a separate run: (a) conductance at $T=10\text{K}$ in the parallel configuration for the $V_{Desc}=+3\text{V}$ states and $V_{Desc}=-3\text{V}$ states. (b) Temperature evolution of IVs in the parallel configuration between 10K and 40K . (c) Closeup at low amplitude of the bias dependence of TMR and differential TMR. Diff TMR $\equiv (dI_P/dV - dI_{AP}/dV)/dI_{AP}/dV$

Figure 7.18 presents the applied field dependence of resistance from $H=6\text{kG}$ to 0 , at negative bias values ranging in amplitude from 0.9V to 2.8V in 0.1V decrements. For purposes of comparison, all curves were normalized to the value found at $H=3\text{kG}$. A linear high-field CMR background was then subtracted so as to flatten all curves at fields beyond $H=5\text{kG}$. As described by the curve at $V=-0.9\text{V}$, as applied field is decreased toward 0 , junction resistance increases from a low state due to a departure from strictly collinear interfacial spins astride the junction barrier.⁹ In general, the extent to which this occurs at high fields qualitatively describes electronic disorder at the LSMO/STO interface.

Changes in this loss of collinearity seem to occur as the electron, then the

⁹This increase at large applied fields does not reflect the amplitude of TMR, which is measured at low field in the AP state contained between the coercive fields of the two ferromagnetic electrodes. See Figure 4.1 pages 71.

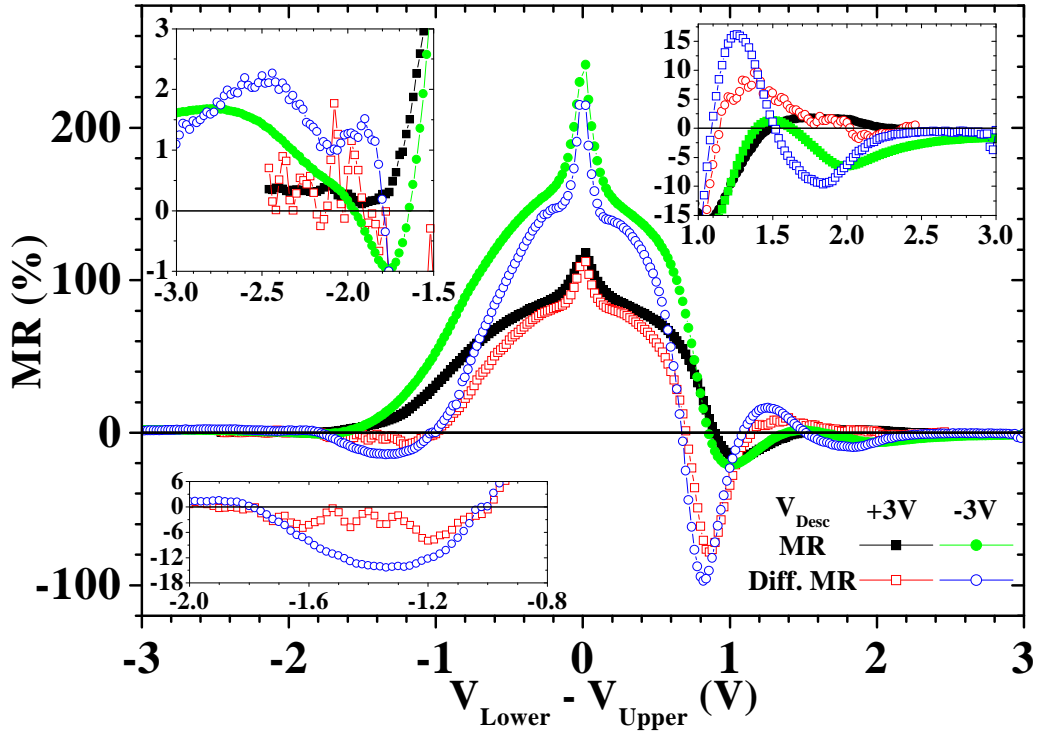


Figure 7.17: LSMO/STO/LSMO, Junction C on a separate run: Bias dependence of TMR and differential TMR in the $V_{Desc}=+3V$ and $V_{Desc}=-3V$ states. The insets represents closeups. An overall legend applies to all graphs.

hole barrier heights Φ_U^e and Φ_L^h are reached and exceeded. Indeed, past $V=-1.05V$, while the MR is still positive, resistance first decreases with decreasing applied field before shooting up. This dip, present at $H\sim 2kG$, increases in amplitude as Φ_U^e is further exceeded. Above Φ_L^h , an opposite trend is observed, as a peak near $H\sim 1kG$ appears, and eventually drives the entire resistance response above the CMR slope. The amplitude of both these effects appears to be itself bias-modulated, though difficult to quantitatively ascertain given the bias resolution of our data. A similar trend at broadly the same values of applied field is noted at positive bias as Φ_L^e , then Φ_U^h , are exceeded (data not shown).

7.2.5.2 Discussion

When the electron barrier height of SrTiO₃ is exceeded through an applied junction bias which distorts the barrier profile, electrons enter the first conduction band. Similarly to the case of LaTiO₃, this electron doping results in metallic behavior. In the strictly parallel state, this Ti spin \uparrow conduction

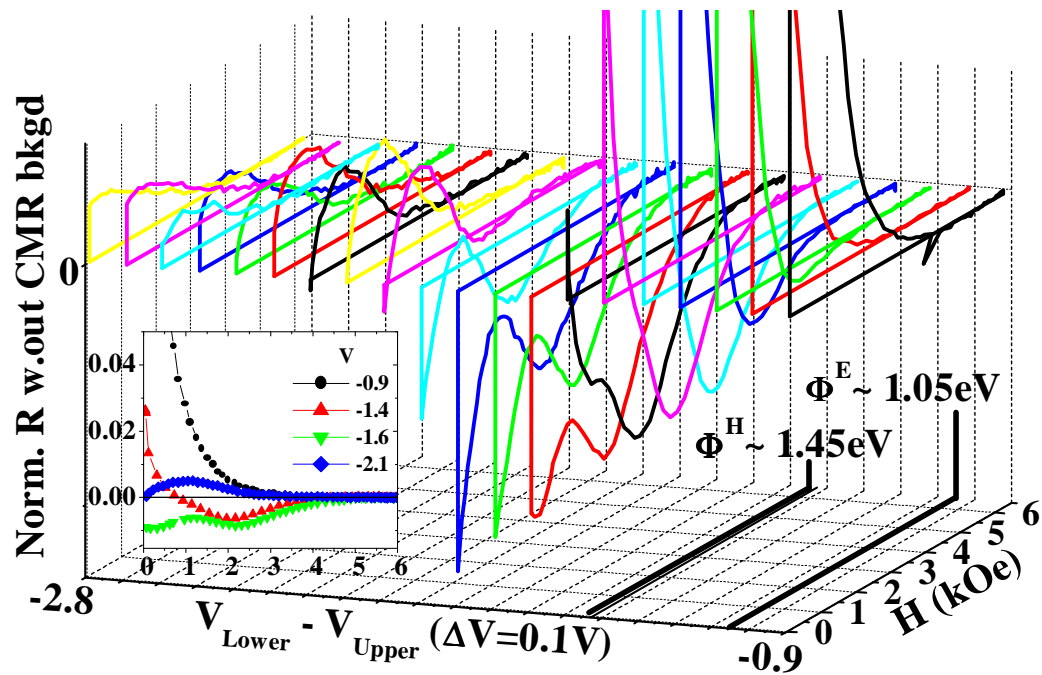


Figure 7.18: LSMO/STO/LSMO, Junction C: Evolution of junction resistance with decreasing applied field for a set of bias values ranging from -0.9V to -2.8V in 0.1V decrements. The inset provides a 2D perspective on remarkable data from this set.

electron injected toward the collecting interface will carry a spin collinear with that on the originating Mn site. In a direct ferromagnetic coupling picture, this enduring parallel state may result from direct ferromagnetic coupling between the Ti $3d^1$ and Mn sites at the collecting interface. Exceeding the hole barrier height in turn destabilizes this mechanism by promoting loss of collinearity at the electron-injecting interface through a reverse effect within the valence band.

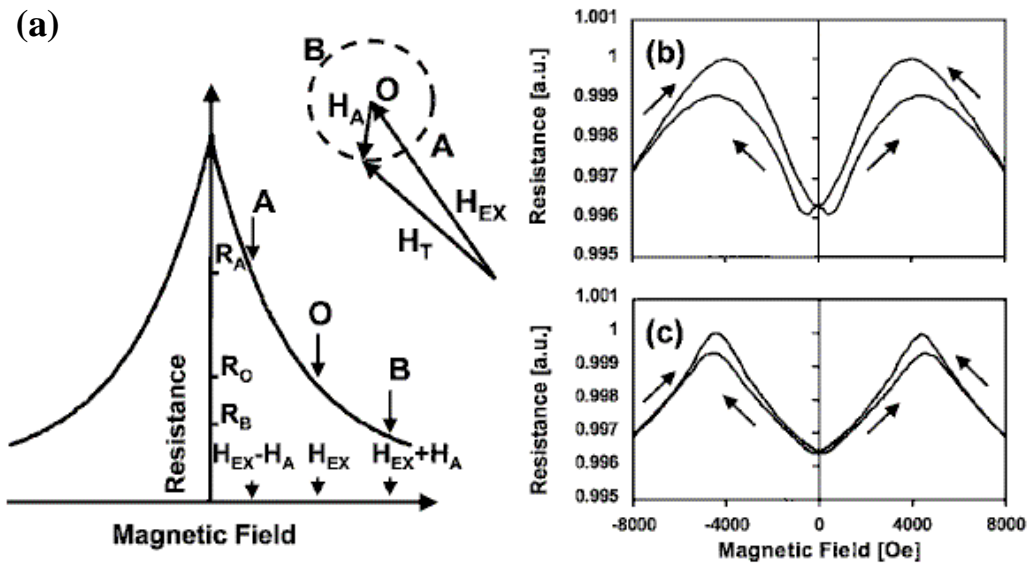


Figure 7.19: (a) A schematic dependence of resistance on magnetic field for an unbiased manganite film due to the CMR effect. The effective magnetic field H_T is the vector sum of the applied field H_A and the exchange field H_{EX} . (b) Experimental and (c) theoretical resistance dependencies on applied field for $\text{La}_{0.7}\text{Ba}_{0.3}\text{MnO}_3/\text{LaNiO}_3$ multilayers with antiferromagnetic exchange coupling. From Krivorotov *et al.* [64]

As recapped in Figure C.2 (page 266), Nikolaev *et al.* of the Dan Dahlberg group (Minneapolis, USA) have shown that varying the thickness of the metallic LaNiO_3 spacer in $\text{La}_{0.7}\text{Ba}_{0.3}\text{MnO}_3/\text{LaNiO}_3$ multilayers modifies the Colossal Magnetoresistance slope due to evolving competition between direct and indirect magnetic coupling between the ferromagnetic manganite layers. [63, 64, 176] Figure 7.19 outlines their model of such interactions. Notably, this model is able to reproduce experimental data on the evolution of multilayer resistance with applied field for a spacer thickness which promotes antiferromagnetic coupling. Of interest is the similar change in collinearity, reflected by the $R(H)$ at large applied field. In their case it is due to the

additional field resulting from interlayer exchange. In our case, we infer that exceeding the barrier heights results in changes to magnetic coupling between the two junction electrodes as the tunneling electrons probe an effective spacer with different electronic properties as per a Fowler-Nordheim picture (see Section 2.3.1). At the time of this writing, we have not tried to apply our results within this quantitative framework.

7.2.6 Summary

We have presented magnetotransport experiments on fully epitaxial magnetic tunnel junctions comprising $\text{La}_{0.7}\text{Sr}_{0.3}\text{MnO}_3$ half-metallic electrodes. Beyond the spin wave excitation regime, electrons impinging on the collecting interface may retain their nearly total spin polarization to probe intrinsic features of the interface. At larger applied bias values effects resulting from the effective energetic profile of the collecting interface come into play. Though quantitatively the two interfaces present different magnetotransport behavior, on a qualitative level the two interfaces are comparable.

To explain our results at large bias, we have introduced the novel concept that the tunneling process, though dominated by the barrier height represented by the closest of the valence and conduction bands to the Fermi level within the barrier, is nevertheless influenced by the other barrier height. At the time of this writing, this concept has not been placed into theoretical perspective. Nevertheless, we base this picture on our reported experimental magnetotransport behavior, which may be understood as the result of sequentially exceeding the electron barrier height of one interface, then the hole barrier height at the other. Importantly, this implies that, since the bias dependence of magnetotransport reflects changes in the energetic profile of the *collecting* interface, that the bias dependence of magnetotransport for a given direction of applied bias will first probe the interface which collects carriers overcoming the lowest barrier height, then the *other* interface once the larger barrier height is exceeded. In the case of a SrTiO_3 barrier, the position of the Fermi level closer to the conduction band implies that first the electron, then the hole barrier heights will be exceeded as applied bias is increased. At this point in our comprehension, it is difficult to explain how exceeding the electron barrier height in LSMO/STO/LSMO junctions does not lead to a sizeable rise in junction conductance, as it is claimed in the case of the hole barrier height. In the spirit of band structure effects in Fe/MgO/Fe heterostructures, this could reflect a wavefunction symmetry mismatch between the Δ_2 conduction band of $\text{La}_{0.7}\text{Sr}_{0.3}\text{MnO}_3$ and the Δ_5 SrTiO_3 conduction band.

The effects of exceeding either the electron or the hole barrier heights were

shown to have repercussions on magnetotransport, in the form of oscillations in the MR and differential MR responses. This behavior was attributed to interference effects within the conduction and valence bands of the barrier in the Fowler-Nordheim regime, leading to the formation of quantum well states. The implied change in the magnetic interlayer exchange coupling between the two ferromagnetic electrodes was also observed. On both of these points, our observations remain, at the time of this writing, only qualitative. In the very near future, it may be possible to apply the model of Krivorotov *et al.* [64] to buttress our claim. In Section 7.3.3.5 we present similar data for the LSMO/STO/Co system.

7.3 On LSMO/STO/Co junctions

The aim of this Section is to illustrate the influence of the effective barrier profile on $\text{La}_{0.7}\text{Sr}_{0.3}\text{MnO}_3/\text{SrTiO}_3/\text{La}_{0.7}\text{Sr}_{0.3}\text{MnO}_3$ junction, discussed in Section 7.2, with magnetotransport results on $\text{La}_{0.7}\text{Sr}_{0.3}\text{MnO}_3/\text{SrTiO}_3/\text{Co}$ junctions. Section 7.3.1 presents another perspective on the original spin-dependent tunneling results on LSMO/STO/Co junction through a comparison with junctions comprising SrTiO_3 barriers of lesser crystalline quality. Section 7.3.2 presents evidence pointing to the interplay of density of states and barrier profile effects in determining the magnetotransport response of such junctions through annealing and forming experiments. Finally, Section 7.3.3 investigates the magnetotransport response of a junction exhibiting electrical instability due to the trilayer deposition process. The resulting reversible electromigration processes enable a controlled study of the bias-dependent magnetotransport response while modifying the effective barrier profile and possibly affecting the interfacial densities of states.

7.3.1 Barrier crystallinity

In previously described experiments on LSMO/STO/LSMO junctions, oscillations in the TMR, leading to possible sign changes, were attributed to exceeding a tunneling barrier height. In addition, it was argued that the origin of this behavior lies with the formation of quantum well states. In that case, the crystallinity of the tunneling barrier should play a capital role. To assess this claim, we measured junctions comprising barriers of poorer crystalline quality.

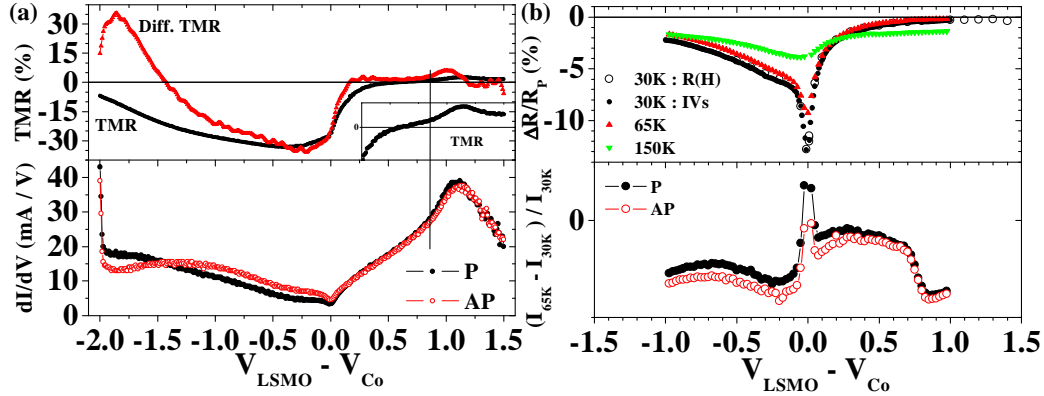


Figure 7.20: Comparison of the magnetotransport behavior between LSMO/STO/Co MTJs with (a) epitaxial and (b) polycrystalline quality. The top of each panel represents the bias dependence of TMR, while the bottom presents information on the tunneling barrier heights. Panel (a): oscillations in the differential TMR of reflect smoothing artifacts; the inset shows a closeup of TMR data.

7.3.1.1 SrTiO₃

Figure 7.20 presents a comparison of magnetotransport behavior between two junctions with similar R·A products; but in panel (a) with an epitaxial barrier grown under standard conditions and (b) with a polycrystalline barrier grown at room temperature instead of 700°C. The amplitude of TMR at low bias, while different by nearly a factor of two, does not impede the comparison since the broad behavior of the epitaxial junction has been reproduced on other junctions yielding much lower TMR amplitudes at low bias. This broad behavior includes the presence of an inverse TMR peak at negative bias, and an eventual TMR sign inversion. When comparing the top and lower graphs of panel (a), and given previous arguments outlined in the case of LSMO/STO/LSMO junctions (*e.g.* Figure 7.12 on page 141 and accompanying text), the change in the trend of TMR and differential TMR, and the ensuing oscillation, may be attributed to exceeding the tunneling barrier height.

Regarding the junction with a barrier of lesser crystalline quality, the tunneling barrier height is shown (bottom graph of panel (b)) to lie at ≈ 0.7 eV at both interfaces. Yet exceeding this barrier height does not promote either a TMR sign change or an oscillation. This comparison confirms the role that constructive wavefunction interference in a Fowler-Nordheim tunneling regime may play in promoting TMR oscillations once the tunneling process

exceeds a barrier height. Nor does the inverse TMR peak at negative applied bias appear. The absence of this feature could reflect the crystalline quality of the Co counter-electrode grown atop the STO barrier.

7.3.1.2 $\text{Ce}_{0.69}\text{La}_{0.31}\text{O}_{1.845}$

Since many aspects of the junction have changed, it is difficult to pinpoint the origins of the differences between the two bias dependencies of TMR. To clarify possible explanations, we propose to compare these results with those found on the $\text{La}_{0.7}\text{Sr}_{0.3}\text{MnO}_3/\text{Ce}_{0.69}\text{La}_{0.31}\text{O}_{1.845}/\text{Co}$ system. The barrier is also epitaxial, but as shown in the TEM picture of Figure 7.21a, the $\text{La}_{0.7}\text{Sr}_{0.3}\text{MnO}_3/\text{Ce}_{0.69}\text{La}_{0.31}\text{O}_{1.845}$ interface is fraught with stacking faults. In this sense comparing $\text{La}_{0.7}\text{Sr}_{0.3}\text{MnO}_3/\text{Ce}_{0.69}\text{La}_{0.31}\text{O}_{1.845}/\text{Co}$ with $\text{La}_{0.7}\text{Sr}_{0.3}\text{MnO}_3/\text{SrTiO}_3/\text{Co}$ results should help distinguish strictly barrier crystallinity effects, to the extent that the spin polarization of $\text{La}_{0.7}\text{Sr}_{0.3}\text{MnO}_3$ isn't drastically affected due to disorder at the barrier interface. This comparison is also interesting since, as argued in Section 4.1.2, both barriers favor the transmission of wavefunctions with a similar electronic character.

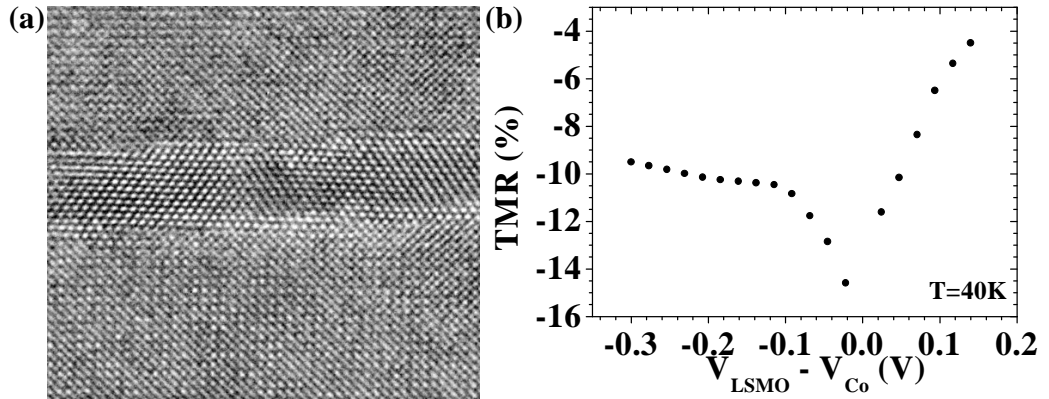


Figure 7.21: The $\text{La}_{0.7}\text{Sr}_{0.3}\text{MnO}_3/\text{Ce}_{0.69}\text{La}_{0.31}\text{O}_{1.845}$ interface: (a) HRTEM picture of a $\text{La}_{0.7}\text{Sr}_{0.3}\text{MnO}_3/\text{Ce}_{0.69}\text{La}_{0.31}\text{O}_{1.845}/\text{La}_{0.7}\text{Sr}_{0.3}\text{MnO}_3$ heterostructure by J.-L. Maurice. (b) Bias dependence of TMR at $T=40\text{K}$ for $\text{La}_{0.7}\text{Sr}_{0.3}\text{MnO}_3/\text{Ce}_{0.69}\text{La}_{0.31}\text{O}_{1.845}/\text{Co}$.

As shown in panel (b), the bias dependence of TMR does not exhibit a peak at $V \neq 0$ either. As per the above arguments, the comparison with results using an epitaxial and polycrystalline SrTiO_3 barrier lends credence to an explanation of the inverse TMR peak in terms of barrier band structure effects.

7.3.2 Annealing and forming effects

The previous Section discussed manganite-based junctions which integrate an oxide barrier and exhibit a good level of stability. However, the chemistry of a stable junction is apt to change under certain conditions. We address in this Section annealing and forming effects on magnetotransport properties of otherwise stable junctions. In the upcoming Section 7.3.3, we explicitly consider forming effects on junctions tailored to exhibit resistance instabilities.

7.3.2.1 Annealing

The high effective spin polarization of transition metals at the interface with oxide tunneling barriers relies on a chemically sharp interface in which the metal composing the barrier is fully oxidized while the transition metal at the interface remains metallic. Thus a common trend in the field of magnetic tunnel junctions is to anneal the junctions before performing transport measurements. This technique relies on differing enthalpies of oxide formation between the barrier material - usually Al, and the transition metal. As shown in Table 3.4, such a technique will favor the further oxidation of the barrier while reducing most transition metal oxides. Sousa *et al.* have studied the effect of annealing at various temperatures on TMR, and found that a temperature of about 500K will result in the highest TMR response. [53,177] Beyond that temperature, intermixing at the interface is presumed to occur as the TMR amplitude drops again.

During the course of this Thesis we have also investigated the effects of junction annealing on the transport properties of our junctions. An overarching reason has been the mediocre magnetotransport response of junctions on some samples. Typically, an annealing cycle involves a 45 minute ramp-up to the required temperature designed to minimize any temperature overshoot to less than 8° for fewer than 10 minutes. Following the annealing cycle at the required temperature for three hours, the junction is cooled to under 80°C over 3-5 hours. Throughout the annealing cycle, the sample is exposed to an oxygen atmosphere.¹⁰ No bias was applied during the annealing cycle.

Figure 7.22 presents the case of annealing a LSMO/STO (8ML)/Co/CoO/Au junction of area $314\mu\text{m}^2$ synthesized using Process I, with an aim to improve magnetotransport properties as discussed by Sousa *et al.*. [53] Panels (a) and (b) present magnetotransport data for the junction in the nominal state after patterning, and after a 3 hour anneal cycle at 210°C, respectively. As shown from IV data taken in the

¹⁰We have concluded that since the sample is encapsulated in Si_3N_4 , the nature of the thermal exchange gas matters little at this stage in the lithography process.

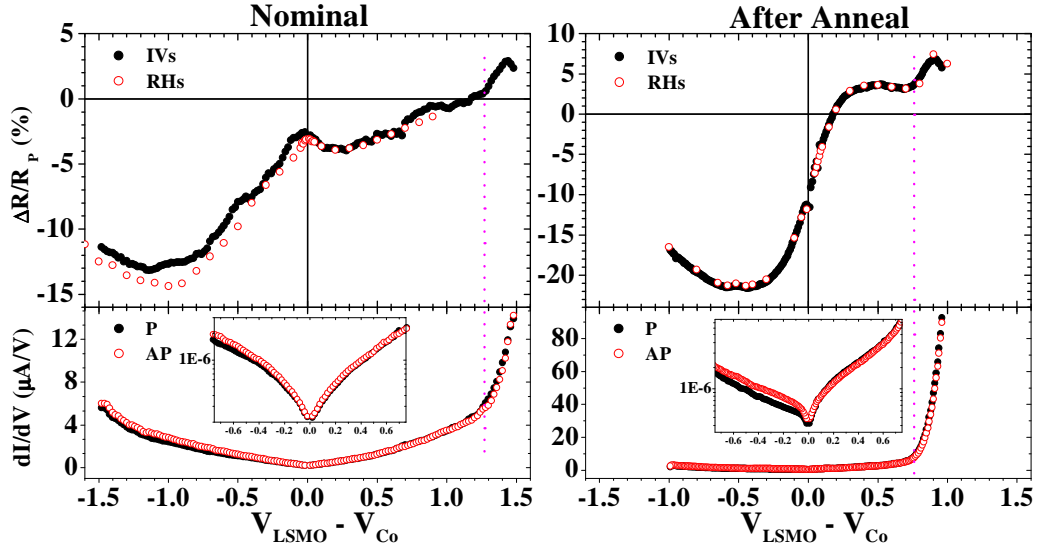


Figure 7.22: Magnetotransport properties at $T=30\text{K}$ of a LSMO/STO/Co junction of area $314\mu\text{m}^2$ (a) after processing and (b) after annealing at $T=210^\circ\text{C}$ for 3 hours. TMR bias dependence (top panel) and conductance curves in the parallel (P) and antiparallel (AP) states (lower panel). The lower-panel insets represent the same data at low bias on a logarithmic scale.

parallel (P) and antiparallel (AP) states, and confirmed by $R(H)$ loops, in the nominal state (panel (a)) the junction exhibits both a depressed TMR (top graph) at low bias and a bias dependence with markedly different features from that usually found in such a junction. As reflected in the inset to the bottom graph, this junction presents a fairly symmetric zero-bias conductance anomaly of quite large bias extent $\sim 0.4\text{V}$. This could result from sizeable spin-dependent scattering at interfaces with poorly defined magnetism.

The magnetotransport properties of the junction improved dramatically after annealing (see Figure 7.22b). Indeed, the low-bias TMR more than doubled as the junction exhibited a bias-dependent TMR response, and a zero-bias conductance anomaly more akin to that expected of the LSMO/STO/Co system (see Figure 2.19). Interestingly, the inverse TMR peak shifted from $\sim -1\text{V}$ in the nominal state to $\sim -0.5\text{V}$ after annealing. In fact, this junction exhibited a rare occurrence of a set of *two* inverse TMR peaks at -0.45V and -0.6V , as reflected by the IV measurements and confirmed by $R(H)$ loops. In the study reported by Oepts, [83] and reproduced in Figure 2.16a (page 33), the occurrence of a double peak involved the oxidation state of Co at the interface with the barrier.

We argue that changes in the oxidation state of both the STO/Co interface and the LSMO/STO oxide bilayer have occurred as the result of annealing. Indeed, the electronic structure of the STO barrier appears to have changed owing to the annealing. As pegged by the sharp rises in junction conductance, the barrier heights are broadly symmetric at the LSMO/STO and STO/Co interfaces with amplitude $\sim 1.3\text{eV}$ in the nominal state, while after annealing the STO/Co hole barrier height is decreased to $\sim 0.8\text{eV}$, while the LSMO/STO hole barrier height still exceeds 1eV . This reduction in the STO/Co hole barrier height and the asymmetry of this STO electronic feature across the thickness of the barrier reflect a likely oxygen migration toward the STO/Co interface (p-type doping of STO; see Section A.2.3). This direction of oxygen electromigration from LSMO to STO may be expected given that LSMO may act as an oxygen reservoir, and given the large enthalpy of STO oxidation. [178]

This change in the barrier profile appears to affect both the position of the inverse TMR peak as well as the onset of the TMR oscillation. The latter, whether before or after annealing corresponds quite well to reaching the tunneling barrier height pinpointed by the large conductance increase. The shift in the inverse TMR peak may be explained by considering how the annealing process sharpened the chemical profile of the interface. This could reflect a reduced Co interface, in which case the inverse TMR peak may be interpreted in a Co DOS manner. However, this interpretation implies the presence of a similar feature in the DOS of a CoO oxide. This observation could also reflect simply a change in the sharpness of the barrier profile as discussed by Montaigne *et al.* [21] This shift in the bias position of the inverse TMR peak is reexamined in Section 7.3.3.

7.3.2.2 Forming

As a precursor to results presented in the upcoming section on electromigration effects on a nominally unstable junction, Figure 7.23 shows the TMR bias dependence at 4K of the $80\mu\text{m}^2$ junction on sample A11531. Magneto-transport results on this junction were presented in Section 5.2. Toward the end of the multi-week study, and after several connections and disconnections from the measurement benches, this junction exhibited resistance instability which led to this hysteresis of TMR bias dependence. As confirmed by $R(H)$ measurements along the bias loop, once the junction has been biased to $+V_{Max}$, the subsequent sweep of successive IV curves in the parallel and antiparallel junction configurations leads to a low TMR inversion point at $\sim +200\text{mV}$ and a large inverse TMR peak position at $V \sim -300\text{mV}$. In contrast, starting from $-V_{Max}$, the subsequent sweep of successive IV curves in the par-

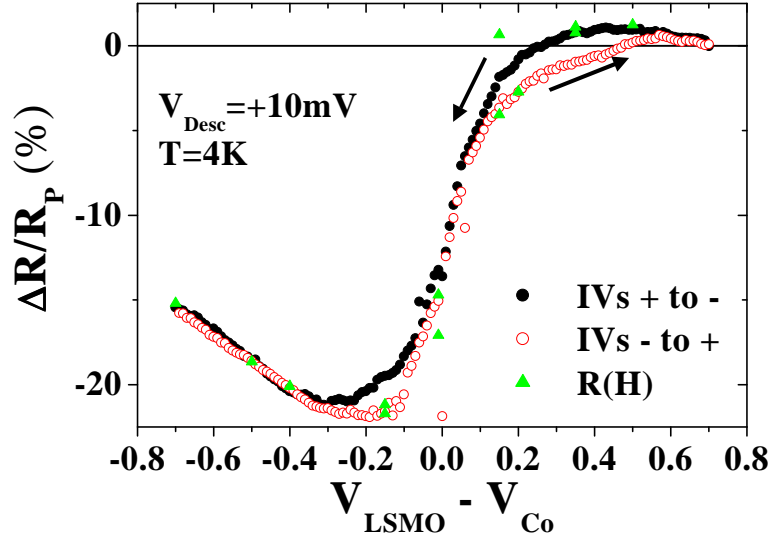


Figure 7.23: Bias dependence of TMR for a $80\mu\text{m}^2$ LSMO/STO/Co junction (Al1531) at $T=4\text{K}$, starting from $+700\text{mV}$ toward -700mV (closed circles), and in reverse (open circles). The hysteresis is confirmed by $R(H)$ loops (triangles).

allel and antiparallel junction configurations leads to a low inverse TMR peak (at $V \sim -150\text{mV}$) and a large TMR inversion point (at $\sim +450\text{mV}$).¹¹ Along with results presented above on junction annealing, these forming-induced shifts in the positions of the inverse TMR peak and TMR sign change in the bias dependence of TMR in LSMO/STO/Co junctions definitely involve changes to the junction's chemistry.

7.3.3 Electromigration effects

This Section presents magnetotransport results on a LSMO/STO/Co junction patterned from a trilayer grown with an added step. In an attempt to eliminate any contaminants adsorbed onto the SrTiO_3 surface during sample transfer in a N_2 or O_2 environment, as well as air, from the PLD chamber to the sputtering system, a light O_2 plasma etch of the SrTiO_3 surface was performed *in-situ* just before the Co counterelectrode was deposited. Through a standard etch of the Co surface, we thereafter obtain a 25\AA -thick CoO layer. As shown in Figure 7.24, magnetization reversal is symmetric at room temperature, and exhibits an exchange bias response at $T=20\text{K}$ from the

¹¹Only two IV measurements in the P and AP states with positive and negative sweeps from V_{Max} were used to obtain this full set of data.

CoO-pinned Co layer. Magnetotransport data discussed in this Section were measured on one representative junction patterned using Process II of area $314\mu\text{m}^2$.

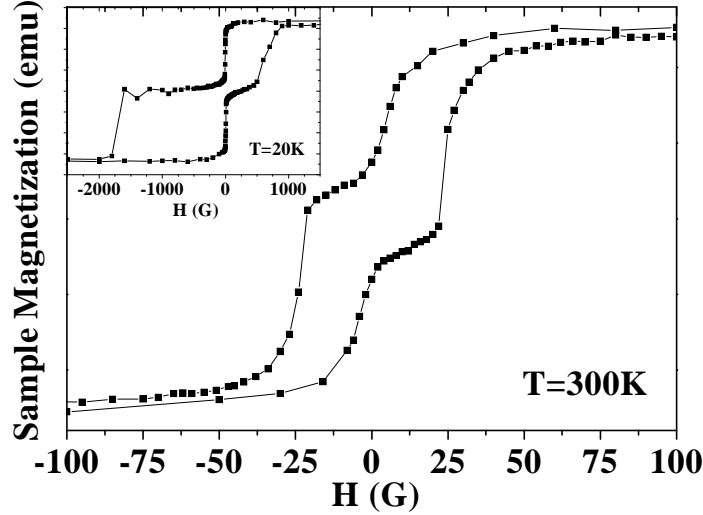


Figure 7.24: Magnetization loops of the as-synthesized $\text{La}_{0.7}\text{Sr}_{0.3}\text{MnO}_3$ (350Å)/ SrTiO_3 (7ML) + O_2 etch / Co (125Å) / CoO (25Å) / Au (150Å) heterostructure (Al1597). While symmetric at $T=300\text{K}$, the shifted Co coercive fields reflect the exchange bias of that layer with CoO at $T=20\text{K}$ after field-cooling in $H=1\text{kG}$.

7.3.3.1 Resistance instability & state preparation

Initial magnetotransport measurements at $T=290\text{K}$, which showed a junction TMR of -2% at low bias, reaching -4% at -200mV, uncovered an obvious resistance creep effect illustrated in Figure 7.25 for a reasonably low bias value of $\pm 100\text{mV}$, which we have not encountered in junctions without the barrier etch step. A set of 6 $R(H)$ loops at $V=+100\text{mV}$ were taken in succession after a 200 minute waiting period at that bias (panel (a)). Thus, even in the steady state, such a junction exhibits resistance creep resulting from magnetic field-cycling. Taken immediately afterwards, the data in panels (b), (c) and (d) illustrates both the correlation between the direction of resistance creep and the direction of applied bias, as well as the dependence of field-cycle-induced resistance creep on time spent at the prescribed bias value prior to measurement (panel (e)). Care must therefore be taken to stabilize a junction state before temperature cooldown (panel (f)). A positive sign of

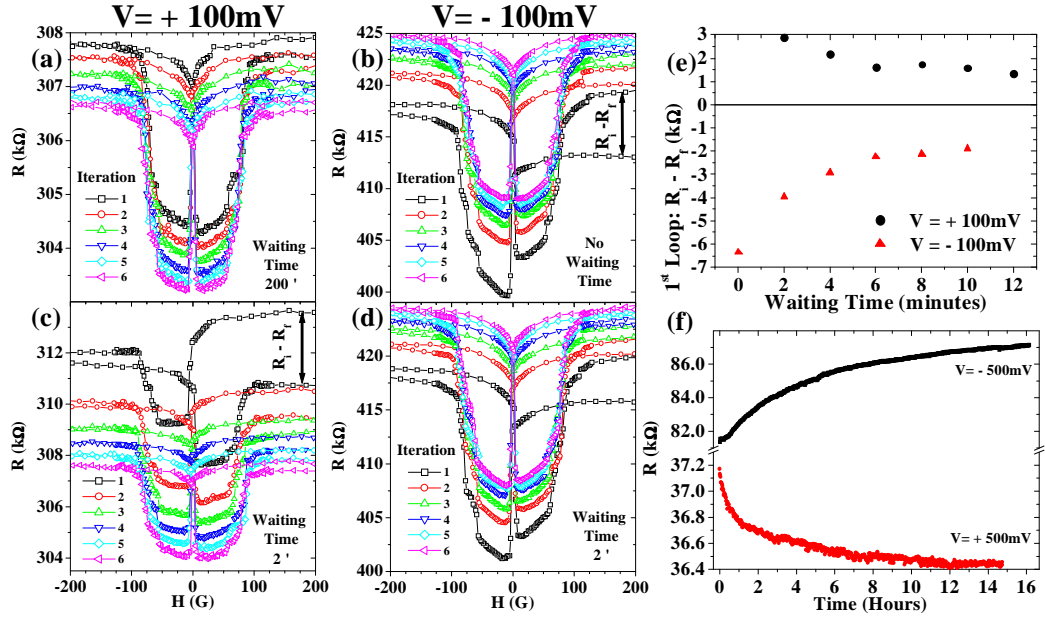


Figure 7.25: Time and field-cycling behavior of a $\text{La}_{0.7}\text{Sr}_{0.3}\text{MnO}_3$ (350 \AA)/ SrTiO_3 (7ML) + O_2 etch / Co (125 \AA) / CoO (25 \AA) / Au (150 \AA) (A11597) junction at $T=290\text{K}$. The order of panels (a)-(d) strictly respects junction history. $R(H)$ loops were iteratively taken following the indicated waiting time at the prescribed bias. Each $R(H)$ loop was completed in 15 minutes. Panel (e) shows the evolution of $R(H)$ loop closure following the waiting time at $V = +100\text{mV}$ and $V = -100\text{mV}$. Panel (f) shows junction state preparation for cooldown at a given applied bias.

applied bias corresponds to electron injection from Co toward SrTiO_3 and $\text{La}_{0.7}\text{Sr}_{0.3}\text{MnO}_3$. We note that this effect could result from electrochemical changes to the topmost Co/CoO interface.

Resistance measurements were performed while temperature was lowered for several applied bias values after stabilization (see Figure 7.26). During each low-temperature run, applied bias never exceeded $|V|=0.5\text{V}$, and the state of the junction was found to remain stable. Referring to the results on a stable junction presented in Section 6.2.1, the resistance peak at $\sim 275\text{K}$ for $V_{Desc}=+10\text{mV}$ pinpoints the $\text{La}_{0.7}\text{Sr}_{0.3}\text{MnO}_3$ interface transport T_C , and should remain constant (see Figure 6.2 on page 112). However, when this unstable junction is in a negatively-biased state (Figure 7.26a), the $\text{La}_{0.7}\text{Sr}_{0.3}\text{MnO}_3$ interface T_C is shifted to lower temperatures and the resistance peak broadens. In addition, the drop in junction resistance associated with the increase in $\text{La}_{0.7}\text{Sr}_{0.3}\text{MnO}_3$ carrier states at E_F is severely mit-

igated at $V=-300\text{mV}$ and all but suppressed at $V=-500\text{mV}$. In contrast, for positive biases the shift in $\text{La}_{0.7}\text{Sr}_{0.3}\text{MnO}_3$ interface T_C is not as pronounced (Figure 7.26b), and the $\text{La}_{0.7}\text{Sr}_{0.3}\text{MnO}_3/\text{SrTiO}_3$ interface maintains a more metallic character even as junction bias is increased.¹²

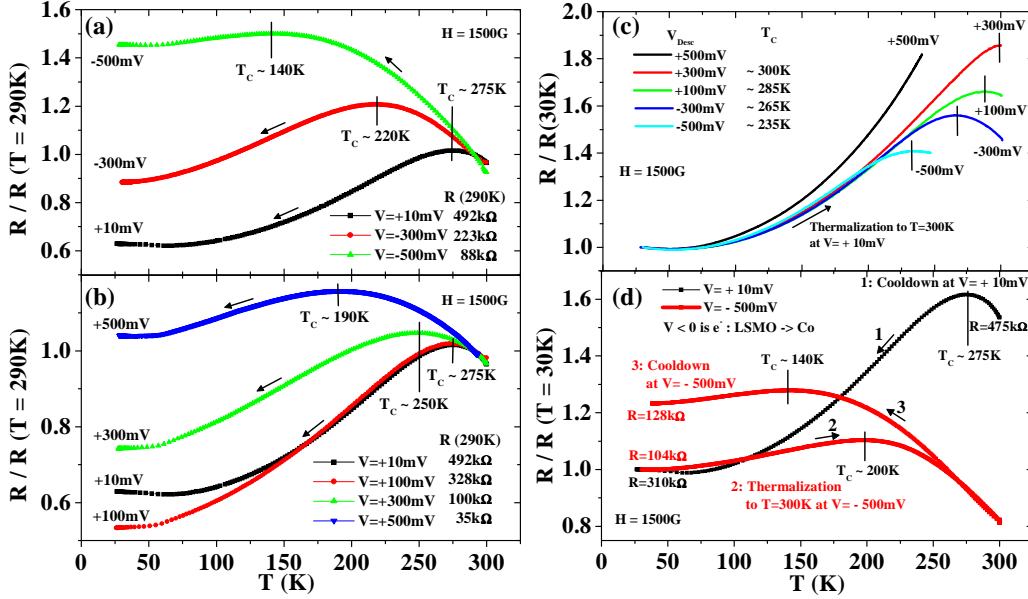


Figure 7.26: Temperature evolution of $\text{La}_{0.7}\text{Sr}_{0.3}\text{MnO}_3$ (350\AA)/ SrTiO_3 (7ML) + O_2 etch / Co (125\AA) / CoO (25\AA) / Au (Al1597) junction resistance for various applied biases V_{Desc} : a lower interface T_C and a more insulating low-temperature state are found for negative biases (a) compared to positive biases (b) as temperature is lowered. (c) Junction thermalization at $V=+10\text{mV}$ exhibits a trend of improved interface as cooldown bias V_{Desc} is swept from negative to positive values. (d) After a cooldown at $V=+10\text{mV}$, the junction is allowed to thermalize to $T=300\text{K}$ at $V=-500\text{mV}$, before cooling down again to a different resistance state. All data were taken in the same magnetic field $H=1.5\text{kG}$.

We believe that the oxygen etching step of the STO surface during tri-layer deposition may have induced defects in the barrier. Electrochemically active elements in SrTiO_3 include Ti and O. [179] The electromigration of these species could explain the resistance instabilities. The incidence on $\text{La}_{0.7}\text{Sr}_{0.3}\text{MnO}_3$ is to promote a more insulating state by altering the

¹²It is worth noting that for $V=+100\text{mV}$, there is virtually no shift in interface T_C , and the junction exhibits a more metallic low-temperature state than for $V=+10\text{mV}$, for T lower than $\sim 150\text{K}$.

$\text{Mn}^{4+}/\text{Mn}^{3+}$ ratio which governs the strength of the double exchange interaction. [180] Such departures from nominal stoichiometry can explain the observed drop in T_C . [181, 182] Also, Ti doping of $\text{La}_{0.7}\text{Sr}_{0.3}\text{MnO}_3$, which would occur at negative V_{Desc} , promotes a larger metal-insulator transition as reflected by the broader resistance peaks. This could reflect Ti doping of $\text{La}_{0.7}\text{Sr}_{0.3}\text{MnO}_3$ for this direction of cooldown bias. [183] The incidence of either O or Ti electromigration within SrTiO_3 is to promote a shift in the chemical potential level within the band gap: a fall for increasing O or decreasing Ti concentrations, and inversely a rise for decreasing O or increasing Ti concentrations. It is worth noting the complementary roles that oxygen stoichiometry in STO and LSMO play in affecting the LSMO/STO interfacial barrier heights. As illustrated in Figure A.16 (page 250), an increasing oxygen (*e.g.* anionic) concentration will lower the Fermi level much as what occurs with STO. [184]

Panel (c) compares the relative evolution of resistance at $V=+10\text{mV}$ as the junction thermalizes overnight to room temperature after having been cooled down at V_{Desc} . The resistance peak shifts to larger temperatures as V_{Desc} is swept from negative to positive values. Thus the $\text{La}_{0.7}\text{Sr}_{0.3}\text{MnO}_3/\text{SrTiO}_3$ interface improves, in support of the above oxygen and titanium electromigration picture and doping effect on $\text{La}_{0.7}\text{Sr}_{0.3}\text{MnO}_3$. Finally, panel (d) lends credence to the notion of preparing states at room temperature by applying a bias: after cooling down the junction at $V=+10\text{mV}$, a bias of $V=-500\text{mV}$ was applied. After verifying that the resistance remained stable, the junction was slowly thermalized to 300K, then cooled down again while maintaining that bias value. Although taken at the same $V=-500\text{mV}$ bias value, the thermalization data resulting from the $V=+10\text{mV}$ -prepared junction state yielded both a higher interface T_C and a more metallic low-temperature state than the cooldown data. Thus, at least within the $|V|=0.5\text{V}$ limit of our low-temperature measurements, the junction does retain its cooldown-prepared state. Therefore, the data in panels (c) and (d) of Figure 7.26 confirm the concept that if one prepares this junction in a given state before cooldown, it remains stable at low temperature.¹³

Figure 7.27 presents $R(H)$ loops at low temperature for low and high positive V_{Desc} values. No remarkable shift occurs in either the major loops or the minor loops, and the TMR value is unchanged. Since this direction of V_{Desc} could have promoted reduction at the Co interface, we conclude that the oxidation state of Co at the STO/Co interface is not affected by oxygen electromigration effects.

¹³within a reasonable bias range such as the $\pm 500\text{mV}$ chosen.

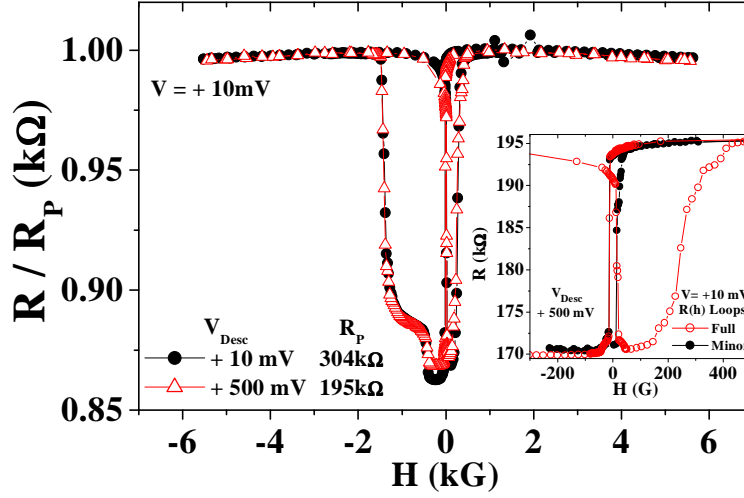


Figure 7.27: $R(H)$ loops at $T=30\text{K}$ and $V= + 10\text{mV}$ for cooldown bias values $V_{Desc} = + 10 \text{ mV}$ and + 500mV. Inset: a comparison between a full loop and a minor loop at $V= + 10\text{mV}$ for $V_{Desc} = + 500 \text{ mV}$. The low-T resistance is stable.

7.3.3.2 Ti electromigration

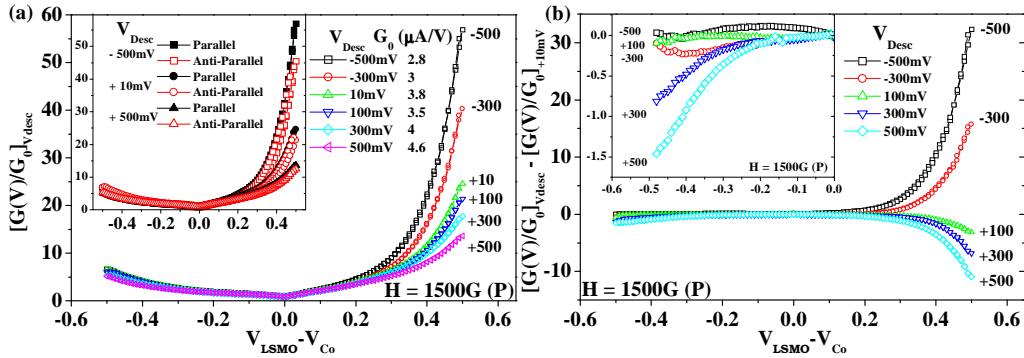


Figure 7.28: Evolution of normalized junction conductance with cooldown bias V_{Desc} at $T=30\text{K}$: (a) in the parallel alignment. Inset: parallel and antiparallel conductances for remarkable V_{Desc} values. (b) Comparison between conductance at a given V_{Desc} and the reference at $V_{Desc} = +10\text{mV}$. Inset: closeup of data at negative applied bias. All data was normalized to $G_0 = G(V = +10\text{mV})$. $G(V) \equiv dI/dV$.

As discussed previously, we expect the electromigration of Ti and O to affect the junction's barrier profile. Figure 7.28 presents junction conductance

data at $T=30\text{K}$ in the $V_{D_{esc}}$ states. Since the low-temperature resistances vary quite a bit (see Figure 7.26), all conductance data was normalized to the value G_0 found at $V=+10\text{mV}$ to promote a comparison of the bias evolution of conductance as $V_{D_{esc}}$ is varied. As expected, G_0 evolves with $V_{D_{esc}}$ in the same way that the low-temperature resistance measured at $V_{D_{esc}}$ does. Panel (a) presents the normalized conductance data for all values of $V_{D_{esc}}$ explored. Relative to the conductance obtained for $V_{D_{esc}}=+10\text{mV}$, and at positive bias values, the conductance measured for $V_{D_{esc}}=+500\text{mV}$ does not rise as sharply, while that measured for $V_{D_{esc}}=-500\text{mV}$ shows a much more pronounced upswing. At negative bias values, no overarching influence of $V_{D_{esc}}$ on conductance can be noted. This effect of $V_{D_{esc}}$ on junction behavior is more easily observable in panel (b) of Figure 7.28 which shows conductance behavior at a given $V_{D_{esc}}$ relative to the reference conductance $V_{D_{esc}}=+10\text{mV}$. To discern junction behavior at negative V , the inset of panel (b) offers a closeup of the data.

The changes in junction conductance with $V_{D_{esc}}$ appear to be spin-independent. An explanation must arise from changes in the interfacial barrier heights or to the chemical structure (*i.e.* defects) of the barrier. To assess any changes in the junction's barrier heights, Figure 7.29 shows the temperature evolution of junction conductance,¹⁴ alongside the bias dependence of TMR and differential TMR. The following interpretation mirrors closely that made regarding LSMO/STO/LSMO junctions (see Section 7.2.2). At $V_{D_{esc}}=-500\text{mV}$, a clear spin-independent peak located at $V\approx+0.3\text{V}$ reflects the STO/Co hole barrier height Φ_{Co}^h as argued previously. In addition, a shoulder at $V\approx+0.15\text{V}$ defines another spin-independent feature in the junction profile, which we therefore attribute to the LSMO/STO electron barrier height Φ_{LSMO}^e . This feature coincides with the sign reversal of the junction's differential TMR response, which reflects the instantaneous spin-dependent response at that bias value. The data for $V_{D_{esc}}=+500\text{mV}$ is not as salient. Nevertheless, we may pinpoint Φ_{LSMO}^e to the shoulder in the I-V data and the corresponding sign change in the differential TMR. As expected from electromigration considerations, Φ_{LSMO}^e decreases when going from negative to positive $V_{D_{esc}}$. Assuming that the effective STO band gap $E_g'=\Phi_{LSMO}^e+\Phi_{Co}^h\approx 0.42\text{eV}$ remains constant, we extract a value $\Phi_{Co}^h\approx 0.35\text{eV}$ at $V_{D_{esc}}=+500\text{mV}$, which appears to fit a shoulder in the G-V data. Thus $V_{D_{esc}}$ does appear to influence barrier heights.

At low applied bias, a peak appears in the TMR bias dependence. This *zero-bias TMR peak* is more prevalent in the $V_{D_{esc}}=-500\text{mV}$ state compared

¹⁴We present the relative evolution of junction conductance, instead of current, so as to enhance any local change in the bias-dependent junction response

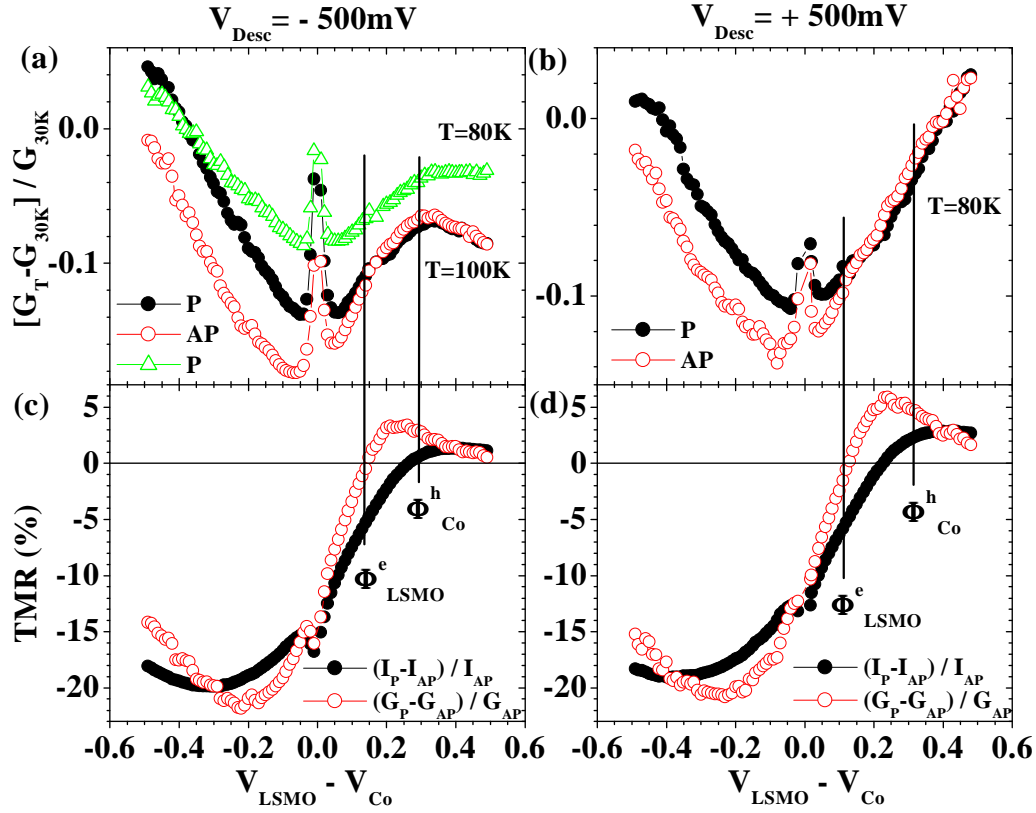


Figure 7.29: Temperature evolution of LSMO/STO+etch/Co junction conductance in the parallel (P) and antiparallel (AP) configurations for (a) $V_{\text{Desc}}=-500\text{mV}$ and (b) $V_{\text{Desc}}=+500\text{mV}$, and the respective bias dependence of TMR and differential TMR in (c) and (d). $G(V) \equiv dI/dV$

to the $V_{\text{Desc}}=+500\text{mV}$ state. The temperature dependence of this TMR peak is also unusual. Figure 7.32a presented hereafter, which shows the temperature dependence of TMR at low bias for $V_{\text{Desc}}=-500\text{mV}$ and $V_{\text{Desc}}=+500\text{mV}$. In the bias range $-500\text{mV} < V_{\text{LSMO}} - V_{\text{Co}} < -50\text{mV}$, the TMR decreases monotonically with temperature, much as what was found for a nominal junction (see Figure 6.4b). However, while in that case this monotonical behavior extended to low applied bias, in this case the TMR in the $-40\text{mV} < V < +40\text{mV}$ bias range, which reflects the zero-bias TMR peak, decreases more markedly with temperature. Once the peak has disappeared, for T beyond $\approx 130\text{K}$, this decrease adopts a monotonic character similar to that found at larger negative biases. This decrease in TMR with increasing temperature is more pronounced for $V_{\text{Desc}}=-500\text{mV}$ than for $V_{\text{Desc}}=+500\text{mV}$.

As reported by White *et al.*, [72], the presence of defect states within a

tunneling barrier results in a more rapid decrease in TMR with rising bias and temperature. Furthermore, one study reports [185] a 0.09eV energy level of STO trap centers in $\text{La}_{0.85}\text{Sr}_{0.15}\text{MnO}_3/\text{SrTiO}_3/\text{La}_{0.05}\text{Sr}_{0.95}\text{TiO}$ heterostructures grown by pulsed laser deposition under fairly similar conditions to ours. This position of trap centers above the Fermi energy is somewhat close to the inflection point in the TMR bias dependence past the zero bias TMR peak. As such the above data support a picture of defect states within the tunneling barrier induced by the oxygen etch step of the STO surface. In addition to the resistance instabilities the more marked drop in TMR at low bias in the $V_{Desc}=-500\text{mV}$ state compared to that for $V_{Desc}=+500\text{mV}$ may be explained by the creation of Ti trap centers left within the barrier after electromigration of this species toward LSMO. This explanation also accounts for the conductance increases observed for $V_{Desc}=-500\text{mV}$ in Figure 7.28 since defects within a tunnel barrier are expected to result in increased conductance. [71] This explanation in terms of defect states is buttressed by magnetotransport measurements on several junctions from other LSMO/STO/Co junctions with thicker ($d_{STO}=35\text{-}39\text{\AA}$), non-etched SrTiO_3 barriers, which also display a zero-bias TMR peak (data not shown).

7.3.3.3 Magnetotransport features

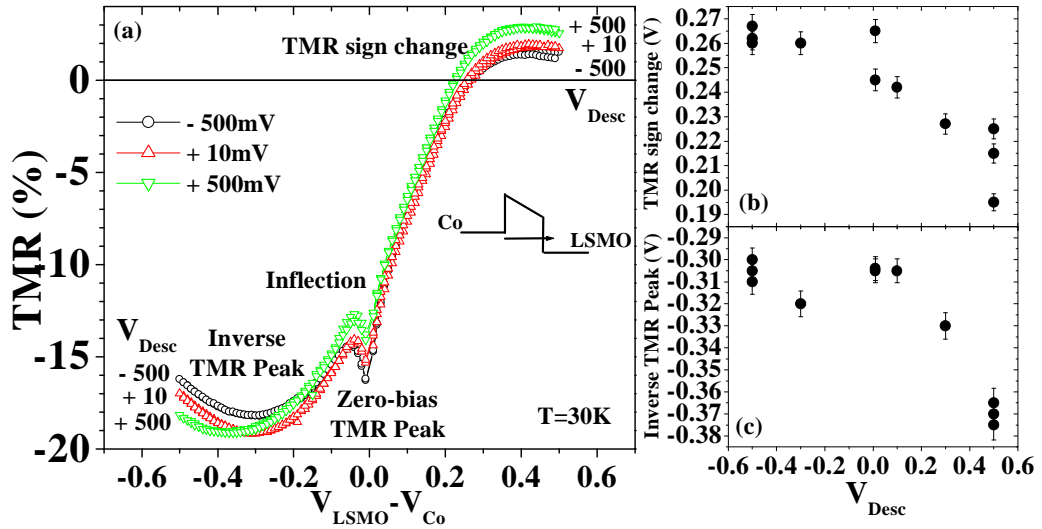


Figure 7.30: (a) TMR bias dependence of a LSMO/STO/Co junction with an etched STO surface (Al1597), at $T=30\text{K}$ for several values of V_{Desc} . Bias evolution of (b) the TMR sign change and (c) the inverse TMR peak with V_{Desc} .

Results Figure 7.30 presents the bias dependence of TMR of this junction for several values of V_{Desc} . Both the TMR sign change and the inverse TMR peak bias positions appear to evolve with V_{Desc} , as illustrated in panels (b) and (c), respectively. While constant for negative V_{Desc} , the TMR inversion point shifts to lower bias values with positive V_{Desc} , while the inverse TMR peak shifts to higher bias values with positive V_{Desc} . At negative V_{Desc} , both remain constant.

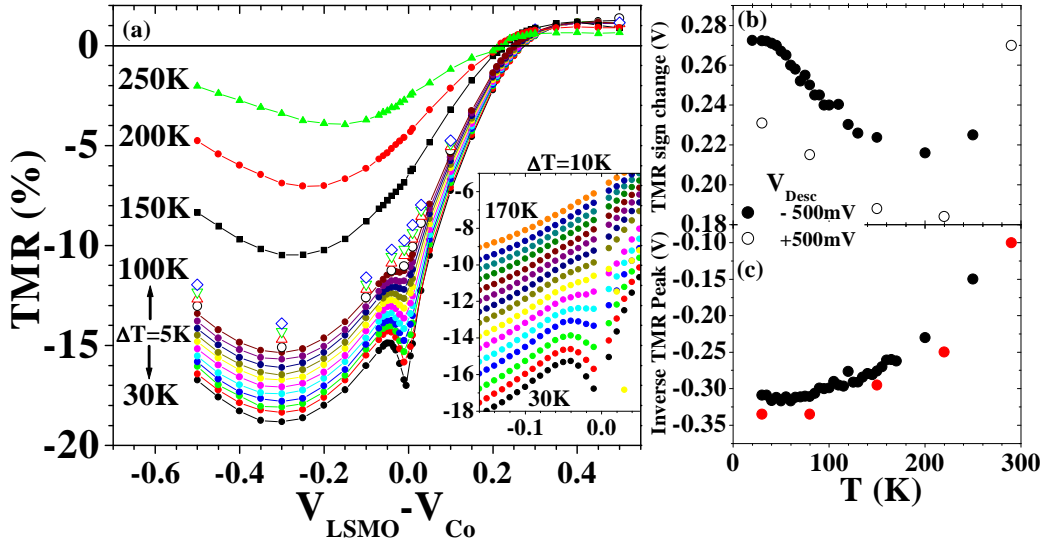


Figure 7.31: Temperature evolution of TMR for a LSMO/STO/Co junction with an etched STO surface: (a) bias dependence, (b) TMR sign change and (c) inverse TMR peak for $V_{Desc}=-500\text{mV}$ (closed circles) and $V_{Desc}=+500\text{mV}$ (open circles). Data from R(H) loops. The inset to panel (a) provides additional I-V data on the temperature evolution of the TMR bias dependence.

Figure 7.31 presents the temperature evolution of the TMR bias dependence in panel (a), along with the bias positions of the TMR sign change (panel (b)) and inverse TMR peak (panel (c)). Both appear to evolve similarly for $V_{Desc}=-500\text{mV}$ and $V_{Desc}=+500\text{mV}$ states. Interestingly, the bias position of the TMR sign change begins to decrease past $T=40\text{K}$, once thermally-assisted processes which mix the two spin channels become prevalent. However, the bias position of the inverse TMR peak stays constant up to $T=80\text{K}$ before decreasing.

Discussion These evolutions of the TMR sign inversion and inverse TMR peak with V_{Desc} and temperature may be explained in terms of electrode density of states (DOS) effects, and/or in terms of barrier profile effects. If

the electromigration process does indeed affect the DOS by changing the chemical environment at each junction interface, it also changes the chemical sharpness of the potential profile. As such it is difficult to separate each contribution to these effects with certainty.

Let us first consider electromigration effects in a defect picture. For negative V_{Desc} , Ti (O) may migrate toward LSMO (Co). Referring to Figure 7.28b, the changes in relative conductance at positive bias are straightforwardly attributed to Ti defects within the barrier for negative V_{Desc} . For negative V_{Desc} , the negative conductance stagnates. This could reflect the competing effects of an increased conductance through defects and a rising electron barrier height at the STO/Co interface. For positive V_{Desc} the conductance at negative and positive bias values falls relative to that for $V_{Desc}=+10\text{mV}$. The TMR amplitude at the zero-bias TMR peak decreases monotonically with increasing V_{Desc} , so that the influence of defects is always present.

In addition to a defect picture, a barrier asymmetry picture may be advanced. As discussed in Section 2.6.2.2, the work function of Co is larger than that of LSMO. This should lead to an asymmetric barrier profile at $V=0$. Due to STO doping from both electrochemical species, E_F within the barrier will tend to fall(rise) at the STO/Co(LSMO/STO) interface with negative V_{Desc} . The reverse occurs for positive V_{Desc} . Therefore, a negative V_{Desc} will tend to correct any asymmetry, while a positive V_{Desc} will increase this asymmetry. This explanation accounts in a simple manner for the increase(decrease) in the inverse TMR peak(TMR sign inversion) at positive V_{Desc} . At negative V_{Desc} , the influence of Ti defect mobility on transport may overshadow this consideration, leading to the stagnation of any reverse shift. Underlying this asymmetric electromigration response is the hybrid nature of the junction, and the inability for Ti to migrate into the Co counterelectrode to promote barrier defects at positive V_{Desc} .

One may also argue the shift in the inverse TMR peak at positive V_{Desc} in terms of a Co DOS change. Indeed, this results in an accumulation of Ti and a desorption of O at the STO/Co interface. The accumulation of non-magnetic Ti should decrease the exchange splitting of the Co d band believed to be responsible for the peak, [186] so that in this case the peak position should decrease, in opposition to what is observed. A similar case may be made regarding O desorption from the STO/Co interface. However, a reduction of Co from CoO should lead to an increase in the exchange splitting, mirroring the increase in bias position of the inverse TMR peak. It should be noted, however, that an opposite trend was observed from annealing experiments presented in Section 7.3.2.1.

We now discuss the temperature dependence of both magnetotransport

features. The decrease beyond $T=40\text{K}$ of the bias position for the TMR sign inversion may be interpreted as reflecting a barrier feature since this temperature is associated with the onset of thermally-assisted tunneling processes. That this decrease lessens, then reverses around the temperature range where the manganite's carrier localization overtakes other conduction processes, reflects the influence of the manganite's metal-insulator transition on the effective barrier profile of the junction. As shown in Figure 7.26c (page 163), the LSMO interface T_C in the $V_{Desc}=-500\text{mV}$ state is 235K . Such effects are argued to occur at $T_C/2$, [77, 156] in good agreement with the change in trend at $T=120\text{K}$ of the decrease in the position of the TMR sign inversion. In the $V_{Desc}=-500\text{mV}$ state, though data is lacking, from extrapolation the LSMO interface $T_C \geq 300\text{K}$. Qualitatively, this corresponds to the observed shift toward higher temperatures of the TMR sign inversion position temperature dependence.

The temperature dependence of the inverse TMR peak does not change past $T=40\text{K}$, and remains constant up to $T=90\text{K}$. The subsequent decrease past this temperature is in good agreement with the loss of LSMO half-metallicity at $0.4T_C$ with decreasing exchange coupling. [77] In a DOS picture, the decrease in the bias position of the inverse TMR peak may reflect a mixing of Co spin \uparrow and \downarrow features. As shown in Figure 2.20 (page 40), such a mixing could lead to an effective decrease in the Co DOS peak. Though such spin channel mixing should have occurred at $T>40\text{K}$, since tunneling is occurring from an electrode with nearly total spin polarization, this shifting will only take place once half-metallicity is lost. Thus, the DOS picture provides a consistent explanation for this temperature dependence of the peak regarding $V_{Desc}=-500\text{mV}$ data. However, a similar curve is found in the $V_{Desc}=500\text{mV}$ state, even though $0.4T_C=120\text{K}$ given a lower estimate of 300K for the LSMO interface T_C . This casts some doubt regarding the attribution of the decrease in the inverse TMR peak position with temperature to an electrode DOS effect. The lack of extensive data in the $V_{Desc}=+500\text{mV}$ state does not confirm or infirm this contradiction with certainty, so that additional measurements are needed.

7.3.3.4 On the TMR sign inversion and Fowler-Nordheim tunneling

Figure 7.32 presents the temperature evolution of TMR at remarkable bias values in given V_{Desc} states. As remarked previously, the TMR decreased monotonically at negative bias, similarly to a nominal junction (see Figure 6.4 on page 116), aside from the defect-induced change in behavior near $V=0$. As the amplitude of positive bias is increased, a more pronounced

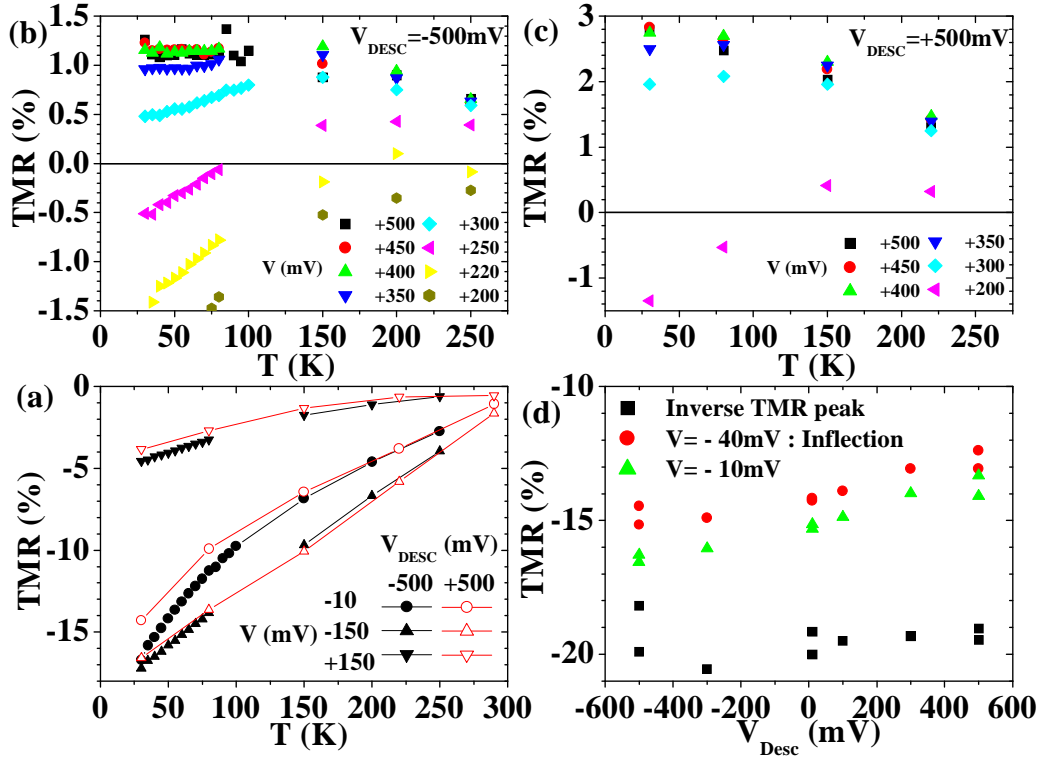


Figure 7.32: Temperature evolution of TMR at (a) remarkable bias values for $V_{Desc}=-500\text{mV}$ (closed symbols) and $V_{Desc}=+500\text{mV}$ (open symbols); (b) for $V_{Desc}=-500\text{mV}$ and (c) for $V_{Desc}=+500\text{mV}$. (d) Evolution of TMR amplitude at remarkable bias values as a function of V_{Desc} . Lines in panel (a) are guides to the eye. All data from R(H) loops.

curvature appears in the temperature dependence of TMR. This behavior is represented for $V_{Desc}=-500\text{mV}$ (panel (b)) and for $V_{Desc}=+500\text{mV}$ (panel (c)). In corroboration to the data from sample A11531 (see Figure 6.4b), a TMR plateau extending to $0.4T_C$ reflects the intrinsic LSMO spin polarization. [77]

However, this more exhaustive dataset provides evidence for a TMR oscillation which may, at specific values of applied bias (*e.g.* $V_{Desc}=-500\text{mV}$: $V=+220\text{mV}$), result in an oscillation in the sign of TMR. Furthermore, the evolution with applied bias of this oscillation appears to change with V_{Desc} . Indeed, for $V=+300,+350,+400\text{mV}$, while the TMR ratio increases +44%, +10% and +0.9% between 30K and 80K at $V_{Desc}=-500\text{mV}$, at $V_{Desc}=+500\text{mV}$ the ratio changes by +6%, +2% and -2%. Thus far we have argued that the appearance of these bulk effects results from exceeding the

LSMO/STO electron barrier height Φ_{LSMO}^e . These relative changes in TMR amplitude corroborate a picture of the onset of bulk behavior *at lower bias* for $V_{Desc}=+500\text{mV}$ relative to $V_{Desc}=-500\text{mV}$ due to a *lower* Φ_{LSMO}^e at positive V_{Desc} . Indeed, equating the relative TMR increases for $V_{Desc}=\pm 500\text{mV}$ amounts to a $\sim 50\text{mV}$ *decrease* from dataset to dataset going from negative to positive V_{Desc} . This shift is in good agreement with both the observed $\sim 50\text{meV}$ *decrease* in Φ_{LSMO}^e (see Figure 7.29) and the observed *increase* in LSMO/STO hole barrier height Φ_{LSMO}^h from negative to positive V_{Desc} . In addition, the behavior of the bias value at which the TMR changes sign (see Figure 7.30b) follows the same trend as that of Φ_{LSMO}^e as per oxygen doping considerations. Finally, the temperature evolution of the TMR sign change at positive bias (see Figure 7.31b) is constant below $T\approx 40\text{K}$ before shifting to lower bias values with increasing temperature. The phenomenon therefore promotes an interpretation in terms of the barrier profile, which may evolve with the onset of thermally-assisted tunneling processes past $T\sim 40\text{K}$. In general, however, this description of bulk states above a barrier height cannot account for the eventual decrease in TMR between 30K and 80K at high enough bias.

In Section 7.2.4 on magnetotransport in the LSMO/STO/LSMO system, it was shown that exceeding a barrier height could lead to oscillations in the magnetotransport response arising from wavefunction interference effects. We believe that these TMR oscillations with increasing temperature also underscore interference effects which have occurred above Φ_{LSMO}^e as quantum well states are formed in the barrier conduction band. This discussion remains qualitative at the time of this writing, as numerous questions remain regarding a more quantitative interpretation of this data.

7.3.3.5 Fowler-Nordheim tunneling and exchange coupling

Section 7.2.5 investigated the consequence of changes in the effective barrier profile to LSMO/STO/LSMO junction current at a given applied bias. An explanation for the observed changes in the field dependence of resistance with sweeping bias above barrier heights was provided in terms of changes to the magnetic interlayer coupling between the two electrodes, with qualitative analytical support from magnetization and transport experiments on $\text{La}_{0.7}\text{Ba}_{0.3}\text{MnO}_3/\text{LaNiO}_3$ multilayers. [63,64,176] This Section buttresses the claims made there with a similar study in the LSMO/STO/Co system.

Figure 7.33 presents an introduction to the junction under study here. Panel(a) presents the bias dependence of junction conductance in the parallel (P) and antiparallel (AP) states. Both curves exhibit a sharp rise at $V\approx +425\text{mV}$. As argued in Section 6.2.1, this spin-independent effect reflects

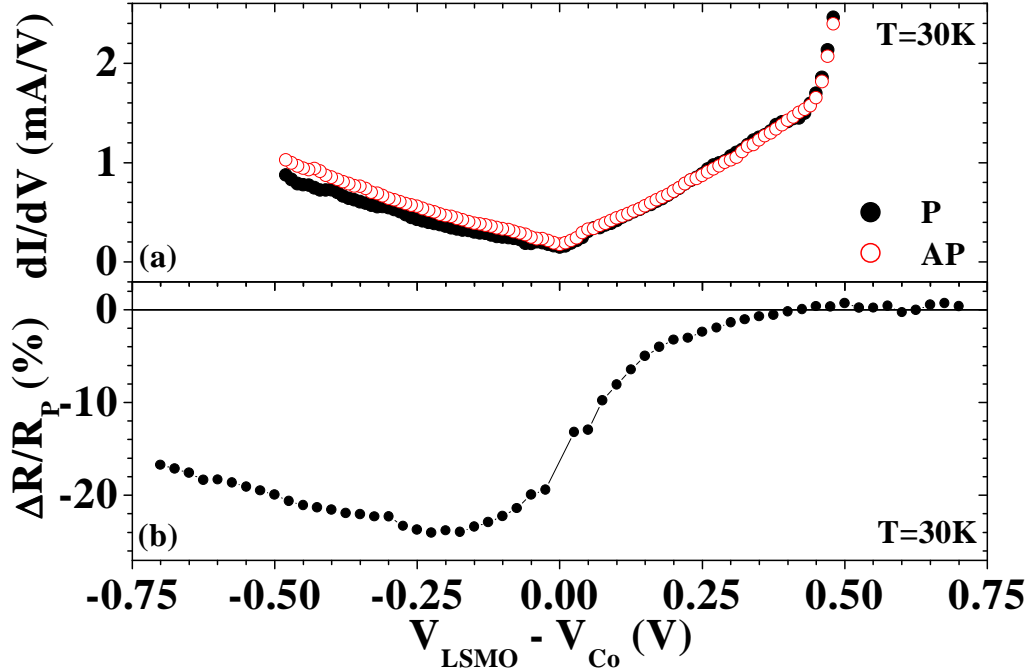


Figure 7.33: LSMO/STO/Co: (a) junction conductance in the parallel (P) and antiparallel (AP) states. (b) Bias dependence of TMR from $R(H)$ data.

reaching, then exceeding the tunneling barrier height. Panel (b) presents the bias dependence of TMR for this junction, obtained from $R(H)$ loops. The TMR changes sign at $V=+375\text{mV}$.

The $R(H)$ loops used to obtain the data in Figure 7.33b are represented in Figure 7.34. Panel (a) focuses on the bias range below and above the 425meV barrier height at positive bias. In this panel, a linear CMR contribution at large applied field was subtracted from the data. For $V < 425\text{mV}$, resistance solely increases as the applied field is decreased to $H=0$. However, for $V \geq 425\text{mV}$, a dip develops in the field dependence of junction resistance. This anomaly oscillates about the CMR slope as the applied bias is further increased.

Panel (b) presents data in the $+275\text{mV} > V > +25\text{mV}$ range. The $R(H)$ approaches to $H=0$ change markedly for $V > 50\text{mV}$ as oscillations develop with increasing bias. These oscillations then become attenuated for $V > +200\text{mV}$. Finally, panel (c) shows how the $R(H)$ evolve with negative applied bias.

A comprehensive understanding of the trends in the $R(H)$ data is difficult to discern here. This isn't surprising given the increased complexity of the LSMO/STO/Co system compared to its LSMO/STO/LSMO coun-

terpart. In particular, both electrodes aren't half-metallic here, and the STO/Co interface isn't epitaxial. Nevertheless, several points may be raised. We first focus on positive bias values, for which electrons are injected toward the LSMO/STO interface much as was described in Section 7.2.5 for LSMO/STO/LSMO junctions. The relative dip in resistance once the applied bias exceeds the barrier height at $V=+425\text{mV}$ is similar to what was found for LSMO/STO/LSMO. Also, the change in $R(H)$ trend for $V>50\text{mV}$ may reflect exceeding another barrier height. If this is the case, then these results lend further credence to the picture of exceeding an electron, then a hole barrier height for a given direction of applied bias. However, in this case the barrier height at 425meV would reflect the STO/Co hole barrier height, so that argumentation in terms of this dataset should be treated cautiously.

The third point regards the ever-changing $R(H)$ trend for $V<+200\text{mV}$ and into the negative bias range. If the explanation in terms of magnetic interlayer exchange coupling is correct, then these data corroborate the picture of a LSMO/STO/Co tunnel junction with asymmetric barrier heights. This asymmetry is enhanced for negative applied bias values, leading to changes in the effective thickness of the spacer. This in turn would affect the coupling suggested to explain these $R(H)$ oscillations.

7.3.4 Summary

In this Section we endeavored to understand the effects of junction barrier profile on the magnetotransport response of LSMO/STO/Co junctions, in comparison with DOS effects discussed in Section 5.2. With the hindsight provided by Sections 5.1 & 7.2 on DOS and barrier profile considerations in LSMO/STO/LSMO junctions, several points may now be addressed.

The TMR sign inversion at positive bias in the LSMO/STO/Co system results from a barrier profile effect related to exceeding a tunneling barrier height toward coherent wavefunction interference in the Fowler-Nordheim regime. The absence of such an inversion for junctions with barriers of lesser crystalline quality (Section 7.3.1), and the observation of quantum well states in this tunneling regime (Section 7.3.3.4) appear consistent. A correlation between barrier heights and magnetotransport behavior was independently investigated through annealing/forming experiments (Section 7.3.2). Finally, we voluntarily altered a standard LSMO/STO/Co trilayer stack. The ensuing electrical instability was then utilized to probe the incidence on magnetotransport of electrochemical changes to the junction (Section 7.3.3). In particular, we observe changes in the trend of magnetization collinearity in $R(H)$ data as the barrier height is exceeded, in similar fashion to that found in LSMO/STO/LSMO junctions. This implies that the barrier profile of a

LSMO/STO/Co junction is (quite arguably) asymmetric, so that this consideration may drive the bias-dependent magnetotransport behavior of such a junction.

We were not entirely successful in distilling a clearcut interpretation on the origin of the inverse TMR peak in the bias dependence of TMR in LSMO/STO/Co junctions. As attested by the transport data, the position of this peak may vary by as much as 150mV from junction to junction. On a given junction, annealing may change this position by several hundred mV. Junction forming was shown to shift the peak position (by as much as 100mV), as does temperature. In spite of difficulties to imagine that a feature in the Co DOS could shift in such extensive manners, no discussion of the presented data could dispel with certainty this DOS interpretation of the inverse TMR peak. This said, the barrier profile interpretation of forming experiments provides the most straightforward explanation of the observed bias shift, especially since this shift occurs in similar fashion to that of the TMR sign inversion point (see Figures 7.23 on page 7.23 & 7.30 on page 168).

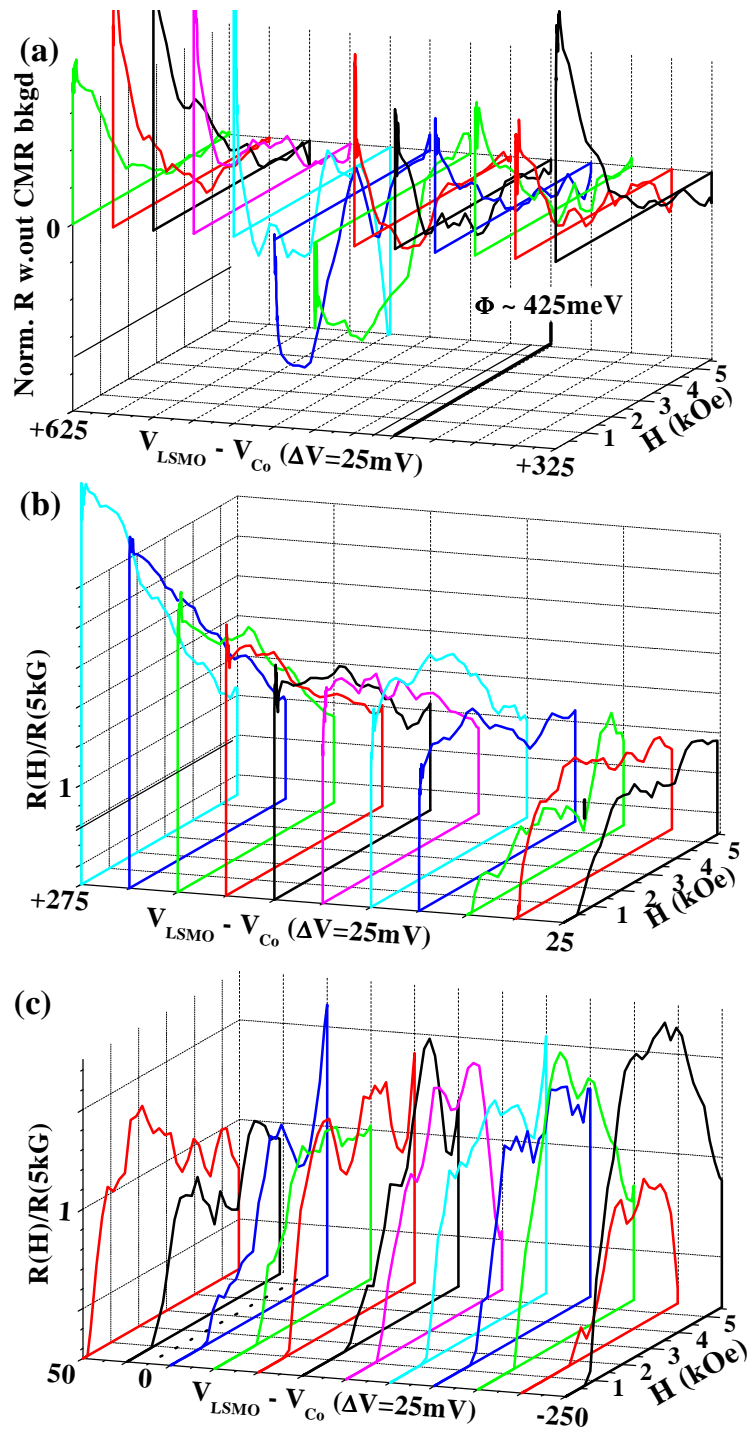


Figure 7.34: LSMO/STO/Co: evolution of normalized junction resistance with decreasing applied field for a set of bias values $V_{LSMO} - V_{Co}$ ranging from (a) +625mV to +325mV, (b) +275mV to +25mV and (c) +50mV to -250mV in 25mV decrements. In panel (a) the CMR contribution at high field has been subtracted.

Chapter 8

Conclusions & perspectives

"The more I study physics the more I am drawn to metaphysics." - Albert Einstein

At a time of renewed interest in the intensely studied field of spin-dependent tunneling, this experimental Thesis has attempted to bridge an existing gap between theory and experiment in understanding this effect in solid state heterostructures. To this end, we have studied partly and fully epitaxial magnetic tunnel junctions (MTJs). An important asset has been the integration of the manganite $\text{La}_{0.7}\text{Sr}_{0.3}\text{MnO}_3$ with nearly total tunneling spin polarization into such structures. We confirmed this fact with a measurement of 1860% tunneling magnetoresistance (TMR) in a $\text{La}_{0.7}\text{Sr}_{0.3}\text{MnO}_3/\text{SrTiO}_3/\text{La}_{0.7}\text{Sr}_{0.3}\text{MnO}_3$ MTJ. Within the Jullière model, we conclude that tunneling spin polarization at the $\text{La}_{0.7}\text{Sr}_{0.3}\text{MnO}_3/\text{SrTiO}_3$ interface exceeds 95%.

This feature allowed us to use the $\text{La}_{0.7}\text{Sr}_{0.3}\text{MnO}_3$ electrode as a spin analyzer to probe the role of the solid state tunneling in promoting a certain orbital character of electronic tunneling transmission. Both chemical bonding at the ferromagnet/insulator interface and metal-induced gap states within the insulator are shown to promote an efficient tunneling transmission of electron wavefunctions with Δ_1 symmetry (“*s*-character”) in the case of Al_2O_3 or MgO , or Δ_5 symmetry (“*d*-character”) in the case of SrTiO_3 , $\text{Ce}_{0.69}\text{La}_{0.31}\text{O}_{1.845}$ and TiO_2 . Separate experiments on fully epitaxial $\text{Fe}/\text{MgO}/\text{FeCo}$ and $\text{LSMO}/\text{STO}/\text{MgO}/\text{Fe}$ MTJs also buttress this picture. In this vein, theoretical calculations regarding chemical bonding at the ferromagnet/insulator interface predict the appearance of an induced moment within the paramagnetic tunnel barrier. To test this groundwork, we performed X-Ray Magnetic Circular Dichroism experiments at the European Synchrotron Radiation Facility. However, despite good experimental conditions, this element-specific technique did not demonstrate the presence of an induced moment on either the Al or O sites in a Al_2O_3 barrier at the interface with Co, nor on the Mg or O sites in a MgO barrier at the interface with Fe.

In a straightforward picture of the tunneling process across a junction with an applied bias V , charge carriers originate from the Fermi level of the injecting electrode and tunnel toward unoccupied states at $E = E_F + eV$ of the collecting electrode. This Thesis explicitly confirms the spectroscopic nature of spin-dependent tunneling with transport experiments on $\text{La}_{0.7}\text{Sr}_{0.3}\text{MnO}_3/\text{SrTiO}_3/\text{La}_{0.7}\text{Sr}_{0.3}\text{MnO}_3$ and $\text{La}_{0.7}\text{Sr}_{0.3}\text{MnO}_3/\text{SrTiO}_3/\text{Co}$ MTJs. Once a bias regime of spin wave excitations is exceeded, the tunneling current then increasingly regains the amplitude of spin polarization from the injecting electrode. It is then possible to evidence salient spin-dependent features in the electrode density of states. In particular, the energetic gap between the Fermi level and the lowest band of minority states in $\text{La}_{0.7}\text{Sr}_{0.3}\text{MnO}_3$ was found to lie at $E = E_F + 0.35 \pm 0.05eV$, in good quantitative agreement with the

value $E = E_F + 0.38 \pm 0.03eV$ found independently through the well-established technique of Spin-Polarized Inverse Photoemission Spectroscopy. This study will have led to the strong affirmation of the ideally half-metallic character of the $\text{La}_{0.7}\text{Sr}_{0.3}\text{MnO}_3/\text{SrTiO}_3$ interface. We extended this spectroscopic picture to the SrTiO_3/Co interface with experiments on $\text{La}_{0.7}\text{Sr}_{0.3}\text{MnO}_3/\text{SrTiO}_3/\text{Co}_{1-x}\text{Cr}_x$ junctions designed to modify the Co spin-dependent density of states in a controlled manner. The evolution of the bias dependence of TMR with Cr concentration x may be interpreted in terms of this modification if the $\text{STO}/\text{Co}_{1-x}\text{Cr}_x$ interface is assumed to remain chemically nominal.

An impediment to integrating manganite materials into tunneling devices operating at room temperature lies with what has been reported as a diminished Curie temperature at the interface with the tunneling barrier. This decrease has been argued in terms of disruptions in the oxide's electronic properties at the interface. Magnetotransport experiments on $\text{La}_{0.7}\text{Sr}_{0.3}\text{MnO}_3/\text{SrTiO}_3/\text{La}_{0.7}\text{Sr}_{0.3}\text{MnO}_3$ junctions showed that the tunneling spin polarization at the $\text{La}_{0.7}\text{Sr}_{0.3}\text{MnO}_3/\text{SrTiO}_3$ interface does indeed follow the interface magnetization, which disappears at a lower temperature than the $T_C = 350\text{K}$ of bulk thin films. Using a Co electrode with a much higher T_C in $\text{La}_{0.7}\text{Sr}_{0.3}\text{MnO}_3/\text{SrTiO}_3/\text{Co}$ junctions, this decrease in interface T_C was mainly ascribed to the disruptive incidence of spin wave excitations on the manganite's electronic properties at the junction interface. Beyond the spin wave excitation regime of applied bias, the temperature dependence of both junction resistance and TMR follow trends intrinsic to bulk properties of the $\text{La}_{0.7}\text{Sr}_{0.3}\text{MnO}_3$ thin film.

Finally, this Thesis presented careful experiments which utilize electromigration effects in tunnel junction heterostructures to probe the incidence of the interfacial density of states and the junction's effective potential profile on spin-dependent tunneling. The incidence of forming at a MTJ's interfaces is explicitly demonstrated through experiments on $\text{La}_{0.7}\text{Sr}_{0.3}\text{MnO}_3/\text{SrTiO}_3/\text{Co}_{1-x}\text{Cr}_x$ junctions. Reversible electrochemical activity at the $\text{SrTiO}_3/\text{Co}_{1-x}\text{Cr}_x$ interface due to the high reactivity of Cr was shown to modify junction resistance, and alter the amplitude and sign of TMR, leading in favorable experimental conditions to junction states exhibiting -30% and +40% TMR. This result was explained in terms of electrochemical engineering of the $\text{SrTiO}_3/\text{Co}_{1-x}\text{Cr}_x$ interface. These studies undermine the aforementioned spectroscopy experiments using this system.

Electromigration effects were also utilized to investigate the incidence of changes in the junction's effective potential profile on spin-dependent transport. This additional parameter proved crucial in probing the Fowler-Nordheim tunneling transport regime, as it qualitatively offered a separate

degree of freedom in probing the influence of the thickness and wavefunction interference effects in the metallic spacer resulting from exceeding the junction barrier height. Notably, we observed reproducible, multi-period oscillations of TMR up to $|V| = \pm 3V$ which varied in amplitude and period as the barrier profile was changed. The results were interpreted in terms of quantum well state formation within, and magnetic interlayer exchange coupling across, the tunnel barrier as the mediating charge carriers experience changes in the electronic landscape with applied bias. In this sense our transport experiments on tunnel junctions in the Fowler-Nordheim regime hint at a unified picture of spin electronics between giant magnetoresistance and tunnel magnetoresistance systems. Also, our results advanced the novel concept that tunneling at very large bias values should take into account both the electron and hole barrier heights at each interface which are reached for a given direction of applied bias. At the time of this writing, a sound theoretical basis for this experimental situation which could describe our results, and buttress our explanation, is lacking.

The magnetotransport results presented in this Thesis attest to the ideally half-metallic character of the $\text{La}_{0.7}\text{Sr}_{0.3}\text{MnO}_3/\text{SrTiO}_3$ interface. As such, a wide range of experiments aimed at studying the finer aspects of spin electronics may be considered. For instance, it could be rewarding to reexamine the Giant MagnetoResistance effect in a $\text{La}_{0.7}\text{Sr}_{0.3}\text{MnO}_3$ -based stack, using LaNiO_3 spacers. Furthermore, this Thesis has underscored the need to carefully consider the interplay between the band structures of the ferromagnet and insulator. As such more research into novel barriers is required. Regarding the specific case of the $\text{La}_{0.7}\text{Sr}_{0.3}\text{MnO}_3/\text{SrTiO}_3$ interface, the spin \uparrow and \downarrow bands at or near the Fermi level in $\text{La}_{0.7}\text{Sr}_{0.3}\text{MnO}_3$ are of e_g and t_{2g} symmetry; while the octahedral coordination of SrTiO_3 implies that its conduction band be defined first by a t_{2g} band, and then a e_g band. Interfacial electronic disorder aside, if $\text{La}_{0.7}\text{Sr}_{0.3}\text{MnO}_3$ were matched up with an insulator with tetrahedral oxygen coordination, then the insulator's conduction band would be defined first by a e_g band. In this case, in addition to the nearly total spin polarization of the manganite, additional spin filtering effects due to the band structure of an otherwise paramagnetic barrier could be attained, thereby sidestepping the issue of magnetic decoupling inherent to spin filtering through a ferromagnetic insulator.

Progress in the field of spin-dependent tunneling should, thanks to refinements in junction quality, mirror the level of intricacy attained in the semiconductor field over the past 40 years. In the near future, it should be possible to devise spin-dependent tunneling devices which take into account the interplay of electronic structure between all layers. For instance, if the $\text{MgO}(001)$ barrier filters electron states with Δ_1 symmetry, then in a similar

fashion to Fe(001) for one spin, will a Cr(001) layer with no Δ_1 band crossing E_F constitute an additional tunneling barrier for these barrier-filtered Δ_1 electrons? What spin electronic potential can a three-terminal device with barriers of different electronic transmission symmetry offer?

Through the experimental results presented in this Thesis, it is clear that inelastic processes play an important role in the tunneling transport phenomenon. In a similar fashion to research performed on semiconductor heterostructures, optical characterization could shed additional light on the physical picture underlying transport in magnetic tunnel junctions. In addition, on a more long-term scale, the field of solid state tunneling could widen with other techniques, such as Electron Energy Loss Spectroscopy or Spin-Polarized Tunneling Microscopy, to study evolutions in the electronic structure on a sample with appropriate geometry which has been biased.

The electromigration experiments presented in this Thesis embody a new way of characterizing and tailoring magnetic tunnel junctions. The impact of this concept on magnetotransport in the field of spin electronics should lead to enhanced device parametrization and control.

Chapter 9

Transport Tunnel Polarisé en Spin

Transport Tunnel Polarisé en Spin à l'État Solide

9.1 Le transport tunnel polarisé en spin et motivations de Thèse

9.1.1 Introduction

L'étude de l'effet tunnel fait partie des premières découvertes intellectuelles qu'il est possible de faire dans l'univers de la mécanique quantique. Dans son expression la plus simple, cet effet témoigne de l'interaction ondulatoire d'une particule, par exemple un électron, lorsque confrontée à une marche de potentiel que son énergie cinétique ne lui permettrait pas de franchir. Sa probabilité d'occupation au sein de cette barrière de potentiel décroît alors exponentiellement au-delà de l'interface. À une échelle macroscopique, l'électron ne traverse pas l'isolant. En revanche, si l'épaisseur de la barrière est suffisamment mince, la probabilité d'occupation est non-nulle de l'autre côté de la barrière, et ainsi l'électron peut la traverser. Ceci est appelé *effet tunnel*.

L'effet tunnel se manifeste à de nombreux égards dans le monde de la recherche scientifique. Le plus bel exemple demeure sa mise à contribution au sein d'un Scanning Tunneling Microscope (STM): une pointe épaisse de quelques atomes est balayée juste au-dessus d'une surface cristalline. La dépendance exponentielle du courant passant de la pointe vers l'échantillon par effet tunnel permet alors d'observer le relief atomique de cette surface. Cet effet se manifeste aussi au travers de barrières à l'état solide, c'est à dire d'un isolant électrique de quelques nm d'épaisseur séparant deux couches métalliques.

9.1.2 Fondements du transport tunnel

Plusieurs modèles ont été proposés pour rendre compte des paramètres clés du phénomène. [3–5] On retiendra que la conductance tunnel $G \propto e^{-d\sqrt{m\Phi}}$ où m est la masse effective de l'électron au sein de la barrière, d l'épaisseur de la barrière et Φ sa hauteur, c'est à dire la différence énergétique entre le niveau de Fermi et le bas de la bande de conduction.

L'effet tunnel conserve le spin de l'électron. [16] On peut alors supposer que le transport tunnel polarisé en spin soit constitué de deux canaux correspondant à la conduction d'électrons de spin \uparrow et \downarrow . Si les deux électrodes métalliques de part et d'autre de la barrière sont magnétiques, alors le nombre d'états disponibles pour accueillir un canal de spin donné changera en fonction d'un alignement parallèle (P) ou antiparallèle (AP) de l'aimantation des deux électrodes. Le changement relatif de résistance de la jonction entre

ces deux états s'appelle magnétorésistance tunnel (TMR). Dans le modèle de Jullière, [7] elle est définie par:

$$TMR = \frac{I_P - I_{AP}}{I_{AP}} = \frac{R_{AP} - R_P}{R_P} = \frac{2P_{Inj}P_{Col}}{1 - P_{Inj}P_{Col}} \quad (9.1)$$

où P est la polarisation de spin de l'électrode injectrice/collectrice d'électrons

$$P = \frac{\rho^\uparrow(E_F) - \rho^\downarrow(E_F)}{\rho^\uparrow(E_F) + \rho^\downarrow(E_F)} \quad (9.2)$$

9.1.3 Sur le degré de polarisation de spin tunnel

Le transport tunnel polarisé en spin s'est beaucoup développé aux années 1960 avec l'étude de jonctions ferromagnétique/isolant/supraconducteur. [15] L'application d'un champ magnétique scinde le gap supraconducteur, ouvrant une fenêtre d'énergie pour laquelle sa densité d'états est totalement polarisée en spin. Il est alors possible de sonder l'amplitude et le signe de la polarisation de spin du ferromagnétique (FM). A partir de cette recherche, Bardeen formula [1] une expression phénoménologique basée sur la règle d'or de Fermi qui relie la conductance tunnel aux densités d'états (DOS) des deux électrodes:

$$I(V) = \int_{-\infty}^{+\infty} \rho_{Inj}(E)\rho_{Col}(E + eV)|M(E, V)|^2 f(E)[1 - f(E + eV)] dE \quad (9.3)$$

où $\rho(E)$ est la DOS, $f(E)$ la distribution de Fermi-Dirac et $M(E, V)$ la matrice de transfert tunnel. David et MacLaren montrent que puisque la tension appliquée implique de nouveaux états $E=E_F + eV$ dans l'électrode collectrice, cet élément de matrice M dépend de l'énergie et de la tension appliquée. [2] En revanche, l'approximation WKB, qui permet une résolution analytique du problème exprimée par les modèles mentionnés ci-dessus, élimine toute expression de la DOS dans la conductance tunnel. [6]

Pour des raisons technologiques, ces études de transport tunnel furent menées sur le système modèle FM/ Al_2O_3 /Al. De manière surprenante, un signe positif de la polarisation de spin tunnel fut mesuré, alors qu'il devrait être négatif pour certains métaux de transition tels que Co ($\rho(E_F)^\downarrow > \rho(E_F)^\uparrow$). Cette controverse resurgit avec le renouveau du sujet en 1995 grâce aux améliorations technologiques permettant la croissance de jonctions FM/ Al_2O_3 /FM performantes. [32] La résistance dans l'état parallèle

d'alignement des aimantations était toujours plus faible que dans le cas antiparallèle: d'après l'Equation 9.1, cette amplitude positive de TMR traduit un même signe de polarisation de spin pour les deux électrodes quelles que soient celles-ci.

Il s'avère que, dans un dispositif tunnel à l'état solide, la barrière isolante ne joue pas simplement le rôle de marche de potentiel, mais qu'il faut prendre en compte l'interaction de la structure de bande entre le ferromagnétique et l'isolant à l'interface par le biais du facteur de transmission M . Ce constat, soulevé de manière théorique, [30, 33–35] fut clairement démontré en 1999 lorsque des mesures au travers d'autres barrières telles que Ta_2O_5 [51] ou SrTiO_3 témoignèrent d'une TMR inverse: $R_{AP} < R_P$. Cette observation, au sein de notre laboratoire, dans le système $\text{lsmo}/\text{SrTiO}_3/\text{Co}$ fut particulièrement révélatrice, [22] car le niveau de Fermi de la manganite n'est traversé que par une bande \uparrow . Au vu de l'Equation 9.1, la TMR inverse traduit alors une polarisation de spin tunnel négative pour Co à l'interface avec SrTiO_3 , en accord avec $\rho^\downarrow(E_F) > \rho^\uparrow(E_F)$ pour ses bandes d et l'Equation 9.2. Par ailleurs, la dépendance en tension de la TMR dans ce système diffère sensiblement de la décroissance monotone observée pour des jonctions à barrière d' Al_2O_3 . L'explication proposée repose sur une spectroscopie tunnel polarisée en spin de la densité d'états du Co à partir d'états à E_F de $\text{La}_{0.7}\text{Sr}_{0.3}\text{MnO}_3$ (LSMO).

De nombreux concepts soutendent la notion de degré de polarisation de spin tunnel. D'une part, il est important de prendre en considération l'influence des liaisons chimiques à l'interface ferromagnétique/isolant, [34, 36, 151] ainsi que les Metal-Induced Gap States (MIGS) reflétant le caractère orbital des bandes de valence et de conduction de l'isolant, [38, 39, 41] pour cerner le caractère orbital de la transmission électronique tunnel au travers d'une barrière solide. [46] Dans le système idéal $\text{Fe}/\text{MgO}/\text{Fe}$, il apparaît par ailleurs que ce degré de polarisation de spin tunnel à une interface donnée ne peut être dissocié de l'autre interface pour des raisons d'interactions de structure de bande entre $\text{Fe}(001)$ et $\text{MgO}(001)$. [46, 47] D'autre part, le profil de potentiel de la jonction, défini par l'alignement des structures de bandes des matériaux composant l'hétérostructure, ainsi que par l'abruptesse chimique des interfaces qui régit de fait la levée spatiale de potentiel, peuvent affecter l'amplitude voire le signe de la polarisation de spin tunnel à une telle interface. [21, 35] Ce profil de potentiel de la jonction peut lui-même être affecté par le positionnement du niveau de neutralité de charge (CNL) au sein du gap de l'isolant, car celui-ci peut piéger le niveau de Fermi. [40] La Figure 9.1 illustre ces concepts dans le cas particulier de $\text{SrTiO}_3(001)$ (STO). Ainsi, le CNL n'est pas placé au centre du gap comme cela serait le cas pour un isolant ordinaire. Dans cet oxyde de métal de transition, la bande de con-

duction arbore un caractère orbital “ d ” (orbitale t_{2g}). [187] Et par ailleurs, de nombreuses études sur SrTiO_3 (001) ont démontré que le niveau de Fermi se situe très près de la bande de conduction. [105, 188, 189]. Ainsi les MIGS d'évanescence κ plus faible ont un caractère orbital “ d ”. Ceci pourrait expliquer la polarisation de spin négative de Co à l'interface avec cette barrière en accord avec les bandes d de cet élément de transition.

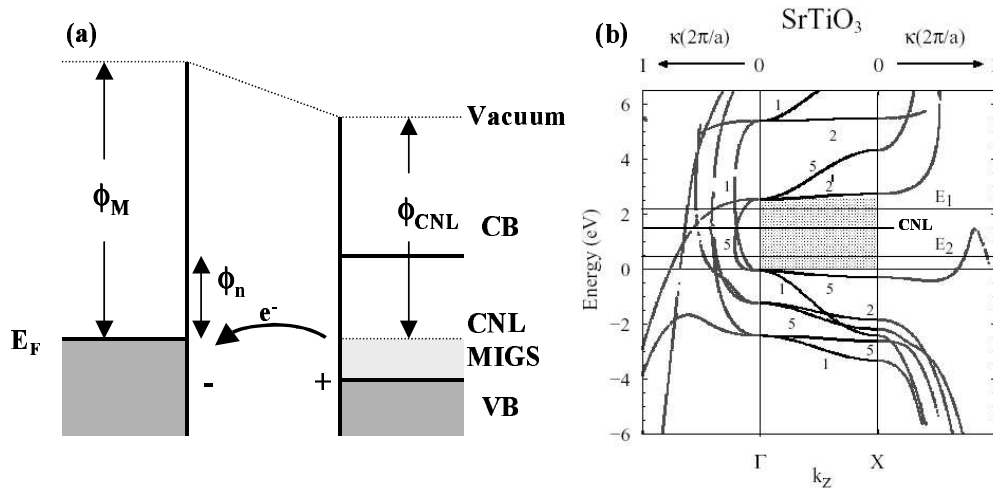


Figure 9.1: (a) Schéma de structure de bande de MIGS à une interface Métal/Semiconducteur. (b) Structure de bande complexe de SrTiO_3 (001) d'après Bellini [41]

9.1.4 Sur le transport inélastique

Plusieurs effets physiques peuvent affecter un mode de transport tunnel purement élastique d'une électrode vers l'autre. Puisque les deux électrodes sont magnétiques, la présence de magnons à température non-nulle permet l'activation de processus inélastiques. Par exemple, à tension donnée, un électron dit “chaud” car injecté à partir du niveau de Fermi vers des états vides à $E=E_F+eV$ peut se désexciter à l'interface en émettant un magnon. [67, 68] Ce processus inélastique tend à brouiller les canaux de conduction polarisés en spin. En dépit du caractère demi-métallique au niveau de Fermi dans les manganites, la génération d'ondes de spin est néanmoins possible. [69] Au-delà de la limite énergétique de génération de magnons, observée vers $\sim 100\text{meV}$, le régime en tension appliquée de transport tunnel peut sonder des propriétés intrinsèques des électrodes.

Bien que peu étudiée, la génération de phonons lors du transport tunnel à l'état solide a aussi été observée. [68] Enfin, le transport assisté par défauts amène à une augmentation de conductance, [71] ainsi qu'à une décroissance plus marquée de la TMR avec la température et la tension. [72, 73]

9.1.5 Motivations de Thèse

Au-delà d'une meilleure compréhension du magnéto-transport dans le système LSMO/STO/Co, cette Thèse a eu pour but de mieux comprendre les mécanismes qui soutendent le transport tunnel polarisé en spin à l'état solide. Nos motivations furent d'explorer le rôle que joue la barrière dans l'effet tunnel polarisé en spin en remplaçant SrTiO₃ par d'autres matériaux I dans des jonctions La_{0.7}Sr_{0.3}MnO₃/I/Co. De plus, nous avons effectué quelques mesures sur des jonctions entièrement épitaxiées à base de Fe/MgO(001) afin de sonder des effets de structure de bande au travers de toute la tricouche. Cet effort fut complété par des mesures de Dichroïsme Magnétique Circulaire X visant à corroborer la vision théorique [34, 36, 151] de moments induits dans la barrière à l'interface FM/I, proposée pour expliquer le rôle de la barrière. Par ailleurs, un important effort de recherche fut consacré à la mise en évidence manifeste du caractère spectroscopique de l'effet tunnel polarisé en spin, c'est à dire lorsque des électrons injectés de E_F viennent sonder des états vides à $E=E_F+eV$ dans l'électrode collectrice. L'objectif général de cette Thèse aura été de favoriser le rapprochement dans la compréhension de l'effet tunnel à l'état solide entre la théorie, qui se base sur des structures idéales, et l'expérimentation, qui de manière générale étudie cet effet au travers de barrières amorphes, par le biais de mesures sur des jonctions partiellement ou entièrement épitaxiales.

9.2 Travail expérimental

9.2.1 Echantillons

Le travail expérimental de l'Auteur consista à effectuer l'élaboration et la mesure de jonctions tunnel à partir de tricouches préparées par E. Jacquet (La_{0.7}Sr_{0.3}MnO₃, SrTiO₃, Ce_{0.69}La_{0.31}O_{1.845}, TiO₂ par ablation laser), A. Vaurès et J. Humbert (métaux de transition par pulvérisation cathodique/MBE) au sein de notre laboratoire, ainsi que par C. Martínez-Boubeta du groupe Cebollada à Madrid (Fe/MgO par pulvérisation cathodique/ablation laser). La Figure 9.2 présente un cliché TEM haute résolution qui rend compte de la qualité épitaxiale d'un échantillon

LSMO/STO/LSMO.

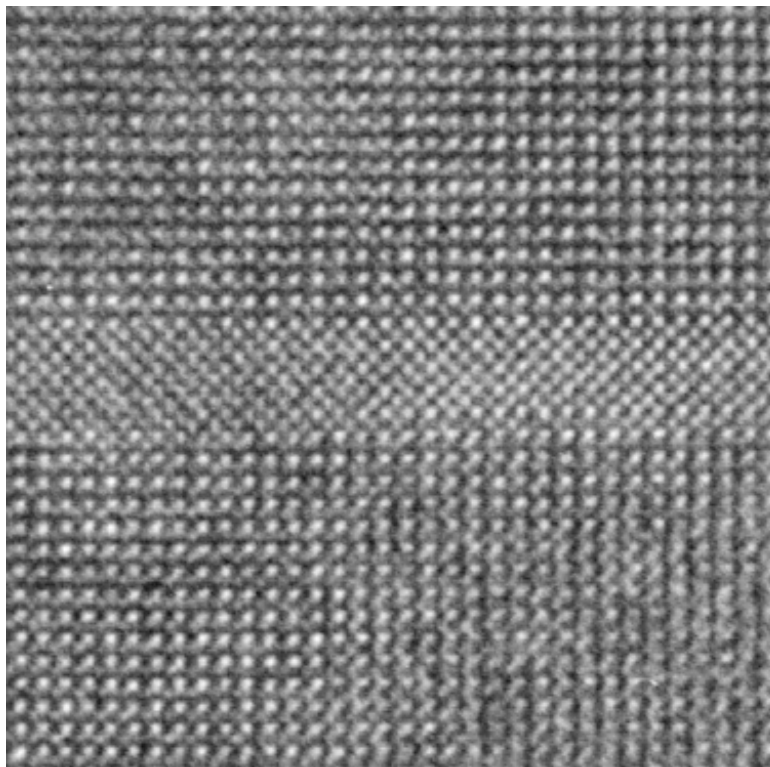


Figure 9.2: TEM haute résolution d'une barrière de STO prise entre deux couches LSMO dans cette hétérostructure entièrement épitaxiée sous contrainte. Les colonnes MnO_2 au sein de LSMO de fort contraste sont séparées par le paramètre de maille $a=3.905\text{\AA}$ de STO. Cliché par J.-L. Maurice.

9.2.2 Lithographie & transport

Une part importante de ce travail consista à réviser le procédé de lithographie optique, développé initialement pour traiter des échantillons à base de métaux de transition, [190] afin de minimiser la dégradation des oxydes. En particulier, la conduction, le ferromagnétisme et la forte polarisation de spin de $\text{La}_{0.7}\text{Sr}_{0.3}\text{MnO}_3$ sont dûs au mécanisme électronique de double échange entre sites Mn au travers d'un site O. [191] Ainsi la tendance de cet oxyde à la désoxygénation au-delà de 85°C dut être prise en compte tout au long du procédé. [182] Au terme de deux révisions, notre laboratoire est désormais capable de fabriquer jusqu'à 144 jonctions sur un échantillon typique de $10\times 10\text{mm}$, avec une surface de jonction minimale de $12\mu\text{m}^2$, alors que le

procédé original ne permettait que 3 jonctions de taille minimale $80\mu\text{m}^2$. De plus, le problème d'une trop grande résistance d'accès au barreau inférieur de $\text{La}_{0.7}\text{Sr}_{0.3}\text{MnO}_3$ fut aussi résolu.

Nos mesures de magnéto-transport sont effectuées en géométrie quatre-pointes afin d'isoler la réponse du pilier comprenant la jonction. Nous mesurons toujours en source de tension - afin de placer la mesure dans une perspective spectroscopique, en mode non-dynamique (pas de rétro-contrôle).

Les hétérostructures à base d'oxydes peuvent être sujettes à des phénomènes électrochimiques qui font migrer les espèces. L'électromigration a été longuement étudiée dans des pérovskites telles que BaTiO_3 ou $\text{Pb}(\text{Zr},\text{Ti})\text{O}_3$. [123]. Dans ces oxydes, les lacunes d'oxygène semblent soutenir de tels effets. [127] Pour le cas de SrTiO_3 , une très faible enthalpie d'activation $\sim 1\text{meV}$ promeut la diffusion d'oxygène. [126] Dans ces expériences, un champ électrique $\sim 10^5\text{V/cm}$ est suffisant pour induire une électromigration. Sur nos jonctions, une tension de 1V appliquée au travers d'une barrière de $\approx 30\text{\AA}$ de STO induit un champ électrique $\sim 10^6\text{ V/cm}$. Ainsi, de tels effets doivent être pris en compte lors d'études en tension sur nos jonctions tunnel magnétiques. Au-delà de l'instabilité de jonction que ces effets occasionnent, lorsque les conditions et l'évolution de l'expérience sont suffisamment contrôlées, il est possible de mettre à profit ces effets afin de sonder le magnéto-transport au regard des modifications apportées à la jonction.

9.2.3 Dichroïsme Magnétique Circulaire X

Afin d'effectuer des mesures de moment induit sur les sites de la barrière paramagnétique, la technique de Dichroïsme Magnétique Circulaire X fut utilisée. Héritage des premières investigations par Faraday, [133] puis par Kerr, [134] de l'effet magnétooptique, cette technique utilise la lumière cohérente et polarisée d'un synchrotron afin de sonder une éventuelle asymétrie dans l'efficacité de transition interbandes entre des électrons de spin \uparrow et \downarrow . En particulier, la technique s'intéresse à l'effet de détection de spin que peut offrir la bande d lors d'excitations $2p \rightarrow 3d$ dans des métaux de transitions. En effet, le déséquilibre de populations électroniques \uparrow et \downarrow va promouvoir, suivant la phase entre l'hélicité du photon et l'aimantation du matériau, une efficacité différente qui reflète le magnétisme du site. Puisque l'énergie de telles transitions dépend intimement de la structure électronique, cette technique permet de sonder le magnétisme d'un élément particulier au sein d'un échantillon.

La mesure du courant recueilli en émission de champ à partir du niveau de Fermi, et sa caractérisation selon la phase, permettent, par le biais des règles

de somme, [136, 137], de remonter au magnétisme par atome de l'élément sondé. Les règles ci-dessous omettent la petite contribution des transitions $2p \rightarrow 4s$ afin de ne considérer que les transitions $2p \rightarrow 3d$ prédominantes: [138, 139]

$$\frac{\int_{j^+ + j^-} (I^{-1} - I^{+1}) d\omega}{\int_{j^+ + j^-} (I^{-1} + I^{+1} + I^0) d\omega} = \frac{\langle L_Z \rangle}{ln_h} \quad (9.4)$$

$$n_h = 2(2l + 1) - n$$

$$\frac{\int_{j^+} (I^{-1} - I^{+1}) d\omega - \frac{l}{l-1} \int_{j^-} (I^{-1} - I^{+1}) d\omega}{\int_{j^+ + j^-} (I^{-1} + I^{+1} + I^0) d\omega} = \frac{2}{3n_h} (\langle S_Z \rangle + \frac{2l+3}{l} \langle T_Z \rangle) \quad (9.5)$$

où I^{-1}, I^{+1} et I^0 dénotent les sections efficaces d'absorption de photons de polarisation circulaire gauche, droite, et linéaire. j^+ and j^- reflètent les seuils d'absorption L_3 et L_2 . A partir de ces règles de somme, on peut déduire:

- le moment orbital magnétique : $m_L = -\frac{\mu_B}{\hbar} \langle L_Z \rangle$
- le moment de spin magnétique : $m_S = -\frac{2\mu_B}{\hbar} \langle S_Z \rangle$
- le moment de dipôle magnétique : $m_T = +\frac{\mu_B}{\hbar} \langle T_Z \rangle$

Puisque ces règles impliquent des différences entre intégrales aux seuils L_3 et L_2 , les débuts et fins de spectres doivent comporter une "baseline" stable et reproductible .

9.3 Résultats expérimentaux

9.3.1 Polarisation de spin quasi totale de $\text{La}_{0.7}\text{Sr}_{0.3}\text{MnO}_3$

Alors que la plus forte polarisation de spin tunnel P mesurée sur une manganite était de 88%, [92] le caractère demi-métallique de la manganite $\text{La}_{0.7}\text{Sr}_{0.3}\text{MnO}_3$ (LSMO) à l'interface avec une barrière de SrTiO_3 (STO) fut réaffirmé par la mesure d'une TMR de 1860% à $T=4.2\text{K}$ dans une jonction LSMO/STO/LSMO (voir Figure 9.3). [116] D'après le modèle de Jullière, nous estimons que cette mesure reflète une polarisation de spin tunnel supérieure à 95% pour cette interface.

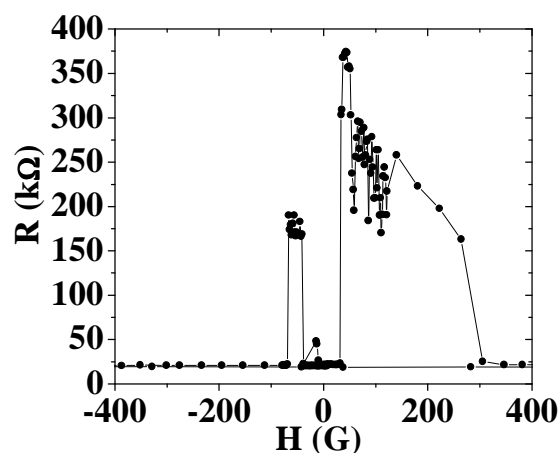


Figure 9.3: Magnétotransport de LSMO/STO/LSMO à $T=4K$. Jonction A de surface $64\mu m^2$: résistance en fonction du champ appliqué à $V_{DC}=1mV$.

9.3.2 Rôle de la barrière dans l'effet tunnel polarisé en spin

9.3.2.1 Transport

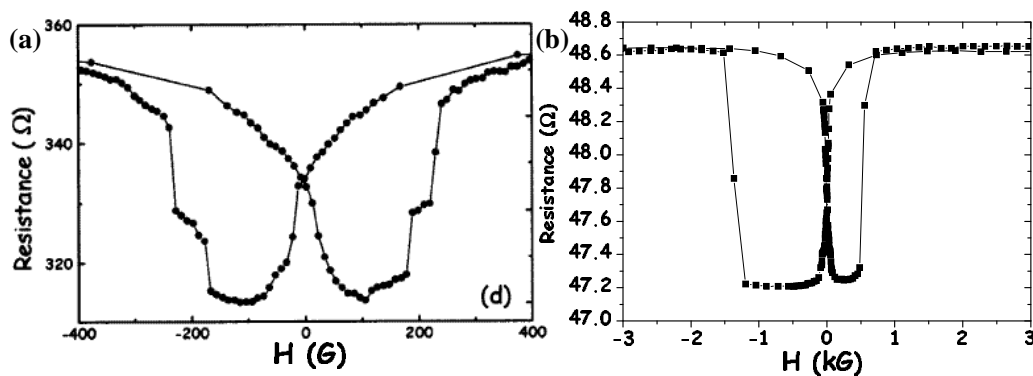


Figure 9.4: LSMO/I/Co: cycles $R(H)$ à $V=10mV$ pour (a) $I=Ce_{0.69}La_{0.31}O_{1.845}$ et (b) $I=TiO_2$. Le cycle asymétrique dans le cas TiO_2 reflète le couplage antiferromagnétique de CoO sur Co .

Ce résultat réaffirme la capacité pour la manganite de jouer le rôle d'analyseur du signe de la polarisation de spin d'un métal de transition tel que Co à l'interface avec d'autres barrières. Nous avons ainsi mesuré la TMR sur des jonctions LSMO/I/Co ($I=Al_2O_3$, $SrTiO_3/Al_2O_3$, $Ce_{0.69}La_{0.31}O_{1.845}$, TiO_2). [23, 142] Lorsque $I=(Ce_{0.69}La_{0.31}O_{1.845}, TiO_2)$ la TMR est inverse, ce

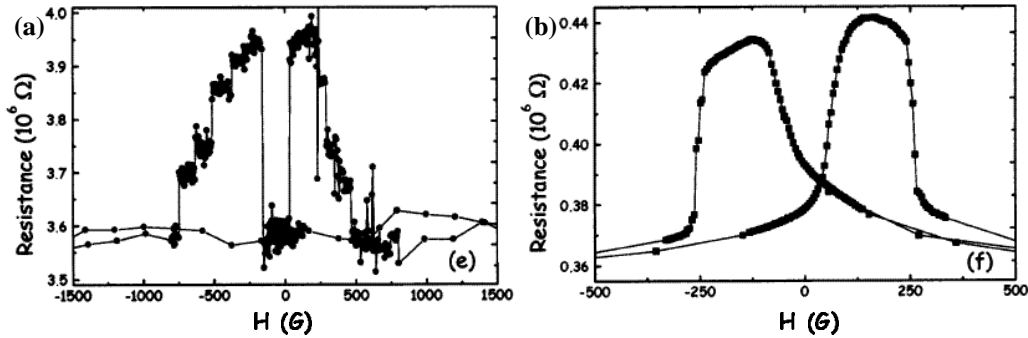


Figure 9.5: LSMO/I/Co: cycles $R(H)$ à $V=10\text{mV}$ pour (a) $I=Al_2O_3$ et (b) $I=Al_2O_3/SrTiO_3$.

qui correspond à un signe négatif de $P_{Co@I}$ (voir Figure 9.4). De même que $SrTiO_3$, ces oxydes de métaux de transition comprennent une bande de conduction à caractère orbital d . Ainsi, outre un couplage plus efficace de fonctions d'onde de caractère d en raison des liaisons chimiques $d-d$ à l'interface, la transmission évanescence de telles fonctions d'onde au travers de la barrière est favorisée. Le degré de polarisation de spin tunnel reflète alors directement celle des bandes d à E_F . Lorsque $I=Al_2O_3$, un signe positif de TMR est observé (voir Figure 9.5a). Afin de distinguer un éventuel effet d'interfaces, nous avons aussi tenté $I=SrTiO_3/Al_2O_3$. Dans ce cas, l'interface avec LSMO demeure STO, tandis que l'interface avec Co est Al_2O_3 . Une telle jonction montre aussi une TMR normale, ainsi qu'une décroissance en tension de la TMR monotone semblable à celle observée communément dans des jonctions à barrière d' Al_2O_3 (voir Figure 9.5a). Ainsi donc, $P_{Co@STO} < 0$, alors que $P_{Co@ALO} > 0$ d'après ces mesures.

Nous avons étendu ces aspects à l'étude du transport tunnel au travers d'une barrière epitaxiée de $MgO(001)$. Figure 9.6 présente la dépendance en tension de la TMR sur une jonction $Fe(001)/MgO(001)/FeCo(001)$. Nous avons mesuré une forte magnétorésistance de 60% à $T=30\text{K}$ et $V=+10\text{mV}$ - une première pour ce type de barrière. [90] La comparaison avec le résultat [146] de 13% de TMR observée sur une jonction $Fe(001)/Al_2O_3/FeCo$ réaffirme la nécessité de prendre en compte le couple ferromagnétique/isolant dans le transport tunnel polarisé en spin. Par ailleurs, la décroissance monotone de la dépendance en tension de la TMR s'apparente à celle observée dans des jonctions à base d' Al_2O_3 . Ceci n'est pas étonnant compte tenu du caractère électronique semblable des bandes de valence et de conduction des deux matériaux. Ainsi, d'après des calculs effectués par Butler *et al.*, [46], en dépit d'une polarisation de spin négative à

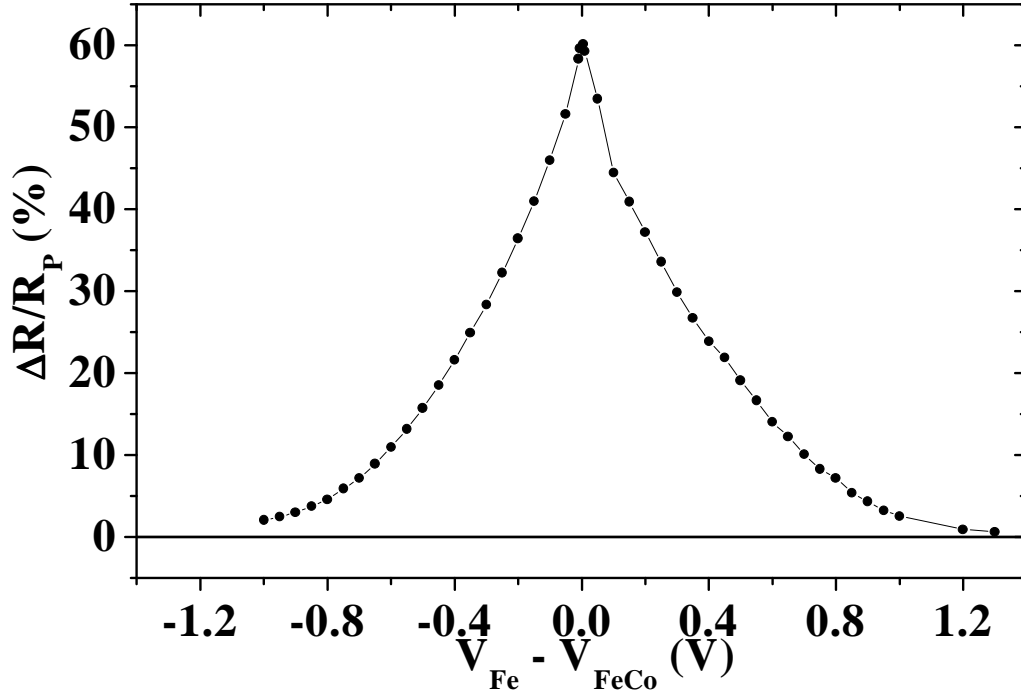


Figure 9.6: Fe/MgO/FeCo: dépendance en tension de la TMR à $T=30K$ à partir de cycles $R(H)$.

l'interface Fe(001)/MgO(001), la transmission évanescence favorable de fonctions d'onde de symétrie électronique Δ_1 au travers de la barrière, accouplée à la seule présence à E_F d'une bande Δ_1^\uparrow pour Fe(001), conduirait à une polarisation de spin positive pour l'interface Fe(001)/MgO(001). Afin de distinguer un effet habituel de densité d'états d'un effet de structure de bande à l'œuvre, nous avons analysé le signe de la polarisation de spin de cette interface au moyen d'une jonction entièrement épitaxiée LSMO/STO/MgO/Fe. La TMR normale observée, qui de fait implique que $P_{Fe(001)@MgO(001)} > 0$, confirme l'effet de ces interactions de structure de bande entre Fe(001) et MgO(001) dans le transport tunnel à partir de cette interface (voir Figure 9.7).

9.3.2.2 Dichroïsme Magnétique Circulaire X

Afin d'expliquer $P_{Co@STO} < 0$, alors que $P_{Co@ALO} > 0$, Oleinik, Tsymbal et Pettifor ont effectué des calculs ab-initio aux interfaces idéales Co cfc(111)/ α -Al₂O₃ (0001) et Co cfc(111)/SrTiO₃ (001). [34,36] Leurs résultats mettent en évidence la présence d'un moment sur les sites O et Al, et Ti, de ces deux barrières au contact avec le métal ferromagnétique. Afin de confirmer cette

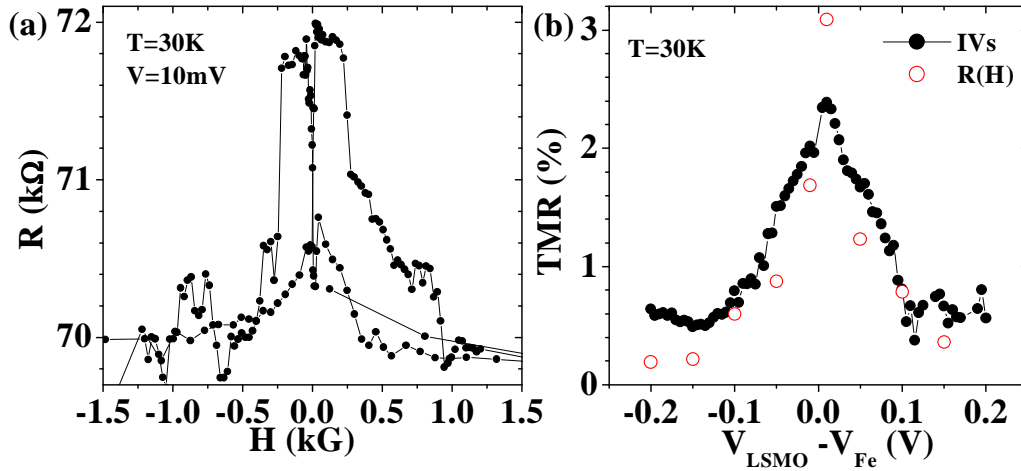


Figure 9.7: LSMO/STO/MgO/Fe: $R(H)$ à $V=+10mV$, et (b) dépendance en tension de la TMR à $T=30K$.

description du rôle de la barrière dans l'effet tunnel, nous avons effectué des mesures de Dichroïsme Magnétique Circulaire X aux seuils K de O et Al sur des échantillons comprenant une interface Co/Al_2O_3 , ainsi qu'aux seuils K de O et Mg sur des échantillons comprenant une interface Fe/MgO . Nous montrons à titre d'exemple le résultat obtenu pour un échantillon épitaxié comprenant une interface $Fe/MgO(001)$ dans la Figure 9.8. Nous nous attendions à un moment de $0.2\mu_B$ sur le site O induit par Fe. [151] Sur cet échantillon, les moments de spin et orbital du Fe ont été calculés à $2.19\mu_B$ and $0.03\mu_B$ par atome, dans la barre d'erreurs des valeurs bulk $2.25\mu_B$ and $0.08\mu_B$ par atome. [150]

Malgré la qualité de nos échantillons et de bonnes conditions expérimentales, aucun dichroïsme reflétant un moment induit n'a été observé. Il est possible que l'incidence d'autres difficultés expérimentales, telles que la mesure d'un moment induit à une interface et non pas simplement au sein d'un environnement magnétique, rendent une telle observation plus ardue.

9.3.3 Spectroscopie tunnel polarisée en spin

Grace à $P_{LSMO@STO} > 95\%$, il est possible de sonder de manière explicite la densité d'états d'une contre-électrode par effet tunnel dépendant du spin. Nous avons ainsi effectué des études sur la dépendance en tension de la TMR dans des jonctions LSMO/STO/LSMO (voir Figure 9.9) et LSMO/STO/Co (voir Figure 9.11) dans le but de réaffirmer l'aspect spectroscopique de cette

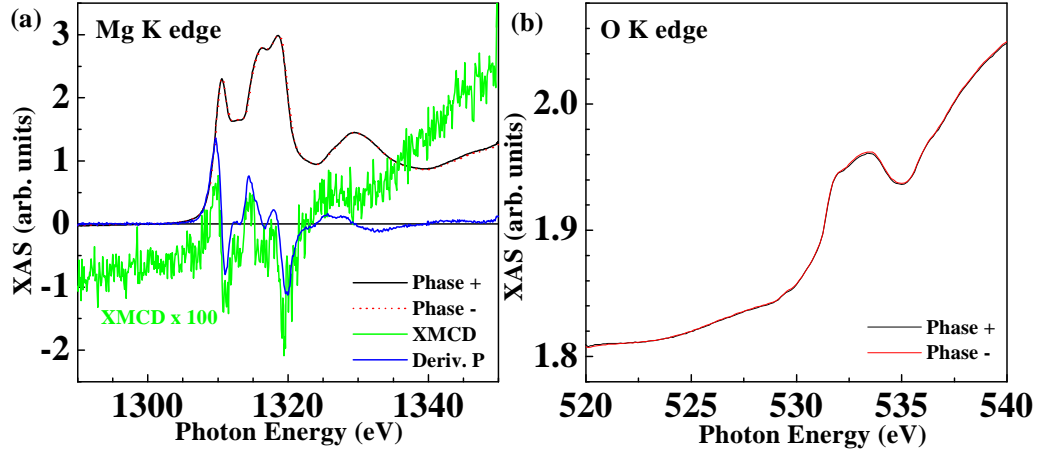


Figure 9.8: MgO(001)//MgO(100Å)/Fe(250Å)/MgO(10Å)/Fe(20Å)/Pt(20Å): absorption aux rayons X en phases positive et négative at $T=5\text{K}$, aux seuils (a) Al K et (b) O K. Aucune correction n'a été effectuée.

technique.

Dans un régime de faible tension, l'excitation d'ondes de spin aux interfaces de la jonction brouille les canaux de conduction polarisés en spin, entraînant une perte de polarisation de spin et la chute de la TMR. Cependant, lorsque la tension appliquée dépasse le seuil énergétique de génération de magnons, une proportion prépondérante du courant tunnel collecte conserve la polarisation de spin établie par l'électrode injectrice. Nous avons ainsi pu sonder le gap minoritaire δ de la manganite. D'après nos mesures de magnéto-transport vers l'interface LSMO/STO dans des jonctions LSMO/STO/LSMO et LSMO/STO/Co, ce gap a été évalué à $\delta = 0.35 \pm 0.05\text{eV}$, en accord quantitatif avec une mesure effectuée par photoémission inverse résolue en spin. [157, 192] Lorsque l'électrode injectrice est LSMO, les résultats expérimentaux sont plus limpides du fait de cette source de courant tunnel presque totalement polarisée en spin. La dépendance en tension de la TMR marque un point d'inflexion à $V=0.35\text{V}$ au terme d'un plateau avant de chuter de nouveau (voir Figure 9.9). De plus, P^2 marque un aussi un plateau à cette valeur avant de chuter de nouveau (voir insert de gauche). L'apparition de la bande minoritaire à δ entraîne une augmentation relative de la conductance antiparallèle lorsque les électrons \uparrow parviennent à occuper les premiers états au bas de cette bande \downarrow (voir Figure 9.10). Ces deux comportements avaient été prévus de manière théorique par Bratkovsky (voir Figure 9.10b). [31]

L'implication de ce résultat de spectroscopie tunnel polarisée en spin est

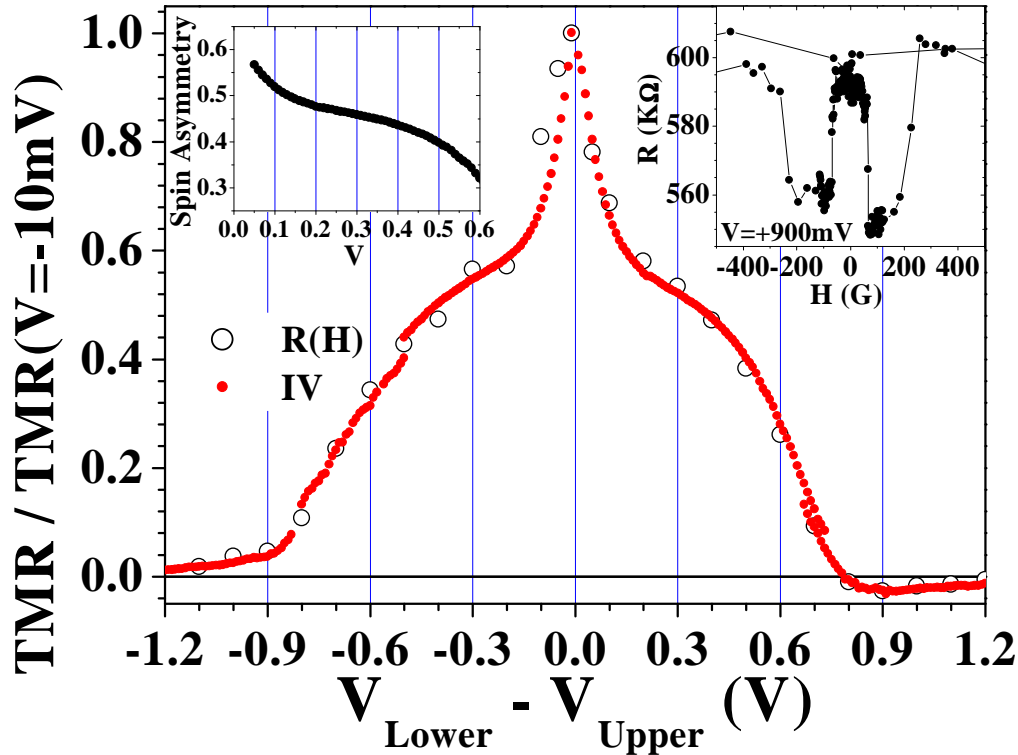


Figure 9.9: LSMO/STO/LSMO: dépendance en tension de la TMR à $T=4\text{K}$. Inset de gauche: dépendance en tension de P^2 . Inset de droite: cycle $R(H)$ à $V=+900\text{mV}$ montrant une TMR de -8% .

que le courant tunnel, malgré les excitations d'ondes de spin à faible tension, recouvre son degré de polarisation lorsque ce régime de tension est dépassé.

Grâce à ces résultats sur LSMO/STO/LSMO, il est possible de revisiter la dépendance en tension de la TMR dans le système LSMO/STO/Co (voir Figure 9.11).

Dans le système LSMO/STO/Co, le pic de TMR inverse observé à $V < 0$ a été tout d'abord attribué à un pic de densité d'états minoritaires de Co à $E \sim E_F + 0.3\text{eV}$ sondé pour ce signe de tension appliquée par LSMO (voir Figure 9.11). Pour confirmer cette interprétation spectroscopique de la dépendance en tension de la TMR, nous avons modifié de manière contrôlée cette densité d'états en dopant l'électrode de Co avec du Cr. Le potentiel perturbateur de l'impureté est suffisamment répulsif pour repousser les états d^\uparrow au-dessus du niveau de Fermi. Ces états s'hybrident par résonance avec ceux de la bande s pour former un état lié virtuel de très forte densité \uparrow juste au-dessus de E_F (voir Figure 9.12). [163] L'effet de ce dopage est donc de réduire la contribution du pic de DOS minoritaire de Co.

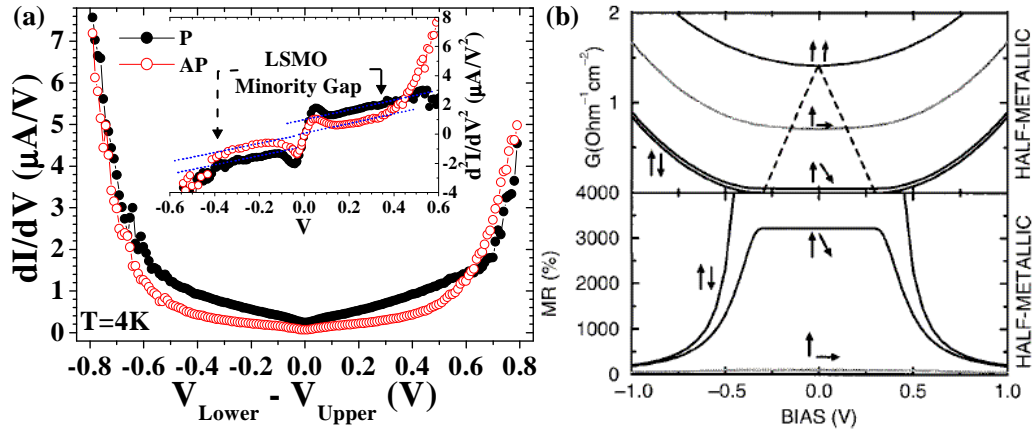


Figure 9.10: Effet tunnel entre demi-métaux: (a) LSMO/STO/LSMO, Jonction B: conductance $(dI)/(dV)$ dans les états parallèle (P: cercles fermés) et antiparallèle (AP: cercles ouverts). Insert: deuxième dérivée du courant mettant en évidence le gap minoritaire de LSMO aux deux interfaces. (b) Conductance (haut) et TMR (bas) calculées pour un gap demi-métallique $\delta=0.3eV$. D'après Bratkovsky [31]

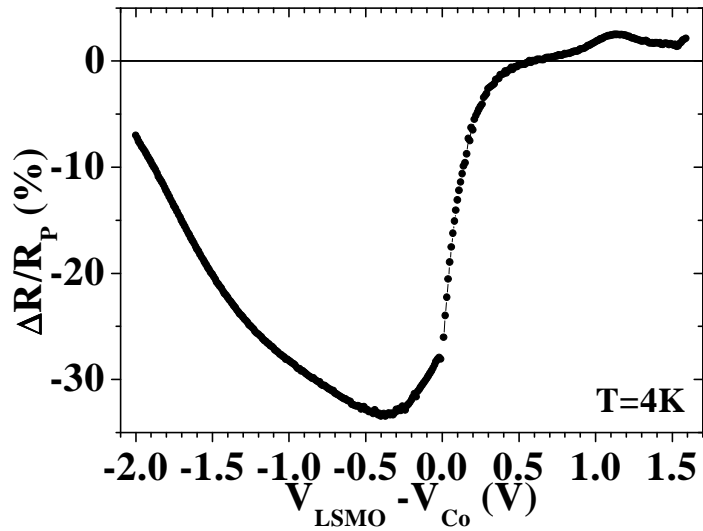


Figure 9.11: LSMO/STO/Co: dépendance en tension de la TMR à $T=4K$.

Nous avons ainsi étudié la dépendance en tension de la TMR dans le système LSMO/STO/Co_{1-x}Cr_x (voir Figure 9.13). Lorsque x augmente, le pic de TMR inverse semble se déplacer vers les tensions plus faibles, et à $x=0.16$ n'est plus visible, ainsi que l'on pouvait espérer de l'influence du dopage sur la DOS du Co sondée pour cette direction de tension ap-

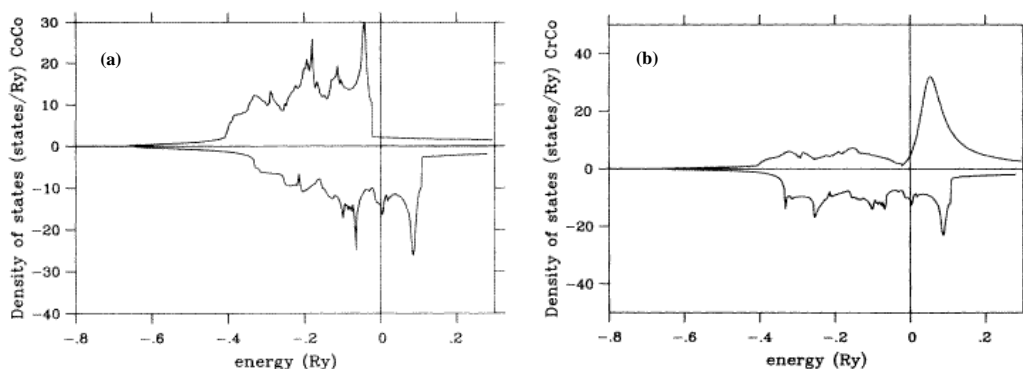


Figure 9.12: Calcul de la densité d'états résolue en spin de (a) Co , (b) sur le site d'une impureté de Cr. D'après Stepanyuk *et al.* [163]

pliquée. Il faut remarquer, cependant, que cette interprétation suppose une interface nominale $\text{SrTiO}_3/\text{Co}_{1-x}\text{Cr}_x$ sans réaction chimique. Nous réexaminerons ce système ci-après dans le cadre de résultats qui démontrent la forte réactivité chimique de cette interface, et la propension de celle-ci à des effets d'électromigration.

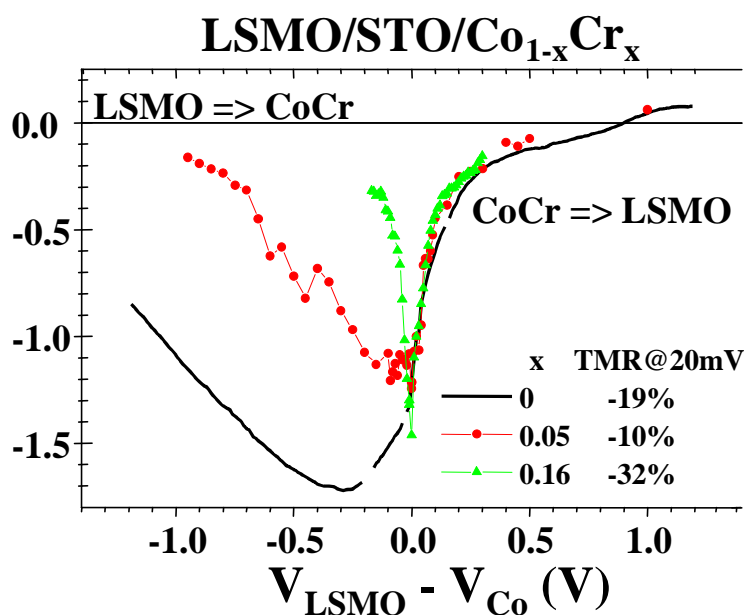


Figure 9.13: Dépendance en tension normalisée de jonctions $\text{LSMO}/\text{STO}/\text{Co}_{1-x}\text{Cr}_x$ à $T=30\text{K}$. Les valeurs de TMR observées sont rapportées dans la légende. Les flèches indiquent le sens du transport d'électrons.

9.3.4 Sur la température de Curie amoindrie à l'interface $\text{La}_{0.7}\text{Sr}_{0.3}\text{MnO}_3/\text{SrTiO}_3$

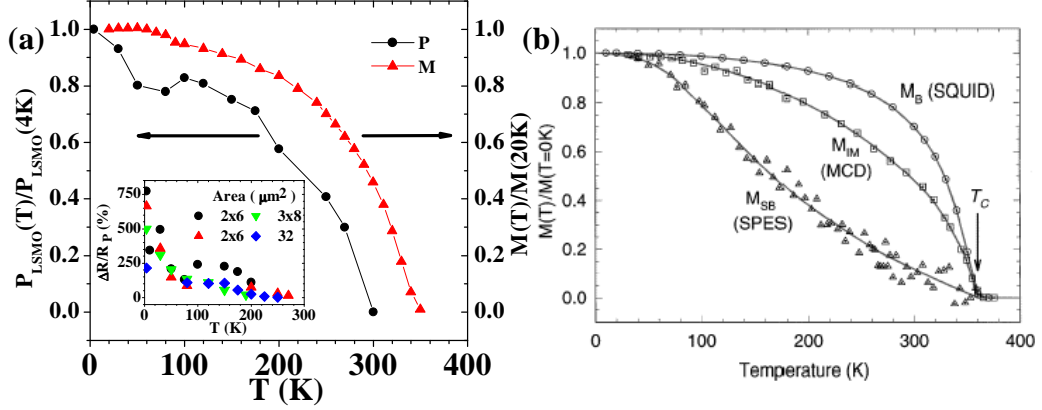


Figure 9.14: Dépendance en température du magnéto-transport à l'interface LSMO/STO: (a) P_{LSMO} normalisée, obtenue à partir des données de l'insert, comparée à l'aimantation M de l'échantillon. (b) Dépendance en température de l'aimantation bulk, celle de surface, et de la polarisation de spin de surface pour $\text{La}_{0.7}\text{Sr}_{0.3}\text{MnO}_3$, d'après Park *et al.* [164].

Malgré une température de Curie $T_C=350\text{K}$ dans des couches minces de LSMO, la TMR dans des jonctions LSMO/STO/LSMO ne subsiste jamais à cette température, au grand dam des perspectives d'applications à température ambiante d'un tel dispositif. En général, la TMR mesurée à faible tension devient nulle aux alentours de la température marquée par un pic de résistance. Il est supposé que ce pic correspond à la transition métal-isolant de la manganite à l'interface avec la barrière, et ainsi dénote une T_C d'interface amoindrie par rapport au bulk de la couche. À partir de la dépendance en température de la TMR dans nos jonctions LSMO/STO/LSMO, nous avons comparé la dépendance en température de la polarisation de spin moyenne des deux interfaces $P(T)$ (voir Equation 9.1) avec celle de l'aimantation $M(T)$ de notre tricouche (voir Figure 9.14a). Toutes deux semblent suivre une loi $\propto (1 - \alpha T^{3/2})$ établie pour des métaux de transition [75] ainsi que pour des électrodes à conduction par double échange. [165] Cependant, dans le cas de $P(T)$, $T_C < 300\text{K}$. Il faut noter que cette évolution d'interface enfouie est très différente de celle d'une surface non-protégée ainsi mesurée par Park *et al.* (voir Figure 9.14b). [164]

Afin de mieux comprendre les mécanismes de conduction à l'œuvre dans cette T_C amoindrie, nous avons examiné la dépendance en température du

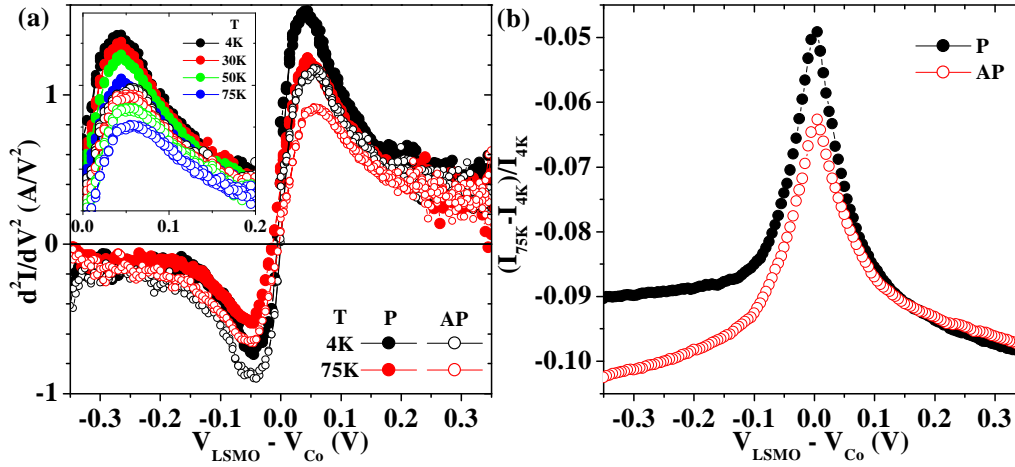


Figure 9.15: LSMO/STO/Co (Al2232): $A=48\mu\text{m}^2$: (a) deuxième dérivée du courant dans les états parallèle (cercles fermés) et antiparallèle (cercles ouverts). L'insert représente un agrandi comprenant une gamme de température plus complète. (b) Evolution en température du courant dans les états parallèle et antiparallèle.

magnéto-transport dans des jonctions LSMO/STO/Co. La Figure 9.15 montre la deuxième dérivée du courant dans les états parallèle and antiparallèle. Le comportement non-linéaire à faible tension est plus marqué lorsque les électrons chauds ($E=E_F + eV$) se désexcitent à l'interface LSMO/STO ($V>0$), par rapport à l'interface STO/Co ($V<0$). Ceci traduit la génération de magnons plus faible à cette interface du fait d'une T_C bien plus forte.

Nous avons mis à profit cette différence pour sonder l'influence de magnons sur le magnéto-transport à l'interface LSMO/STO. La Figure 9.16 présente l'évolution en température de la résistance de jonction à tension de descente V_{Desc} donnée. Alors qu'à faible tension un pic de résistance apparaît à la valeur amoindrie de température correspondant à la supposée T_C d'interface, lorsque la tension appliquée promeut l'injection d'électrons vers l'interface LSMO/STO ($V>0$) avec une énergie supérieure au seuil de génération de magnons d'interface, un deuxième pic apparaît à $T=340\text{K}$ de façon prédominante par rapport au premier. A tension négative l'apparition du pic est beaucoup moins marquée. Nous concluons qu'un régime de transport non-dominé par les excitations d'ondes de spin permet de sonder des propriétés électroniques intrinsèques à la manganite.

Ainsi, alors que la dépendance en température de la TMR à $V=+10\text{mV}$ décroît de manière monotone, de même que celle à $V=-500\text{mV}$, celle à $V=+500\text{mV}$ marque un plateau jusqu'à $T\approx 0.4T_C$ avant de décroître (voir

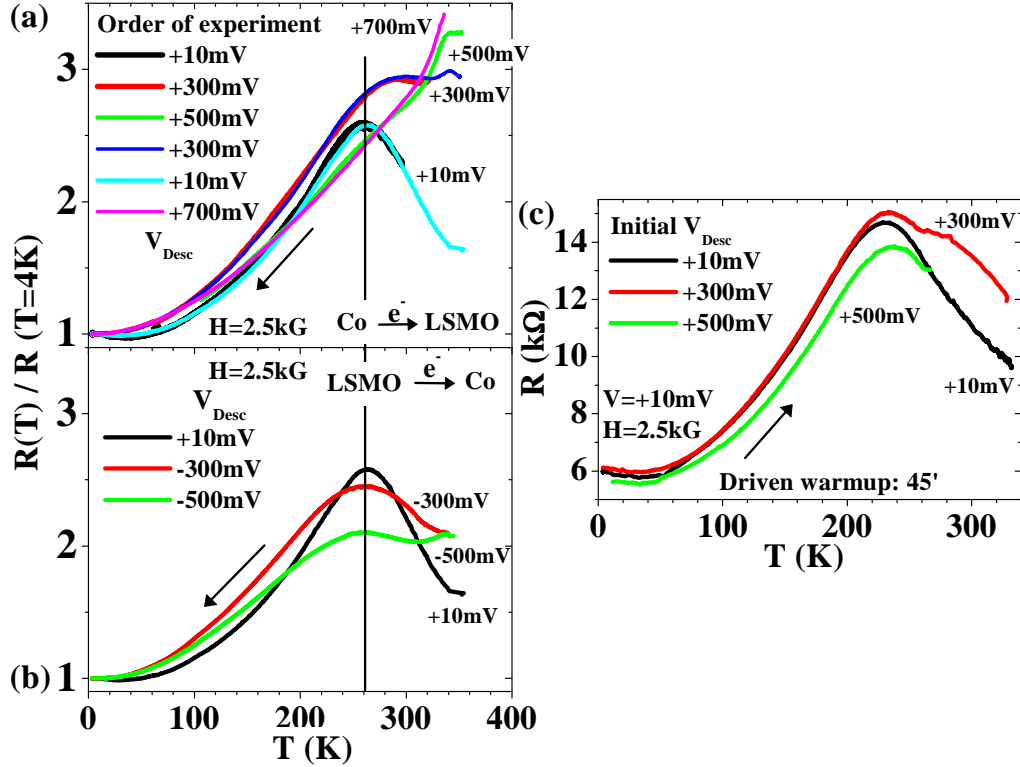


Figure 9.16: LSMO/STO/Co (Al1531): dépendance en température de la résistance de jonction à V_{Desc} , au sein et au-delà du régime d'excitations d'ondes de spin, lorsque les électrons sont injectés (a) vers LSMO, et (b) vers Co. (c) Résistance à $V=+10mV$ lors de remontées forcées après une descente à V_{Desc} .

Figure 9.17). Cette différence de comportement reflète l'influence des magnons sur la TMR(T) lorsque celle-ci est mesurée à faible tension, alors qu'à plus forte tension, la TMR(T) reflète le comportement intrinsèque de la manganite sujette à la perte de son caractère demi-métallique au-delà de $T=0.4T_C$, ainsi calculée par Itoh *et al.* [77] (voir Figure 2.13 page 29). De fait, ces résultats indiquent que la T_C d'interface n'est pas forcément amoindrie par rapport au bulk de la couche, mais reflète l'influence des magnons sur les propriétés électroniques de celle-ci. A tension négative, la montée d'un signal à $T=340K$ pourrait refléter un ferromagnétisme accru à l'interface LSMO/STO grâce à l'influence de la conduction par double échange sur les propriétés électroniques de celle-ci. [155]

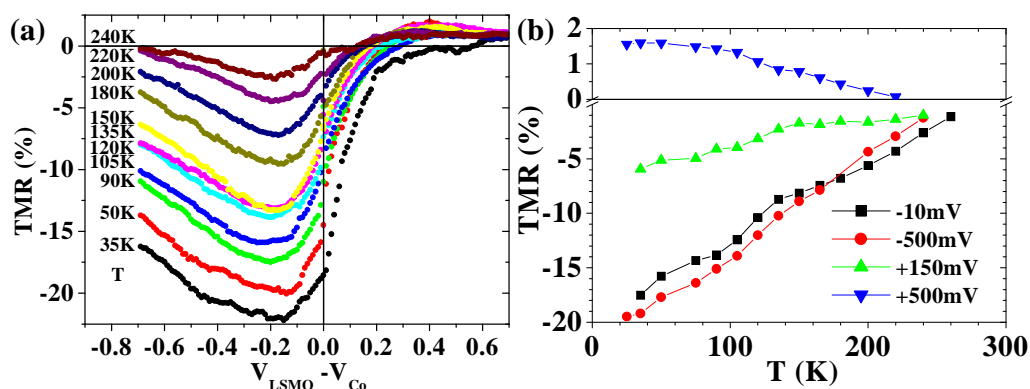


Figure 9.17: Dépendance en tension et en température de la TMR dans LSMO/STO/Co: (a) évolution de la dépendance en tension de la TMR à plusieurs températures, et (b) évolution en température de la TMR à plusieurs tensions.

9.3.5 Effets de barrière tunnel

Nous avons réalisé une série d'expériences qui mettent en avant l'influence de la barrière isolante sur le transport tunnel. Ces expériences dépendent très souvent de la prise en compte d'effets électromigrateurs au sein de l'hétérostructure afin d'expliquer les modifications apportées au magnéto-transport de la jonction. La Section 9.3.5.1 présente une série d'expériences sur LSMO/STO/CoCr qui tendent à illustrer les conséquences électromigratrices d'une interface chimiquement mal contrôlée, de forte réactivité due à la présence de Cr, sur les propriétés de magnéto-transport du système. Nous examinons ensuite la réponse à forte tension du magnéto-transport dans le système LSMO/STO/LSMO. Cette Section 9.3.5.2 met à profit l'effet d'électromigration afin de modifier le profil de potentiel de la barrière. Enfin, la Section 9.3.5.3 aborde les mêmes questions au regard de jonctions LSMO/STO/Co, plus particulièrement celles dont l'instabilité a été induite volontairement.

9.3.5.1 Électromigration à l'interface $\text{SrTiO}_3/\text{Co}_{1-x}\text{Cr}_x$

La démonstration de l'importance de ces effets est faite par le biais de mesures sur des jonctions $\text{La}_{0.7}\text{Sr}_{0.3}\text{MnO}_3/\text{SrTiO}_3/\text{Co}_{1-x}\text{Cr}_x$. Une étude à l'échelle nanoscopique de l'interface STO/CoCr effectuée par Spectroscopie électronique de pertes d'énergie témoigne d'une ségrégation de Cr et de son oxydation (Voir Section 7.1.1 page 123). La forte réactivité du Cr expliquerait ainsi l'instabilité électrique remarquée sur toutes les jonctions mesurées. En

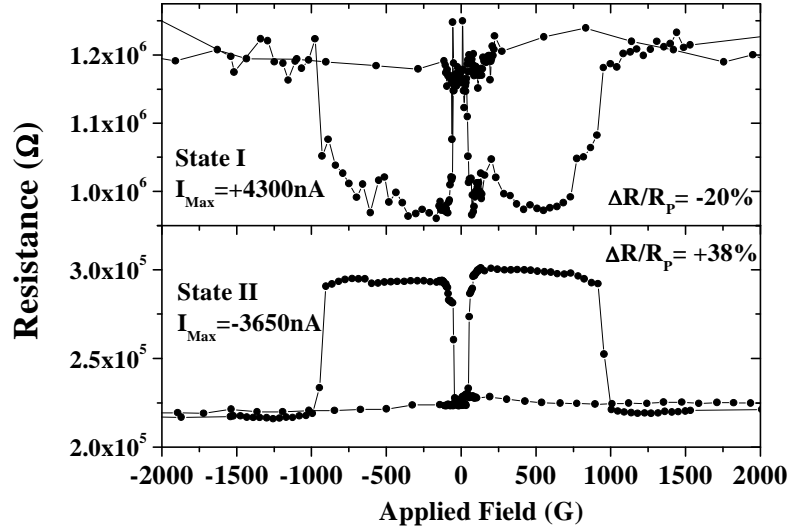


Figure 9.18: LSMO/STO/CoCr₈₀Cr₂₀, $A=12\mu\text{m}^2$. Cycles $R(H)$ à $V=+500\mu\text{V}$ dans les états de jonction I et II.

tenant bien compte de l'historique et de l'état de la jonction, il est possible d'affecter son magnéto-transport de manière généralement réversible en appliquant une tension suffisamment forte. Les résultats présentés sur trois d'entre elles font état d'un même comportement: lorsque la tension appliquée est positive, un abaissement de résistance et une caractéristique IV moins non-linéaire sont assorties dans cet état d'une TMR inverse. Lorsque la tension appliquée est négative, l'augmentation de résistance est accompagnée d'une TMR mal définie ou normale. Dans le cas extrême, il est possible de partir d'une jonction vierge ne présentant que quelques % de TMR mal définie, et après plusieurs cycles de "forming" de l'interface instable, d'obtenir sur cette jonction des TMR de -30% et +40% dans chacun des deux états (voir Figure 9.18). Le plateau d'alignement antiparallèle est le même dans les deux cycles, correspondant aux champs coercitifs des électrodes LSMO et CoCr. Ceci porte à croire que la réponse en champ magnétique de l'interface STO/CoCr est régie par l'électrode CoCr au travers d'un couplage ferromagnétique direct, mais que l'état chimique de l'interface détermine le signe de la polarisation de spin tunnel de celle-ci. En avançant des arguments d'électromigration de Cr et d'O à cette interface, il est possible de rendre compte de ces résultats: à tension négative, l'oxygène peut migrer vers CoCr alors que Cr peut migrer vers STO; à tension positive, une réduction de Cr aurait lieu. Cette activité électrochimique produirait alors une interface efficace de CrO₂ à tension négative, et CoCr à tension positive, avec un isolant

tel que Cr_2O_3 apte à rendre compte du signe de polarisation de spin des bandes d du ferromagnétique à l'interface avec celui-ci.

9.3.5.2 Jonctions $\text{La}_{0.7}\text{Sr}_{0.3}\text{MnO}_3/\text{SrTiO}_3/\text{La}_{0.7}\text{Sr}_{0.3}\text{MnO}_3$

Nous avons étudié la réponse en magnéto-transport de jonctions entièrement épitaxiées LSMO/STO/LSMO à fortes tensions. Dans la mesure où nous savons par le biais d'expériences de pertes d'énergies que les deux interfaces, bien que semblables, ne sont pas strictement identiques, [118] il n'est pas surprenant d'observer des différences quantitatives de magnéto-transport. Néanmoins, ces deux interfaces produisent une réponse similaire sur le plan qualitatif.

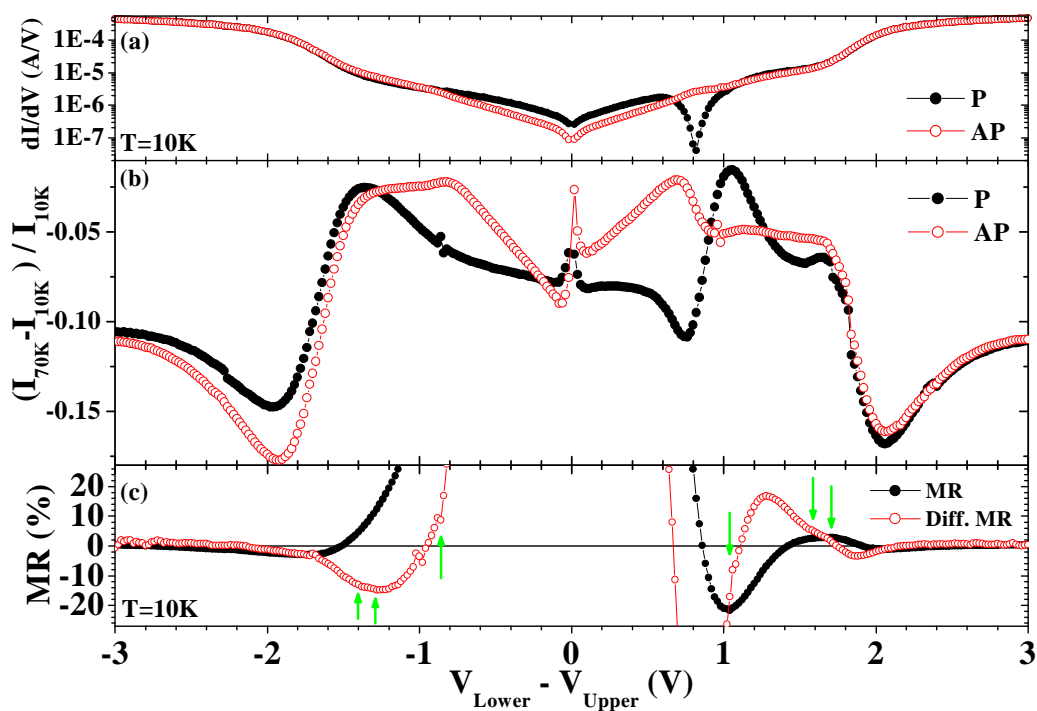


Figure 9.19: LSMO/STO/LSMO, jonction C dans l'état $V_{\text{Desc}}=+3\text{V}$: (a) conductance à $T=10\text{K}$ dans les états parallèle (P) et antiparallèle (AP). (b) Evolution en température d'IVs dans les états P et AP. (c) Détail à faible amplitude de la dépendance en tension de la TMR et de la TMR différentielle. $\text{Diff TMR} \equiv (dI_P/dV - dI_{AP}/dV) / dI_{AP}/dV$

Grâce à l'utilisation d'électrodes à forte polarisation de spin, il est possible de sonder une nouvelle gamme d'effets dans les jonctions tunnel lorsque la hauteur de barrière des porteurs de charge est franchie. La Figure 9.19

renseigne sur la relation entre le profil de potentiel de l'hétérostructure et sa réponse en magnétotransport. A partir de la tendance des conductances dans les états parallèle (P) et antiparallèle (AP) (panneau (a)), et de l'évolution en température des IVs P et AP (panneau (b)), [122] il est possible d'extraire une appréciation des hauteurs de barrière de la jonction et d'examiner l'incidence sur le magnétotransport (panneau (c)). Dans le régime tunnel Fowler-Nordheim qui décrit le transport au-delà de la hauteur de barrière, [50] les porteurs de charge quittant le niveau de Fermi de l'électrode injectrice tunnelent au travers d'une barrière d'épaisseur réduite avant d'entrer dans une bande d'états de l'isolant.

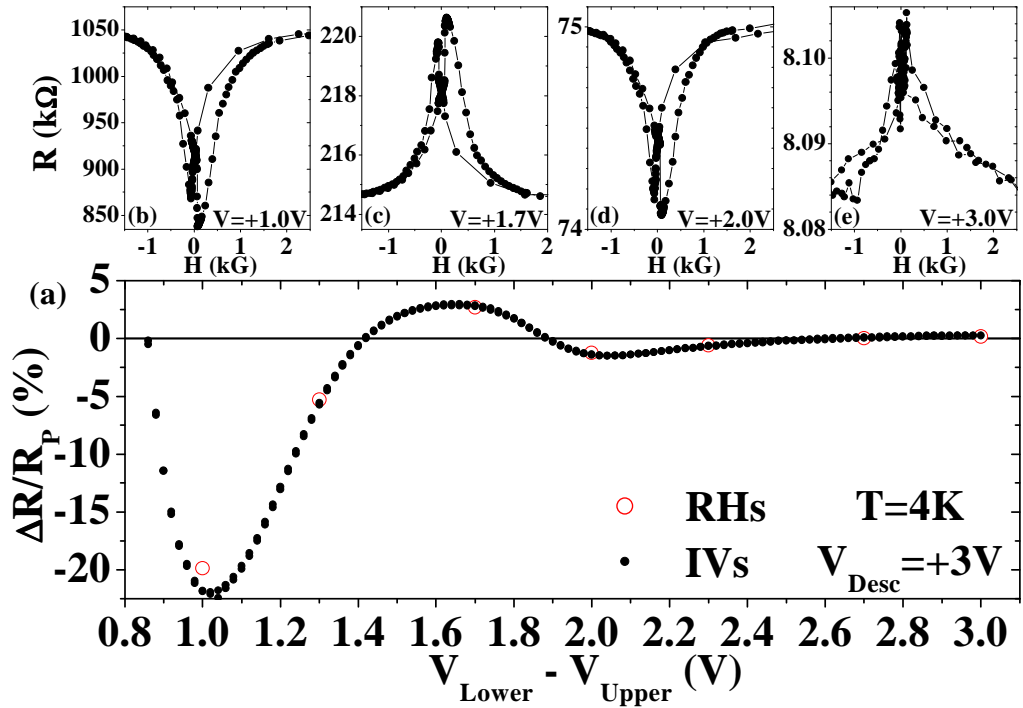


Figure 9.20: LSMO/STO/LSMO: (a) dépendance en tension de la TMR à $T=10\text{K}$, confirmée par des cycles $R(H)$ à (b) $V=+1\text{V}$, (c) $V=+1.7\text{V}$, (d) $V=+2\text{V}$, et (e) $V=+3\text{V}$.

Il en découle de multiples oscillations de TMR, observées jusqu'à $|V|=3\text{V}$ (voir Figure 9.20). Même à $V=+3\text{V}$, la résistance de jonction $R \approx 8\text{k}\Omega$ est suffisamment élevée pour exclure des effets d'injection inhomogène de courant dans le pilier. [115] De plus, des modifications de profil de barrière induites par électromigration (voir Figure 9.21) provoquent l'évolution en amplitude et la période de ces oscillations (voir Figure 9.22) en accord qualitatif avec la théorie concernant les répercussions de l'abruptesse des interfaces

et des interférences de fonctions d'onde dans le régime tunnel de Fowler-Nordheim. [21]

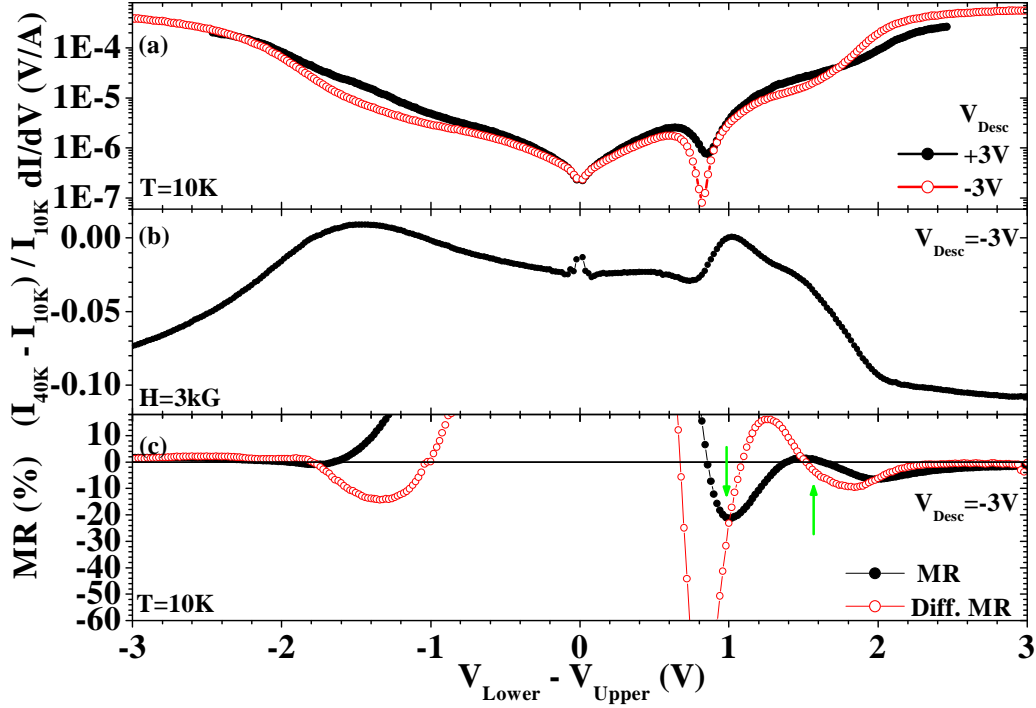


Figure 9.21: LSMO/STO/LSMO: (a) conductance à $T=10\text{K}$ dans les états parallèle (P) et antiparallèle (AP). (b) Evolution en température d'IVs dans l'état P. (c) Détail à faible amplitude de la dépendance en tension de la TMR et de la TMR différentielle. $\text{Diff TMR} \equiv (dI_P/dV - dI_{AP}/dV) / dI_{AP}/dV$

Ce résultat s'apparente à celui rapporté [88] par Yuasa *et al.* sur l'oscillation de TMR observée lorsque l'épaisseur d de Cu est augmentée dans des jonctions $\text{Co}(001)/\text{Cu}(d)/\text{Al}_2\text{O}_3/\text{Fe}_{80}\text{Ni}_{20}$.¹ Ce résultat ressemble lui-même à celui rapporté par Moodera *et al.* sur des échantillons similaires mais de moins bonne qualité. [52] Dans les deux cas, la formation d'états quantifiés soutend un tel comportement. Cependant, la grande originalité de notre résultat est que ces états se trouvent au sein d'une portion métallique de la barrière dans un régime Fowler-Nordheim de transport tunnel. La spectroscopie tunnel de ces états est plus ardue puisque la sonde spectroscopique que représente l'application de tension modifie par ailleurs l'épaisseur de l'intercouche métallique, et donc l'énergie de ces états. C'est pourquoi il est très intéressant de mettre à profit l'électromigration comme

¹Voir Figure 2.18 page 36

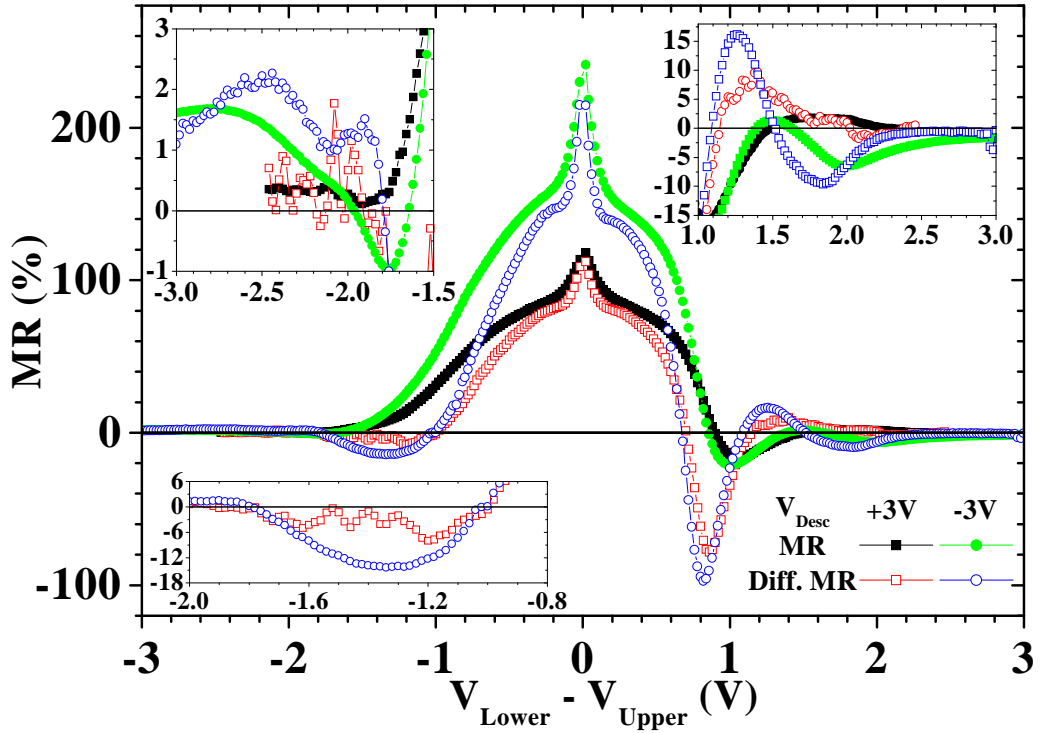


Figure 9.22: LSMO/STO/LSMO: dépendance en tension de la TMR et de la TMR différentielle dans les états $V_{Desc}=+3V$ and $V_{Desc}=-3V$. Des agrandis sont présentés dans les inserts. Une légende générale s'applique à tous les graphes.

paramètre supplémentaire pour influencer de manière indépendante la position énergétique des états quantifiés que reflète l'évolution en tension de la TMR dans un tel régime de conduction (voir Figure 9.22).

La conjonction des conductances parallèle et antiparallèle, de l'évolution relative du courant à tension donnée avec la température, et des magnétorésistances directe et différentielle (voir Figures 9.19& 9.21), met en évidence un aspect absolument novateur du transport tunnel à très forte tension. Dans le cas d'une barrière de $SrTiO_3$, le niveau de Fermi se retrouve plus près de la bande de conduction que de celle de valence, à la fois de manière intrinsèque, et du fait d'un éventuel transfert de charge au contact avec un métal. Ceci implique une hauteur de barrière plus faible pour les électrons que pour les trous. Ainsi, pour un signe de tension appliquée, le transport tunnel va d'abord franchir la hauteur de barrière électronique correspondant à l'interface qui collecte les électrons. Cependant, pour une tension suffisamment forte, la hauteur de barrière de trous correspondant à l'autre

interface - celle qui collecte les trous, peut à son tour être franchie. Un tel scénario peut expliquer le comportement en tension de la TMR différentielle, qui sonde l'évolution instantanée du magnéto-transport à tension donnée. Grâce à l'évolution relative du courant à tension donnée avec la température, une série de deux pics indépendants du spin peuvent être attribués au franchissement d'une hauteur de barrière pour chaque sens de tension appliquée. À chacune de ces valeurs de tension correspond une brisure dans la courbe de TMR différentielle (voir Figure 9.19). L'évolution de ces valeurs de tension avec la tension de descente en froid V_{Desc} peut s'expliquer par des arguments d'électromigration qui modifient la position du niveau de Fermi à chaque interface.² Alors que la TMR différentielle demeure stable en-dessous de ladite barrière électronique avec V_{Desc} , au-delà de cette valeur le magnéto-transport peut évoluer. Des changements se produisent aussi lorsque la barrière de trous est alors franchie. Comme nous l'avons argumenté ci-dessus, ces changements peuvent traduire une modification de l'énergie des états quantifiés au sein de la barrière franchie en régime Fowler-Nordheim.

L'effet de magnétorésistance géante entre deux couches magnétiques (FM) est expliqué par la formation d'états quantifiés au sein de l'intercouche métallique non-magnétique (NM) au vu du confinement électronique apporté par le mésalignement de structures de bandes entre FM et NM, ainsi que la propriété de nesting de la surface de Fermi du NM permettant la rétrodiffusion cohérente et résonante de l'onde électronique dans l'intercouche. À cette description de l'effet en correspond une autre, celle du couplage d'échange magnétique intercouches qui régit le signe du couplage entre les deux FM par le biais d'interactions RKKY au travers du NM en fonction de son épaisseur. Bien que cet effet ait été principalement étudié dans des systèmes simples de métaux élémentaires, tels que Co(001)/Cu(001), plusieurs expériences décrivent des effets similaires lorsque le NM est un oxyde, métallique [63] ou isolant. [62] En particulier, le composé SrTiO₃ (001) remplit la condition de nesting de la surface de Fermi³ du NM et par ailleurs promeut un couplage d'échange indirect entre des couches La_{0.7}Sr_{0.3}MnO₃. [65, 66]

Ainsi donc, la formation d'états quantifiés en régime Fowler-Nordheim décrite ci-dessus devrait s'accompagner d'un changement dans le couplage d'échange. Sur les traces de Krivorotov *et al.*,⁴ nous avons examiné la réponse à fort champ de la résistance de notre jonction tandis que nous franchissons tour à tour les barrières d'électrons et de trous. Un changement

²Voir Tableau 7.1 page 142

³Voir Figure A.4 page 229

⁴Voir Figure 7.19 page 152

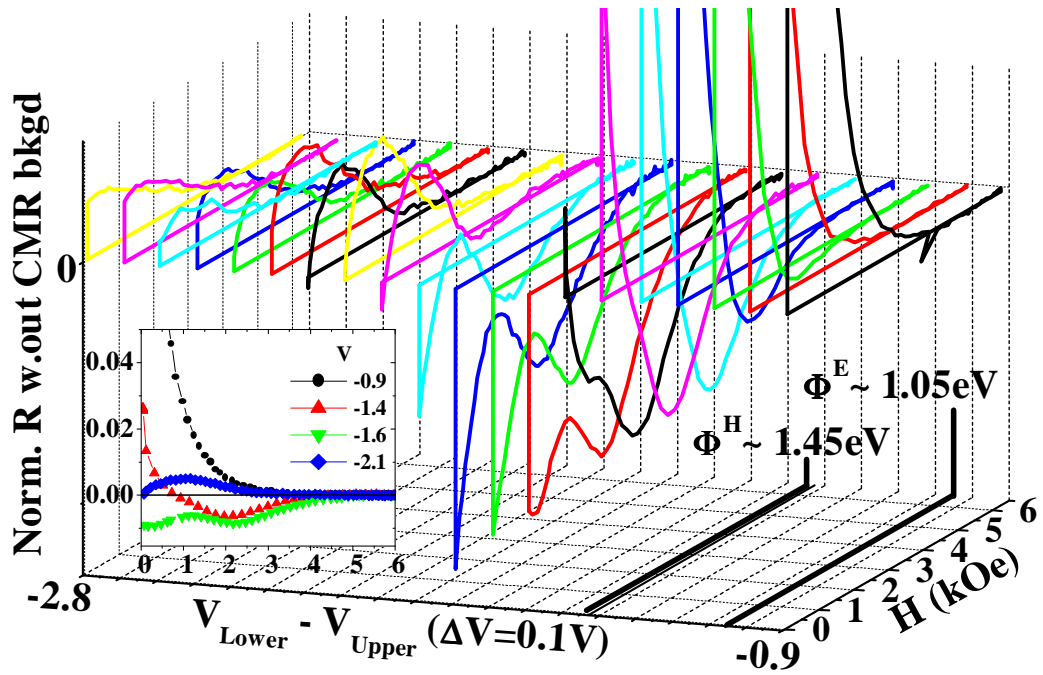


Figure 9.23: LSMO/STO/LSMO: Dépendance en champ magnétique appliqué décroissant de la résistance de jonction sur la gamme de tensions $-0.9\text{V} < V < -2.8\text{V}$, par pas $\Delta V = 0.1\text{V}$. L'insert fournit une perspective 2D sur quelques courbes de cet ensemble de données. Une contribution linéaire de CMR à été soustraite.

dans le comportement de cette réponse se produit à chacune des deux valeurs de tensions correspondant au dépassement de ces hauteurs de barrière (voir Figure 9.23). Ainsi, le changement dans l'évolution de la TMR différentielle et dans le comportement de la jonction à fort champ traduit les deux images d'états quantifiés et de couplage d'échange indirect à l'œuvre lorsque le régime Fowler-Nordheim est atteint pour électrons et trous à très forte tension dans une jonction tunnel LSMO/STO/LSMO.

9.3.5.3 Jonctions $\text{La}_{0.7}\text{Sr}_{0.3}\text{MnO}_3/\text{SrTiO}_3/\text{Co}$

Au vu des effets de barrière tunnel observés ci-avant dans des jonctions LSMO/STO/LSMO, nous distillons maintenant une compréhension accrue du magnéto-transport dans le système LSMO/STO/Co. Nous avons tout d'abord examiné l'influence de la cristallinité de la barrière tunnel. Puis nous avons observé l'effet de recuits sur le profil de potentiel de la barrière et l'incidence sur le magnéto-transport. Enfin, nous mettons à profit une instabilité électrique volontairement occasionnée pour examiner ce lien de manière plus systématique.

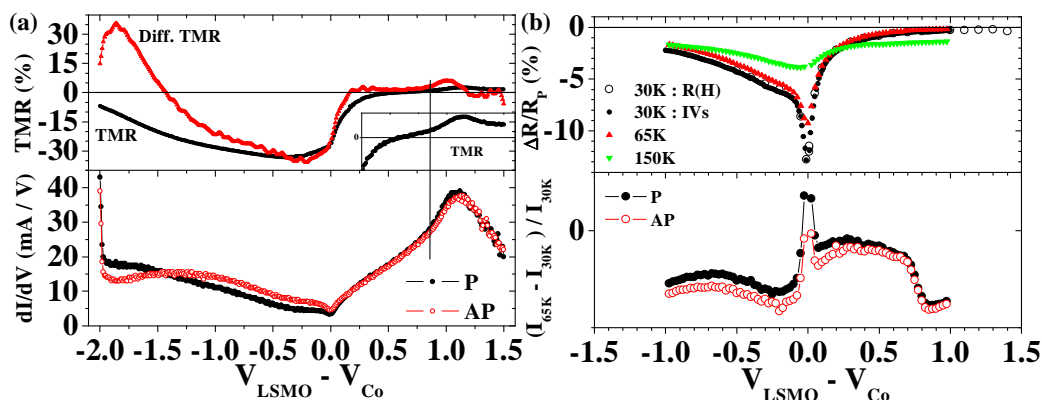


Figure 9.24: LSMO/STO/Co: comparaison du magnéto-transport lorsque la barrière est (a) épitaxiée ou (b) polycristalline. Le panneau du haut représente la dépendance en tension de la TMR, tandis que celui du bas renseigne sur les hauteurs de barrière tunnel. Les oscillations de TMR dans le panneau (a) représentent un artéfacte numérique.

Cristallinité de la barrière tunnel Lorsque SrTiO_3 est moins bien cristallisé, la dépendance en tension de la TMR ne montre plus le pic de TMR inverse ni l'inversion du signe de TMR (voir Figure 9.24).

En comparaison avec le cas d'une barrière epitaxiée, ce système introduit de nombreux changements. Outre la qualité cristalline moindre de la barrière, les interfaces ont pu aussi changer. Afin de cerner chaque contribution, nous examinons alors le magnéto-transport dans la jonction $\text{La}_{0.7}\text{Sr}_{0.3}\text{MnO}_3/\text{Ce}_{0.69}\text{La}_{0.31}\text{O}_{1.845}/\text{Co}$. D'après le cliché TEM,⁵ cette jonction présente une interface $\text{La}_{0.7}\text{Sr}_{0.3}\text{MnO}_3/\text{Ce}_{0.69}\text{La}_{0.31}\text{O}_{1.845}$ bien différente de $\text{La}_{0.7}\text{Sr}_{0.3}\text{MnO}_3/\text{SrTiO}_3$ par la présence d'importants défauts d'empilements sur deux monocouches. La comparaison du magnéto-transport entre les deux systèmes se justifie par une transmission tunnel de caractère électronique semblable (voir la Section sur le rôle de la barrière). Ainsi, dans le système $\text{La}_{0.7}\text{Sr}_{0.3}\text{MnO}_3/\text{Ce}_{0.69}\text{La}_{0.31}\text{O}_{1.845}/\text{Co}$, il n'y a pas de pic de TMR inverse à $V \neq 0$.⁶ Notre mesure ne permet pas de conclure sur la présence ou non d'une inversion de signe de TMR. Cette comparaison entre STO épitaxié, STO de moindre qualité cristalline et $\text{Ce}_{0.69}\text{La}_{0.31}\text{O}_{1.845}$ montre un lien entre la cristallinité de la barrière et le pic de TMR inverse.

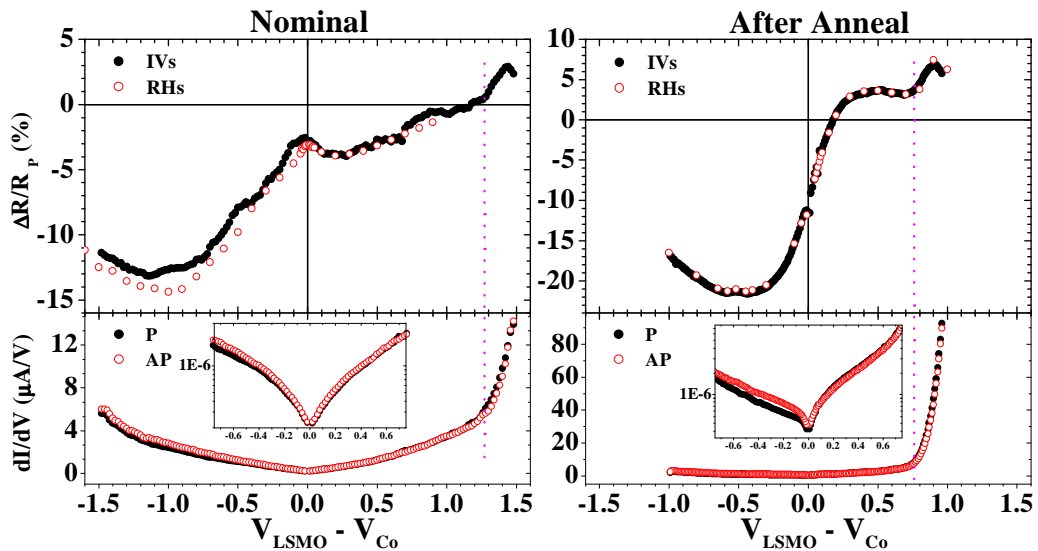


Figure 9.25: LSMO/STO/Co: Évolution des propriétés de magnéto-transport d'une jonction atypique (a) vierge et (b) après recuit : dépendance en tension de la TMR et de la conductance dans les états parallèle (P) et antiparallèle (AP). Les inserts aux panneaux inférieurs représentent les mêmes données à faible tension sur une échelle logarithmique.

⁵voir Figure 7.21a page 156

⁶Voir Figure 7.21 page 156

Recuit de jonctions La Figure 9.25 résume les changements sur le profil de l'hétérostructure qui peuvent survenir lors de recuits de jonctions aux propriétés inhabituelles. La position en tension de du pic de TMR inverse peut varier, non seulement d'échantillon à échantillon, mais aussi sur le même échantillon par le biais de cette technique. De plus, le dépassement de la hauteur de barrière tunnel, qui varie aussi après ces modifications, est toujours associé avec un changement dans la dépendance en tension de la TMR, de la même manière qu'avec une jonction LSMO/STO/LSMO.

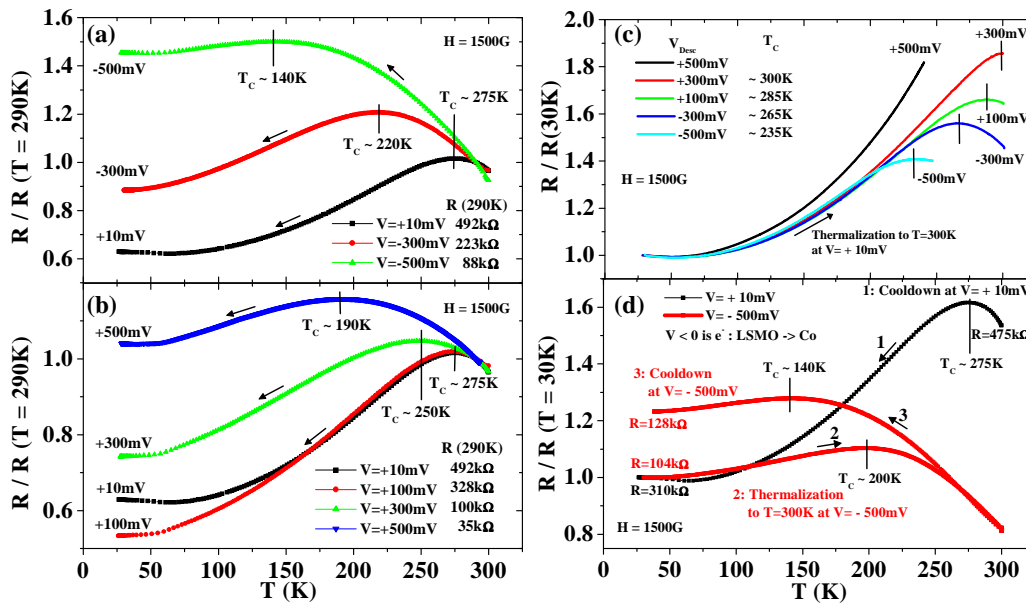


Figure 9.26: $\text{La}_{0.7}\text{Sr}_{0.3}\text{MnO}_3$ (350\AA)/ SrTiO_3 (7ML) + O_2 etch / Co (125\AA) / CoO (25\AA) / Au (Al1597): évolution en température de la résistance à tension V_{Desc} : une plus faible T_C d'interface et un état de basse température plus résistif reflètent les états formés (a) à $V_{Desc} < 0$ par rapport à (b) $V_{Desc} > 0$. (c) La thermalisation de la jonction à $V=+10\text{mV}$ traduit l'amélioration de la T_C d'interface lorsque V_{Desc} passe de valeurs négatives à des valeurs positives. (d) Après un refroidissement à $V_{Desc}=+10\text{mV}$, la jonction est réchauffée à $V=-500\text{mV}$ avant un nouveau refroidissement vers un état de résistance différent. Pour toutes ces données, $H=1.5\text{kG}$.

Electromigration Nous avons montré auparavant sur des jonctions LSMO/STO/LSMO comment des effets électromigrateurs pouvaient engendrer des modifications sur le profil de potentiel de la jonction, en notant les répercussions sur le magnéto-transport. En effectuant un nettoyage par

plasma O_2 de la surface de STO avant le dépôt de la contre-électrode de Co, les jonctions ensuite conçues par lithographie sur un tel échantillon montrent toutes une instabilité électrique ainsi que l'avaient remarqué Sun *et al.* [131]. Nous avons alors mis à profit les effets électromigrateurs qui soutiennent cette instabilité électrique afin de sonder l'influence du profil de barrière sur le magnéto-transport. Plus précisément, il est possible de préparer la jonction dans un état stable à basse température en appliquant une tension V_{Desc} de préparation (pendant plusieurs heures) avant la descente en froid (voir Figure 9.26).

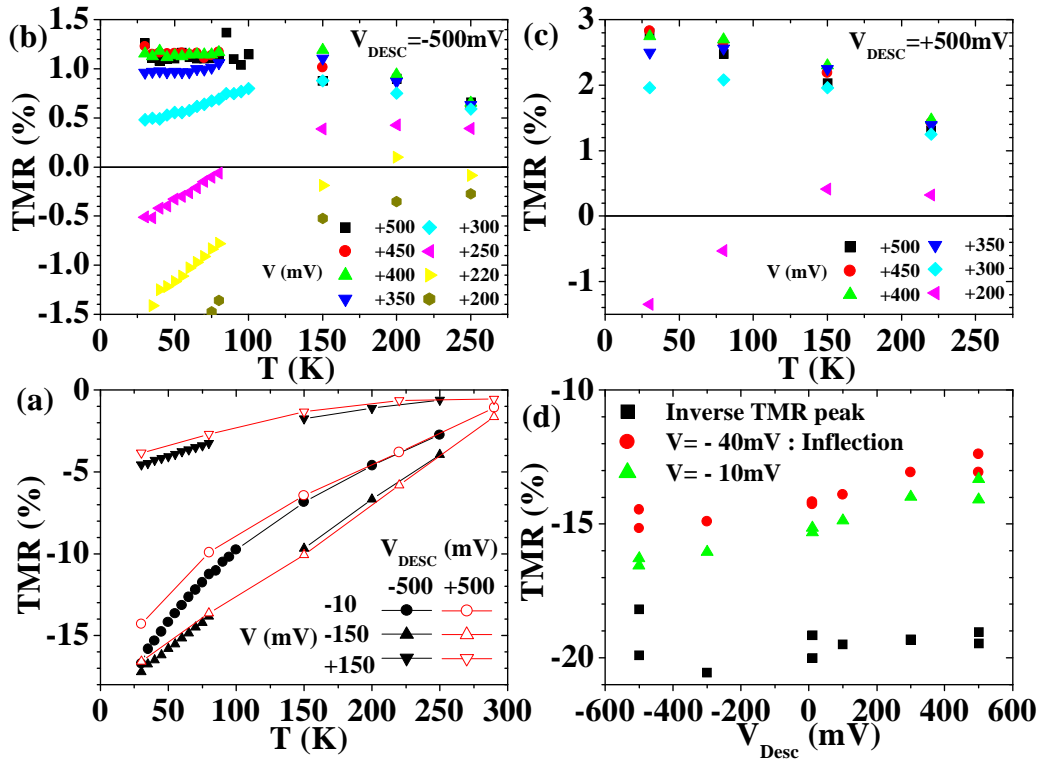


Figure 9.27: Evolution en température de la TMR (a) pour des valeurs remarquables de tension dans les états $V_{Desc} = -500$ mV (symboles pleins) et $V_{Desc} = +500$ mV (symboles ouverts); (b) pour $V_{Desc} = -500$ mV et (c) $V_{Desc} = +500$ mV. (d) Amplitude de TMR pour certaines valeurs de tension en fonction de V_{Desc} . Les lignes dans le panneau (a) servent de guide. Toutes ces données ont été obtenues à partir de cycles $R(H)$.

Dans ce type de jonction, la présence de défauts dans la barrière induit une conduction accrue par états localisés. [71] S'ensuit aussi une décroissance plus marquée de la TMR à faible tension avec la température. [72] Si l'on

rapporte le signe de V_{Desc} à des effets électromigrateurs, alors cette signature du transport tunnel assisté, plus marquée pour $V_{Desc} < 0$, peut être attribuée à une électromigration de Ti (voir Figure 9.27).

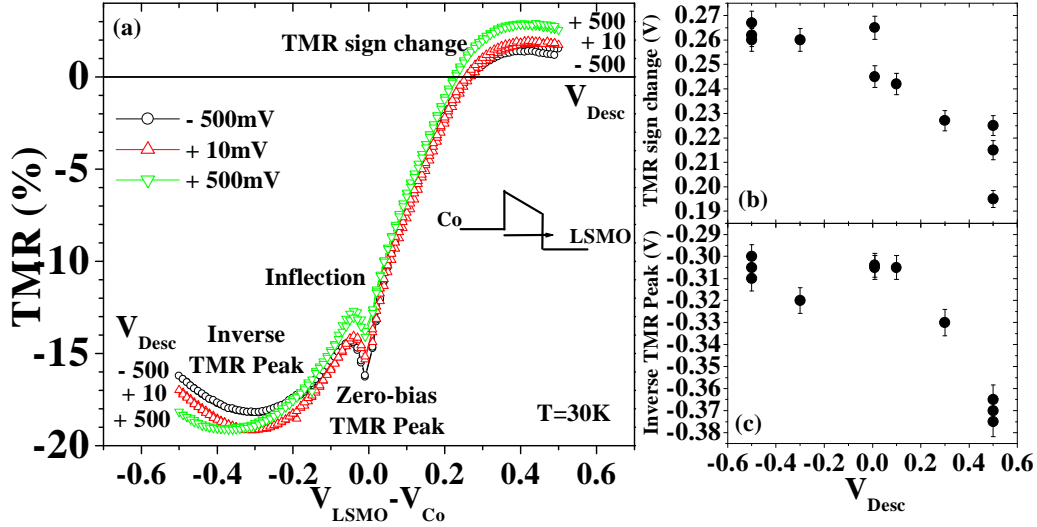


Figure 9.28: (a) dépendance en tension de la TMR d'une jonction LSMO/STO/Co avec une surface de STO etchée, à $T=30$ K selon V_{Desc} . Evolution en tension (b) du point de renversement de la TMR et (c) du pic de TMR inverse, selon V_{Desc} .

Cet effet électromigrateur influence de manière complémentaire les positions en tension du pic de TMR inverse et de l'inversion de signe de la TMR. Alors qu'à $V_{Desc} < 0$, ces positions demeurent constantes, à $V_{Desc} > 0$ elles se déplacent de la même amplitude: la première augmente, tandis que la seconde décroît (voir Figure 9.28). Toujours dans une perspective d'électromigration au sein de la barrière, ces changements pourraient traduire une modification du niveau de Fermi à chaque interface.

La dépendance en température du magnéto-transport renseigne aussi sur les effets soutenant la réponse en tension (voir Figure 9.29). Outre l'affaîsment du pic de TMR à $V=0$ lorsque la conduction dans $\text{La}_{0.7}\text{Sr}_{0.3}\text{MnO}_3$ adopte elle-aussi un caractère localisé au-delà de $T_C/2$, les positions en tension du pic de TMR inverse et du renversement de signe de la TMR évoluent aussi. Cette dernière chute lorsque des effets de transport thermiquement assistés viennent brouiller les canaux de conduction pour $T > 40$ K. Cela peut ainsi traduire l'influence des DOS des électrodes sur cette caractéristique de magnéto-transport. Quant au pic de TMR inverse, son affaîsment au-delà de $T=90$ K pourrait refléter la participation de fluctuations d'ondes de spin à l'interface LSMO/STO au-delà de $0.4T_C$. [77]

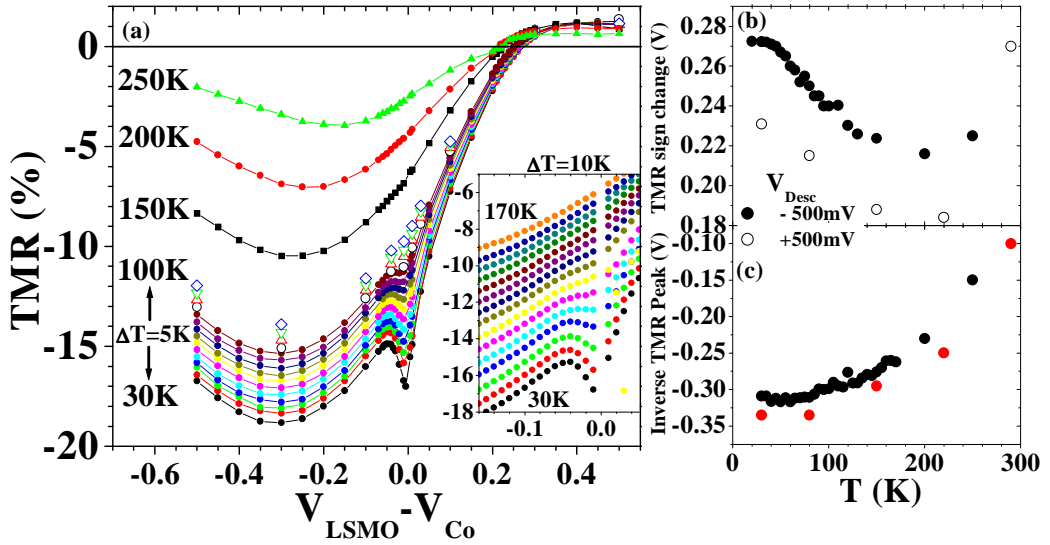


Figure 9.29: dépendance en température de la TMR d'une jonction LSMO/STO/Co avec une surface de STO etchéedé: (a) dépendance en tension. Evolution en tension (b) du point de renversement de la TMR et (c) du pic de TMR inverse, avec la température. Toutes ces données ont été obtenues à partir de cycles $R(H)$. L'insert du panneau (a) fournit le détail de l'évolution en température de la dépendance en tension de la TMR à partir de données IV.

Ainsi que décrit précédemment, nous avons aussi étudié la dépendance en température de la TMR à diverses tensions, mais ici par ailleurs pour $V_{Desc} = \pm 500mV$. De même que dans le cas d'une jonction stable, une jonction instable présente aussi une décroissance monotone de TMR pour $V \leq +100mV$, et un plateau jusqu'à $T = T_C/2$ pour $V > +100mV$ (voir Figure 9.27). Cependant, l'approche en tension vers ce régime traduit une oscillation de TMR pour certaines valeurs de tension appliquées. Cette oscillation varie avec V_{Desc} . Vu que la hauteur de barrière semble évoluer aussi (ainsi caractérisée par l'évolution en température du point d'inversion de la TMR), ces oscillations pourraient refléter l'influence d'états quantifiés dans un régime Fowler-Nordheim de transport tunnel.

De même qu'avec le système LSMO/STO/LSMO, nous avons alors examiné l'évolution de la résistance à fort champ avec la tension appliquée au vu des hauteurs de barrière (voir Figure 9.30). Un changement survient lorsque une hauteur de barrière, clairement démontrée à $V = +425mV$, est franchie (voir Figure 9.31). Par ailleurs, un autre changement survient à une très faible tension $V = +50mV$. Ceci pourrait indiquer la présence d'une barrière

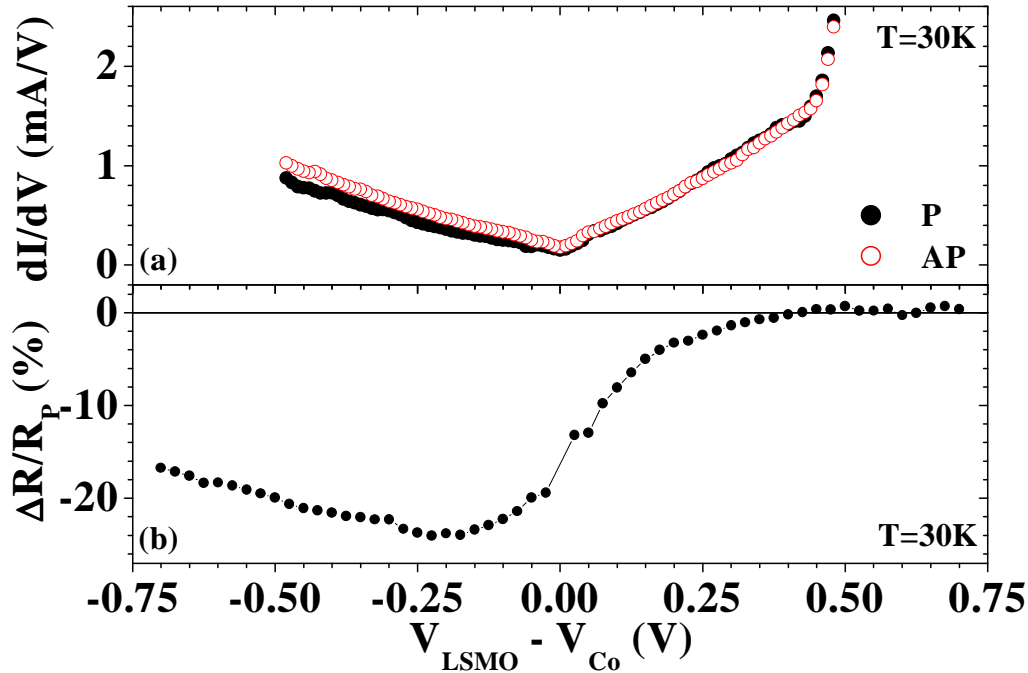


Figure 9.30: LSMO/STO/Co: (a) conductance dans les états parallèle (P) et antiparallèle (AP). (b) Dépendance en tension de la TMR.

électronique de faible amplitude à l'interface LSMO/STO, auquel cas la seconde barrière serait celle de trous à l'interface STO/Co. Évidemment, cette argumentation suppose ici encore la confirmation théorique d'un tel schéma physique. Enfin, il est intéressant de noter à tension négative une évolution constante d'oscillations à fort champ de la résistance avec la tension appliquée. Cette observation reflèterait alors l'évolution du couplage d'échange indirect dans une jonction dont le profil de barrière est asymétrique.

9.4 Conclusions et perspectives

L'objectif de cette Thèse aura été de rapprocher la description théorique de l'effet tunnel polarisé en spin de la réalité expérimentale dans des dispositifs à l'état solide. Au cours de ces travaux, la polarisation de spin quasi-totale de la manganite $\text{La}_{0.7}\text{Sr}_{0.3}\text{MnO}_3$, que nous avons évaluée à plus de 95%, aura servi d'outil pour favoriser la compréhension du transport tunnel polarisé en spin. Une série d'expériences de magnéto-transport, assortie de manipulations XMCD, a en partie mis en évidence le rôle que joue le matériau formant la barrière tunnel. De plus, l'aspect spectroscopique du transport tunnel

polarisé en spin a été explicitement démontré. En particulier, le rôle que joue la génération de magnons a été bien souligné dans cette optique. Ce rôle est reconfirmé au travers de la dépendance en température de la TMR: la T_C amoindrie de la manganite à l'interface avec la barrière pourrait provenir de l'influence des magnons sur les propriétés électroniques de celle-ci. Ce constat devrait relancer l'objectif d'intégrer des composés demi-métalliques tels que les manganites dans des dispositifs tunnel fonctionnant à température ambiante.

Une avancée majeure, peut-être controversée, dans le sujet des jonctions tunnel aura été la compréhension expérimentale du magnéto-transport à forte tension en fonction du franchissement des hauteurs de barrières d'électrons et de trous à chacune des deux interfaces sondées pour une direction de tension donnée. Cette description fournit une base afin de comprendre des effets d'états quantifiés et de couplage d'échange indirect au sein de la barrière tunnel dans un régime Fowler-Nordheim. À ce stade de notre compréhension, il est difficile d'expliquer comment le fait de franchir la hauteur de barrière électronique ne produit pas une augmentation conséquente de conductance ainsi que c'est le cas concernant la barrière de trous. Dans l'esprit d'effets de structure de bande au travers de la tricouche Fe/MgO/Fe [46], ce fait pourrait traduire la différente symétrie électronique Δ_2 des électrons de $\text{La}_{0.7}\text{Sr}_{0.3}\text{MnO}_3$ et Δ_5 de la bande de conduction de SrTiO_3 .

L'évolution du sujet des jonctions tunnel magnétiques devrait, avec l'amélioration constante des échantillons élaborés, s'inscrire sur un même schéma d'idées que celui des semiconducteurs voici déjà 40 ans. À terme, il devrait être possible de concevoir des dispositifs tunnel polarisés en spin qui prennent en compte l'interaction de structure de bande entre toutes les couches afin de sonder des effets semblables avec le paramètre additionnel du spin. De tels effets commencent à être observées dans des jonctions épitaxiées Fe/MgO/Fe(001). [91] Ainsi, si la barrière de MgO filtre les fonctions d'onde de symétrie électronique Δ_1 , à la manière de Fe(001) pour une direction de spin, est-ce que dans le cas de Cr(001), pour lequel aucune bande Δ_1 ne croise le niveau de Fermi, le transport tunnel perdurerait-il au travers de cette couche métallique?

Au travers des résultats présentés dans cette Thèse, il est évident que les processus inélastiques jouent un rôle important dans le transport tunnel. De façon semblable aux recherches portées sur les semiconducteurs, des expériences de magnéto-transport tunnel à l'état solide comprenant une caractérisation de l'activité optique résultant de ces processus offriraient un outil de compréhension supplémentaire. Par ailleurs, à moyen terme, l'étude du transport tunnel à l'état solide pourrait se diversifier par l'application

d'autres techniques de caractérisation électronique, telles que Electron Energy Loss Spectroscopy ou encore le STM polarisé en spin, sur des échantillons de géométrie appropriée mis sous tension.

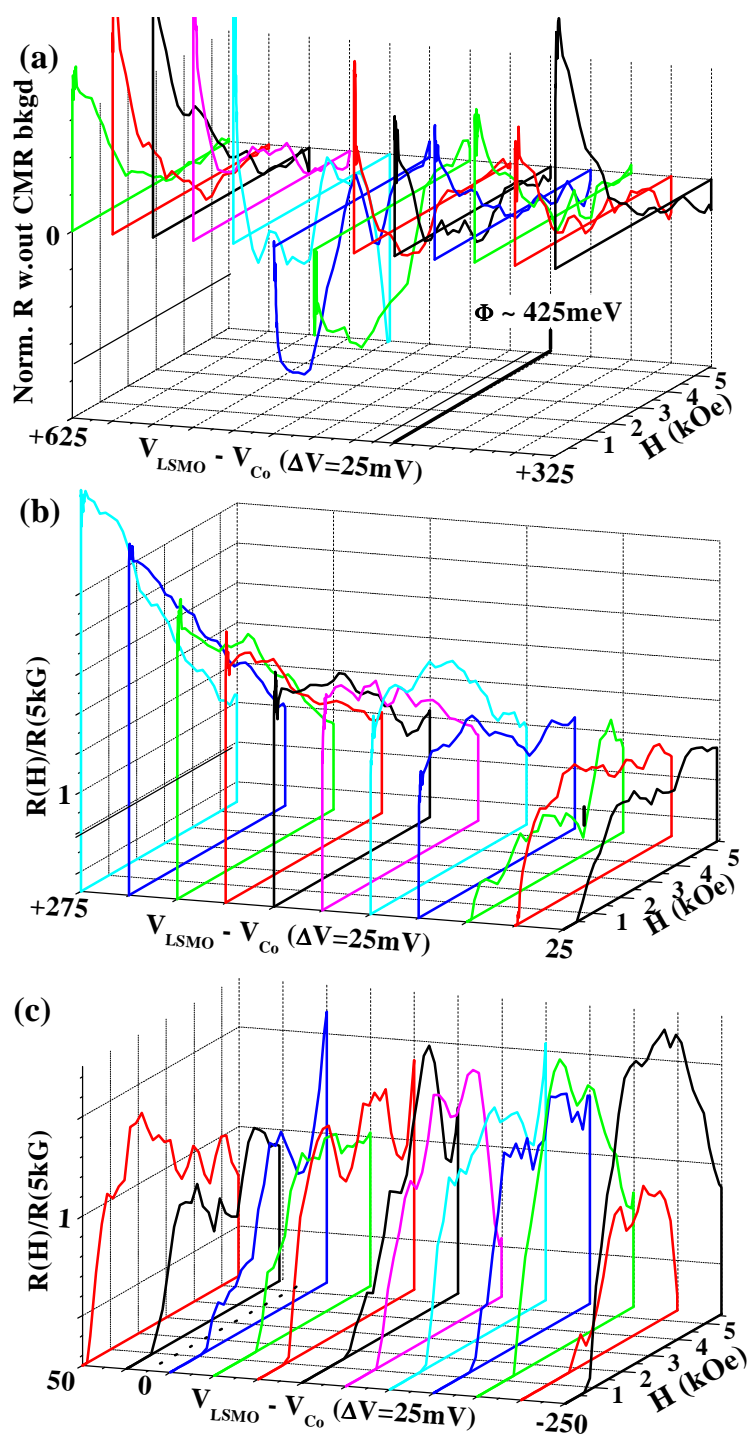


Figure 9.31: LSMO/STO/Co: Dépendance en champ magnétique appliqué décroissant de la résistance de jonction pour $V_{LSMO}-V_{Co}$ sur une gamme de tensions (a) $V=+625\text{mV}$ à $V=+325\text{mV}$, (b) $V=+275\text{mV}$ à $V=+25\text{mV}$ et (c) $V=+50\text{mV}$ à $V=-250\text{mV}$, par pas $\Delta V=25\text{mV}$. Une contribution linéaire de CMR à été soustraite dans le panneau (a).

Appendix A

Bulk band structures & interfacial interplay

With a view to understanding band structure effects throughout our LSMO/STO/Co and LSMO/STO/LSMO heterojunctions, this Appendix offers a detailed description of the electronic structure of SrTiO_3 and $\text{La}_{0.7}\text{Sr}_{0.3}\text{MnO}_3$. Section A.1 discusses the band structures of regular and transition metal oxides. In Section A.2 we examine the band structure and DOS of SrTiO_3 . Section A.3 then discusses the specific case of Metal-Induced Gap States at the STO/Co interface within a more general overview of the topic in the context of transition metal oxides. The band structure of $\text{La}_{0.7}\text{Sr}_{0.3}\text{MnO}_3$ is discussed in Section A.4. Finally, the interfacial interplay between the band structures of $\text{La}_{0.7}\text{Sr}_{0.3}\text{MnO}_3$ and SrTiO_3 is then broached in Section A.5.

A.1 On the energy bands of transition metal oxides

To correctly understand the role of the oxide materials used as tunneling barriers in MTJs, attention must be paid to the energy bands and the position of the Fermi level in these materials. Several approaches have been used to describe the energy bands of transition metal oxides. Approaches such as the crystal field or molecular orbital models convey a local picture of the chemical interactions within the oxide. A delocalized approach such as band theory takes into account the periodic potential landscape electrons evolve in. We will develop the crystal field and molecular orbital methods to draw attention to overarching features in the band structure and DOS of the oxides considered. The comparison with calculated band structures and

experimental data will provide a quantitative complement on features in the electronic structure of our heterojunctions. A more thorough account of the electronic structure of transition metal oxides has been written by Cox. [193]

A.1.1 Crystal field model

A paramount consideration in localized models is the electronic environment of the metal ion. As an ionic model, crystal field theory examines the chemical interaction resulting from the coordination of a transition metal's (TM) five d orbitals with the surrounding oxygen atoms. The formation of ligand states between oxygen $2p$ and the TM $3d$ orbitals lifts the degeneracy of the $3d$ states, which split in energy due to the anisotropic environment. Figure A.1 offers a schematic representation of these considerations. In an octahedral oxygen environment, the d_{z^2} and $d_{x^2-y^2}$ orbitals with e_g symmetry which point toward O $2p$ orbitals with σ symmetry see their energy raised. The d_{xy} , d_{xz} and d_{yz} orbitals pointing away at 45 degree in t_{2g} symmetry from the TM-O axis fall in energy as they couple to oxygen $2p$ orbitals with π symmetry. The difference in energy between these two sets of orbitals is called the *crystal field splitting* Δ_{Cryst} . In a tetrahedral environment, e_g levels lie below t_{2g} levels.

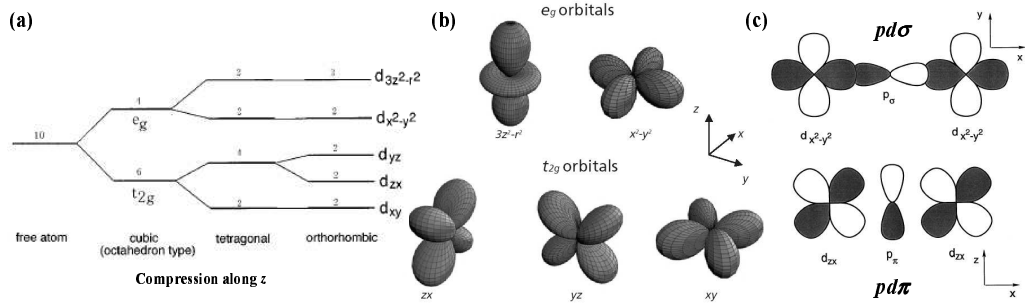


Figure A.1: (a) The energy levels of a $3d$ transition metal element in a cubic octahedral oxygen environment as the crystal anisotropy increases due to a compression along z . Numbers indicate the degeneracy of the level. (b) Spatial representation of orbitals and (c) their overlap with oxygen $2p$ orbitals to form ligand states. From Tokura [191, 194]

According to the Jahn-Teller theorem, a molecule with orbital degeneracy may lower its energy by distorting so as to reduce its symmetry and thus lift degeneracy. [195] If the environment loses cubic symmetry and becomes tetragonal due to a lengthening of two opposite TM-O bonds, then a further lifting of degeneracy occurs. If the octahedral environment is compressed

along the z axis, all orbitals with a z component will rise in energy as the overlap with O $2p$ orbitals increases, while those independent of z will fall in energy. Figure A.1 illustrates the case of a compression along z and the resulting Jahn-Teller energy split Δ_{JT} . If along this z axis expansion occurs, then d_{z^2} states will lie below $d_{x^2-y^2}$ states. Lifting of the remaining degeneracies may occur through a lowering of the cell symmetry (*e.g.* trigonal). Spin degeneracy may be lifted when considering the energy required to flip the electron spin at a given energy level: the energy level with opposite spin is raised by Hund's exchange energy J_H . The application of a magnetic field will also lift this degeneracy through Zeeman splitting.

A.1.2 Molecular orbital model

Figure A.2 presents a molecular orbital approach to the question of oxide energy bands for a metal ion in an octahedral configuration, whereby the hybridization between metal and oxygen wavefunctions is considered over several atomic sites. As such this approach is categorized as a cluster model. Given a wavefunction constructed from a linear combination of atomic orbitals, energy minimization in conjunction with the symmetry considerations of the problem yields bonding and antibonding (*) sets of orbitals with dominant oxygen $2p$ and metallic $3d$ character respectively. In this approach the crystal field splitting is already taken into account. It is interesting to note the larger energy shift due to crystal field splitting for e_g relative to t_{2g} states. While both e_g and t_{2g} sets reflect d hybridization, the larger overlap of e_g orbitals - a metallic feature, implies a more antibonding character compared to t_{2g} orbitals.

In all oxides, the top of the valence band is defined by a O $2p$ ligand band. An *ionic* band gap E'_g separates that σ bonding band from the unoccupied anti-bonding σ^* band of s and p character between the metallic ion and the oxygen ion. When undoped, the Fermi level of the intrinsic oxide lies approximately in the center of this ionic band gap. Optical band gaps of 8.8eV and 7.8eV have respectively been reported for Al_2O_3 [196] and MgO [197]. In general, band gap values may be reduced in thin films for which the effective band structure departs from bulk properties. [101] Moreover, the case of post-oxidized metallic layers is rather complex due to the absence of perfect stoichiometry in such films [198,199]. Indeed, the presence of Al cations in a Al_2O_3 barrier due to local underoxidation will introduce states several eV below the conduction band, thereby lowering the effective Fermi level ([200] and references therein) in addition to reducing the band gap. Nevertheless, present techniques [201,202] yield oxidized-Al macroscopic barrier heights reaching $\sim 3.5\text{eV}$ [68] as ascertained from Simmons [3] or Brinkman [4] mod-

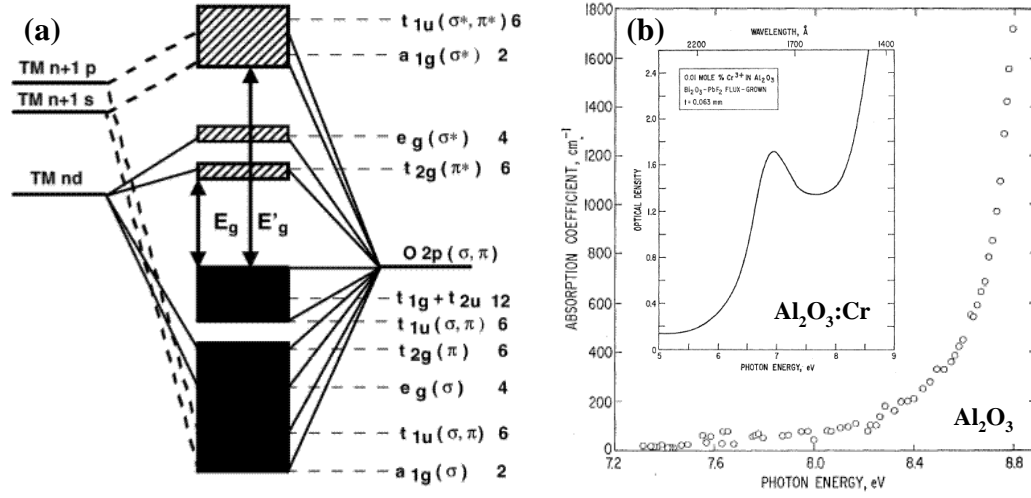


Figure A.2: (a) Molecular orbital energy band diagram for a metal ion in an octahedral bonding geometry with six oxygen atom neighbors. [193] (b) The 8.8eV optical band gap of Al₂O₃ is reduced to 6.9eV upon doping with 1% atm. Cr as t_{2g} and e_g bands appear within the gap. [196]

els. This upward value of the barrier height indeed places the Fermi level at the center of a reduced 7eV Al₂O₃ band gap.

If transition metals are present in the oxide, additional anti-bonding d bands appear within the ionic band gap, thus defining an *effective* band gap E_g for such barrier materials (Figure A.2 a). [193, 203] For instance, 0.003 (0.01) mole % concentration of Ti (Cr) in Al₂O₃ will reduce the optical band gap from 8.8eV to 6.9eV [196] (panel (b)). Therefore, in transition metal oxides, the Fermi level position defined by the ionic band gap may be very close to the top of the effective band gap. As such, the integration of transition metal oxides as barriers in MTJs yields a very low electron barrier height along with a hole barrier height spanning most of the oxide gap. Table A.1 presents ionic as well as effective band gap values for several transition metal oxides alongside those for MgO and Al₂O₃. The valence band position as verified experimentally or theoretically constitutes the reported hole barrier height. From the effective band gap an estimate of the electron barrier height may be deduced.

A.2 The perovskite SrTiO₃

Strontium titanate has been an extensively studied perovskite, mainly within the fields of dielectrics and high- T_C superconductors, where it is used both

Oxide	E'_g	E_g	VB edge Φ_h	CB edge Φ_e	Refs.
MgO	7.8	NA	4.2	3.6	[145, 197]
Al ₃ O ₃	8.8	NA			[196]
TiO ₂	8.1	3.1	~ 3	~ 0	[204, 205]
Cr ₂ O ₃	~ 7	4.7	~ 2.2	~ 2.5	[206, 207]
ZrO ₂	8.3	5.5			[204]
La ₂ O ₃	$\sim 6.2 - 7.2$	5.6			[204, 208]
HfO ₂	8.2	5.8			[204]
Ta ₂ O ₅	8.0	4.4			[204]

Table A.1: Values of the ionic gap E'_g and effective gap E_g for conventional and transition metal oxides (as defined in Figure A.2a), along with valence (VB) and conduction band (CB) positions relative to E_F .

Element	Electronic Structure	Ion	Ionic Electronic Structure
Sr	[Kr]5s ²	Sr ²⁺	[Kr]
Ti	[Ar]4s ² 3d ²	Ti ⁴⁺	[Ar]
O	[He]2s ² 2p ⁴	O ²⁻	[Ne]
Sc (\rightleftharpoons Ti)	[Ar]4s ² 3d ¹	Sc ³⁺	[Ar]
La (\rightleftharpoons Sr)	[Xe]6s ² 5d ¹	La ³⁺	[Xe]
V (\rightleftharpoons Ti)	[Ar]4s ² 3d ³	V ⁴⁺	[Ar]4s ⁰ 3d ¹
Nb (\rightleftharpoons Ti)	[Kr]5s ² 4d ³	Nb ⁴⁺	[Kr]5s ⁰ 4d ¹

Table A.2: Electronic state of elements in SrTiO₃.

as a substrate and as a capacitive layer. As summarized in Table A.2, electroneutrality considerations for SrTiO₃ imply that both Sr and Ti ionize to a $3d^0$ state, so that SrTiO₃ is termed a d^0 insulator, and as such is not magnetic.

A.2.1 Perovskite crystal structure

SrTiO₃ crystallizes in the perovskite structure ABO₃ with cubic symmetry depicted in Figure A.3. A lies at the center of a cubic cell with B at its corners. Oxygen atoms placed in the middle of the cube vertices define octahedra surrounding the B element. The symmetry of the perovskite cell depends on the ionic radii of elements A and B through the Goldschmidt tolerance factor. [209] In an ideal case such as that of SrTiO₃, cubic symmetry is possible, resulting in a 180° angle between B and O bonds. As this angle departs from 180 degrees, the cell distorts to lower symmetries. A critical angle of 156° will stabilize the perovskite structure. As will be

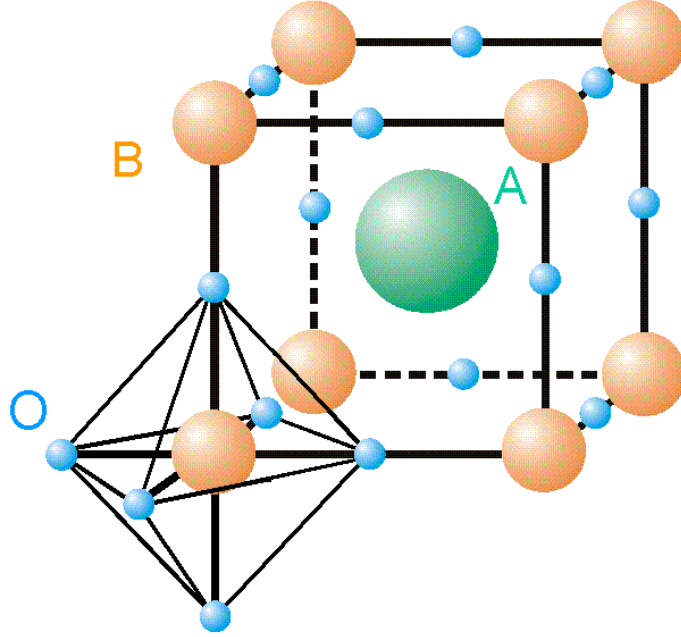


Figure A.3: Crystal structure of a cubic perovskite ABO_3 .

discussed thereafter, the electronic properties of the manganite perovskite $La_{0.7}Sr_{0.3}MnO_3$ depend sensitively on the Mn-O-Mn bond angle.

A.2.2 The band structure of intrinsic $SrTiO_3$

The first report of band structure calculations comes from Mattheiss in 1972, [187] who also considered the effect of the tetragonal distortion induced by the STO phase transition at $T=110K$. [210] Figure A.4 presents a recent calculation performed [189] by Aiura *et al.* using FLAPW code, annotated with group symmetry information from Mattheiss. [187] In a good approximation, the authors made E_F coincide with the CB edge.

Let's first consider the (100) orientation, taken from the Γ and X points in the first Brillouin zone and labelled Δ . The first three conduction bands are of t_{2g} symmetry. There has been some debate as to whether the band gap of $SrTiO_3$ (001) is direct or indirect, owing to the fairly flat $\Delta_{2'}$ conduction band [211]. Aiura *et al.* have recently compared band structure calculations (Fig. A.4a) with angle-integrated ultra-violet photoemission spectroscopy and angle-resolved photoemission spectroscopy [189]. The lowest conduction band around the Γ point of intrinsic $SrTiO_3$ is the $\Delta_{2'}$ band, which promotes an indirect band gap associated with a 51meV LO phonon process (see Figure A.4c). Given its flatness, the large effective mass of electrons

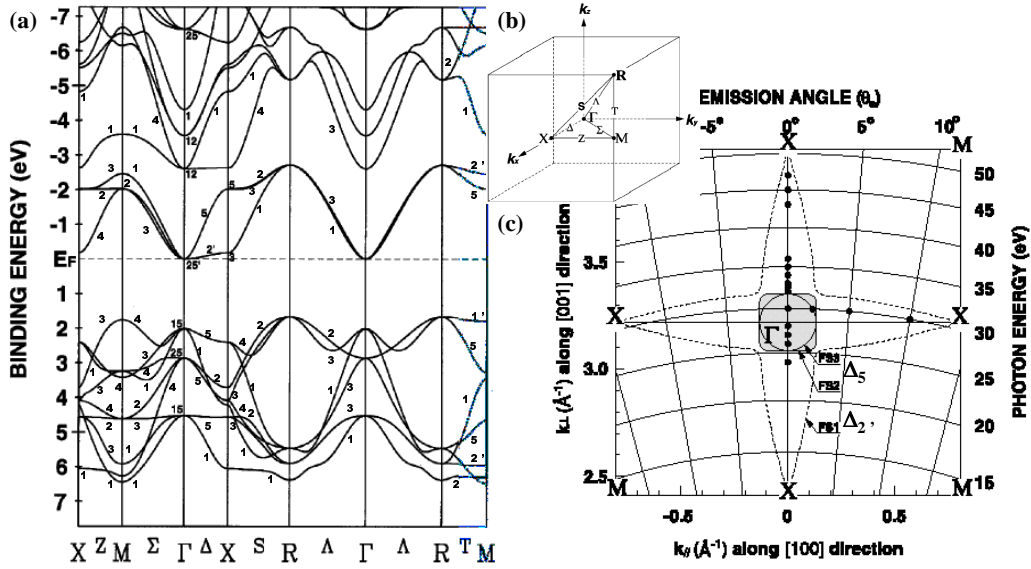


Figure A.4: (a) Band structure of SrTiO₃ with group symmetry annotations from Mattheiss [187]. (b) Schematic of crystalline orientations and notable Brillouin zone points for a cubic cell. (c) Calculated Fermi surface along Γ -X of the three t_{2g} conduction bands in a free-electron final state model. The photon energy $h\nu$ and emission angle from the normal during ARPES measurements (solid circles) are plotted against the momentum components parallel and perpendicular to the surface. From Aiura *et al.* [189]

in this band [187] impedes their contribution to tunneling and eventual CB transport in STO. Aiura *et al.* argue that a small amount of electron doping will place E_F above the top of this band. In contrast to the case of the flat $\Delta_{2'}$ band, the Fermi surface of the "light-electron" Δ_5 band presents nesting features which should support quantum well states [212] to be observed through CB transport once that band edge has been reached.

In a similar fashion hole conduction in STO over the hole barrier height will preferably occur through the Δ_1 band rather than the Δ_5 band, though the difference in band curvature is not as pronounced in the VB compared to the CB. In Section A.2.3, we outline offsets in conduction/valence band minima/maxima. Finally, it should be noted that the LSMO conduction band is of Δ_2 character.

The (110) orientation is of interest due to a distinct indirect band gap between the Γ and M points, along Σ . Upcoming studies in progress at the time of this writing aim to determine the influence of phonon-assisted tunneling through SrTiO₃ (110) by comparing it to (100)-oriented STO tunneling

results.

A.2.3 Experimental band positions in SrTiO₃ (001)

As illustrated in Section A.1, the presence of transition metal elements in SrTiO₃ implies a band gap limited by Ti 3*d* bands which may lie very close to the Fermi level. This fact has been substantiated by a number of experiments. On intrinsic SrTiO₃ (001), metastable impact electron spectra and photoelectron spectra placed the VB at 3.1eV below a Fermi level which lies at the bottom of the CB [105].

Oxide growth is always fraught with defects which may affect the electronic structure. As such it is more realistic to consider nominally doped oxides with an intent to driving the doping tendency and understand its effect on the electronic structure. The electronic configuration of typical SrTiO₃ dopants is listed in Table A.2. Photoemission spectroscopy experiments [188, 189] reveal a shift of the VB away from E_F when switching from *p*-doped (Sc) to *n*-doped (Nb) SrTiO₃ (see Figure A.5a), reflecting an upward shift of the Fermi level. This trend also leads to the appearance of impurity bands at 1.3eV below E_F and near the Fermi level as reflected by a metallic cutoff (see inset). The energy separation reflects a Hubbard gap due to Coulomb interaction between impurity electrons which thus populate the gap. [213] Peaks A and B refer to the non-bonding and Ti 3*d*-mixed oxygen bonding states respectively, which make up the VB. SrTiO₃ is deemed metallic when carrier concentration $n \approx 3 \times 10^{18} \text{cm}^{-3}$, and conductivity $\sigma \approx 10 \Omega \cdot \text{cm}^{-1}$. [179, 188]

As shown in Figure A.5b, oxygen deficiency results in a *n*-type electronic state of SrTiO₃: the metallic Fermi cutoff and polaronic state at 1.3eV [214] disappear as the oxygen-deficient SrTiO₃ crystal is exposed to O₂. The authors tentatively reason that the transition to an insulating state could reflect a return to intrinsic SrTiO₃ band positions relative to E_F over a $\Delta z = 70 \text{\AA}$ depletion depth of oxygen vacancies given reasonable considerations. [189] This picture is supported by surface characterization [178], oxidation and reduction experiments which monitor O₂ effusion from the SrTiO₃ crystal, [215] as well as from photoemission and Bremsstrahlung isochromat spectra of stoichiometric and oxygen-deficient scraped SrTiO₃ surfaces. [216] According to the analysis of a STO(001) surface treated as per our growth conditions, the oxidation results in a 4x2 surface reconstruction rich in TiO_{*x*} consisting of bulk-like TiO₂ and Ti₂O₄ [217, 218] which possess a different electronic structure. [219] Given the possibility of oxygen electromigration in SrTiO₃, such a metal-insulator transition with oxygen concentration has been used in an oxide field-effect transistor heterostructure. [220] The same group thereafter

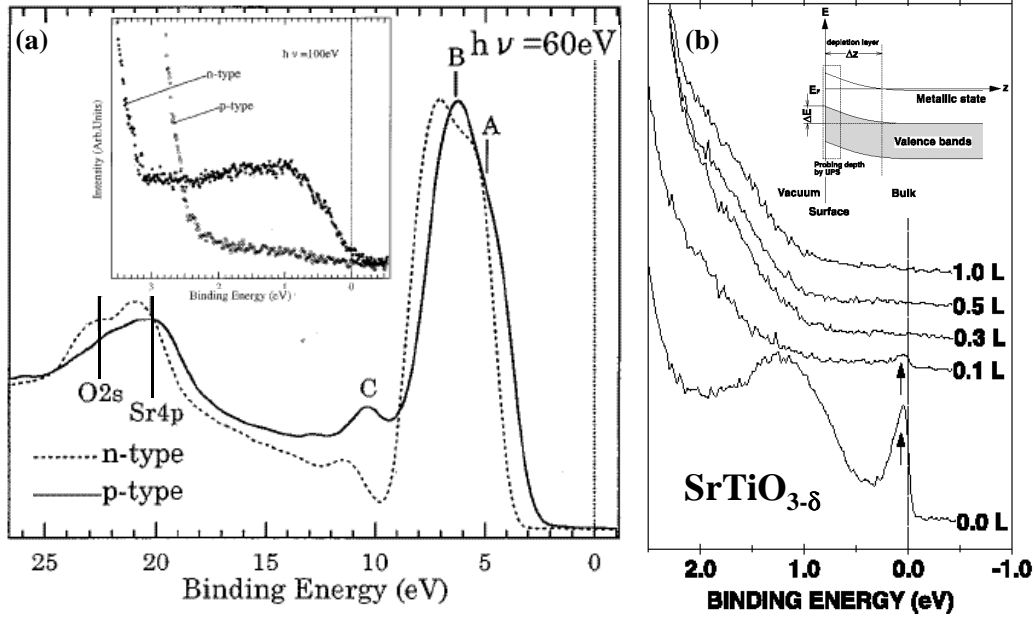


Figure A.5: Photoemission spectroscopy of: (a) scraped p -doped $\text{SrTi}_{0.98}\text{Sc}_{0.02}\text{O}_3$ and n -doped $\text{SrTi}_{0.98}\text{Nb}_{0.02}\text{O}_3$ surfaces revealing a 0.7eV shift toward E_F of the VB edge with p -doping and the creation of states within the band gap for n -doping (inset); (b) the fractured surface of an oxygen-deficient SrTiO_3 crystal as oxygen is introduced. The metallic surface state disappears as the stoichiometric insulating state is recovered. The inset provides a schematic of the incidence of oxygen substoichiometry on the energy bands near the surface. From Higuchi *et al.* [188] and Aiura *et al.* [189]

achieved nanoscale electrical circuits on STO surfaces by using an AFM tip which is biased so as to remove oxygen atoms from the surface. [221]

Regarding oxygen superstoichiometry, it is known that oxygen excess in $\text{LaTiO}_{3+\delta}$ may induce a metal-insulator for $\delta > 0.04$ due to band-filling change of this d^1 insulator toward d^0 , in similar fashion to Sr substitution for La. [191] To our knowledge, no work has been performed to evaluate the positions of the valence and conduction band edges in over-oxygenated SrTiO_3 of relevance to our junctions. Nevertheless, supposing that this situation amounts to p -doping, then one may expect a decrease in the chemical potential within the gap.

Figure A.6 summarizes DOS considerations for SrTiO_3 (001) with (inverse) photoemission spectra of the (conduction) valence bands of lightly-doped and oxygen-deficient SrTiO_3 . Though not explicitly representative of the intrinsic state of SrTiO_3 , the use of spectra taken on lightly-doped

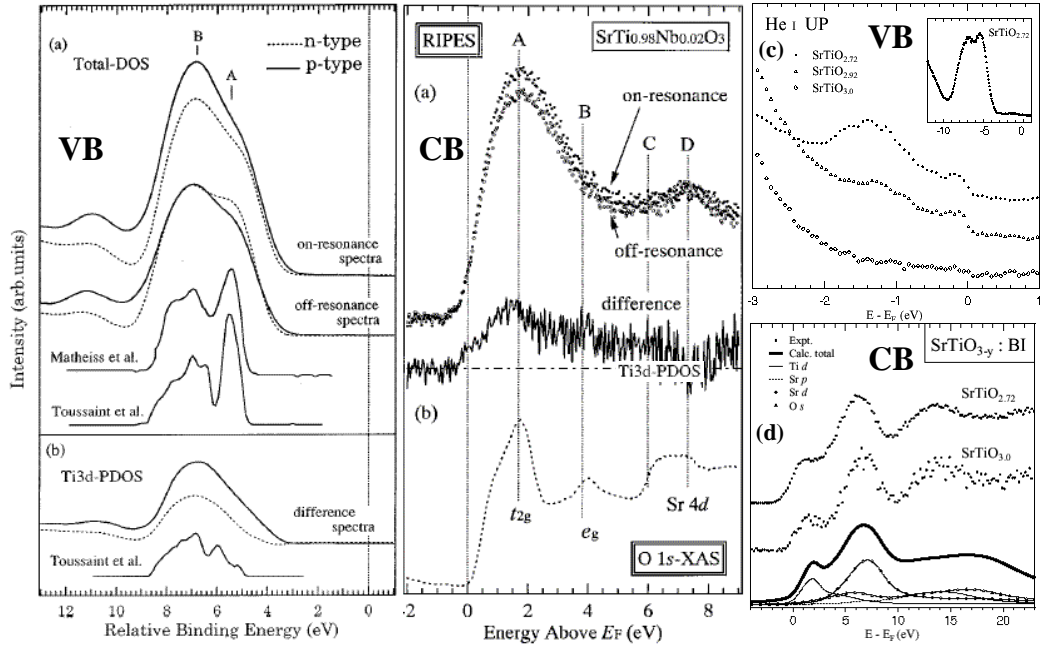


Figure A.6: Valence (Conduction) bands VB (CB) of lightly-doped SrTiO₃, including the Ti 3d DOS revealed by the Ti 3p→3d resonance effect, probed by (Inverse) Photoemission spectroscopy. (a) p-doped SrTi_{0.98}Sc_{0.02}O₃ and n-doped SrTi_{0.98}Nb_{0.02}O₃ surfaces; (b) the difference between on- and off-resonance spectra. (c) Photoemission and (d) Bremsstrahlung isochromat spectra of valence and conduction bands in oxygen-deficient SrTiO₃. From Higuchi *et al.* [188, 222] and Sarma *et al.* [216]

samples is both a technical necessity to avoid charging effects and a good approximation as discussed above. We merely recall that intrinsic SrTiO₃ has a conduction band edge at 3.1eV below the Fermi level located at the bottom of the conduction band. [105] The difference between spectra taken on and off the Ti 3p→3d resonance reveals the Ti 3d DOS. Non-bonding and bonding valence band peaks A and B occur at 4.7eV and 6.7eV below E_F for the n-doped sample with a valence band edge of 3.2eV corresponding to the effective band gap. [188] In the conduction band, the Ti 3d t_{2g} and e_g peaks are respectively located at ~1.7eV and 3.9eV above E_F and the conduction band edge. [222] These DOS features around the gap are broadly reproduced theoretically [187] in agreement with molecular orbital DOS considerations (see Figure A.2). Table A.3 summarizes DOS features for SrTiO₃ (001) including Bloch state symmetry.

Band Center Position	Band Symmetry	SrTiO ₃	SrTiO ₃ : <i>n</i>
Ti 3 <i>d e_g</i>	Δ_1, Δ_2		+3.9
Ti 3 <i>d t_{2g}</i>	$\Delta_{2'}, \Delta_5$		+1.7
CB edge		~0	~0
E _F		0	0
1 st Gap State (<i>n</i> type)	$\Delta_{2'}$		~0
2 nd Gap State (<i>n</i> type)	surface, Ti 3 <i>d</i> ?		-1.3
VB Edge		2.6	-3.2
O 2 <i>p π</i>	Δ_1		-4.7
Ti-O <i>pdσ</i>	Δ_5		-6.7
References	[187, 189]	[105]	[188, 189, 222]

Table A.3: Energy position of bands in SrTiO₃ and SrTiO₃:Nb with crystal field and group symmetry nomenclature.

A.2.4 Phase transitions in SrTiO₃

Of the several phase transitions reported for SrTiO₃, the most notable is the cubic-to-tetragonal structural transition as temperature is lowered past 110K. This transition results from condensation of the Γ_{25} optical phonon mode at the Brillouin zone boundary. Mattheiss considered the repercussions of such a transition on the band structure of SrTiO₃: [210] the rotation of the TiO₆ octahedra lifts the degeneracy at the Γ point of the *t_{2g}* bands. An estimated 90meV at 4.2K separates the heavy electron $\Delta_{2'}$ band from the light-electron Δ_5 band for a 2.1° rotation angle. As the rotation angle is increased, along the [100] direction the Δ_5 band remains constant while the $\Delta_{2'}$ band is rigidly shifted upward. Along the distorted [010] direction, the degeneracy of the Δ_5 band is lifted as one of the bands is raised in energy, while the others remain constant. Though similar to the ferroelectric phase transition for other perovskites such as BaTiO₃ or PbTiO₃, the opposite sign for the band shift in SrTiO₃ precludes ferroelectricity in this compound. Mattheiss also predicts changes in the Fermi surface, namely that the heavy electron sheet shrinks from a cross to a spiked sphere, possibly because, below the transition, the Brillouin zone is halved. [223] Such calculations of Fermi surfaces have been confirmed, within experimental error, by de Haas van Alphen experiments. [224] Other phase transitions reported include one at 65K, below which symmetry is lowered as the two remaining similar axes become no longer equivalent. [225] Also, the paraelectric Curie temperature of SrTiO₃ is ~35K. XXX Another transition at 35,10K.

A recent electron spin resonance study of SrTiO₃ single crystals revealed that the 110K transition results in a rotation of TiO₆ octahedra of 8 degrees

due to a 0.15\AA expansion of the Ti-O bond. [226] This expansion along z results in a fall in energy of all orbitals with a z contribution due to the lifting of degeneracy. As such the following energy splits relative to the d_{xy} level with lowest energy could be extracted: 0.11eV for d_{yz} , 0.81eV for d_{xy} , 2.88eV for d_{z^2} and 3.75eV for $d_{x^2-y^2}$.

A.3 Chemical bonding, Metal-Induced Gap States and spin-polarized DOS at the Ferromagnet/Insulator interface

This Section uses the specific example of the SrTiO_3/Co interface to discuss general concepts regarding the effective transmission of a wavefunction of given electronic character through an insulator.

A.3.1 The Co band structure and DOS

Though in our junctions we only achieve a hcp(0001) texture due to the lattice mismatch between SrTiO_3 (001) and Co, for the sake of completeness we present the band structure of Co and CoO in Figure A.7. Rather than consider the band shifts and hybridization owing to spin degeneracy, the authors opted to represent the band structure with Fermi levels for both electron spin populations. [227] The calculated DOS of Co at the interface with Al_2O_3 and SrTiO_3 is examined in Figure A.9. CoO is sometimes used in our structures as an antiferromagnetic pinning layer for Co. Though the T_N is reportedly 290K , the blocking temperature may be lower, between 80K and 190K depending on the interplay of this magnetic anisotropy with other sources. The calculation [228] used to illustrate the band structure of CoO is in broad agreement with angle-resolved photoemission spectroscopy measurements. [229]

A.3.2 The SrTiO_3/Co interface

Band bending due to charge transfer may be mitigated by metallic interface states within the semiconductor gap which pin the Fermi level. These virtual gap states, or metal-induced gap states [38] (MIGS) are represented by Bloch evanescent wavefunctions with a complex wavevector κ which penetrate the insulator over several \AA . As discussed by Tersoff, [39] the spectral weight of MIGS at a given energy level depends on the efficiency for metallic wavefunctions to hybridize with valence and conduction band states as evanescent

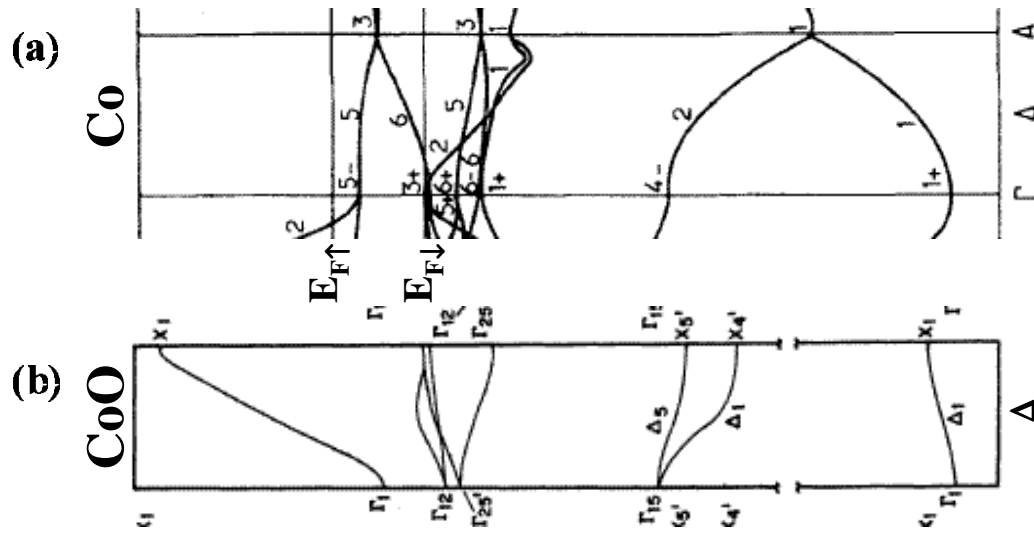


Figure A.7: Band structure of (a) hcp Co(0001) and (b) rock-salt (NaCl) CoO(001). From [227] and [228]

MIGS. This coupling efficiency depends on wavefunction symmetry matching as well as energy band overlap so as to promote interband transitions. With energy rising from the VB edge to the conduction band edge, the electronic character of these states shifts from the semiconductor's valence to conduction band character. Electroneutrality considerations imply that the MIGS spectral weight of valence band character reflect the electron occupation of these states up to the charge neutrality level (CNL). Above this level the spectral weight favors electronic symmetry from the empty conduction band. [39] These considerations are summarized in Figure A.8a alongside Bellini's calculation of the SrTiO₃ (001) complex band structure (panel (b)). The intersection between the complex bands of Δ_1 and Δ_5 character which span the ionic and effective band gaps E'_g and E_g defines the CNL.

MIGS present within the semiconductor at the Fermi energy have been argued to play a paramount role in determining the sign of a ferromagnet's effective tunneling spin polarization when at the interface with an insulating barrier. [39] Oleinik, Tsymbal and Pettifor have conducted DOS calculations of the fcc(111)Co/ α -Al₂O₃ (0001) [34] and fcc(111) Co/SrTiO₃ (001) [36] ideal interfaces (see Figure A.9). In the case of Al₂O₃, the p - d wavefunction hybridization due to Co-O bonding leads to a positive charge transfer on O atoms. The spin-polarized density of MIGS states flips sign within 10Å of the Metal/Semiconductor interface owing to a larger decay length for majority electrons. The authors argue that this change in sign explains the positive sign of spin polarization of all transition metals at the interface with

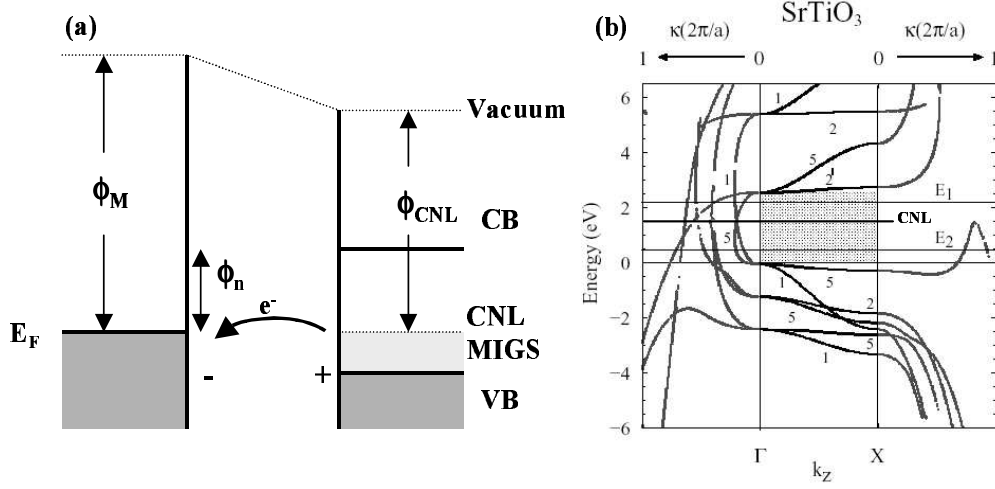


Figure A.8: (a) Schematic band structure of MIGS at a Metal/Semiconductor interface. (b) Complex band structure of SrTiO₃ (001) by Bellini [41]

Al₂O₃. In comparison to the case of Al₂O₃, the authors find an additional d - d bonding between Co and Ti of d_{xz} and d_{yz} symmetry mediated by O $2p$ states (see panel c) which induces a magnetic moment on the Ti atom. This $pd\pi$ hybridization leads to antiferromagnetic coupling of Co and Ti through superexchange [37] (see Section A.4.1). The authors do not explain how the inversion in sign of the MIGS spin polarization, reportedly present for both barrier types, may lead to opposite signs of the Co effective spin polarization at the interface with these semiconductors.

In the limit of complete Fermi level pinning, the hole and electron barrier heights result from the position of the CNL relative to that of the valence and conduction band edges. The height of the Schottky barrier would thus be intrinsic to the semiconductor and not depend on the metal. Furthermore, the MIGS at the CNL-equated Fermi level derive their orbital character equally from the conduction and valence bands, and so reflect a spin-polarized DOS - and an eventual sign of spin polarization, resulting from this equal mixing. In this case, the much larger density of spin-polarized d states in Co may tip the balance toward electronic transmission of that character, if present in the electronic structure of the insulator.

An intermediate pinning efficiency will displace the Fermi level from the CNL in the direction of band bending and toward the intrinsic Fermi energy. Robertson and Chen have calculated a SrTiO₃ (001) CNL of 2.6eV above the VB edge as well as a moderately strong pinning factor. [103] This CNL position relative to the VB and CB is correctly reproduced in proportions by

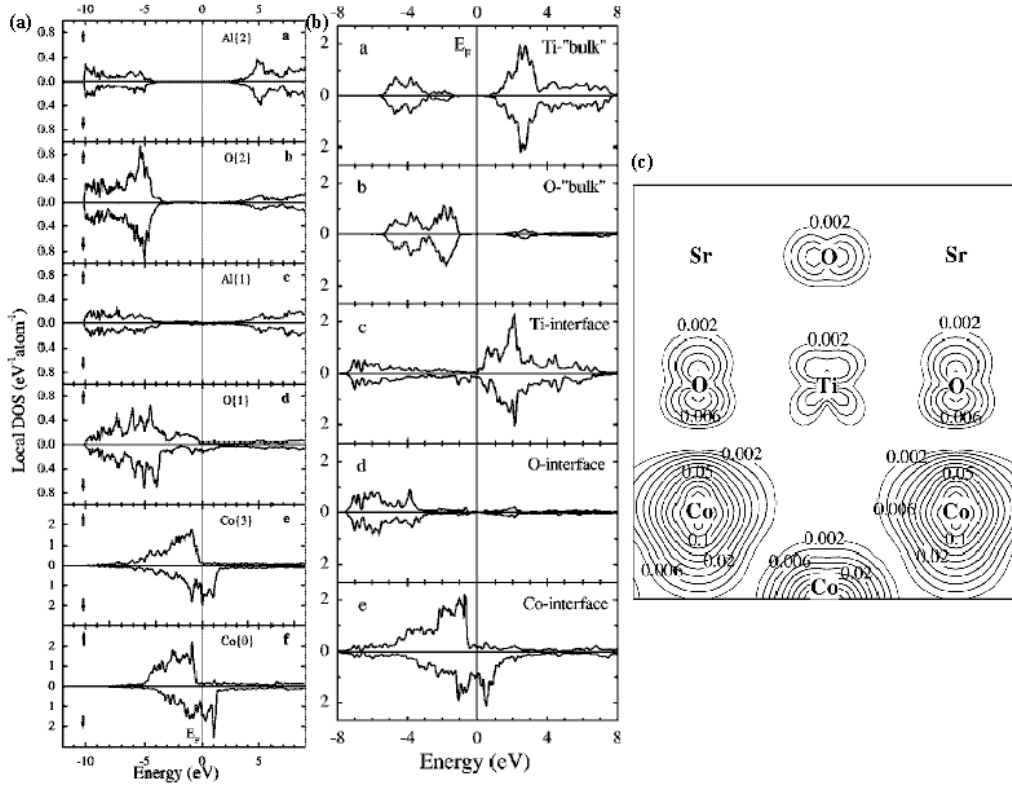


Figure A.9: Spin-polarized LDOS calculations of the (a) fcc(111)Co/ α -Al₂O₃(0001) [34] and (b,c) fcc(111) Co/SrTiO₃(001) [36] ideal interfaces. (c) Charge density contour at the Co/SrTiO₃ interface for the minority-spin states in the 1.3eV energy window below E_F in the (010) plane. From Oleinik, Tsymbal and Pettifor. [34, 36]

Bellini's calculation of a CNL of 2eV above the VB edge for a 2.6eV effective band gap. Given the proximity of E_F to the CB edge in intrinsic SrTiO₃ (see Section A.2.3), and the moderate pinning strength, it is reasonable to suppose that the Fermi level should lie above the CNL. Since the spectral weight of those MIGS states above the CNL favors a 3d t_{2g} state, the spin-polarization of transition metals at the interface with SrTiO₃ conforms in sign to that of the transition metal. A change in Fermi level will modify the proportion of valence and conduction band MIGS. This change may occur through deviations from nominal oxygen stoichiometry as discussed in Section A.2.3. Interestingly, the calculation for SrTiO₃ indicates that there is little chemical interaction between Sr and other atoms. As such, SrTiO₃ and TiO₂ should exhibit the same dominant $pd\pi$ hybridization.

A.3.3 A generalization

In this sense SrTiO₃ exemplifies the case of efficient coupling of transition metal d states to d states in the conduction band. However, if the Fermi level lies below the CNL, then MIGS states of valence band character will dominate efficient evanescence considerations in proportion to the pinning factor. Figure A.10 presents band structure and DOS calculations for α -Al₂O₃ (sapphire), perovskite LaAlO₃, 7-fold La coordinated La₂O₃ and anatase TiO₂. Within the Al₂O₃ ionic gap of 8.8eV appear La 3*d* bands at 5.6eV above the VB for LaAlO₃ and La₂O₃ which define the effective gap much as Ti 3*d* bands do for TiO₂. Referring to Table A.1, in La₂O₃ the 3*d* band onset is much closer to that of the 4*s*/4*p* bands which define the ionic gap than in SrTiO₃ or TiO₂. This result reflects a trend in transition metal oxides for effective gaps E_g to decrease as the transition metal series is traversed, and to increase when switching from 3*d* to 4*d* and 5*d* series; [230] while the *s* band remains broadly constant. [228] As such La oxides should have the largest effective gap. Since the ionic gap in these oxides remains approximately constant, it is reasonable to suppose that the Fermi level relative to the valence band would remain broadly constant. Therefore, in the oxide of a transition metal element at the beginning of the series, the CNL lies above E_F , so that the more efficient coupling into such a barrier will reflect the character of the O 2*p* valence band. In this sense La oxides represent the best opportunity to verify *s* character electronic transmission through a barrier containing transition metal elements according to the MIGS picture described above.

A.4 The band structure and DOS of La_{0.7}Sr_{0.3}MnO₃

Band structure considerations for La_{0.7}Sr_{0.3}MnO₃ follow general trends in transition metal oxides (Section A.1.1) and particular considerations of the perovskite structure (Section A.2.1) this manganite crystallizes in. The parent compounds of La_{0.7}Sr_{0.3}MnO₃ are LaMnO₃ and SrMnO₃. As such our study of La_{0.7}Sr_{0.3}MnO₃ will first outline salient properties of LaMnO₃, then consider the effect of hole doping with Sr on the electronic structure. As Table A.4 reveals, the absence of a filled-shell ionized state for Mn will drive the electronic properties of the manganite. Tetragonal distortions of the unit cell will also be discussed with a view to interpreting magnetotransport results.

The topic of colossal magnetoresistive materials such as La_{0.7}Sr_{0.3}MnO₃ exhibits a wide variety of physical phenomena which

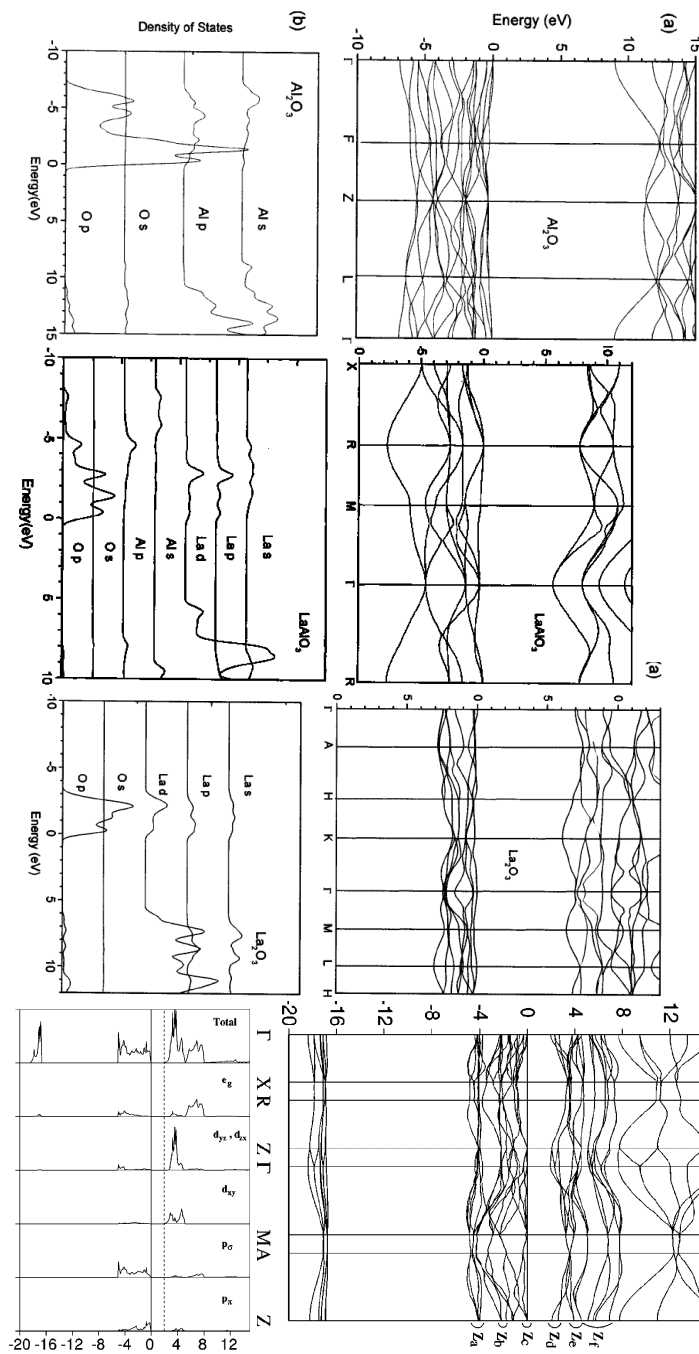


Figure A.10: (a) Band structure and (b) DOS calculations for for α - Al_2O_3 (sapphire), perovskite LaAlO_3 , 7-fold La coordinated La_2O_3 and anatase TiO_2 . [208, 231]

Element	Electronic Structure	Ion	Ionic Electronic Structure
La	[Xe]6s ² 5d ¹	La ³⁺	[Xe]
Sr	[Kr]5s ²	Sr ²⁺	[Kr]
Mn	[Ar]4s ² 3d ⁵	Mn ^{3+ / 4+}	[Ar] 4s ⁰ 3d ^{4 / 3}
O	[He]2s ² 2p ⁴	O ²⁻	[Ne]

Table A.4: Electronic configuration of elements in La_{0.7}Sr_{0.3}MnO₃.

determine the electronic structure of these oxides. Initiated in the 1950s, the topic has received renewed interest more recently when predictions of half-metallic conduction were put forth. This review will suffice to underscore those aspects relevant to our experimental study. A more complete overview may be found through several exhaustive reviews by Tokura, [191, 232] or from M. Bibes's Thesis. [233]

A.4.1 LaMnO₃: Superexchange between 3d⁴ sites

Introduced by Kramers [234] in 1934 and refined in the 50s by Goodenough, [235, 236] Kanamori [37] and Anderson, [237, 238] the *superexchange* interaction describes orbital ordering between a TM-O ligand complex and another M ligand state. Particular attention is given to the compound LaMnO₃ as the 3d⁴ Mn state and its octahedral oxygen environment embody a set of interesting conditions on the possible interactions between Mn sites through O.

LaMnO₃ crystallizes in the perovskite ABO₃ structure (see Section A.2.1). The presence of La at the A site - and its filled shell La³⁺ ionized state, implies for electroneutrality considerations that Mn take on a ³⁺ state. The four electrons from the Mn³⁺ ion (3d⁴) occupy energy levels so as to satisfy Hund's first rule. As such, in a regular octahedral environment, all three orbitals of the *t*_{2g} subband of same energy and one *e*_g orbital are occupied by spin ↑ electrons. A schematic may be found in Figure A.1. Though *e*_g ↓ levels are available, their position ~2eV above those with spin ↑ due to the Hund exchange energy *J*_H precludes any consideration of these orbital levels when placing electrons on a given site due to the smaller crystal field splitting Δ ~1.5eV.

Let's now consider the electronic interaction between Mn and O ligand states. Each of the three Mn *t*_{2g} orbitals may bond with a O π orbital to form a *pdπ* ligand complex of ionic nature. However the low orbital overlap precludes delocalization of the *t*_{2g} electrons, which therefore form a S=3/2 moment localized on the Mn site. This localized moment will determine the moment of the only Mn *e*_g electron through Hund's first rule. Thus Mn is in

a high-spin state. The only Mn e_g orbital may bond with a O σ orbital to form a $pd\sigma$ ligand complex as illustrated in Figure A.1c.

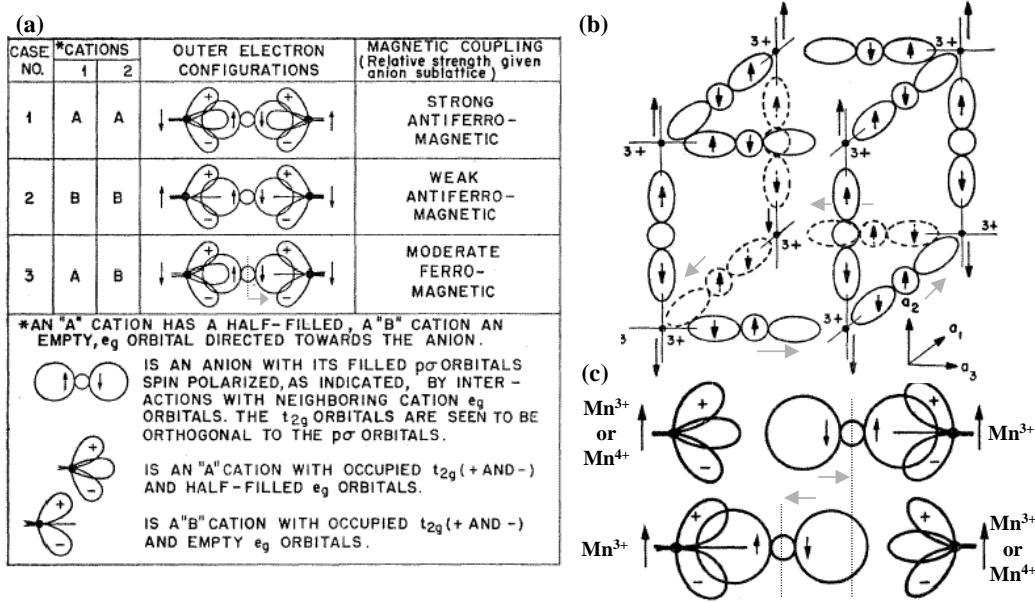


Figure A.11: (a) Superexchange interactions between d^4 sites mediated by O. In the legend only cation \uparrow states are considered. (b) Interaction between Mn e_g and $p\sigma$ orbitals in a cubic lattice. (c) Initial and final states pursuant to a double exchange charge transfer. Gray arrows indicate O site distortion due to the Jahn-Teller effect. From Goodenough [235, 236]

Case 1: strong AF coupling As depicted in Figure A.11a, there are three possible prototypical Mn-O-Mn bonding arrangements involving a single Mn e_g electron in either a d_{z^2} or a $d_{x^2-y^2}$ orbital; and the O σ orbital, which is occupied by two electrons of opposite spin. The following self-consistent discussion assumes an orbital order has been reached, *i.e.* the system is below the Curie temperature T_C . Suppose that the two Mn sites provide their e_g electron toward covalent bonding with the intermediate O. Consequent to the Pauli exclusion principle, electrons within overlapping Mn e_g and O σ orbitals must be of opposite spin. As such, for instance, a spin \downarrow O σ electron will spend more time on the side of the Mn orbital populated by a e_g spin \uparrow electron. Since the two O σ electrons are of opposite spin, the e_g electrons of the two Mn sites will therefore be of opposite spin. This bonding configuration leads to an antiferromagnetic (AF) coupling between the two Mn sites (Case 1). Given the strong orbital overlap, this pair of

Mn-O covalent bonds promotes a strong AF coupling strength. Since the O anion is bonded on each side by Mn, this site suffers no distortion. As such, along this lattice direction, a Mn e_g electron of given spin is associated with surrounding O σ electrons of opposite spin, resulting in an AF coupling of Mn moments along this lattice direction.

Case 2: weak AF coupling If neither Mn site provides an e_g electron, then semi-covalent bonding between Mn and O may occur through delocalization onto each empty e_g orbital of a O σ electron, which couples ferromagnetically to the moment localized on the Mn site. Indeed, the electron with spin similar to the Mn on-site $S=3/2$ macrospin will spend more time on that side of the Mn-O-Mn bond. This leads to a weak AF coupling of Mn sites.

Case 3: moderate F coupling If only one Mn site can provide an e_g electron, which couples AF to the O electron through covalent bonding, then the second O electron with opposite spin will couple ferromagnetically to the Mn site with empty e_g orbital. Such semi-covalent bonding may be achieved through partial delocalization of one O electron from its σ orbital to the overlapping empty Mn e_g orbital. The resulting coupling between the two Mn sites is ferromagnetic (F); and of moderate strength due to the weaker orbital overlap across the Mn-O-Mn bond. The differing strength of bonding to the O site by the Mn sites promotes a distortion of the O site toward the Mn site lacking the e_g electron (Figure A.11c).

The self-consistent ordering of an e_g orbital throughout the cubic sublattice of Mn sites, given these above superexchange interactions with the enmeshed O orthorhombic sublattice, has three consequences and one implication (see Figure A.11b). Firstly, along one sublattice direction Mn sites will couple AF as per Case 1. Secondly, Mn sites along sublattice planes perpendicular to this direction will couple F as per Case 3. Thirdly, the O distortions within a F plane order so as to move away from a Mn site in one direction while moving toward that site in the other (*cf* Figure A.1a and the gray arrows of Figure A.11b). As discussed by Goodenough *et al.*, [236] such a distortion of the oxygen octahedral environment around the Mn site leads to a degenerate lowering of symmetry of Jahn-Teller type which is energetically favorable, [195] so that in the ground state the e_g electron may occupy both d_{z^2} and $d_{x^2-y^2}$ orbitals in a linear combination. As such, in LaMnO_3 both t_{2g} and $e_g \uparrow$ levels are occupied, while corresponding \downarrow levels remain empty since $J_H > \Delta$. The manganite is therefore an AF insulator; the temperature T_N below which these *cooperative* Jahn-Teller distortions lead to this *orbitally ordered* AF state is 140K. [191] A schematic of the LaMnO_3 crystal structure

with enmeshed cubic Mn and orthorhombic O sublattices is presented in Figure A.12a. Early studies of the LaMnO₃ crystal structure assumed a linear distortion of the O sites along the main crystalline directions. More realistically, these distortions result in a rotation of the MnO₆ octahedra around the Mn site commonly referred to as a GdFeO₃-type tilting distortion of the oxygen sublattice. In this review, [191] Tokura provides a more complete picture of O sublattice distortion models for LaMnO₃ page 1122. Figure A.12b shows the results of a spin-dependent DOS calculation [239] for AF LaMnO₃ in this crystal structure. Just below the Fermi level, the main DOS contribution arises from spin ↑ e_g states. Spin ↓ states with t_{2g} symmetry appear only at $E \sim E_F + 0.5\text{eV}$.

As shown in Table A.4, the $3d^4$ electronic configuration of the Mn³⁺ site arises from electroneutrality considerations determined by the ionization of La to La³⁺. Since the Jahn-Teller distortion of the oxygen octahedral environment at each $3d^4$ site leads to an orbital order of lower energy, Mn³⁺ is called a *Jahn-Teller ion*.

Much research has occurred over the past 50 years to investigate the rich orbital structure and the exact role the varying physical mechanisms such as superexchange, double exchange, electron-phonon and electron-electron correlations play in driving the electronic properties of perovskite transition metal oxides. The prototypical system LaMnO₃ still serves as a testbed for investigation into these highly correlated electron systems. [240]

A.4.2 From LaMnO₃ to La_{0.7}Sr_{0.3}MnO₃: the special case of double exchange

If a fraction x of an element ionized to a ²⁺ state (such as Ca, Sr, Ba) is substituted for La³⁺, then a fraction x of Mn sites must ionize to a Mn⁴⁺ state corresponding to a $3d^3$ electronic configuration. Since this state does not involve any e_g electron, such Mn⁴⁺ sites do not experience any Jahn-Teller distortion. Such a substitution may be considered as hole doping the LaMnO₃ e_g band. With less than one e_g electron, the degeneracy between d_{z^2} and $d_{x^2-y^2}$ orbitals is lifted, promoting metallicity.

In support of the first experimental conductivity measurements on mixed valence manganites exhibiting metallic ferromagnetism, [241] the case of electronic conduction between a Mn³⁺ and a Mn⁴⁺ site through an O intermediary was considered by Zener [242] in 1951 to involve a *double exchange* process of electron transfer from the Mn³⁺ site to the filled O $2p$ shell as an electron from that shell simultaneously hopped to the Mn⁴⁺ site. Since the process must conserve spin, the carrier leaving the Mn site must have the

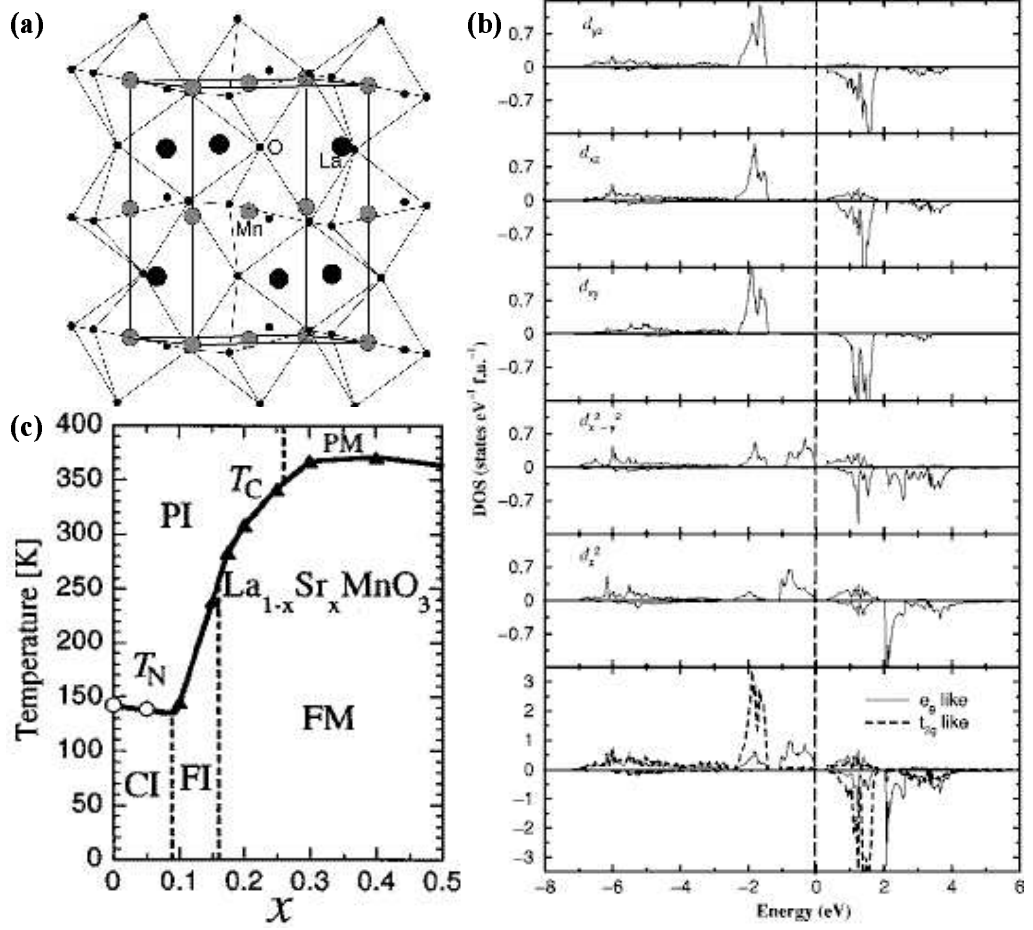


Figure A.12: LaMnO_3 in the perovskite structure with a GdFeO_3 -type orthorhombic distortion of the oxygen sublattice: (a) crystal structure and (b) orbital-resolved spin-dependent DOS. (c) Phase diagram of $\text{La}_{0.7}\text{Sr}_{0.3}\text{MnO}_3$ denoted as follows: PI, paramagnetic insulating; PM, paramagnetic metallic; CI, spin-canted insulating; COI, charge-ordered insulating; AFI, antiferromagnetic insulating (in the COI); CAFI, canted antiferromagnetic insulating (in the COI). From Refs. [191,239]

same spin as the one arriving on the adjacent site. Given that each carrier spin must align ferromagnetically with the Mn on-site $S=3/2$ macrospin, this implies a ferromagnetic alignment of the Mn on-site moments. Thus $e_g \uparrow$ conduction resulting from the double exchange mechanism is associated with long-range ferromagnetic order and, of course, entails *half-metallicity* of the manganite.

This double exchange picture is supported by the exchange interactions

considered above which lead to the ferromagnetic superexchange of Case 3 *if* the conduction process involves a linear combination of states reflecting the initial and final Mn-O-Mn states of the carrier transfer. The second necessity of such a model is a lifting of degeneracy between initial and final states so as to favor state change leading to the proposed conduction mechanism. This condition was placed within the context of superexchange theory by Goodenough [235], then formalized by Anderson and Hasegawa [243], de Gennes [244], and by Kubo and Ohata in the framework of a quantum model [245]. In the past decade, this double exchange requirement for a lifting of degeneracy between initial and final states was examined as resulting from electron-phonon interactions leading to the needed distortion. Millis *et al.* ascribed a crucial role to Jahn-Teller (JT) distortions in driving the double exchange mechanism. [246] So-called breathing modes of the MnO_6 octahedra, in competition with JT effects, [247] may also in principle lift this degeneracy, [248] though in $\text{La}_{0.7}\text{Sr}_{0.3}\text{MnO}_3$, as the manganite with the highest one-electron bandwidth, this type of lattice vibration occurs on a much lower time scale than carrier hopping. As such the charge carriers do not experience this distortion. Since electronic conduction is necessarily associated with a localized lattice distortion, the charge carrier is commonly considered to be a polaron. Above T_C a polaronic picture of transport has been determined to characterize transport. Below T_C several models have been proposed. [191]

As LaMnO_3 is doped with a divalent cation, the crystal structure evolves from orthorhombic to pseudocubic, [249] commensurate with the ratio of the ionic radii of La and the doping cation through the Goldschmidt tolerance factor. [209] Thus the electronic properties of hole-doped manganites do not depend as much on Jahn-Teller distortions present in the parent compound LaMnO_3 . Rather, rotation of the oxygen octahedra about the Mn site occurs, setting the Mn-O-Mn bond angle and the ensuing strength of the double exchange mechanism. [250] The case of Sr doping is especially favorable to double exchange in that its very nearly cubic lattice promotes better orbital overlap and the highest one electron bandwidth among doped manganites. [191] With a width $\sim 3\text{eV}$ in such systems, this e_g band center lies approximately at the Fermi level. [251]

The result of Sr doping on the electronic phase of $\text{La}_{1-x}\text{Sr}_x\text{MnO}_3$ may be appreciated in Figure A.12c. For concentrations above $x=0.1$, the orbital ordering of d_{z^2} and $d_{x^2-y^2}$ states melts, and in the case of Sr doping leads to ferromagnetism for $x\approx 0.16$. [232] The requirement [235] that a Mn^{3+} site be adjacent to at most one Mn^{4+} site leads to a maximal efficiency of the double exchange mechanism for doping fraction $x\sim 0.3$. Past a doping fraction of $X\sim 0.6$, the large ionic radius of Sr^{2+} prevents the formation of the perovskite

structure.

A.4.3 Lattice distortions, half-metallic considerations and pseudogaps

Aside from Banach's calculations (see Section A.5), all other reported studies [99,100] describe manganites such as $\text{La}_{0.7}\text{Sr}_{0.3}\text{MnO}_3$ as *nearly* half-metallic, with the minority band crossing E_F , by as much as 0.15eV.

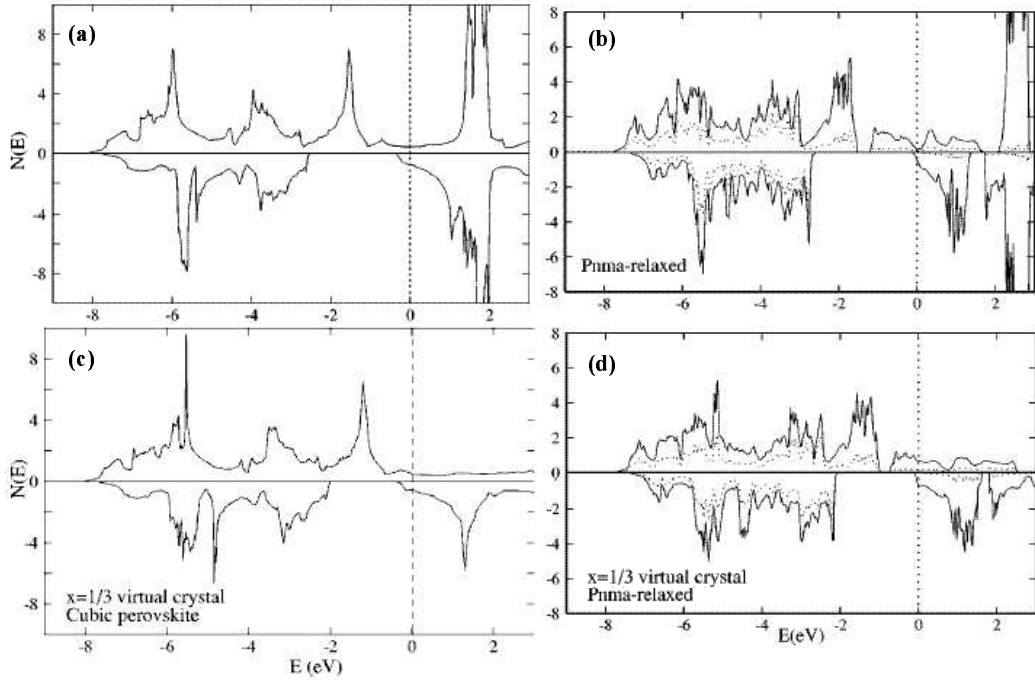


Figure A.13: Spin-polarized DOS of ferromagnetic LaMnO_3 and $\text{La}_{2/3}\text{Ba}_{1/3}\text{MnO}_3$ for (a),(c) cubic and (b),(d) $Pnma$ -relaxed structures. Doping shifts the majority band to higher energies. A deviation in Mn-O-Mn bond angle from 180° favors half-metallicity at E_F while opening pseudogaps above E_F in both spin channels. From Pickett % Singh. [250]

Several arguments can be invoked to explain the effective half-metallic character of $\text{La}_{0.7}\text{Sr}_{0.3}\text{MnO}_3$. According to Pickett and Singh [252], bending in the Mn-O-Mn bond angles away from the ideal 180° value will decrease the Mn $3d$ bandwidth, raising the bottom edge of the minority band (see Figure A.13b,d). This defines a *minority gap* for the half-metallic manganite. This distortion, along with random occupation of the doping site, promotes Anderson localization. This mechanism doesn't affect e_g majority carriers,

which retain metallic conduction at E_F . However, t_{2g} minority carriers at the bottom of the conduction band may thus lay below the mobility edge. [251] These minority states therefore do not contribute to overall conduction so that, in essence, manganites such as $\text{La}_{0.7}\text{Sr}_{0.3}\text{MnO}_3$ represent a *transport* half-metallic system. [250] This picture is corroborated by point-contact Andreev reflection (PCAR) experiments [140], although tenuously since these measurements were performed on a $\text{La}_{0.7}\text{Sr}_{0.3}\text{MnO}_3$ surface exposed to air and not a clean surface or buried interface.

In addition to bandwidth reduction, this non-cubic environment lifts Mn $3d$ orbital energy degeneracy, which applies to all bands with e_g and t_{2g} symmetry (see Figure A.1a). As such *pseudogaps* in the DOS may for example appear between d_{z^2} and $d_{x^2-y^2}$ subbands with e_g symmetry, as illustrated in Figure A.13b,d for $\text{La}_{2/3}\text{Ba}_{1/3}\text{MnO}_3$. Given the $\sim 2\text{eV}$ exchange splitting energy, Mn spin-resolved subbands are staggered in energy, so that these pseudogaps may result in a nearly total spin polarization at that energy above E_F . The energy extent of the pseudogap and the ensuing spin polarization at its center decrease as divalent doping increases. [250]

A.4.4 Band structure and Fermi surface of $\text{La}_{0.7}\text{Sr}_{0.3}\text{MnO}_3$

The band structure of LSMO in the cubic perovskite structure is presented in Figure A.14. In this calculation using a modified linearized muffin-tin orbital method, Livesay and coworkers find [99] that the bottom of the minority bands touches the Fermi level in the (001) orientation. However, as seen in Figure A.13, a slight distortion of the Mn-O-Mn bond angle will push the minority band above E_F , and the system will become half-metallic. [250] As expected, one of the two $e_g \uparrow$ bands crosses E_F , while the $t_{2g} \uparrow$ bands lie several eV below.

As is usually the case in perovskites, the Fermi surface exhibits two main sheets: an electron spheroid centered about the Γ point, and a hole spheroid centered around the R point. These sheets join along the [111] direction. As predicted from calculation [251] and experimentally confirmed by Livesay *et al.*, the Fermi surface of (nearly) cubic $\text{La}_{0.7}\text{Sr}_{0.3}\text{MnO}_3$ exhibits Fermi surface nesting for the hole cuboid as well as for the electron spheroid (see Figure A.15). The nesting wavevector of the former lies along the M-R direction, that is in the [001] direction but away from the Γ point at the center of the Brillouin zone, through which spans the latter. As has been demonstrated for several metallic spacers, quantum well states (QWS) with large spanning vectors (*e.g.* the belly of the Fermi surface of fcc Cu, see Fig-

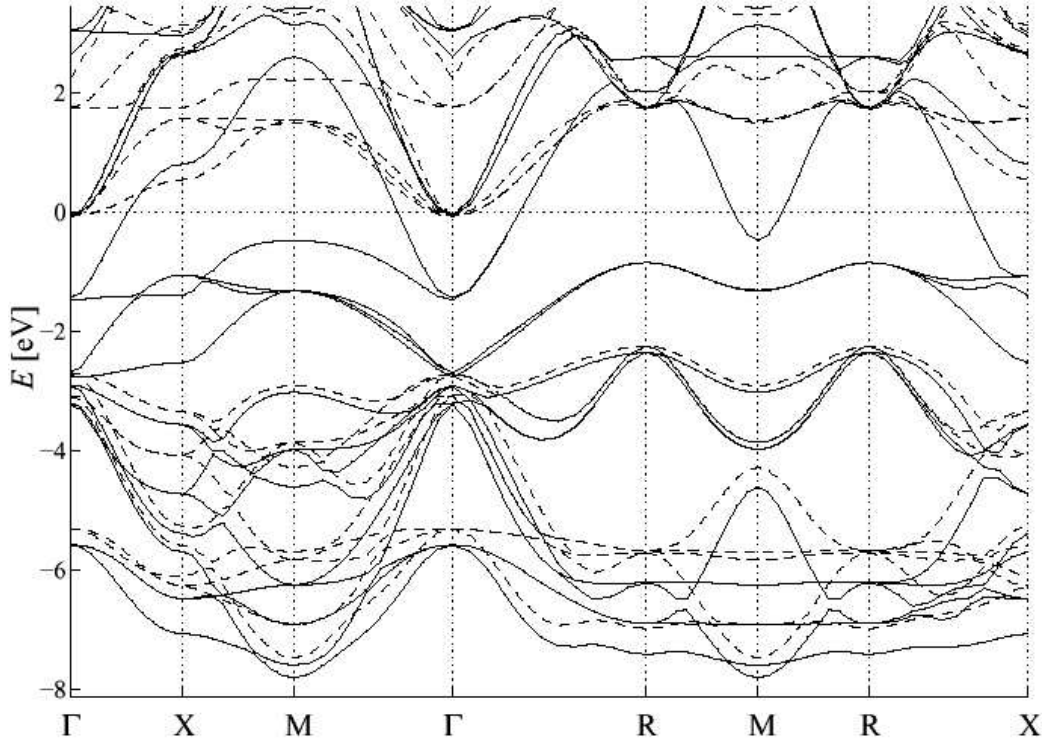


Figure A.14: Band structure of $\text{La}_{0.7}\text{Sr}_{0.3}\text{MnO}_3$ in the cubic perovskite structure. Solid (Dashed) lines correspond to spin \uparrow (\downarrow) bands. From Livesay *et al.* [99]

ure C.1) are much more sensitive to interfacial roughness. [60] This could explain why Livesay's experiment doesn't reveal the long nesting wavevector spanning the electron spheroid. Pickett and Singh also predict the possibility for carriers to "skip" along the edge of the hole cuboid surface, though this mechanism is killed in the transport process. [251] We recall that Fermi surface nesting also occurs with cubic SrTiO_3 (see Figure A.4c), from the zone center along the [001] direction. As regards our experimental results, $\text{La}_{0.7}\text{Sr}_{0.3}\text{MnO}_3/\text{SrTiO}_3$ heterostructures are grown on $\text{SrTiO}_3(001)$. Thus the $\text{La}_{0.7}\text{Sr}_{0.3}\text{MnO}_3$ cell is expected to be slightly non-cubic, while that of SrTiO_3 should remain cubic.

A.4.5 Deviations in the $\text{La}_{0.7}\text{Sr}_{0.3}\text{MnO}_3$ electronic structure

The rich physics abounding in the electronic properties of $\text{La}_{0.7}\text{Sr}_{0.3}\text{MnO}_3$ underscore the delicate chemical interplay between its

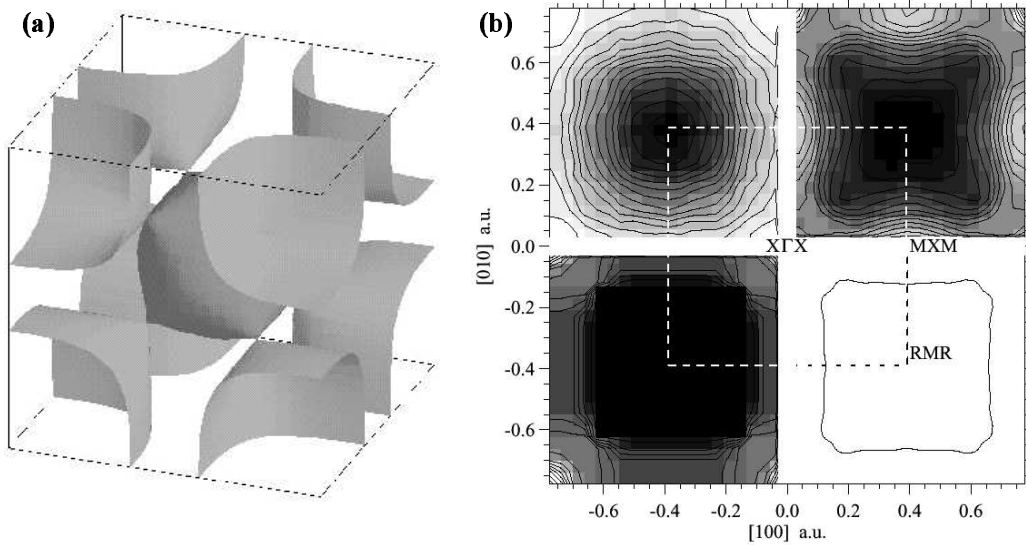


Figure A.15: Fermiology of $\text{La}_{0.7}\text{Sr}_{0.3}\text{MnO}_3$: (a) Hole cuboids centered at the R points, and electron spheroid at the Γ point of the Brillouin zone. (b) Two-dimensional angular correlation of electron-positron annihilation radiation reflecting occupancy along [001] (top left) and extracted Fermi surface of the hole cuboid (bottom right), compared with calculated electron-positron momentum density (top right) and electron occupancy (bottom left). The Brillouin zone is denoted by the dotted line and annotated with the projected symmetry points. From Livesay *et al.* [99]

atomic constituents. As such, it isn't surprising that any change in the stoichiometry of this manganite will affect its electronic properties. We first review the consequences of deviations in oxygen stoichiometry on the manganite's electronic structure (Section A.4.5.1). We then examine the more general topic of electronic phase segregation in manganites as a generic consequence of the double exchange mechanism (Section A.4.5.2).

A.4.5.1 Deviations in oxygen stoichiometry

Deviations in oxygen content will affect the strength of the double exchange mechanism and the underlying half-metallic conduction and ferromagnetism of the system. Dörr and coworkers report [182] that oxygen deficiency resulting from diffusion at temperatures above 80 degree C may result in a magnetically phase-separated ground state. This observation of phase separation, induced by the nominal stoichiometry of the sample, reflects a generic phase separation state in double exchange systems, whether at a symmetry-

breaking interface or within the bulk. Section A.4.5.2 discusses this more at length.

An increase of δ in the O₂ stoichiometry of La_{0.7}Sr_{0.3}MnO_{3± δ} leads to a decrease in E_F (see [184] and references therein). We have compiled data from the relevant references into the graph of Figure A.16. Similarly to SrTiO₃ (see Section A.2.3), this increase in anion concentration may be viewed as a form of p -doping.

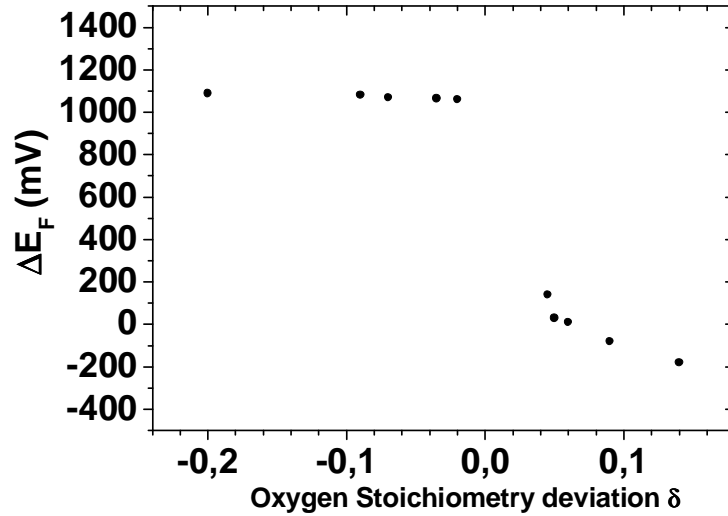


Figure A.16: Evolution of the Fermi level of La_{0.9}Sr_{0.1}MnO_{3± δ} at 873K with oxygen concentration. Adapted from Ref. [184]

A.4.5.2 Electronic phase segregation in double exchange systems

Dagotto and coworkers have reviewed the key role phase separation plays as an integral property of double exchange systems. [247] These phases arise from the formation of D- (D=Sr,Ca) or La-rich manganite clusters in La_{1-x}D_xMnO₃. The deviation from nominal stoichiometry results in a local change from the nominally expected phase. While early theories on the electronic structure of mixed valence manganites considered a homogeneous system, recent experimental evidence points to a more realistic multi-phase picture. Such phase segregation has been observed experimentally at surfaces [253] or interfaces, [254] as could be expected from symmetry breaking present at these boundaries. Nevertheless, phase separation has also been reported [255] within bulk manganites.

Phase segregation in mixed valence oxides has been argued to originate either from extrinsic or intrinsic considerations. An extrinsic approach con-

siders the presence of multiple phases due to sample preparation. Bibes *et al.* recently confirmed the presence of a non-stoichiometric envelope surrounding grains in thin films. [256] This microscopic picture could therefore explain the magnetoresistance observed at high magnetic fields.

Intrinsic arguments consider the effect of competing mechanisms in promoting electronic order on a local scale. A thorough review of this topic, as may be found in the work of Dagotto and coworkers, [247] is beyond the scope of this Thesis. We nevertheless wish to emphasize the possibility for phase separation to occur in our $\text{La}_{0.7}\text{Sr}_{0.3}\text{MnO}_3$ films and $\text{La}_{0.7}\text{Sr}_{0.3}\text{MnO}_3/\text{SrTiO}_3$ interfaces. It is therefore important to consider a conduction of filamentary type within the multiphase environment. Below T_C , percolation of a ferromagnetic phase leads to conduction paths which lower the macroscopic resistance.

A.5 The $\text{La}_{0.7}\text{Sr}_{0.3}\text{MnO}_3/\text{SrTiO}_3$ (001) interface

The electronic structure of the perovskites SrTiO_3 (STO) and $\text{La}_{0.7}\text{Sr}_{0.3}\text{MnO}_3$ (LSMO) incur symmetry breaking at a LSMO/STO interface. This Section reviews the current state of the art regarding the theoretical understanding of such an interface.

A.5.1 Electronic structure

Within the framework of the Computational Magnetoelectronics European Network, a collaboration was initiated with G. Banach and W. Temmerman of “Daresbury Laboratory” on a theoretical investigation of the electronic structure of a $\text{La}_{0.7}\text{Sr}_{0.3}\text{MnO}_3/\text{SrTiO}_3$ (001) cubic interface. A self-interaction corrected local spin density approximation was used within rigid band and supercell models to consider the DOS at the interface. [158, 257]

Their results depart in interpretation from the standard double exchange description of conduction within a mixed Mn valence environment, to bolster other physical theories at play, as reviewed by Dagotto. [247] In particular, half-metallicity may occur in a Mn^{3+} environment at the interface, merely due to its lower coordination relative to Mn^{4+} , for which they find metallicity. These results are comprised in Figure A.17. In the case of a TiO_2 interface, a small number of Ti $3d \downarrow$ states lie at E_F , so that the system isn’t half-metallic.

It should be noted that since the supercell of a mixed compound such as $\text{La}_{0.7}\text{Sr}_{0.3}\text{MnO}_3$ consists of alternating LaO and SrO planes enmeshed within

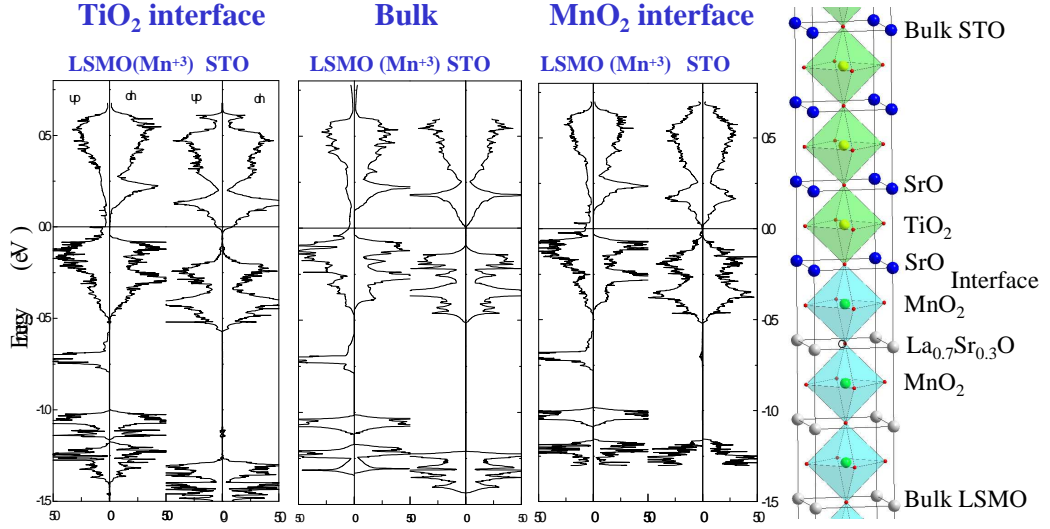


Figure A.17: DOS of TiO_2 - and MnO_2 -terminated LSMO/STO interfaces compared with bulk DOS. From Banach and Temmerman. [158]

MnO_2 planes, it is difficult for the calculation to reflect the correct stoichiometry at an interface. In addition, this model assumes a static lattice with no distortions, even though these drive the electronic properties of $\text{La}_{0.7}\text{Sr}_{0.3}\text{MnO}_3$ as described previously.

A.5.2 Exchange considerations between $\text{La}_{0.7}\text{Sr}_{0.3}\text{MnO}_3$ (001) and SrTiO_3 (001)

As emphasized in the theoretical description of the LSMO/STO interface presented above, the two interfacial scenarii differ in the valency of Mn. Much as was done in the case of the Co/STO interface by Oleinik and collaborators [36] (see Section A.9 p. 237), we propose to consider the nature of oxygen-mediated exchange interactions between Ti and $\text{Mn}^{3+}/\text{Mn}^{4+}$ at one LSMO/STO interface (Section A.5.2.1), then to ponder the interplay between two such interfaces in a magnetic tunnel junction in the conventional and Fowler-Nordheim¹ tunneling regimes (Section A.5.2.2).

A.5.2.1 The $\text{La}_{0.7}\text{Sr}_{0.3}\text{MnO}_3/\text{SrTiO}_3$ (001) interface

In SrTiO_3 Ti assumes a 4+ valence so that its electronic configuration is $[\text{Ar}]4s^03d^0$. In this nominal state, all t_{2g} and e_g orbitals are empty. Therefore,

¹See Section 2.3.1.1 page 23

any exchange interaction with a Mn e_g level will involve the delocalization of an oxygen electron onto the Ti t_{2g} level of lowest energy. This assumes a degree of non-orthogonality between oxygen $p\sigma$ and $p\pi$ orbitals. This mechanism is present at both Mn sites in Goodenough's Case 2 (see Figure A.11 page A.11 and text page 242). With Mn the $S=3/2$ macrospin arising from the three localized $t_{2g}\uparrow$ electrons imposes a ferromagnetic coupling with this delocalized O $2p$ electron. With Ti the absence of a macrospin places no condition on the oxygen electron spin. The resulting ligand with O will be of $pd\pi$ nature, as verified theoretically between Co and Ti at the Co/STO interface. [36]

At a Mn⁴⁺ site, superexchange with Ti leads to *antiferromagnetic* coupling as in Case 2: one oxygen electron ferromagnetically couples to the static Mn moment, so that the Ti moment carried by the other O electron is opposite. At a Mn³⁺ site, two situations may arise depending on the orbital direction of the e_g electron. If it does not point toward the O site, then a similar superexchange with Ti leads to *antiferromagnetic* coupling of Case 2. If this filled orbital does, then a Case 3 *ferromagnetic* coupling is expected between Mn and Ti.

Experiments on Ti substitution in manganite perovskites shows that Ti, with a $3d^0$ electronic configuration, does not participate in ferromagnetic coupling. [258] However, this result reflects the case of Ti impurities in a manganite matrix, so care must be taken in applying this conclusion to the possible presence of an induced moment at the LSMO/STO interface.

Assuming the (perhaps naive) picture of a double exchange conduction mechanism, then carriers impinging on the LSMO/STO interface will convey a lattice distortion through the alternate occupancy of the e_g orbital to a Mn site at the interface. The orbital which extends into the insulator will provide the most efficient electronic transmission through the barrier. Filling of the σ orbital (e_g symmetry) pointing toward Ti will result in a ferromagnetic or antiferromagnetic exchange coupling between Mn and Ti. So within a polaronic picture of transport, the sign of interfacial coupling is driven by Jahn-Teller or breathing vibrational modes of the oxygen sublattice. However in LSMO hopping occurs at a much larger frequency than that of such lattice distortions, so that in essence the oxygen sublattice appears to remain static to the conduction electrons. This picture is therefore not accurate in the case of this manganite.

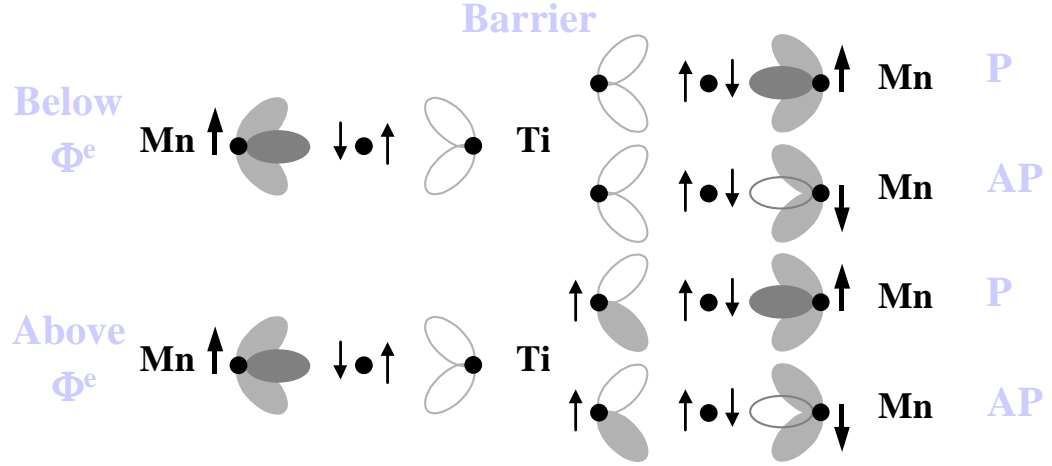


Figure A.18: Superexchange considerations across a manganite/ $3d^0$ insulator/manganite junction for electron injection from left to right, below and above the electron-collecting interfacial barrier height, in the parallel (P) and antiparallel (AP) cases. Only orbitals extending into the barrier with higher transmission probability are considered.

A.5.2.2 Exchange between interfaces in a $\text{La}_{0.7}\text{Sr}_{0.3}\text{MnO}_3/\text{SrTiO}_3/\text{La}_{0.7}\text{Sr}_{0.3}\text{MnO}_3$ (001) junction

If we couple two such interfaces to produce a LSMO/STO/LSMO junction, the relative alignment of magnetization of the two electrodes defines the final coupling between Mn sites across the barrier. In a tunneling regime which conserves spin, the moment induced on Ti sites at both interfaces should be the same. Since the Ti $3d^0$ site does not place an intrinsic condition on the spin of the O delocalized electron, a parallel alignment of the electrodes' magnetization leads to induced ferromagnetic (F) moments on each set of Ti interfacial sites for Mn sites with same filling of the e_g orbital. The interaction is stronger when ferromagnetic coupling (Case 3) occurs between Mn and Ti at each interface, *i.e.* the Mn σ orbital is filled, rather than weak antiferromagnetic coupling, wherein this orbital is empty. An antiparallel alignment of the electrodes' magnetization will couple Mn sites at each interface with a different filling of the σ orbital. These considerations are schematized in Figure A.18. One may infer from this picture a possible requirement of coupling between the lattice distortions at each interface to promote efficient conduction through the junction.

When the barrier height of SrTiO_3 is exceeded through an applied junction bias which distorts the barrier profile, electrons enter the first conduction band, with Ti t_{2g} symmetry. Along with SrVO_3 , materials similar to

SrTiO₃ with an extra electron include LaTiO₃, in which substitution of La for Sr leads to complete filling of the first Ti t_{2g} band and a Ti³⁺ $3d^1$ state which promotes metallic conduction. [191] Assuming purely half-metallic conduction in LSMO, and disregarding the p - n nature of a LSMO/STO interface in such a state, we now consider exchange interactions between an electron injected from a LSMO electrode into the STO conduction band near the interface with the second LSMO electrode. This Ti conduction electron will carry a spin collinear with that on the originating Mn site. Goodenough predicts [236] either Case 2 antiferromagnetic or Case 3 ferromagnetic superexchange coupling between such a Ti³⁺ site and a Mn $3d^4$ site (valence ³⁺). These considerations may be invoked when discussing magnetotransport above the tunneling barrier heights in LSMO/STO/LSMO (see Section 7.2) and LSMO/STO/Co junctions (see Section 7.3). It should be pointed out that this picture of a moment induced on the paramagnetic barrier site by a neighboring ferromagnetic site was tested experimentally without success (see Section 4.2), though this picture may nevertheless remain valid in the Fowler-Nordheim tunneling regime.

Appendix B

Nanoscale chemical analysis of tunnel junction interfaces

An intense background effort was undertaken within our laboratory as well as through collaborations to characterize the interfaces of $\text{La}_{0.7}\text{Sr}_{0.3}\text{MnO}_3$ -based junctions. This Appendix describes X-Ray Photoelectron Spectroscopy (XPS) and Electron Energy Loss Spectroscopy (EELS) analyses of the chemistry at the lower and upper LSMO/STO interfaces in LSMO/STO/LSMO magnetic tunnel junctions (see Section B.1), and EELS experiments at the STO/Co interface in LSMO/STO/Co junctions (see Section B.2).

B.1 Chemical state of the $\text{La}_{0.7}\text{Sr}_{0.3}\text{MnO}_3$ / SrTiO_3 (001) interface

Figure B.1 displays a High-Resolution Transmission Electron Microscopy (HRTEM) image of the epitaxy throughout a LSMO/STO/LSMO trilayer. As described in previous Sections, the perovskite SrTiO_3 consists of alternating TiO_2 (light) and SrO (dark) planes; and the perovskite $\text{La}_{0.7}\text{Sr}_{0.3}\text{MnO}_3$, of MnO_2 (light) and $\text{La}_{0.7}\text{Sr}_{0.3}\text{O}$ (dark) planes. The cell height corresponds to the bulk 3.905\AA of SrTiO_3 . Four different interfacial scenarii are therefore possible in principle, but epitaxial consideration of the interface with perovskite structure reduce that set to two: a MnO_2/SrO or a $\text{La}_{0.7}\text{Sr}_{0.3}\text{O}/\text{TiO}_2$ set of planes will pinpoint the interface through a chemical transition from one structure to the other. Through Electron Energy Loss Spectroscopy (EELS) and X-Ray Photoemission Spectroscopy (XPS) experiments, we believe to have narrowed this set to only the $\text{La}_{0.7}\text{Sr}_{0.3}\text{O}/\text{TiO}_2$ case.

During a visit to our group, R. Bertacco of "the Politecnico di Milan" performed XPS measurements on LSMO surfaces and interfaces with STO.

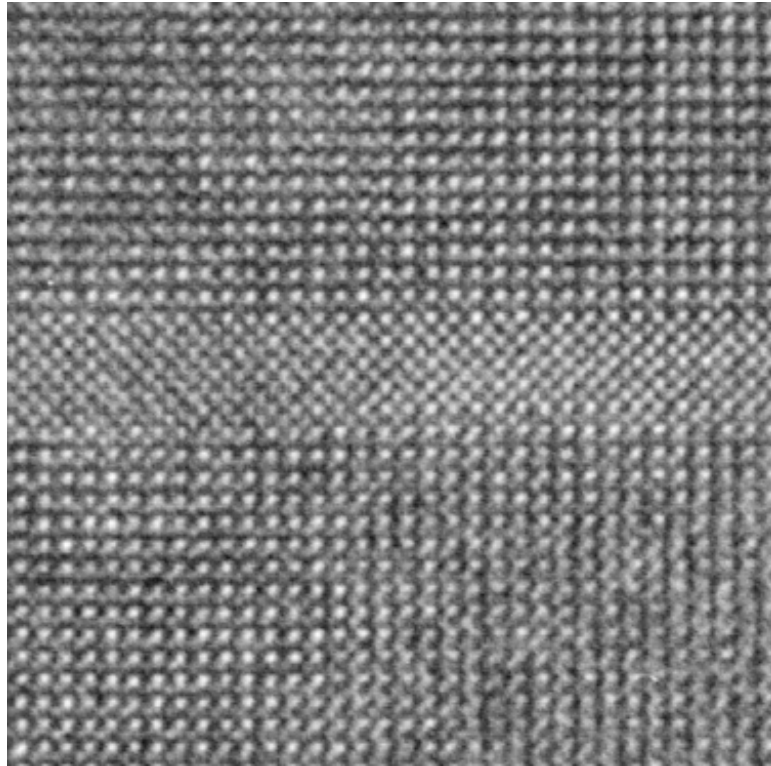


Figure B.1: HRTEM of a STO barrier sandwiched between LSMO layers in this fully epitaxial constrained heterostructure. MnO₂ columns within LSMO, which exhibit bright contrast, are separated by the 3.905Å STO lattice spacing. Picture by J.-L. Maurice.

We refer the reader to a published account of this study, [259] and merely report his conclusions. The growth kinetics of La_{0.7}Sr_{0.3}MnO₃ at 700°C under a 350mTorr oxygen ambient lead to the formation of a Sr-rich surface layer. When capped with SrTiO₃, this Sr-rich LSMO surface is resorbed and does not appear at the interface. However, the presence of Sr in the overlayer may be misleading. It is possible that this monolayer acts as a surfactant in assisting the growth process. It is known that the kinetics of manganite growth are constrained by the rate of oxidation of the topmost layer for a given oxygen ambient. [260] The larger oxidation potential for MnO₂ relative to SrO could thus explain the presence of the Sr-rich layer at the surface. Preliminary examination of the LSMO interface state with CeO₂ confirmed the presence of the Sr-rich overlayer.

HRTEM experiments involving Electron Energy Loss Spectroscopy (EELS) and the accompanying simulations (see Figure B.2) have provided

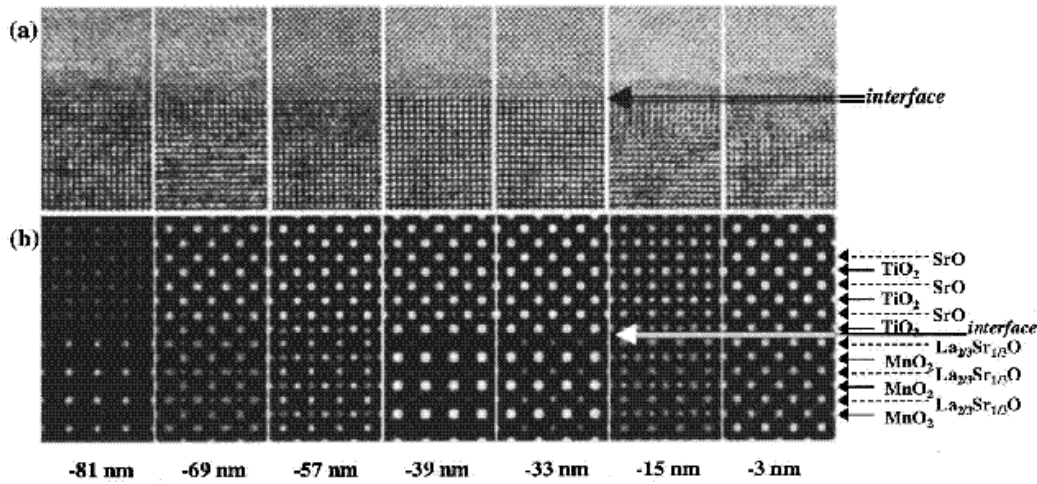


Figure B.2: (a) HRTEM image of a LSMO/STO/LSMO epitaxial trilayer and (b) comparison with simulation for several de-focusing values. From Pailloux *et al.* [117]

further evidence that the final monolayer consists of a Sr-rich plane. This research [117] was performed through a collaboration between our laboratory and D. Imhoff within the group of C. Colliex at the "Université de Paris-Sud Orsay". The EELS spectra taken every 3\AA as the 7\AA probe is scanned across the lower LSMO/STO interface reveal no increase in Mn^{4+} indicative of a foreign phase at the interface (see Figure B.3). As such one hypothesis is that the last MnO_2 atomic plane is capped by a $\text{La}_{0.7}\text{Sr}_{0.3}\text{O}$ plane so as to retain the proper doping environment leading to the Mn mixed valence. The limited number of scans did not cover a large portion of the sample, so that this evidence doesn't rule out the possible presence of segregated interfacial phases. A similar study of the upper STO/LSMO interface likewise revealed no major shift in Mn valency. [118] This result appears surprising if one considers the unit-cell-high layer-by-layer growth mode of the SrTiO_3 interlayer, which should promote differing terminations at the lower and upper interfaces. Nevertheless, the signal decrease of the La/Sr elemental signature is varyingly more abrupt on one interface compared to the other. As illustrated in Figure B.4, the difference in rise of this signal may span several nm. Furthermore, minute signal variations not exceeding 3% of the Mn $3d$ -O $2p$ electronic structure could be detected in the Mn $2p$ fine structure. *This implies that both interfaces are locally dissimilar throughout the sample, with possible deviations from nominal electronic structure.* On a mesoscopic scale, nevertheless, both the lower and upper interface appear to be of good quality when compared to the bulk. As such the authors conclude that the correct

Mn chemical environment is observed in both the lower and upper interfaces, suggesting a $\text{MnO}_2/\text{La}_{0.7}\text{Sr}_{0.3}\text{O}/\text{TiO}_2$ atomic stack at each interface. It should be noted that these measurements were taken at 300K, making the observation of possible phase segregation more arduous given the 360K Curie temperature of LSMO.

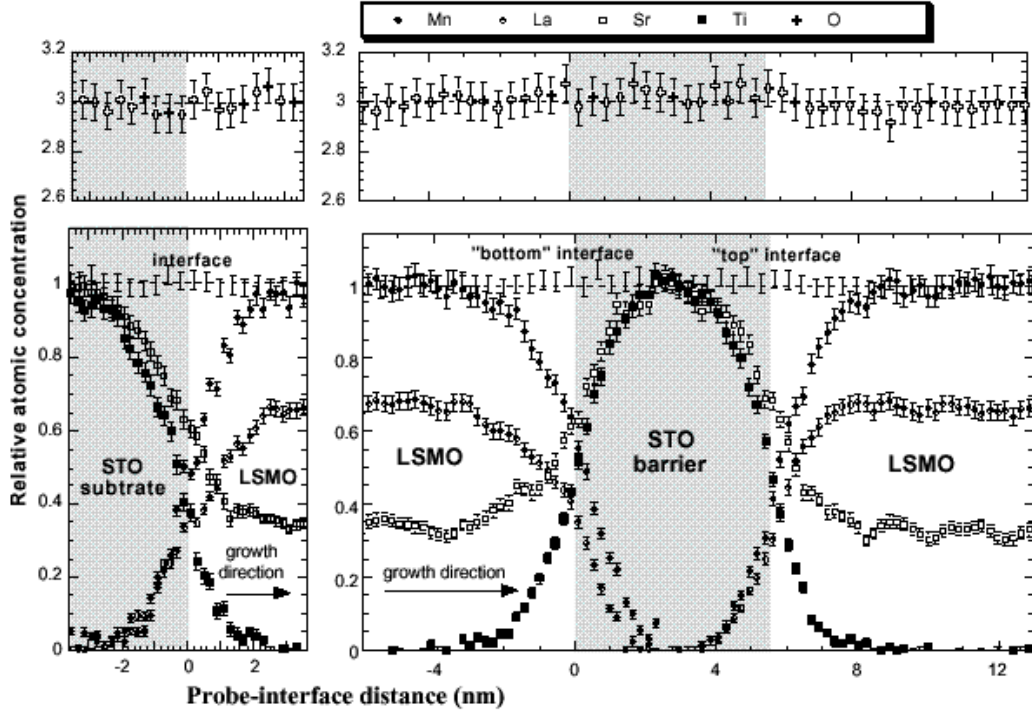


Figure B.3: EELS on LSMO/STO/LSMO: evolution of elemental composition throughout the LSMO/STO/LSMO trilayer structure compared with the substrate interface. From Samet *et al.* [118]

B.2 Chemical state of the STO/Co interface

The oxidation state of Co at the interface with STO is expected to greatly influence the magnetotransport properties of LSMO/STO/Co junctions. To obtain direct information about the chemical state of the STO/Co interface, High-Resolution Transmission Electron Microscopy (HRTEM) was performed by J.L. Maurice and buttressed by Electron-Energy Loss Spectroscopy experiments through a collaboration with D. Imhoff and C. Colliex of the "Université de Paris-Sud Orsay". In this diffraction experiment

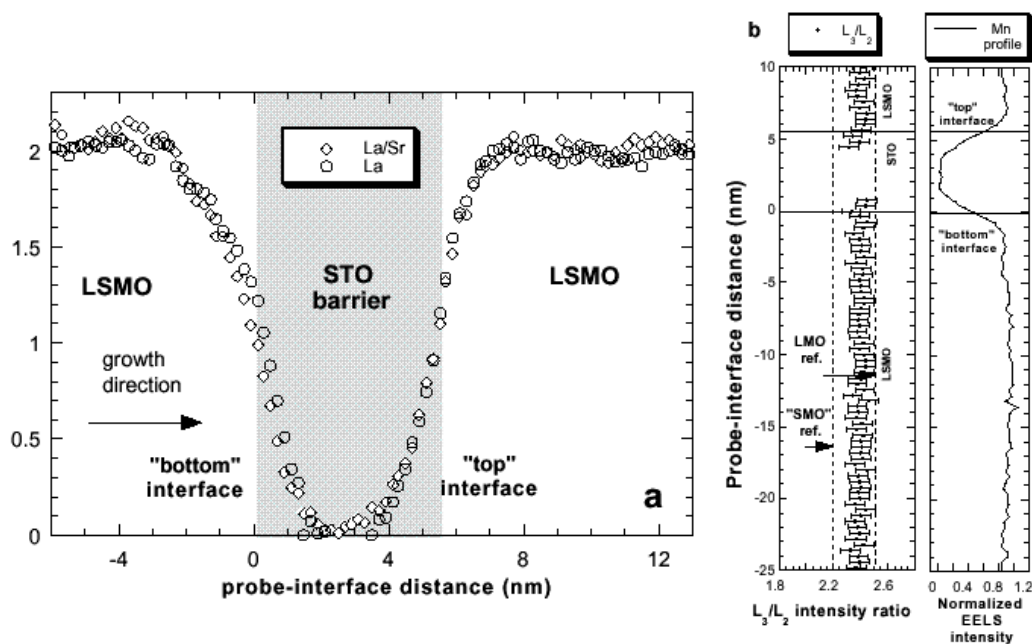


Figure B.4: EELS on LSMO/STO/LSMO: (a) La to Sr atomic ratio and (b) evolution of Mn valence through the LSMO/STO/LSMO trilayer. From Samet *et al.* [118]

through the 50nm-thick TEM slice of the heterostructure, an electron beam of size 7\AA is swept in 3\AA increments across the interface.

The study [119] evidences the presence of a foreign oxide layer at the STO/Co interface (see white band at STO/Co interface Figure B.5). This layer likely results from the chemical interaction between the SrO monolayer at the surface of STO, any contaminants accrued during sample transfer in air, and Co. From the TEM picture, the thickness of this layer doesn't exceed one monolayer. However, the signature of Co in a CoO-like oxygen environment at the interface, which amounted to $\sim 10\%$ of the energy loss signal, points to the presence of a thicker, $\sim 1\text{nm}$ -thick layer.

The incidence of this CoO layer on magnetotransport is unclear. In a worst case scenario, the STO surface in a LSMO/STO bilayer was etched prior to Co counterdeposition, yet no incidence on the reproducibility of $R(H)$ curves could be noted (see Section 7.3.3.1) despite the presumed presence of additional oxygen at the interface. Furthermore, the presence of holes in this oxide layer could channel current and result in tunneling from a clean ferromagnet/barrier interface (see Figure B.5b).

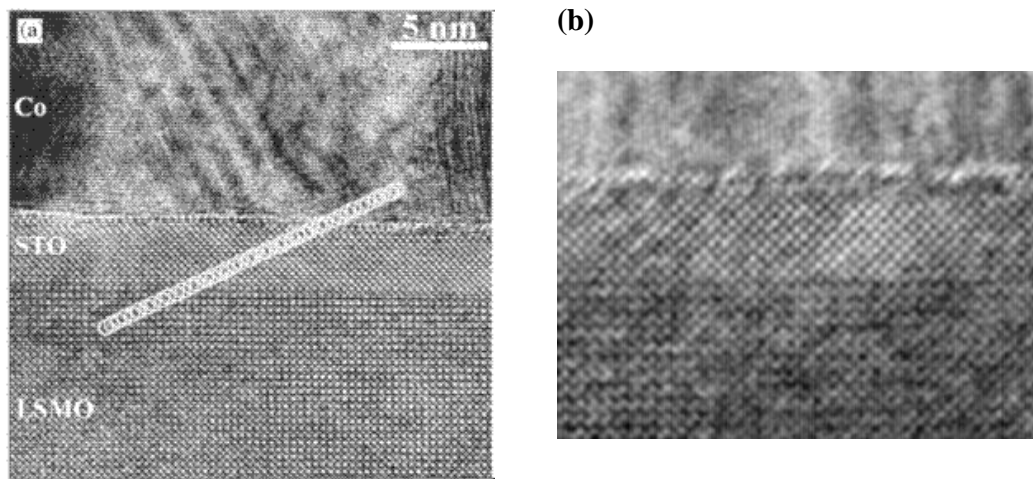


Figure B.5: HRTEM images of the LSMO/STO/Co heterostructure. (a) EELS studies across the STO/Co interface in sample A11523 attribute the white band to a nanometer-thick CoO layer, as confirmed by transport experiments. (b) Holes in this layer may allow for a metallic Co/STO interface to dominate the tunneling current in sample A11531.

Appendix C

Magnetic interlayer exchange coupling & quantum well states

The origin of the spin electronics field lies with the discovery by Grünberg and coworkers in 1986 of oscillations in the magnetic interlayer exchange coupling (MIEC) between two ferromagnetic layers separated by a non-magnetic metallic spacer of varying thickness. [55] The field then expanded dramatically when it was discovered that the ferromagnetic (F) or antiferromagnetic (AF) alignment of magnetization between successive layers results in a sizeable resistance change of the trilayer or multilayer stack. [56] This macroscopic manifestation of spin-polarized currents in artificial magnetic nanostructures has catalyzed the field toward a better physical understanding of the phenomenon due to potential applications, both immediate such as magnetic-field sensing devices or on a more long-term scale. Indeed, the prospect of introducing spin as an additional parameter in conceiving the logic of electrical circuits, and its quantum mechanical implications on information processing, has also galvanized research. This rapid overview of a rich field of condensed matter physics is by no means exhaustive. The interested reader may refer for instance to reviews by Stiles, Himpsel, Qiu/Smith and Milun. [60, 261–263]

The oscillation of MIEC with non-magnetic spacer thickness ($\sim 10\text{\AA}$ for Cu) between ferromagnetic and antiferromagnetic alignments of the magnetic layers was attributed to a Rudermann, Kittel, Kasuya and Yosida interaction, *i.e.* resulting from spin-dependent scattering of electrons at the magnetic/non-magnetic interfaces. The RKKY theory predicts an oscillation periodicity of $\pi/(k_{BZ} - k_F)$, [57–59] where k_{BZ} and k_F are the Brillouin zone boundary and Fermi surface nesting wavevectors, respectively. This theory both explained existing evidence for long-period oscillations, but also predicted the existence of short period oscillations - due to another larger

Fermi surface spanning wavevector, which were thereafter discovered. [264]

C.1 The quantum well state picture

The quantum well state picture considers the magnetic interlayer coupling oscillations as resulting from the quantization of energy levels within the spacer. At such a level, the band structure of the spacer allows for stationary states to appear. The overarching physical requirement is that of a nested Fermi surface, *i.e.* one which promotes a spanning wavevector between two portions of the Fermi surface of same curvature for a given wavevector k value. The opposite sign of k between each portion of the Fermi surface thus allows a carrier to bounce off of an interface and back into the spacer with wavevector $-k$. Constructive interference between the wavefunctions of incoming and outgoing carriers results in the formation of a quantum well state (QWS) at that energy. The condition for constructive interference is embodied in the phase accumulation model $2(k_{BZ} - k_F)d_{spacer} - \phi_C - \phi_B = 2\pi\nu$ which considers phase shifts ϕ_C and ϕ_B in the carrier wavefunction due to interfacial scattering at each of the two interfaces. [265] Should this QWS cross the Fermi level, then energy minimization conditions result in an AF alignment of the two magnetic electrodes.

In a simple picture, this effect is driven solely by the thickness of the non-magnetic spacer. However, a quantum interference model, developed by Bruno, which takes into account not only the spacer and its thickness, but reflections at all interfaces in the heterostructure, demonstrates that quantum interference in the adjacent magnetic layers needs to be taken into account as well. [266] This more complex picture was confirmed by Kawakami *et al.* through photoemission experiments on Cu/Co/Ni/Co(001) with wedged Cu and Co top layers which evidence a modulation of Cu quantum well states as a function of underlying Co thickness. [267]

Figure C.1 presents a comparison between the MIEC and quantum well (QW) state pictures for the case of the Co(001)/Cu(001)/Co(001) system. The spanning wavevectors at the belly and neck of the Cu(001) Fermi surface promote QW states with long and short periodicities as Cu spacer thickness is increased. Notably, the energy position of the QW increases with increasing Cu thickness. Panels (e) and (f) present photoemission intensity at the belly and neck of the Cu Fermi surface. Panel (g) presents X-Ray Magnetic Linear Dichroism data on the topmost Co layer, which probes the magnetic coupling of that layer with respect to the lower Co layer. The two oscillations in MIEC present in this data are well reproduced by a calculation of interlayer coupling. Thus, this comparison between QW and MIEC data

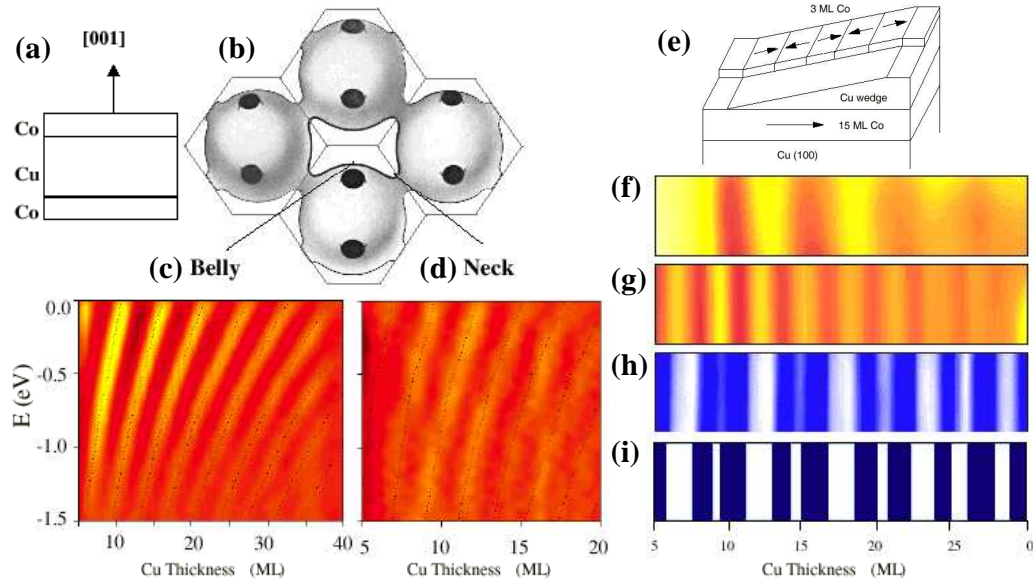


Figure C.1: Confirmation of the link between interlayer coupling and quantum well states in thin films with Fermi surface nesting properties in the case of Co(001)/Cu(001)/Co(001). (a) Schematic of sample. (b) In the [001] direction, fcc Cu exhibits nesting conditions at the (c) belly and (d) neck of the Fermi surface which promote quantum well states as probed by photoemission. (e) A close correlation as a function of Cu interlayer thickness between QW states probed by photoemission at the (f) belly and (g) neck of the Cu Fermi surface, and (h) magnetic coupling of the Co films as probed by XMLD from the top 3 ML Co (dark=F, light=AF), to be compared with interlayer coupling theory (i). From Qiu & Smith [60]

explicitly confirms the identical nature of the magnetic interlayer coupling and quantum well states pictures.

C.2 Spacer materials

Until recently all reports of MIEC concerned metallic spacers. However, as part of his seminal article, Sloncszewski also considered the possibility for the two magnetic electrodes in a magnetic tunnel junction to couple through exchange interactions across the insulating spacer. [30] Metallic-type MIEC across the semiconducting FeSi was recently reported by the Grünberg group, [61] while the case of insulating-type MIEC through MgO(001) was experimentally demonstrated recently by the Schuhl group (Nancy, France). [62]

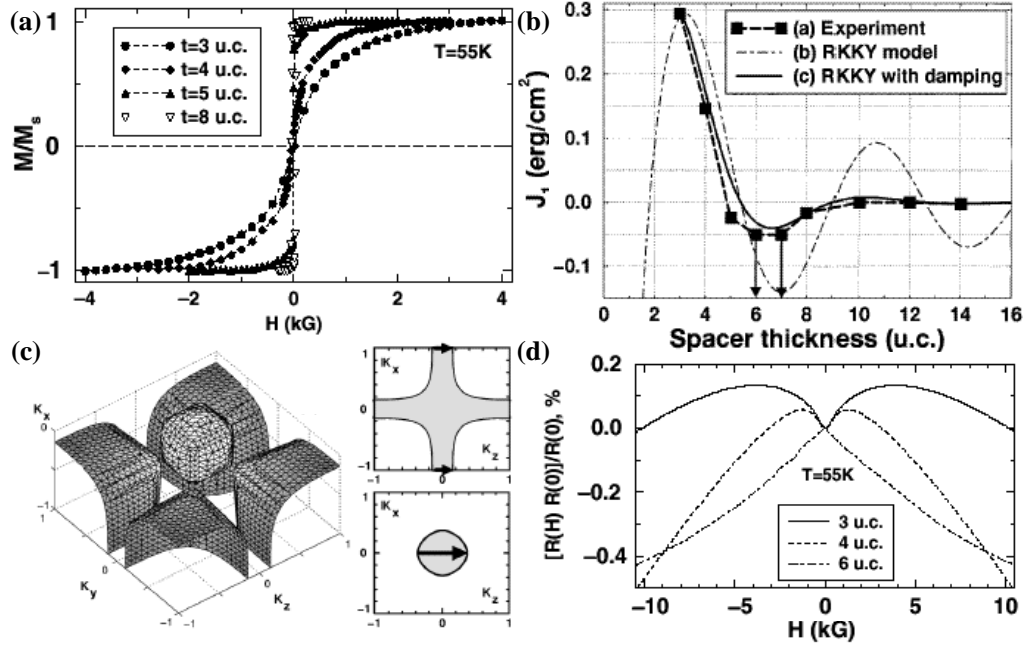


Figure C.2: Oscillatory exchange coupling between $La_{0.7}Ba_{0.3}MnO_3$ layers across a $LaNiO_3$ metallic spacer in superlattices: (a) $M(H)$ curves for remarkable spacer thicknesses. (b) Evolution of the coupling constant with spacer thickness, fitted with both standard, and damped (damping length λ of 3 unit cells) RKKY models. (c) Fermi surface of the perovskite $LaNiO_3$ with insets showing the hole (top) and electron (bottom) spanning vectors. (d) $R(H)$ curves for remarkable spacer thicknesses. From Nikolaev *et al.* [63]

MIEC has also been reported in perovskite oxide systems. Nikolaev *et al.* have reported an oscillation in the magnetic coupling in a superlattice sample of $La_{0.7}Ba_{0.3}MnO_3$ layers separated by $LaNiO_3$, a paramagnetic metal spacer. [63] As shown in Figure C.2a, the remanence of $M(H)$ loops changes significantly as the spacer thickness is increased. Along with minor loop data, the authors extracted a dependence of the coupling constant between $La_{0.7}Ba_{0.3}MnO_3$ layers as a function of spacer thickness (panel (b)). An oscillation period $T_{LP}=7.2$ unit cells was observed, corresponding to a spanning vector across the R-centered hole cuboids (see panel (c) and top inset). Given the smaller size of this spanning vector compared to that across the electron spheroid, it is expected to dominate any Fermi surface nesting considerations in the event of interfacial roughness. The authors were able to fit the MIEC oscillation within a RKKY expression of coupling $J_1 = -A[\cos(2\pi t/T_{LP})/t]exp(-t/\lambda)$ which takes into account strong electron

scattering in the spacer. Here t is the spacer thickness, T_{LP} is the period of the long oscillation, and $\lambda=3$ unit cells is the damping length. As illustrated in panel (d), this change to antiferromagnetic (AF) coupling results in a resistance dip as applied magnetic field is decreased to 0. In a subsequent article comparing this indirect AF coupling to the case of direct AF coupling, the dip is attributed to the competing effects of the exchange field and the applied magnetic fields (see Figure 7.19 page 152). [64] Such AF coupling has been shown to subsist up to the Curie point of the manganite. [176]

Finally, evidence for MIEC between $\text{La}_{0.6}\text{Sr}_{0.4}\text{MnO}_3$ layers across an insulating SrTiO_3 layer has also been reported, though no information regarding the nature of the spanning wavevector was provided. [65, 66]

Bibliography

- [1] J. Bardeen. Tunneling from a many particle point of view. *Phys. Rev. Lett.*, 6:57, 1961.
- [2] A.H. Davis and J.M. MacLaren. Spin dependent tunneling at finite bias. *J. Appl. Phys.*, 87:52247, 2000.
- [3] J.G. Simmons. Generalized formula for the electric tunnel effect between similar electrodes separated by a thin insulating film. *J. Appl. Phys.*, 34:1763, 1963.
- [4] W.F. Brinkman, R.C. Dynes, and J.M. Rowell. Tunneling conductance of asymmetrical barriers. *J. Appl. Phys.*, 41:1915, 1970.
- [5] R. Stratton. Volt-current characteristics for tunneling through insulating films. *J. Phys. Chem. Solids*, 23:1177, 1962.
- [6] W.A. Harrison. Tunneling from an independent particle point of view. *Phys. Rev.*, 123:85, 1961.
- [7] M. Jullière. Tunneling between ferromagnetic films. *Phys. Lett.*, 54A:225, 1975.
- [8] P. Seneor. Jonctions tunnel à base d'oxydes magnétiques demi-métalliques. *Ph.D. Thesis, École Polytechnique, France*, page 27, 1999.
- [9] P.R. Leclair. Fundamental aspects of spin-polarized tunneling. *Ph.D. Thesis, Eindhoven University of Technology, Eindhoven, The Netherlands*, page 16, 2002.
- [10] I.I. Mazin. How to define and calculate the degree of spin polarization in ferromagnets. *Phys. Rev. Lett.*, 83:1427, 1999.
- [11] G.E. Blonder, M. Tinkham, and T.M. Klapwijk. Transition from metallic to tunneling regimes in superconducting microconstrictions: excess

- current, charge imbalance, and supercurrent conversion. *Phys. Rev. B*, 25:4515, 1982.
- [12] S.K. Upadhyay, A. Palanisami, R.N. Louie, and R.A. Buhrman. Probing ferromagnets with Andreev reflection. *Phys. Rev. Lett.*, 81:3247, 1998.
- [13] Jr. R.J. Soulen, J.M. Byers, M.S. Osofsky, B. Nadgorny, T. Ambrose, S.F. Cheng, P.R. Broussard, C.T. Tanaka, J. Nowak, J.S. Moodera, A. Barry, and J.M.D. Coey. Measuring the spin polarization of a metal with a superconducting point contact. *Science*, 282:85, 1998.
- [14] P. Raychaudhuri, A.P. Mackenzie, J.W. Reiner, and M.R. Beasley. Transport spin polarization in SrRuO₃ measured through point-contact Andreev reflection. *Phys. Rev. B*, 67:020411, 2003.
- [15] R. Meservey and P.M. Tedrow. Spin-polarized electron tunneling. *Phys. Rep.*, 238:173, 1994.
- [16] P.M. Tedrow and R. Meservey. Direct observation of spin-state mixing in superconductors. *Phys. Rev. Lett.*, 27:919, 1971.
- [17] J.S. Moodera and G. Mathon. Spin polarized tunneling in ferromagnetic junctions. *J. Magn. Magn. Mater.*, 200:248, 1999.
- [18] D.J. Monsma and S.S.P. Parkin. Spin polarization of tunneling current from ferromagnet/Al₂O₃ interfaces using copper-doped aluminum superconducting films. *Appl. Phys. Lett.*, 77:720, 2000.
- [19] D.C. Worledge and T.H. Geballe. Spin-polarized tunneling in La_{0.7}Sr_{0.3}MnO₃. *Appl. Phys. Lett.*, 76:900, 2000.
- [20] D.C. Worledge and T.H. Geballe. Negative spin-polarization of srRuO₃. *Phys. Rev. Lett.*, 85:5182, 2000.
- [21] F. Montaigne, M. Hehn, and A. Schuhl. Tunnel barrier parameters and magnetoresistance in the parabolic band model. *Phys. Rev. B*, 64(14):144402, 2001.
- [22] J.M. De Teresa, A. Barthélémy, A. Fert, J.P. Contour, R. Lyonnet, F. Montaigne, P. Seneor, and A. Vaurès. Inverse tunnel magnetoresistance in co/SrTiO₃/La_{0.7}Sr_{0.3}MnO₃: new ideas on spin-polarized tunneling. *Phys. Rev. Lett.*, 82:4288, 1999.

- [23] J.M. De Teresa, A. Barthélémy, A. Fert, J.P. Contour, F. Montaigne, and P. Seneor. Role of metal/oxide interface in determining the spin polarization of magnetic tunnel junctions. *Science*, 286:507, 1999.
- [24] K.S. Takahashi, A. Sawa, Y. Ishii, H. Akoh, M. Kawasaki, and Y. Tokura. Inverse tunnel magnetoresistance in all-perovskite junctions of $\text{La}_{0.7}\text{Sr}_{0.3}\text{MnO}_3/\text{SrTiO}_3/\text{SrRuO}_3$. *Phys. Rev. B*, 67:094413, 2003.
- [25] F.J. Himpsel, K.N. Altman, G.J. Mankey, J.E. Ortega, and D.Y. Petrovykh. Electronics states in magnetic nanostructures. *J. Magn. Magn. Mater.*, 200:456, 1999.
- [26] M.B. Stearns. Simple explanation of tunneling spin-polarization of Fe,Co,Ni and its alloys. *J. Magn. Magn. Mater.*, 5:167, 1977.
- [27] J.W. Gadzuk. Band-structure effects in the field-induced tunneling of electrons from metals. *Phys. Rev.*, 182:416, 1969.
- [28] M. Campagna, T. Utsumi, and D. Buchanan. Study of the spin polarization of field-emitted electrons from magnetic materials. *J. Vac. Sci. Technol.*, 13:193, 1976.
- [29] W. H. Butler, X. G. Zhang, T. C. Schultess, and J. M. MacLaren. Reduction of electron tunneling current due to lateral variation of the wave function. *Phys. Rev. B*, 63:092402, 2001.
- [30] J.C. Slonczewski. Conductance and exchange coupling of two ferromagnets separated by a tunneling barrier. *Phys. Rev. B*, 39:6995, 1989.
- [31] A.M. Bratkovsky. Tunneling of electrons in conventional and half-metallic systems: towards very large magnetoresistance. *Phys. Rev. B*, 56:2344, 1997.
- [32] J.S. Moodera, L. R. Kinder, T.M. Wong, and R. Meservey. Large magnetoresistance at room temperature in ferromagnetic thin film tunnel junctions. *Phys. Rev. Lett.*, 74:3273, 1995.
- [33] E.Y Tsymbal and D.G Pettifor. Modelling of spin-polarized electron tunneling from 3d ferromagnets. *J. Phys.: Condens. Matter*, 9:L411, 1997.
- [34] I.I. Oleinik, E.Y. Tsymbal, and D.G. Pettifor. Structural and electronic properties of $\text{Co}/\text{Al}_2\text{O}_3/\text{Co}$ magnetic tunnel junction from first principles. *Phys. Rev. B*, 62:3952, 2000.

- [35] S. Zhang and P.M. Levy. Models for magnetoresistance in tunnel junctions. *Eur. Phys. J. B*, 10:599, 1999.
- [36] I.I. Oleinik, E.Y. Tsymbal, and D.G. Pettifor. Atomic and electronic structure of Co/SrTiO₃/Co magnetic tunnel junctions. *Phys. Rev. B*, 65:020401, 2002.
- [37] J. Kanamori. Superexchange interaction and symmetry properties of electron orbitals. *J. Phys. Chem. Solids*, 10:87, 1959.
- [38] S.G. Louie, J.R. Chelikowsky, and M.L. Cohen. Ionicity and the theory of Schottky barriers. *Phys. Rev. B*, 15:2154, 1977.
- [39] J. Tersoff. Shottky barrier heights and the continuum of gap states. *Phys. Rev. Lett.*, 52:465, 1984.
- [40] V.E. Henrich and P.A.Cox. The surface science of metal oxides. *Cambridge University Press, Cambridge*, 1994.
- [41] V. Bellini. Electronic structure of low-dimensional systems. *Ph.D Thesis: Rheinisch-Westfälischen Technischen Hochschule Aachen*, page 121, 2000.
- [42] Ph. Mavropoulos, N. Papanikolaou, and P.H. Dederichs. Complex band structure and tunneling through ferromagnet/insulator/ferromagnet junctions. *Phys. Rev. Lett.*, 85:1088, 2000.
- [43] J. Callaway and C.S. Wang. Energy bands in ferromagnetic iron. *Phys. Rev. B*, 15:2095, 1977.
- [44] J.M. MacLaren, X.-G. Zhang, and W.H. Butler. Validity of the Jullière model of spin-dependent tunneling. *Phys. Rev. B*, 56:11827, 1997.
- [45] J.M. MacLaren, X.-G. Zhang, W.H. Butler, and X. Wang. Layer KKR approach to Bloch-wave transmission and reflection: application to spin-dependent tunneling. *Phys. Rev. B*, 59:5470, 1999.
- [46] W. H. Butler, X. G. Zhang, T. C. Schultess, and J. M. MacLaren. Spin-dependent tunneling conductance of Fe/MgO/Fe sandwiches. *Phys. Rev. B*, 63:054416, 2001.
- [47] J. Mathon and A. Umerski. Theory of tunneling magnetoresistance of an epitaxial Fe/MgO/Fe(001) junction. *Phys. Rev. B*, 63:220403, 2001.

- [48] P.M. Levy, K. Wang, P.H. Dederichs, C. Heide, S. Zhang, and L. Szunyogh. An approximate calculation for transport in magnetic tunnel junctions in the presence of localized states. *Phil. Mag.*, 82:763, 2002.
- [49] K. Wang, P.M. Levy, S. Zhang, and L. Szunyogh. On the calculation of the magnetoresistance of tunnel junctions with parallel paths of conduction. *Phil. Mag.*, 83:1255, 2003.
- [50] E.L. Wolf. Principles of electron tunneling spectroscopy. *Oxford University Press, New York & Clarendon Press, Oxford*, page 62, 1985.
- [51] M. Sharma, S.X. Wang, and J.H. Nickel. Inversion of spin polarization and tunneling magnetoresistance in spin-dependent tunneling junctions. *Phys. Rev. Lett.*, 82:616, 1999.
- [52] J.S. Moodera, J. Nowak, L.R. Kinder, P.M. Tedrow, R.J.M. van de Veerdonk, B.A. Smits, M. van Kampen, H.J.M. Swagten, and W.J.M. de Jonge. Quantum well states in spin-dependent tunnel structures. *Phys. Rev. Lett.*, 83:3029, 1999.
- [53] R.C. Sousa, J.J. Sun, V. Soares, P.P. Freitas, A. Kling, M.F. da Silva, and J.C. Soares. Temperature dependence and annealing effects on spin dependent tunnel junctions. *J. Appl. Phys.*, 85:5258, 1999.
- [54] A.H Davis and J.M MacLaren. Ballistic transport and tunnelling magnetoresistance in tunnel junctions. *J. Phys.: Condens. Matter*, 14:4365, 2002.
- [55] P. Grünberg, R. Schreiber, and Y. Pang. Layered magnetic structures: Evidence for antiferromagnetic coupling of Fe Layers across Cr interlayers. *Phys. Rev. Lett.*, 57:2442, 1986.
- [56] M.N. Baibich, J.M. Broto, A. Fert, F. Nguyen Van Dau, and F. Petroff. Giant magnetoresistance of (001)Fe/(001)Cr magnetic superlattices. *Phys. Rev. Lett.*, 61:2472, 1988.
- [57] Y. Wang, P. M. Levy, and J.L. Fry. Interlayer magnetic coupling in Fe/Cr multilayered structures. *Phys. Rev. Lett.*, 65:2732, 1990.
- [58] D.M. Edwards, J. Mathon, R.B. Muniz, and M.S. Phan. Oscillations of the exchange in magnetic multilayers as an analog of de Haas-van Alphen effect. *Phys. Rev. Lett.*, 67:493, 1991.

- [59] P. Bruno and C. Chappert. Oscillatory coupling between ferromagnetic layers separated by a nonmagnetic metal spacer. *Phys. Rev. Lett.*, 67:1062, 1991.
- [60] Z.Q. Qiu and N.V. Smith. Quantum well states and oscillatory magnetic interlayer coupling. *J. Phys.: Condens. Matter*, 14:R169, 2002.
- [61] R.R. Gareev, D.E. Bürgler, M. Buchmeier, D. Olligs, R. Schreiber, and P. Grünberg. Metallic-type oscillatory interlayer exchange coupling across an epitaxial FeSi spacer. *Phys. Rev. Lett.*, 61:157202, 2001.
- [62] J. Faure-Vincent, C. Tiusan, C. Bellouard, E. Popova, M. Hehn, F. Montaigne, and A. Schuhl. Interlayer magnetic coupling interactions of two ferromagnetic layers by spin polarized tunneling. *Phys. Rev. Lett.*, 89:107206, 2002.
- [63] K.R. Nikolaev, A.Yu. Dobin, I.N. Krivorotov, W.K. Cooley, A. Bhattacharya, A. L. Kobrinskii, L.I. Glazman, R.M. Wentzovitch, E. Dan Dahlberg, and A. M. Goldman. Oscillatory exchange coupling and positive magnetoresistance in epitaxial oxide heterostructures. *Phys. Rev. Lett.*, 85:3728, 2000.
- [64] I.N. Krivorotov, K.R. Nikolaev, A.Y. Dobin, A.M. Goldman, and E.D. Dahlberg. Exchange field induced magnetoresistance in colossal magnetoresistance manganites. *Phys. Rev. Lett.*, 86:5779, 2001.
- [65] M. Izumi, Y. Ogimoto, Y. Okimoto, T. Manako, P. Ahmet, K. Nakajima, T. Chikyow, M. Kawasaki, and Y. Tokura. Insulator-metal transition induced by interlayer coupling in $\text{La}_{0.6}\text{Sr}_{0.4}\text{MnO}_3/\text{SrTiO}_3$ superlattices. *Phys. Rev. B*, 64:064429, 2001.
- [66] M. Sahana, K. Dörr, T. Walter, K. Nenkov, D. Eckert, and K.H. Müller. Effect of spacer layer thickness on magnetic and electrical properties of $\text{La}_{0.7}\text{Sr}_{0.3}\text{MnO}_3/\text{SrTiO}_3$ superlattices. *IEEE Transactions on Magnetics*, 38:2904, 2002.
- [67] S. Zhang, P. M. Levy, A. C. Marley, and S. S. P. Parkin. Quenching of magnetoresistance by hot electrons in magnetic tunnel junctions. *Phys. Rev. Lett.*, 79:3744, 1997.
- [68] J.S. Moodera, J. Nowak, and R. J.M van de Veerdonk. Interface magnetism and spin wave scattering in Ferromagnet-Insulator-Ferromagnet tunnel junctions. *Phys. Rev. Lett.*, 80:2941, 1998.

- [69] R.Y. Gu, L. Sheng, and C.S. Ting. Quantum spin assisted tunneling in half-metallic manganite tunnel junctions. *Phys. Rev. B*, 63:220406, 2001.
- [70] M. Jaime, M.B. Salamon, M. Rubinstein, R.E. Treece, J.S. Horwitz, and D.B. Chrisey. High-temperature thermopower in $\text{La}_{0.7}\text{Ca}_{0.3}\text{MnO}_3$ films: evidence for polaronic transport. *Phys. Rev. B*, 54:11914, 1996.
- [71] Y. Xu, D. Ephron, and M.R. Beasley. Directed inelastic hopping of electrons through metal-insulator-metal tunnel junctions. *Phys. Rev. B*, 52:2843, 1995.
- [72] J. Zhang and R.M. White. Voltage dependence of magnetoresistance in spin dependent tunneling junctions. *J. Appl. Phys.*, 83:6512, 1998.
- [73] A. Vedyayev, D. Bagrets, A. Bagrets, and B. Dieny. Resonant spin-dependent tunneling in spin-valve junctions in the presence of paramagnetic impurities. *Phys. Rev. B*, 63:064429, 2001.
- [74] A.M. Bratkovsky. Assisted tunneling in ferromagnetic junctions and half-metallic oxides. *Appl. Phys. Lett.*, 72:2334, 1998.
- [75] C.H. Shang, J. Nowak, R. Jansen, and J.S. Moodera. Temperature dependence of magnetoresistance and surface magnetization in ferromagnetic tunnel junctions. *Phys. Rev. B*, 58:R2917, 1998.
- [76] A.H. MacDonald, T. Jungwirth, and M. Kasner. Temperature dependence of itinerant electron junction magnetoresistance. *Phys. Rev. Lett.*, 81:705, 1998.
- [77] H. Itoh, T. Oshawa, and J. Inoue. Magnetoresistance of ferromagnetic tunnel junctions in the double-exchange model. *Phys. Rev. Lett.*, 84:2501, 2000.
- [78] P. LeClair, J. T. Kohlhepp, H. J. M. Swagten, and W. J. M. de Jonge. Interfacial density of states in magnetic tunnel junctions. *Phys. Rev. Lett.*, 86:1066, 2001.
- [79] P. LeClair, B. Hoex, H. Wieldraaijer, J.T. Kohlhepp, H.J.M. Swagten, and W.J.M. de Jonge. Sign reversal of spin polarization in $\text{Co}/\text{Ru}/\text{Al}_2\text{O}_3/\text{Co}$ magnetic tunnel junctions. *Phys. Rev. B*, 64:100406, 2001.

- [80] T. Zhu, X.H. Xiang, F. Shen, Z. Zhang, G. Landry, D.V. Dimitrov, N. García, and J.Q. Xiao. Bulk contributions to tunnel magnetoresistance in magnetic tunnel junctions. *Phys. Rev. B*, 66:099423, 2002.
- [81] T. Valet and A. Fert. Theory of the perpendicular magnetoresistance in magnetic multilayers. *Phys. Rev. B*, 48:7099, 1993.
- [82] M. Hehn. Private communication. 2001.
- [83] W. Oepts, M.F. Gillies, R. Coehoorn, R.J.M. van de Veerdonk, and W.J.M. de Jonge. Asymmetric bias voltage dependence of the magnetoresistance of Co/Al₂O₃/Co magnetic tunnel junctions: Variation with the barrier oxidation time. *J. Appl. Phys.*, 89:8039, 2001.
- [84] X.H. Xiang, T. Zhu, J. Du, G. Landry, and J.Q. Xiao. Effects of density of states on bias dependence in magnetic tunnel junctions. *Phys. Rev. B*, 66:174407, 2002.
- [85] P. LeClair, J.T. Kohlhepp, C.H. van de Vin, H. Wieldraaijer, H.J.M. Swagten, W.J.M. de Jonge, A.H. Davis, J.M. MacLaren, J.S. Moodera, and R. Jansen. Band structure and density of states effects in Co-based magnetic tunnel junctions. *Phys. Rev. Lett.*, 88:107201, 2002.
- [86] T. Nagahama, S. Yuasa, Y. Suzuki, and E. Tamura. Quantum-well effect in magnetic tunnel junctions with ultrathin single-crystal Fe(100) electrodes. *Appl. Phys. Lett.*, 79:4381, 2001.
- [87] D. A. Papaconstantopoulos. *Handbook of the Band Structure of Elemental Solids*, 3:Plenum, New York, 1986.
- [88] S. Yuasa, T. Nagahama, and Y. Suzuki. Spin-polarized resonant tunneling in magnetic tunnel junctions. *Science*, 297:234, 2002.
- [89] Y. Suzuki, T. Nagahama, S. Yuasa, Y. Yokoyama, and E. Tamura. Private communication. 2003.
- [90] M. Bowen, V. Cros, F. Petroff, A. Fert, C. Martínez Boubeta, J.L. Costa-Krämer, J.V. Anguita, A. Cebollada, F. Briones, J. M. de Teresa, L. Morellón, M. R. Ibarra, F. Güell, F. Peiró, and A. Cornet. Large magnetoresistance in Fe/MgO/FeCo(001) epitaxial tunnel junctions on GaAs(001). *Appl. Phys. Lett.*, 79:1655, 2001.
- [91] J. Faure-Vincent, C. Tiusan, E. Jouguelet, F. Canet, M. Sajieddine, C. Bellouard, E. Popova, M. Hehn, F. Montaigne, and A. Schuhl.

- High tunnel magnetoresistance in epitaxial Fe/MgO/Fe tunnel junctions. *Appl. Phys. Lett.*, 82:4507, 2003.
- [92] M.H. Jo, N.D. Mathur, N.K. Todd, and M. Blamire. Very large magnetoresistance and coherent switching in half-metallic manganite tunnel junctions. *Phys. Rev. B*, 61:R14905, 2000.
- [93] M.H. Jo, N.D. Mathur, and M.G. Blamire. Magnetization reversal probed by spin-polarized tunneling. *Appl. Phys. Lett.*, 80:2722, 2002.
- [94] C. Mitra, P. Raychaudhuri, G. Köbernik, K. Dörr, K.-H. Müller, L. Schultz, and R. Pinto. *p-n* diode with hole- and electron-doped lanthanum manganites. *Appl. Phys. Lett.*, 79:2408, 2001.
- [95] F. Matsukura, H. Ohno, and T. Dietl. III-V ferromagnetic semiconductors. *unpublished*, 2003.
- [96] M. Tanaka and Y. Higo. Large tunneling magnetoresistance in GaMnAs/AlAs/GaMnAs ferromagnetic semiconductor tunnel junctions. *Phys. Rev. Lett.*, 87:026602, 2001.
- [97] R. Mattana, J.-M. George, H. Jaffrès, F. Nguyen Van Dau, A. Fert, B. Lépine, A. Guivarc'h, and G. Jézéquel. Electrical detection of spin accumulation in a *p*-type GaAs quantum well. *Phys. Rev. Lett.*, 90:166601, 2003.
- [98] K. Wang. Calculation of junction magnetoresistance. *Ph.D. Thesis, New York University, USA*, 1999.
- [99] E.A. Livesay, R.N. West, S.B. Dugdale, G. Santi, and T. Jarlborg. Fermi surface of the colossal magnetoresistance perovskite $\text{La}_{0.7}\text{Sr}_{0.3}\text{MnO}_3$. *J. Phys.: Condens. Matter*, 11:L279, 1999.
- [100] W.E. Pickett and D.J. Singh. Electronic structure and half-metallic transport in the $\text{La}_{1-x}\text{Ca}_x\text{MnO}_3$ system. *Phys. Rev. B*, 53:1146, 1996.
- [101] A. Ohtomo, D.A. Müller, J.L. Grazul, and H.Y. Hwang. Artificial charge-modulation in atomic-scale perovskite titanate superlattices. *Nature*, 419:378, 2002.
- [102] D.R. Lide. Handbook of Chemistry and Physics. *72nd Ed. (CRC Press, Boca Raton, FL)*, pages 12–97.

- [103] J. Robertson and C. W. Chen. Schottky barrier heights of tantalum oxide, barium strontium titanate, lead titanate, and strontium bismuth tantalate. *Appl. Phys. Lett.*, 74:1168, 1999.
- [104] T. Shimizu, Y. Usui, T. Nakagawa, and H. Okushi. Crystallographic orientation dependence of the Schottky properties of Au/SrTiO₃ junctions. *J. of Electroceramics*, 4(2-3):299, 2000.
- [105] W. Maus-Friedrichs, M. Frerichs, A. Gunhold, Krischok and V. Kempter, and G. Bihlmayer. The characterization of SrTiO₃ (001) with MIES, UPS(HeI) and first-principles calculations. *Surf. Sci.*, 515:499, 2002.
- [106] K. Schulte, M.A. James, L.H. Tjeng, P.G. Steeneken, G.A. Sawatzky, R. Suryanarayanan, G. Dhalenne, and A. Revcolevschi. Work function changes in the double layered manganite La_{1.2}Sr_{1.8}Mn₂O₇. *Phys. Rev. B*, 64:134428, 2001.
- [107] K. Bouzehouane, P. Woodall, B. Marcilhac, A.N. Khodan, D. Cr  t  , E. Jacquet, J.C. Mage, and J.P. Contour. Enhanced dielectric properties of SrTiO₃ epitaxial thin film for tunable microwave devices. *Appl. Phys. Lett.*, 80:109, 2002.
- [108] F. Pailloux, R. Lyonnet, J.-L. Maurice, and J.-P. Contour. Twinning and lattice distortions in the epitaxy of La_{0.7}Sr_{0.3}MnO₃ thin films on (001) SrTiO₃. *Appl. Surf. Sci.*, 177:263, 2001.
- [109] R. Lyonnet, J.-L. Maurice, M. Hytch, D. Michel, and J.-P. Contour. Heterostructures of La_{0.7}Sr_{0.3}MnO₃ /SrTiO₃ /La_{0.7}Sr_{0.3}MnO₃ grown by pulsed laser deposition on (001)SrTiO₃. *Appl. Surf. Sci.*, 162-163:245, 2000.
- [110] R. Lyonnet. H  t  ro-  pitaxie d'oxydes en ablation laser puls  e pour la r  alisation de dispositifs    magn  tor  sistance g  ante. *Ph.D. Thesis, Universit   de Paris XI Orsay, France*, 2000.
- [111] M. Viret, M. Drouet, J. Nassar, J.P. Contour, C. Fermon, and A. Fert. Low-field colossal magnetoresistance in manganite tunnel spin valves. *Europhys. Lett.*, 39:545, 1997.
- [112] J.-L. Maurice, R. Lyonnet, and J.-P. Contour. Transmission electron microscopy of La_{0.7}Sr_{0.3}MnO₃ /SrTiO₃ /La_{0.7}Sr_{0.3}MnO₃ heterostructures grown by pulsed laser deposition on (001)SrTiO₃. *J. Magn. Magn. Mater.*, 211:91, 2000.

- [113] M. Tsunoda, K. Nishikawa, S. Ogata, and M. Takahashi. 60% magnetoresistance at room temperature in Co-Fe/Al₂O₃/Co-Fe tunnel junctions oxidized with Kr-O₂ plasma. *Appl. Phys. Lett.*, 80:3135, 2002.
- [114] F. Montaigne. Effet tunnel dépendant du spin : des simples aux doubles jonctions. *Ph.D. Thesis, Université de Paris XI - Orsay, France*, 1999.
- [115] R.J.M. van de Veerdonk, J. Nowak, R. Meservey, J.S. Moodera, and W.J.M. de Jonge. Current distribution effects in magnetoresistive tunnel junctions. *Appl. Phys. Lett.*, 71(19):2839, 1997.
- [116] M. Bowen, M. Bibes, A. Barthélémy, J.-P. Contour, A. Anane, Y. Lemaître, and A. Fert. Nearly total spin polarization in La_{0.7}Sr_{0.3}MnO₃ from tunneling experiments. *Appl. Phys. Lett.*, 82:233, 2003.
- [117] F. Pailloux, D. Imhoff, T. Sikora, A. Barthélémy, J.-L. Maurice, J.-P. Contour, C. Colliex, and A. Fert. Nanoscale analysis of a SrTiO₃/La_{0.7}Sr_{0.3}MnO₃ interface. *Phys. Rev. B*, 66:014417, 2002.
- [118] L. Samet, D. Imhoff, J.-L. Maurice, J.-P. Contour, A. Gloter, T. Manoubi, A. Fert, and C. Colliex. EELS study of interfaces in magnetoresistive La_{0.7}Sr_{0.3}MnO₃/SrTiO₃/La_{0.7}Sr_{0.3}MnO₃ tunnel junctions. *Euro. Phys. J. B*, 34:179, 2003.
- [119] J.L. Maurice, F. Pailloux, D. Imhoff, J.P. Contour, A. Barthélémy, M. Bowen, C. Colliex, and A. Fert. Nanoscale analysis of a Co/SrTiO₃ interface in a magnetic tunnel junction. *MRS Proceedings*, 746:R3.2.1, 2003.
- [120] F. Chen, T. Zhao, Y.Y. Fei, H. Lu, Z. Chen, G. Yang, and X.D. Zhu. Surface segregation of bulk oxygen on oxidation of epitaxially grown Nb-doped SrTiO₃ on SrTiO₃ (001). *Appl. Phys. Lett.*, 80:2889, 2002.
- [121] J.Z. Sun. Thin-film trilayer manganate junctions. *Phil. Trans. R. Soc. London A*, 356:1693, 1998.
- [122] P. Rottländer, M. Hehn, O. Lenoble, and A. Schuhl. Tantalum oxide as an alternative low height tunnel barrier in magnetic junctions. *Appl. Phys. Lett.*, 78:3274, 2001.
- [123] A. K. Tagantsev, I. Stolichnov, E. L. Colla, and N. Setter. Polarization fatigue in ferroelectric films: basic experimental findings, phenomenological scenarios, and microscopic features. *J. Appl. Phys.*, 90:1387, 2001.

- [124] M. Brazier, S. Mansourk, and M. McElfresh. Ferroelectric fatigue of $\text{Pb}(\text{Zr},\text{Ti})\text{O}_3$ thin films measured in atmospheres of varying oxygen concentration. *Appl. Phys. Lett*, 74:4032, 1999.
- [125] Jürgen Nuffer, D.C. Lupascu, Jürgen Rödel, and Michael Schroeder. Negligible oxygen liberation during bipolar electric cycling of ferroelectric lead zirconate titanate ceramics. *Appl. Phys. Lett*, 79:3675, 2001.
- [126] L.F. Schloss, P.C. McIntyre, B.C. Hendrix, S.M. Bilodeau, J.F. Roeder, and S.R. Gilbert. Oxygen tracer studies of ferroelectric fatigue in $\text{Pb}(\text{Zr},\text{Ti})\text{O}_3$ thin films. *Appl. Phys. Lett*, 81:3218, 2002.
- [127] B. H. Moeckly and D.K. Lathrop and R.A. Buhrman. Electromigration study of oxygen disorder and grain-boundary effects in $\text{YBa}_2\text{Cu}_3\text{O}_{7-\delta}$ thin films. *Phys. Rev. B*, 47:400, 1993.
- [128] I. Stolichnov, A. Tagantsev, N. Setter, S. Okhonin, P. Fazan, J.S. Cross, M. Tsukada, A. Bartic, and D. Wouters. Constant-current study of dielectric breakdown of $\text{Pb}(\text{Zr},\text{Ti})\text{O}_3$ ferroelectric film capacitors. *Int. Ferroelectrics*, 32:737, 2001.
- [129] M. Olette and M.F. Ancey-Moret. *IRSID*, 1962.
- [130] M. Bowen. *unpublished*, 1999.
- [131] J. Z. Sun, K. P. Roche, and S. S. P. Parkin. Interface stability in hybrid metal-oxide magnetic trilayer junctions. *Phys. Rev. B*, 61:11244, 2000.
- [132] K. Bouzehouane. *unpublished*, 2000.
- [133] M. Faraday. Experimental researches in electricity: § 26. On the magnetization of light and the illumination of magnetic lines of force. *Phil. Trans. R. Soc.*, 136:1, 1846.
- [134] J. Kerr. On rotation of the plane of polarization by reflection from the pole of a magnet. *Phil. Mag.*, 3:321, 1877.
- [135] R.P. Feynman, R.B. Leighton, and M. Sands. The Feynman lectures on physics. Addison-Wesley, Reading, MA, 1964.
- [136] B.T. Thole, P. Carra, F. Sette, and G. van der Laan. X-ray circular dichroism as a probe of orbital magnetization. *Phys. Rev. Lett.*, 68:1943, 1992.

- [137] P. Carra, B.T. Thole, M. Altarelli, and X. Wang. X-ray circular dichroism and local magnetic fields. *Phys. Rev. Lett.*, 70:694, 1993.
- [138] J. Stöhr. Exploring the microscopic origin of magnetic anisotropies with X-ray magnetic circular dichroism (XMCD) spectroscopy. *J. Magn. Magn. Mater.*, 200:470, 1999.
- [139] F. Wilhelm. Magnetic properties of ultrathin films, coupled trilayers and 3d/5d multilayers studies by X-ray magnetic circular dichroism. *Ph.D. Thesis, Freie Universität, Berlin, Germany*, 2000.
- [140] B. Nadgorny, I. I. Mazin, M. Osofsky, Jr. R. J. Soulen, P. Brousard, R. M. Stroud, D. J. Singh, V. G. Harris, A. Arsenov, and Ya. Mukovskii. Origin of high transport spin polarization in $\text{La}_{0.7}\text{Sr}_{0.3}\text{MnO}_3$: direct evidence for minority spin states. *Phys. Rev. B*, 63(18):184433, 2001.
- [141] J. Nassar. Magnétorésistance tunnel de jonctions à base de métaux de transition et oxydes ferromagnétiques. *Ph.D. Thesis, École Polytechnique, France*, 1999.
- [142] M. Bibes, M. Bowen, A. Barthélémy, A. Anane, K. Bouzehouane, C. Carretero, E. Jacquet, J.-P. Contour, and O. Durand. Growth and characterization of TiO_2 as a barrier for spin-polarized tunneling. *Appl. Phys. Lett.*, 82:3269, 2003.
- [143] T. Kiyomura, Y. Maruo, and M. Gomi. Electrical properties of MgO insulating layers in spin-dependent tunneling junctions using Fe_3O_4 . *J. Appl. Phys.*, 88:4768, 2000.
- [144] J.S. Moodera and L.R. Kinder. Ferromagnetic-insulator-ferromagnetic tunneling: spin-dependent tunneling and large magnetoresistance in trilayer junctions (invited). *J. Appl. Phys.*, 79:4724, 1996.
- [145] W. Wulfhekel, M. Klaua, D. Ullmann, F. Zavaliche, J. Kirschner, R. Urban, T. Monchesky, and B. Heinrich. Single-crystal magnetotunnel junctions. *Appl. Phys. Lett.*, 78:509, 2001.
- [146] S. Yuasa, T. Sato, E. Tamura, Y. Suzuki, H. Yamamori, K. Ando, and T. Katayama. Magnetic tunnel junctions with single-crystal electrodes: a crystal anisotropy of tunnel magneto-resistance. *Europhys. Lett.*, 52:344, 2000.
- [147] C. Martínez-Boubeta. *unpublished*, 2001.

- [148] H. Jaffrès, D. Lacour, F. Nguyen Van Dau, J. Briatico, F. Petroff, and A. Vaurès. Angular dependence of the tunnel magnetoresistance in transition-metal based junctions. *Phys. Rev. B*, 64:064427, 2001.
- [149] <http://www.esrf.fr/UsersAndScience/Experiments/XASMS/ID08/>.
- [150] O. Hjortstam, J. Trygg, J.M. Wills, B. Johansson, and O. Eriksson. Calculated spin and orbital moments in the surfaces of the 3d metals Fe, Co, and Ni and their overlayers on Cu(001). *Phys. Rev. B*, 53:9204, 1996.
- [151] E.Y. Tsymbal, I.I. Oleinik, and D.G. Pettifor. Oxygen-induced positive spin polarization from Fe into the vacuum barrier. *J. Appl. Phys.*, 87:5230, 2000.
- [152] E. Pellegrin, L.H. Tjeng, F.M.F. de Groot, R. Hesper, G.A. Sawatzky, Y. Moritomo, and Y. Tokura. Soft X-Ray magnetic circular dichroism study of the colossal magnetoresistance compound $\text{La}_{1-x}\text{Sr}_x\text{MnO}_3$. *J. Phys. IV*, 7:C2-405, 1997.
- [153] W.E. Pickett and D.J. Singh. Magnetoelectronic and magnetostructural coupling in the $\text{La}_{1-x}\text{Ca}_x\text{MnO}_3$ system. *Europhys. Lett.*, 32:759, 1995.
- [154] J. Hayakawa, S. Kokado, K. Ito, M. Sugiyama, H. Asano, M. Matsui, A. Sakuma, and M. Ichimura. Bias voltage dependence of tunnel magnetoresistance effect in spin-valve type $\text{MnIr}/\text{NiFe}/\text{Co}_{90}\text{Fe}_{10}/\text{SrTiO}_3/\text{La}_{0.7}\text{Sr}_{0.3}\text{MnO}_3$ tunnel junctions. *Jpn. J. Appl. Phys.*, 41:1340, 2002.
- [155] A. Filippetti and W.E. Pickett. Double-exchange-driven spin pairing at the (001) surface of manganites. *Phys. Rev. B*, 62:11571, 2000.
- [156] M. Bibes, S. Valencia, Ll. Balcells, B. Martínez, J. Fontcuberta, M. Wojcik, S. Nadolski, and E. Jedryka. Charge trapping in optimally doped epitaxial manganite thin films. *Phys. Rev. B*, 66:134416, 2002.
- [157] R. Bertacco, M. Portalupi, M. Marcon, L. Duò, F. Ciccacci, M. Bowen, J.P. Contour, and A. Barthélémy. Unoccupied electron states of $\text{La}_{0.7}\text{Sr}_{0.3}\text{MnO}_3$. *J. Magn. Magn. Mater.*, 242-245:710, 2002.
- [158] G. Banach and W.M. Temmermann. *private communication*, 2002.

- [159] M.J. Calderón, L. Brey, and F. Guinea. Surface electronic structure and magnetic properties of doped manganites. *Phys. Rev. B*, 60:6698, 1999.
- [160] X.H. Xiang, T. Zhu, J. Du, and J.Q. Xiao. Conductance anomaly and density of state effects in magnetic tunnel junctions. *J. Appl. Phys.*, 93:8053, 2003.
- [161] C. Vouille-Machefert. Magnétorésistance géante. *Ph.D. Thesis, Université de Paris XI Orsay, France*, 1998.
- [162] C. Vouille, A. Barthélémy, F.E. Mpondo, A. Fert, P.A. Shroeder, S.Y. Hsu, A. Reilly, and R. Loloee. Microscopic mechanisms of giant magnetoresistance. *Phys. Rev. B*, 60:6710, 1999.
- [163] V.S. Stepanyuk, R. Zeller, P.H. Dederichs, and I. Mertig. Electronic structure and magnetic properties of dilute Co alloys with transition-metal impurities. *Phys. Rev. B*, 49:5157, 1994.
- [164] J.-H. Park, E. Vescovo, H.-J. Kim, C. Kwon, R. Ramesh, and T. Venkatesan. Magnetic properties at surface boundary of a half-metallic ferromagnet $\text{La}_{0.7}\text{Sr}_{0.3}\text{MnO}_3$. *Phys. Rev. Lett.*, 81:1953, 1998.
- [165] P. Lyu, D.Y. Xing, and J. Dong. Temperature dependence of tunneling magnetoresistance in manganite tunnel junctions. *Phys. Rev. B*, 60:4235, 1999.
- [166] J.L. Maurice, F. Pailloux, A. Barthélémy, A. Rocher, O. Durand, R. Lyonnet, and J.P. Contour. Strain and magnetism in $\text{La}_{0.7}\text{Sr}_{0.3}\text{MnO}_3$ very thin films epitaxially grown on SrTiO_3 . *Appl. Surf. Sci.*, 188:176, 2002.
- [167] J.-H. Park, E. Vescovo, H.-J. Kim, C. Kwon, R. Ramesh, and T. Venkatesan. Direct evidence for a half-metallic ferromagnet. *Nature (London)*, 392:794, 1998.
- [168] M. Bowen. unpublished. 2003.
- [169] N. Jiang and J. Silcox. Observations of reaction zones at chromium / oxide glass interfaces. *J. Appl. Phys.*, 87:3768, 2000.
- [170] A. Pundt and C. Michaelsen. Magnetically induced decomposition in Co-Cr thin-film and bulk alloys. *Phys. Rev. B*, 56:14352, 1997.

- [171] A. Christensen and A.V. Ruban, P.Stoltze, K.W. Jacobsen, H.L. Skriver, J.K. Norskov, and F. Besenbacher. Phase diagrams for surface alloys. *Phys. Rev. B*, 56:5822, 1997.
- [172] H. Ouyang and J.-T. Kwan. Occupancy of the 3d electron shell of Co and Cr in nanosized CoCrPt magnetic thin films. *J. Appl. Phys.*, 92:7510, 2002.
- [173] S. Suzuki and M. Tomita. Valence dependence of electron energy loss spectra of chromium oxides. *Jpn. J. Appl. Phys.*, 36:4341, 1997.
- [174] Ruihua Cheng, C.N. Borca, N. Pilet, Bo Xu, L. Yuan, B. Doudin, S.H. Liou, and P.A. Dowben. Oxidation of metals at the chromium oxide interface. *Appl. Phys. Lett.*, 81:2109, 2002.
- [175] M. Balasubramanian, J. McBreen, I.J. Davidson, P.S. Whitfield, and I. Kargina. *In situ* X-Ray absorption study of a layered manganese-chromium oxide-based cathode material. *J. Electrochem. Soc.*, 149:A176, 2002.
- [176] K.R. Nikolaev, A. Yu. Dobin, I. N. Krivorotov, E.D. Dahlberg, and A.M. Goldman. Temperature dependence of interlayer exchange coupling in manganite-based superlattices. *J. Appl. Phys.*, 89:6820, 2001.
- [177] B.F.P. Roos, P.A. Beck, S.O. Demokritov, and B. Hillebrands. Auger electron spectroscopic studies of annealing effects at Fe/FeO_x/Al and Co/CoO_x/Al interfaces. *Surf. Sci. Lett.*, 497:L55, 2002.
- [178] F. Chen, T. Zhao, Y.Y. Fei, Z. Chen H. Lu, G. Yang, and X.D. Zhu. Surface segregation of bulk oxygen on oxidation of epitaxially grown Nb-doped SrTiO₃ on SrTiO₃ (001). *Appl. Phys. Lett.*, 80:2289, 2002.
- [179] P.A. Cox. Transition metal oxides. *Oxford Science Publications, Oxford*, Chapter 4:195, 1992.
- [180] K. Nakamura, M. Xu, M. Kläser, and G. Linker. Excess oxygen in low Sr doping La_{1-x}Sr_xMnO_{3+δ} epitaxial films. *Journal of Solid State Chemistry*, 156:143, 2001.
- [181] K. Conder, G. Zhao, and R. Khasanov. Oxygen stoichiometry and isotope effect in La_{1-x}Ca_xMnO_{3+δ}. *Phys. Rev. B*, 66:212409, 2002.
- [182] K. Dörr, J.M. De Teresa, K.H. Müller, D. Eckert, T. Walter, E. Vlahov, K. Nenkov, and L.Schultz. Preparation and properties

- of epitaxial $\text{La}_{0.7}\text{Ca}_{0.3}\text{MnO}_{3-\delta}$ films with reduced carrier density. *J. Phys.: Condens. Matter*, 12:7099, 2000.
- [183] X. Liu, X. Xu, and Y. Zhang. Effect of Ti dopant on the carrier density collapse in colossal magnetoresistance material $\text{La}_{0.7}\text{Ca}_{0.3}\text{Mn}_{1-y}\text{Ti}_y\text{O}_3$. *Phys. Rev. B*, 62:15112, 2000.
- [184] T. Bak, J. Nowotny, M. Rekas, and C.C. Sorrell. Non-stoichiometry, Fermi energy and work function of $(\text{La,Sr})\text{MnO}_3$. II. Verification of theoretical model. *Journal of Physics and Chemistry of Solids*, 62:737, 2001.
- [185] M. Sugiura, K. Uragou, M. Tachiki, and T. Kobayashi. Estimation of trap levels in SrTiO_3 epitaxial films from measurement of $(\text{LaSr})\text{MnO}_3/\text{SrTiO}_3/(\text{LaSr})\text{TiO}_3$ *p-i-n* diode characteristics. *J. Appl. Phys.*, 90:187, 2001.
- [186] J.Y. Rhee, Y.V. Kudryavtsev, K.W. Kim, and Y.P. Lee. Electronic structures and magnetic properties of near-equiatomic Co-Ti alloys. *IEEE Trans. Magn.*, 35:3745, 1999.
- [187] L.F. Mattheiss. Energy bands for KNiF_3 ; SrTiO_3 , KMoO_3 and KTaO_3 . *Phys. Rev. B*, 6:4718, 1972.
- [188] T. Higuchi, T. Tsukamoto, N. Sata, M. Ishigame, Y. Tezuka, and S. Shin. Electronic structure of *p*-type SrTiO_3 by photoemission spectroscopy. *Phys. Rev. B*, 57:6978, 1998.
- [189] Y. Aiura, I. Hase, H. Bando, T. Yasue, T. Saitoh, and D.S. Dessau. Photoemission study of the metallic state of lightly electron-doped SrTiO_3 . *Surf. Sci.*, 515:61, 2002.
- [190] F. Montaigne, J. Nassar, A. Vaurès, F. Nguyen Van Dau, F. Petroff, A. Schuhl, and A. Fert. Enhanced tunnel magnetoresistance at high bias voltage in double-barrier planar junctions. *Appl. Phys. Lett.*, 73:2829, 1998.
- [191] M. Imada, A. Fujimori, and Y. Tokura. Metal-insulator transitions. *Rev. Mod. Phys.*, 70:1039–1166, 1998.
- [192] M. Bowen. *unpublished*, 2002.
- [193] P.A. Cox. Transition metal oxides. *Oxford Science Publications, Oxford*, Chapter 2, 1992.

- [194] Y. Tokura. Correlated electrons: science to technology. *Japan Soc. Appl. Phys Intl.*, 1:12, 2000.
- [195] A.H. Jahn and E. Teller. Stability of polyatomic molecules in degenerate electronic states I-Orbital degeneracy. *Proc. Roy. Soc. London A*, 161:220, 1937.
- [196] H.H. Tippins. Charge-transfer spectra of transition-metal ions in corundum. *Phys. Rev. B*, 1:126, 1970.
- [197] R.C. Whited, C.J. Flaten, and W.C. Walker. Exciton thermoreflectance of MgO and CaO. *Solid-State-Communications*, 13:1903, 1973.
- [198] Y. Ando, M. Hayashi, M. Kamijo, H. Kubota, and T. Miyazaki. Local transport properties of ferromagnetic tunnel junctions. *J. Magn. Magn. Mater.*, 226:924, 2001.
- [199] M. Hayashi, Y. Ando, and T. Miyazaki. Scanning tunneling microscopy observation of the initial state of oxidation in ferromagnetic tunnel junctions. *J. J. Appl. Phys.*, 40(12A):L1317, 2001.
- [200] L.P.H. Jeurgens, W.G. Sloof, F.D. Tichelaar, and E.J. Mittemeijer. Composition and chemical state of the ions of aluminium-oxide films formed by thermal oxidation of aluminium. *Surf. Sci.*, 506:313, 2002.
- [201] K.S. Yoon, J.H. Park, J.H. Choi, J.Y. Yang, C.H. Lee, C.O. Kim, J.P. Hong, and T.W. Kang. Performance of Co/Al₂O₃/NiFe magnetic tunnel junctions prepared by a two-step RF plasma oxidation method. *Appl. Phys. Lett.*, 79:1160, 2001.
- [202] J.H. Park, G.S. Lee, J.Y. Yang, K.S. Yoon, C.O. Kim, J.P. Hong, and H.J. Kim. Efficient characterization of ultrathin AlO_x insulating barriers in magnetic tunnel junctions fabricated by masked rf plasma oxidation technique. *Appl. Phys. Lett.*, 80:3982, 2002.
- [203] G. Lucovsky, J.L. Whitten, and Y. Zhang. A molecular orbital model for the electronic structure of transition metal atoms in silicate and aluminate alloys. *Microelectronic Engineering*, 59:329, 2001.
- [204] S.-G. Lim, S. Kriventsov, T.N. Jackson, J.H. Haeni, D.G. Schlom, A.M. Balbashov, R. Uecker, P. Reiche, J.L. Freeouf, and G. Lucovsky. Dielectric functions and optical bandgaps of high-K dielectrics for metal-oxide-semiconductor field-effect transistors by far ultraviolet spectroscopic ellipsometry. *J Appl. Phys.*, 91:4500, 2002.

- [205] R. Sanjinés, H. Tang, H. Berger, F. Gozzo, G. Margaritondo, and F. Lévy. Electronic structure of anatase TiO_2 oxide. *J Appl. Phys.*, 75:2945, 1994.
- [206] S. Hong, E. Kim, D-W. Kim, T-H. Sung, and K. No. On measurement of optical band gap of chromium oxide films containing both amorphous and crystalline phases. *J. of Non-Cryst. Solids*, 221:245, 1997.
- [207] T. Uozumi, K. Okada, A. Kotani, R. Zimmermann, P. Steiner, S. Hüfner, Y. Tezuka, and S. Shin. Theoretical and experimental studies on the electronic structure of M_2O_3 (M=Ti,V,Cr,Mn,Fe) compounds by systematic analysis of high-energy spectroscopy. *J. of El. Spectr. and Rel. Phenom.*, 83:9, 1997.
- [208] P.W. Peacock and J. Robertson. Band offsets and Schottky barrier heights of high dielectric constant oxides. *Appl. Phys. Lett.*, 92:4712, 2000.
- [209] V. Goldschmidt. Geochemistry. *Oxford University Press*, 1958.
- [210] L.F. Mattheiss. Effect of the 110K phase transition on the SrTiO_3 conduction bands. *Phys. Rev. B*, 6:4740, 1972.
- [211] D. Goldschmidt and H.L. Tuller. Fundamental absorption edge of SrTiO_3 at high temperatures. *Phys. Rev. B*, 35:4360, 1987.
- [212] J.E. Ortega, F.J. Himpsel, G.J. Mankey, and R.F. Willis. Quantum well states and magnetic coupling between ferromagnets through a noble-metal layer. *Phys. Rev. B*, 47:1540, 1993.
- [213] P.A. Cox. Transition metal oxides. *Oxford Science Publications, Oxford*, Chapter 4:197, 1992.
- [214] A. Fujimori, A.E. Bocquet, K. Morikawa, K. Kobayashi, T. Saitoh, Y. Tokura, I. Hase, and M. Onoda. Electronic structure and electron-phonon interaction in transition metal oxides with d^0 configuration and lightly doped compounds. *J. Phys. Chem. Solids*, 57:1379, 1996.
- [215] K. Szot, W. Speier, R. Carius, U. Zastrow, and W. Beyer. Localized metallic conductivity and self-healing during thermal reduction of SrTiO_3 . *Phys. Rev. Lett.*, 88:75508, 2002.
- [216] D.D. Sarma, S.R. Barman, H. Kajueter, and G. Kotliar. Spectral functions in doped transition metal oxides. *Europhys. Lett.*, 36:307, 1996.

- [217] N. Erdman, K.R. Poeppelmeier, M. Asta, O. Warschkow, D.E. Ellis, and L.D. Marks. The structure and chemistry of the TiO_2 -rich surface of SrTiO_3 (001). *Nature*, 419:55, 2002.
- [218] M. Yoshimoto, T. Maeda, K. Shimozone, H. Koinuma, M. Shinohara, O. Ishiyama, and F. Ohtani. Topmost surface analysis of SrTiO_3 (001) by coaxial impact-collision ion scattering spectroscopy. *Appl. Phys. Lett.*, 65:3197, 1994.
- [219] G. Toussaint, M.O. Selme, and P. Pecher. Tight-binding calculations of surface defects in SrTiO_3 . *Phys. Rev. B*, 36:6135, 1987.
- [220] I. Pallecchi, G. Grassano, D. Marré, L. Pellegrino, M. Putti, and A.S. Siri. SrTiO_3 -based metal-insulator-semiconductor heterostructures. *Appl. Phys. Lett.*, 78:2244, 2001.
- [221] L. Pellegrino, I. Pallecchi, D. Marré, E. Bellingeri, and A. S. Siri. Fabrication of submicron-scale SrTiO_3 devices by an atomic force microscope. *Appl. Phys. Lett.*, 81:3849, 2002.
- [222] T. Higuchi, S. Nozawa, T. Tsukamoto, H. Ishii, R. Eguchi, Y. Tezuka, S. Yamaguchi, K. Kanai, and S. Shin. Unoccupied electronic structure in the surface state of lightly doped SrTiO_3 by resonant inverse photoemission spectroscopy. *Phys. Rev. B*, 66:153105, 2002.
- [223] P.A. Fleury, J.F. Scott, and J.M. Worlock. Soft phonon modes and the 110K phase transition in SrTiO_3 . *Phys. Rev. Lett.*, 21:16, 1968.
- [224] B. Gregory, J. Arthur, and G. Seidel. Measurements of the Fermi surface of $\text{SrTiO}_3:\text{Nb}$. *Phys. Rev. B*, 19:1039, 1979.
- [225] T. Sakudo and H. Unoki. Dielectric properties of SrTiO_3 at low temperatures. *Phys. Rev. Lett.*, 26:851, 1971.
- [226] V.V. Laguta, M.D. Glinchuk, R.O. Kuzian, S.N. Nokhrin, I.P. Bykov, J. Rosa, L. Jastrabík, and M.G. Karkut. The photoinduced Ti^{3+} centre in SrTiO_3 . *J. Phys.: Condens. Matter*, 14:13813, 2002.
- [227] F. Batallan, I. Rosenman, and C.B. Sommers. Band structure and Fermi surface of hcp ferromagnetic cobalt. *Phys. Rev. B*, 11:545, 1974.
- [228] L.F. Mattheiss. Electronic structure of the 3d transition-metal monoxides. I. Energy band results. *Phys. Rev. B*, 5:290, 1972.

- [229] Z.X. Shen, C.K. Shih, O. Jepsen, W.E. Spicer, I. Lindau, and J.W. Allen. Aspects of the correlation effects, antiferromagnetic order, and translational symmetry of the electronic structure of NiO and CoO. *Phys. Rev. Lett.*, 64:2442, 1990.
- [230] P.A. Cox. Transition metal oxides. *Oxford Science Publications, Oxford*, Chapter 3:105, 1992.
- [231] R. Asahi, Y. Taga, W. Mannstadt, and A. J. Freeman. Electronic and optical properties of anatase TiO₂. *Phys. Rev. B*, 61:7459, 2000.
- [232] Y. Tokura and Y. Tomioka. Colossal magnetoresistive manganites. *J. Magn. Magn. Mater.*, 200:1, 1999.
- [233] M. Bibes. Elaboration et étude de couches minces de manganites à valence mixte. *Ph.D Thesis, Institut National des Sciences Appliquées de Toulouse & Universtat Autònoma de Barcelona*, 2001.
- [234] H.A. Kramers. L'interaction entre les atomes magnétogènes dans un cristal paramagnétique. *Physica*, 1:182, 1934.
- [235] J.B. Goodenough. Theory of the role of covalence in the perovskite-type manganites [La,M(II)]MnO₃. *Phys. Rev.*, 100:564, 1955.
- [236] J.B. Goodenough, A. Wold, R.J. Arnett, and N. Menyuk. Magnetic properties of ionic compounds. *Phys. Rev.*, 124:373, 1961.
- [237] P.W. Anderson. Antiferromagnetism. theory of superexchange interaction. *Phys. Rev.*, 79:350, 1950.
- [238] P.W. Anderson. New approach to the theory of superexchange interactions. *Phys. Rev.*, 115:2, 1959.
- [239] P. Ravindran, A. Kjekshus, H. Fjellvåg, A. Delin, and O. Eriksson. Ground-state and excited-state properties of LaMnO₃ from full-potential calculations. *Phys. Rev. B*, 65:064445, 2002.
- [240] M.C. Sánchez, G.Subías, J. García, and J. Blasco. Cooperative Jahn-Teller phase transition in LaMnO₃ studied by X-Ray absorption spectroscopy. *Phys. Rev. Lett.*, 90:045503, 2003.
- [241] G.H. Jonker and J.H. Van Santen. Ferromagnetic compounds of manganese with perovskite structure. *Physica*, 16:337, 1950.

- [242] C. Zener. Interactions between the d shells in the transition metals. ii. ferromagnetic compounds of manganese with perovskite structure. *Phys. Rev.*, 82:403, 1951.
- [243] P.W. Anderson and H. Hasegawa. Considerations on double exchange. *Phys. Rev.*, 100:675, 1955.
- [244] P.H. de Gennes. Effects of double exchange in magnetic crystals. *Phys. Rev.*, 118:141, 1960.
- [245] K. Kubo and N. Ohata. A quantum theory of double exchange. I. *J. Phys. Soc. Japan*, 33:21, 1972.
- [246] A.J. Millis, P.B. Littlewood, and B.I. Shraiman. Double exchange alone does not explain the resistivity of $\text{La}_{0.7}\text{Sr}_{0.3}\text{MnO}_3$. *Phys. Rev. Lett.*, 74:5144, 1995.
- [247] E. Dagotto, T. Hotta, and A. Moreo. Colossal magnetoresistant materials: the key role of phase separation. *Phys. Rep.*, 344:1, 2001.
- [248] J.A. Vergés, V. Martín-Mayor, and L. Brey. Lattice-spin mechanism in colossal magnetoresistive manganites. *Phys. Rev. Lett.*, 88:136401, 2002.
- [249] E. O. Wollan and W. C. Koehler. Neutron diffraction study of the magnetic properties of the series of perovskite-type compounds $[(1-x)\text{La}, x\text{Ca}]\text{MnO}_3$. *Phys. Rev.*, 100:545, 1955.
- [250] W.E. Pickett and D.J. Singh. Pseudogaps, jahn-teller distortions, and magnetic order in manganite perovskites. *Phys. Rev. B*, 57:88, 1998.
- [251] W.E. Pickett and D.J. Singh. Chemical disorder and charge transport in ferromagnetic manganites. *Phys. Rev. B*, 55:R8642, 1997.
- [252] W.E. Pickett and D.J. Singh. Transport and fermiology of the ferromagnetic phase of $\text{La}_{2/3}\text{A}_{2/3}\text{MnO}_3$ ($\text{A} = \text{Ca}, \text{Sr}, \text{Ba}$). *J. Magn. Magn. Mater.*, 172:237, 1997.
- [253] T. Becker, C. Streng, Y. Luo, V. Moshnyaga, B. Damaschke, N. Shannon, and K. Samwer. Intrinsic inhomogeneities in manganite thin films investigated with scanning tunneling spectroscopy. *Phys. Rev. Lett.*, 89:237203, 2002.

- [254] M. Bibes, Ll. Balcells, S. Valencia, J. Fontcuberta, M. Wojcik, E. Jedryka, and S. Nadolski. Nanoscale multiphase separation at $\text{La}_{0.7}\text{Ca}_{0.3}\text{MnO}_3/\text{SrTiO}_3$ interfaces. *Phys. Rev. Lett.*, 87:067210, 2001.
- [255] T. Shibata, B. Bunker, J.F. Mitchell, and P. Schiffer. Indications of intrinsic chemical and structural inhomogeneity in lightly doped $\text{La}_{0.7}\text{Sr}_{0.3}\text{MnO}_3$. *Phys. Rev. Lett.*, 88:207205, 2002.
- [256] M. Bibes, Ll. Balcells, J. Fontcuberta, M. Wojcik, E. Jedryka, and S. Nadolski. Surface-induced phase separation in manganites: A microscopic origin for powder magnetoresistance. *Appl. Phys. Lett.*, 82:928, 2003.
- [257] G. Banach, R. Tyer, and W.M. Temmermann. Study of half-metallicity in $\text{La}_{0.7}\text{Sr}_{0.3}\text{MnO}_3$. *unpublished*, 2003.
- [258] S. Hébert, A. Maignan, C. Martin, and B. Raveau. Important role of impurity e_g levels on the ground state of Mn-site doped manganites. *S. St. Comm.*, 121:229, 2002.
- [259] R. Bertacco, J.P. Contour, and A. Barthélémy. Evidence for strontium segregation in $\text{La}_{0.7}\text{Sr}_{0.3}\text{MnO}_3$ thin films grown by pulsed laser deposition : consequences for tunnelling junctions. *Surf. Sci.*, 511:366, 2002.
- [260] X.D. Zhu, W. Si, X.X. Xi, Qi Li, Q.D. Jiang, and M.G. Medici. Oxidation kinetics in $\text{La}_{0.67}\text{Ba}_{0.33}\text{MnO}_{3-\delta}$ epitaxy on SrTiO_3 (001) during pulsed-laser deposition. *Appl. Phys. Lett.*, 74:3540, 1999.
- [261] M. Stiles. Interlayer exchange coupling. *J. Magn. Magn. Mater.*, 200:322, 1999.
- [262] F.J. Himpsel, K.N. Altmann, G.J. Mankey, J.E. Ortega, and D.Y. Petrovykh. Electronic states in magnetic nanostructures. *J. Magn. Magn. Mater.*, 200:546, 1999.
- [263] M. Milun, P. Pervan, and D.P. Woodruff. Quantum well structures in thin metal films: simple model physics in reality? *Rep. Prog. Phys.*, 65:99, 2002.
- [264] J. Unguris, R.J. Celotta, and D.T. Pierce. Observation of two different oscillation periods in the exchange coupling of Fe/Cr/Fe(100). *Phys. Rev. Lett.*, 67:140, 1991.

- [265] N.V. Smith, N.B. Brookes, Y. Chang, and P.D. Johnson. Quantum-well and tight-binding analyses of spin-polarized photoemission from Ag/Fe(001) overlayers. *Phys. Rev. B*, 49:332, 1994.
- [266] P. Bruno. Theory of interlayer magnetic coupling. *Phys. Rev. B*, 52:411, 1995.
- [267] R.K. Kawakami, E. Rotenberg, E.J. Escorcia-Aparicio, H.J. Choi, T.R. Cummins, J.G. Tobin, N.V. Smith, and Z.Q. Qiu. Observation of the quantum well interference in magnetic nanostructures by photoemission. *Phys. Rev. Lett.*, 80:1754, 1998.

Transport tunnel polarisé en spin à l'état solide

Cette Thèse expérimentale examine le transport par effet tunnel entre deux couches ferromagnétiques séparées par une barrière isolante ultrafine. L'enjeu de ces travaux est de rapprocher la compréhension théorique, basée sur des systèmes idéaux, de la réalité expérimentale dominée par des jonctions comprenant une barrière amorphe. Au moyen de jonctions partiellement ou entièrement épitaxiées intégrant le matériau $\text{La}_{0.7}\text{Sr}_{0.3}\text{MnO}_3$ dont nous avons confirmé la polarisation de spin tunnel quasi-totale, l'influence de la structure électronique de matériaux isolants tels que SrTiO_3 , $\text{Ce}_{0.69}\text{La}_{0.31}\text{O}_{1.845}$, TiO_2 , MgO (épitaxiés) et Al_2O_3 (amorphe) sur le magnéto-transport tunnel est mise en évidence. La théorie soutenant ces résultats est testée au moyen de mesures XMCD effectuées sur des barrières de Al_2O_3 et MgO . La demi-métallicité de $\text{La}_{0.7}\text{Sr}_{0.3}\text{MnO}_3$ est ensuite utilisée dans des jonctions $\text{La}_{0.7}\text{Sr}_{0.3}\text{MnO}_3/\text{SrTiO}_3/\text{La}_{0.7}\text{Sr}_{0.3}\text{MnO}_3$ et $\text{La}_{0.7}\text{Sr}_{0.3}\text{MnO}_3/\text{SrTiO}_3/\text{Co}$ afin d'affirmer quantitativement le caractère spectroscopique du transport tunnel polarisé en spin entre électrodes ferromagnétiques. Ces études en tension montrent l'influence de la génération d'ondes de spin lors du transport tunnel sur l'ordre ferromagnétique de l'interface manganate/isolant proche de sa température de transition métal-isolant. Enfin, nous utilisons l'électromigration aux interfaces afin de modifier la densité d'états et le profil de potentiel des interfaces. Nous montrons comment il est possible de réaliser un dispositif aux propriétés de magnéto-transport bistables; et nous examinons dans le régime tunnel Fowler-Nordheim les répercussions de ces modifications sur la formation d'états quantifiés au sein de la barrière, ainsi que la perturbation du couplage d'échange indirect entre les électrodes ferromagnétiques.

Experimental insights into spin-polarized solid state tunneling

This experimental Thesis investigates spin-polarized solid state tunneling between two ferromagnetic layers separated by an ultrathin insulating barrier, with an aim to bridge the gap between theory, which is based on ideal systems, and experiments dominated by junctions with amorphous barriers. The nearly total tunneling spin polarization of $\text{La}_{0.7}\text{Sr}_{0.3}\text{MnO}_3$, when integrated into partially or fully epitaxial magnetic tunnel junctions, offers insight into the relationship between an insulating material's electronic structure and tunneling magnetotransport. In addition to transport experiments through epitaxial SrTiO_3 , $\text{Ce}_{0.69}\text{La}_{0.31}\text{O}_{1.845}$, TiO_2 , MgO , and amorphous Al_2O_3 , barriers, we have performed XMCD experiments on Al_2O_3 and MgO barriers to probe the theoretical underpinnings of our transport results. The half-metallic nature of $\text{La}_{0.7}\text{Sr}_{0.3}\text{MnO}_3$ is then utilized in $\text{La}_{0.7}\text{Sr}_{0.3}\text{MnO}_3/\text{SrTiO}_3/\text{La}_{0.7}\text{Sr}_{0.3}\text{MnO}_3$ and $\text{La}_{0.7}\text{Sr}_{0.3}\text{MnO}_3/\text{SrTiO}_3/\text{Co}$ junctions to quantitatively confirm the spectroscopic nature of spin-dependent solid state tunneling between ferromagnetic electrodes. These bias-dependent studies underscore the influence of interfacial spin wave generation on the ferromagnetic order of the manganate/insulator interface near its Curie point. Finally, we utilize electromigration to modify both the density of states and the potential profile of the interfaces. We show how harnessing this effect may lead to a device with bistable magnetotransport properties; and we examine within the Fowler-Nordheim tunneling regime the incidence of such junction modifications on the formation of quantized energy states within the barrier, and the perturbation of interlayer exchange coupling between the ferromagnetic electrodes.